ANION PHOTOELECTRON SPECTROSCOPIC STUDIES: FROM BIOMOLECULES, TO SIMPLE ORGANICS, TO METAL COMPOUNDS

by
Angela Marie Buonaugurio

A dissertation submitted to The Johns Hopkins University in conformity with the requirements for the degree of Doctor of Philosophy

Baltimore, Maryland
May, 2014

ABSTRACT

Photoelectron spectroscopic studies on gas phase mass-selected anions were performed on a variety of molecular systems. These studies are grouped by themes culminating into five chapters discussing biomolecules, electron induced proton transfer, alkoxides, metal oxides, metal cluster reactivity, and electron binding to aromatic molecules. These experiments were primarily performed in the Bowen lab at Johns Hopkins University using our continuous negative ion photoelectron spectrometer. The metal oxide studies were performed on our pulsed negative ion photoelectron spectrometer while the metal cluster reactivity studies were carried out on location at Karlsruhe institute of Technology (KIT), Germany under Professor Hansgeorg Schnöckel using an FT-ICR mass spectrometer.

The study of nucleic acid bases (nucleobases) and their interaction with low energy electrons elucidates a better molecular-level understanding of radiation induced mutagenesis (**Chapter 1**). Additionally, studies of hydrated and rare-gas solvated nucleobase anions provide strong evidence supporting the co-existence of dipole-bound and valence anion states. Modified uracil analogues 6-azauracil and 5-substituted derivatives are discussed in relation to their properties as radiosensitizers.

Electron-induced proton transfer studies (**Chapter 2**) yields information on the most fundamental processes in chemistry. Intramolecular hydrogen bonding is important to the aforementioned biomolecule systems, but carrying out experiments on the systems acetoacetic acid and oxalic acid allow for better insight utilizing molecules with a larger vapor pressure. The system of 1,8-bis(dimethylamino)naphthalene, HCl and an excess

electron inducing intermolecular proton transfer presents a novel acid-base interaction that demonstrates the fundamental processes of how salt complexes are formed.

Chapter 3 presents the adiabatic electron affinities and vertical detachment energies of a series of deprotonated alcohols, also referred to as alkoxides. This information yields O-H bond dissociation energies of the corresponding alcohol using the gas phase acidities of the associated alcohol of interest and the thermochemical cycle.

Zirconium and hafnium transition metal oxides presented in **Chapter 4** examines metals with similar physical properties do not necessarily form oxides that will also exhibit similar properties. Reactivity studies were performed with Al/Ga_{13}^- and surrounding cluster sizes reacting with O_2. This is to further study the odd/even reactivity effect and improve characterization of these clusters, Al/Ga_{13}^- specifically, for use in cluster-assembled materials.

Finally, binding of an excess electron to several aromatic systems are discussed in **Chapter 5**. Benzaldehyde exhibits a unique spectral profile as a result of vibrational progressions from electron attachment. p-Nitroaniline and the chiral molecules of N-paranitrophenylsulfonylalanine and N-paranitrophenylalanine were studied to determine how the smaller molecular components may affect the physical properties of the larger molecular complex.

Readers: Dr. Kit H. Bowen
Dr. D. Howard Fairbrother
Dr. Art Bragg

ACKNOWLEDGEMENTS

First and foremost, I would like to thank my advisor, Professor Kit H. Bowen, for allowing me the opportunity to be a part of his research group. I appreciate the opportunity he has given me to work in such an impressive laboratory and learning skills that will be invaluable towards future endeavors.

In addition, I'd like to thank Allyson Buytendyk, who over the years has become like a sister to me and my partner in crime here. I couldn't imagine what my graduate school experience would have been like without her. She's kept the lab running smoothly, is a perfectionist with every experiment or task she undertakes, and has helped in making irreplaceable memories.

To Soren Eustis, the first person I met when I joined the Bowen lab, he was more than welcoming and always a wealth of knowledge. To Yeon Jae Ko, aside from his helpfulness in lab, I appreciate his introduction to amazing Korean food and fashion advice. To Andrej Grubisic and Di Wang, who were hard at work constructing a new pulsed apparatus when I first joined, they were always willing to pause to help and educate. To Jing Chen, who was not only a supportive lab partner during my time here but also became a beloved friend. I'll remember our trouble shooting SNIPES, late nights collecting data, cooking authentic Chinese food, and sharing life's ups and downs. To Jacob Graham and Evan Collins, aside from being my go-to-guys for the heavy lifting jobs, they have been an asset to the group in computer issues, and giving great advice

with calculations and machining. They will no doubt continue to do great things for the lab. To Xin Tang, who has always been so friendly and has made some great contributions with his work in the upstairs lab.

To Mike Nilles, Shoujun Xu, and Sarah Stokes, who were always helpful with the random questions I have had learning along the way on SNIPES. I very much appreciate their patience and quick phone call and emails responses. To several visiting international students including Jennifer Meyer, Lukas An Der Lan and Harald Schobel, I've made long-lasting friendships with and have expanded my cultural experiences. To those in the chemistry department who always keep the ship rolling, Jean Goodwin and Rosalie Elder in the front offices, Dr. Chuck Long for his electronics services, and Boris Steinberg for his excellent facilities management. To all of my friends whom I have grown up with or met along the way up to this point and are too numerous to list, thank you.

Last but certainly not least, I would like to thank my family who have been extremely encouraging and supportive of me during this time in my life. To my loving parents Tom and Rose, my mommom and poppop, my amazing boyfriend David, and the rest of my extended family, thank you for giving one hundred percent of your love and support to all of my endeavors. Thank you for all the trips down to visit, the lunches and dinners, and of course the help with all of the moving. You are all the best support system anyone could ever ask for. They have always been proud of everything I have accomplished so I dedicate this thesis to them.

TABLE OF CONTENTS

LIST OF TABLES

LIST OF FIGURES

INTRODUCTION

Experimental research involving cluster chemistry focuses on agglomerates of atoms and molecules ranging in size from dimer to hundreds of thousands (up to the nanoscale). This constitutes the intermediate regime between molecules existing in the gas and the condensed phases, presenting a unique perspective for studying the physical and chemical properties of molecular interactions in a stepwise manner. The study of molecules and their clusters allows for better insight about the kinetics, reactivity, stabilities, and geometric and electronic structures of these systems, thus bridging the gap between the isolated molecules, i.e. the gas phase, and the macroscopic, i.e. the bulk material. Negative ion photoelectron spectroscopy is an advantageous technique for investigating the aforementioned physical properties. Attachment of an excess electron allows the cluster to be transported and mass selected via mass spectrometry, while obtaining electron affinities and vertical detachment energies from the photodetachment process yields information pertaining to the neutral.

This technique was pioneered by Hall et al.,[1] and the construction of our photodetachment apparatus modeled after Hall et al. has been previously reported in detail in the theses of J. V. Coe,[2] J. T. Snodgrass,[3] C. B. Freidhoff,[4] and K. M. McHugh.[5] Earlier designs of our apparatus employed an E x B Wien velocity filter as the mass spectrometer. However, this was later replaced with a magnetic sector, and its installation is described in the thesis of T. P. Lippa.[6] Laser upgrades and maintenance may be found in the theses of J. M. Nilles,[7] J. Chen,[8] and in Appendix A of this thesis. The current configuration of this apparatus is illustrated in Figure I.1. The instrument, also named

SNIPES (super negative ion photoelectron spectrometer), consists of a continuous anion source, a mass spectrometer for mass-selecting the anion of interest, and a magnetically shielded field-free, collision-free ion/photon interaction region where electrons are photodetached by an argon ion laser operated intracavity and energy analyzed by a high resolution electron energy analyzer.

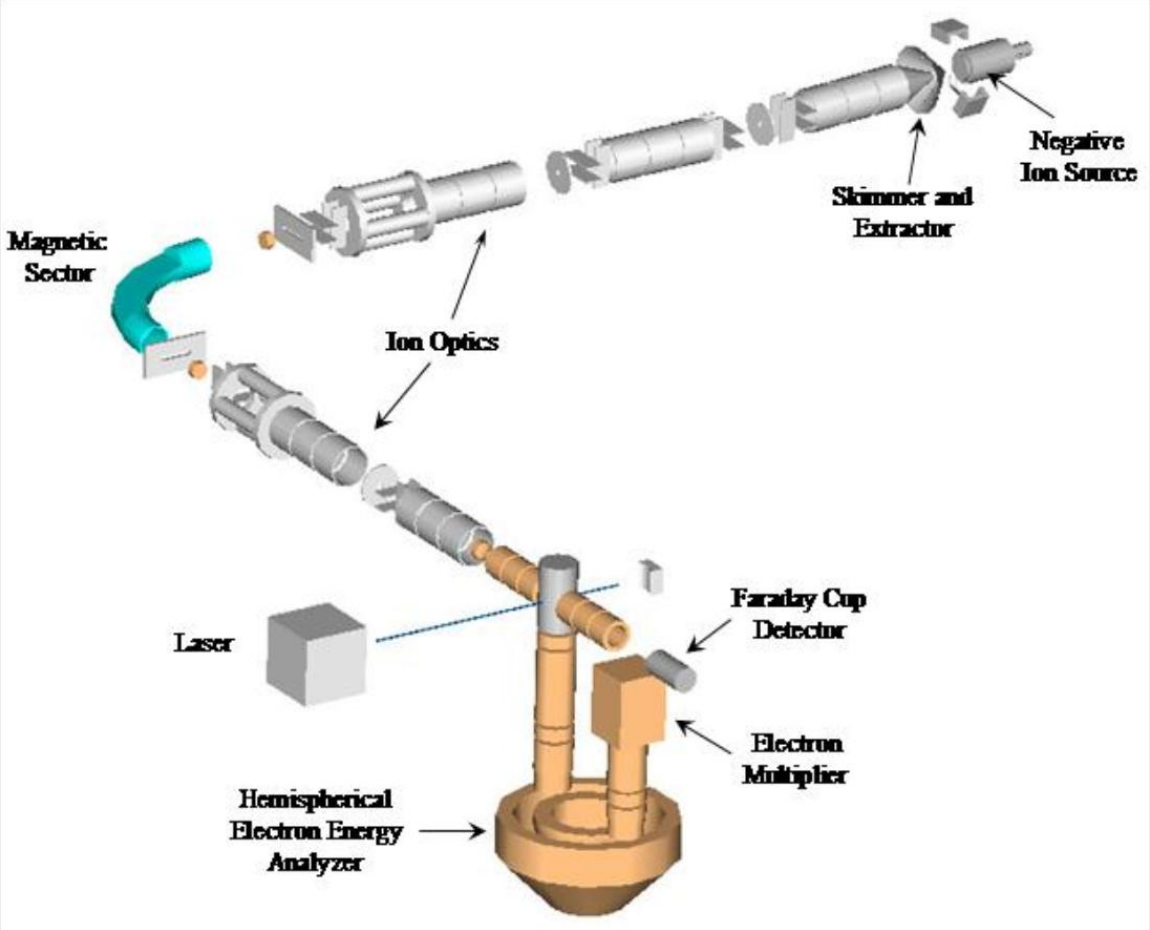

Figure I.1. Schematic diagram of the continuous negative ion photoelectron spectrometer (referred to as SNIPES).

The Ion Source

The anionic species are generated in a supersonic expansion nozzle-ion source. The source is floated at -500 volts in reference to earth ground and is shown in Figure I.2.

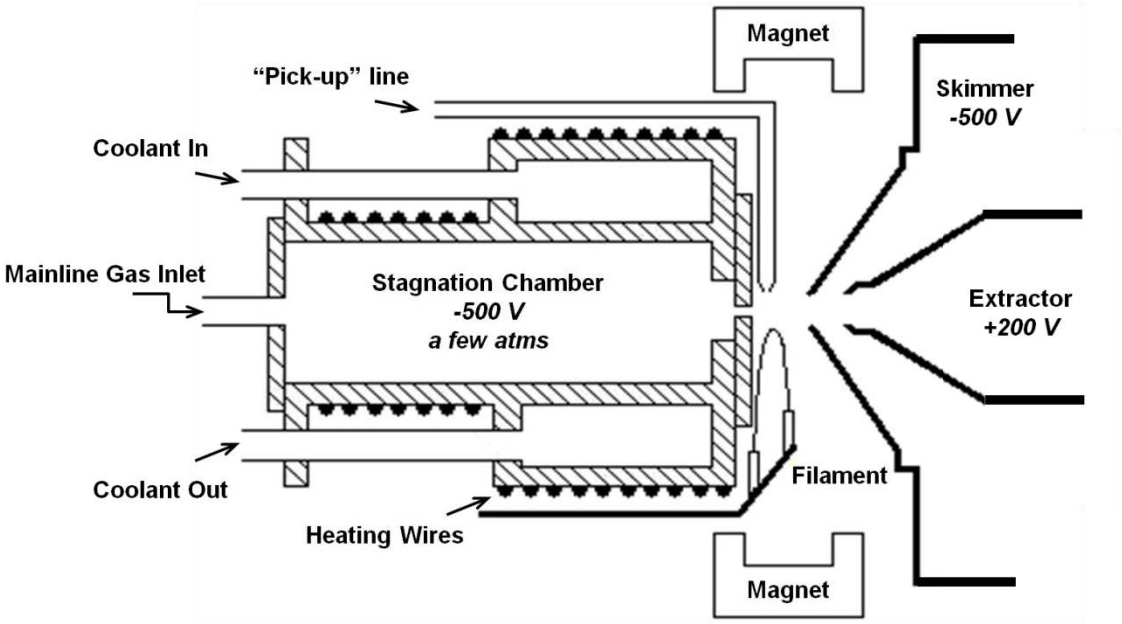

Figure I.2. Illustration of the supersonic expansion nozzle-ion source used on the continuous apparatus (SNIPES).

High pressure argon backing gas seeded with sample vapor is expanded adiabatically through a small stainless steel orifice (10-100 μm) into high vacuum (10^{-5}-10^{-4} torr). The body of the stagnation chamber is equipped with a cooling jacket and resistive heating elements allowing the user to vary the source's temperature from -195 ^{o}C (liquid nitrogen temperature) to ~210 ^{o}C (high-temperature limit of the viton O-ring seals). If the source is to be used at temperatures below -10 °C, a metal indium wire seal must be used for the front nozzle block seal (the rear O-ring seal does not need to be replaced with a metal seal unless temperatures below -77 °C are reached). A negatively biased filament,

ThO_2/Ir (typically for oxidizing gases) or ThO_2/W (typically for reducing gases), is used for ionization, creating a plasma environment of low energy electrons. This plasma is confined by the presence of an axial magnetic field produced by three ~200 G magnets. This magnetic field confines the plasma near the expanding jet beam, as well as enhances anion production.

The primary electrons ejected from the filament collide with the expanding gas and produce even lower energy secondary electrons, which are involved in the electron attachment and are necessary for gentle anion formation. Filament location is an important variable in determining the intensities of the cluster ions produced as well as the types of anions observed. In many cases, for example, dipole-bound anions are formed when the filament position is close to the skimmer, while for valence bound anions the filament is positioned closer to the nozzle of the source. A secondary gas inlet, referred to as the "pick-up" line, was fashioned by crimping a 1/8" copper tubing to a slit length of approximately 1mm x 0.1mm. This is located just outside the nozzle orifice, and the flow rate of the gas for the "pick-up" line is controlled with a variable leak valve. This inlet allows for additional gas mixtures to be added via effusive flow and is then drawn into the supersonic expansion, forming novel cluster anions species that may otherwise not be possible with simply gas expansion solely through the mainline.

Mass Selection

Once generated, the negative ions are skimmed, extracted with a +200 volt potential, and transported through a series of ion optical components towards the 90^o magnet sector for mass-selection (mass resolution = 400). The ions thus possess a kinetic energy given by Equation 1: (based on mass/charge ratio)

$$K.E. = \frac{1}{2}mv^2 = qV \quad (1)$$

Where m is the mass of the ion, v is the ion's velocity, q is the charge of the ion, and V is the voltage applied to the ion optics.

The mass spectrometer is an electromagnet which separates the ions based on their deflection due to a homogenous magnetic field. The centripetal force on an ion in a homogenous magnetic field is:

$$F = q(v \times B) \quad (2)$$

where B is the strength of the magnetic field. The centripetal force is always perpendicular to the ion's velocity, traversing a path determined by the right-hand rule. The ion also experiences a centrifugal force through the flight tube described as:

$$F' = \frac{mv^2}{r} \quad (3)$$

where r is the ion path's radius of curvature. Only ions with a particular mass-to-charge ratio will experience equal centrifugal and centripetal forces and therefore, will pass through the flight tube to the detector. This may be described by combining Equations 1, 2, and 3:

$$\frac{m}{q} = \frac{(B^2r^2)}{2V} \quad (4)$$

Mass selecting the anion species of interest may be accomplished by adjusting the magnetic field, as shown from Equation 4, to allow the specified m/q to pass through the

flight tube while ions of lighter and heavier masses do not make it through the mass window.

Photodetachment

The process of photodetachment is governed by the conservation of energy relationship:

$$h\nu = EKE + EBE$$

where hν is the known energy of the photon beam typically 2.540 eV (488nm), EKE is the measured kinetic energy, and EBE is the electron binding energy determined, i.e., the transition energy between the anion and a particular vibrational state of its neutral counterpart.

A recorded photoelectron spectrum represents the transitions from the negative ion to various energetically accessible states of the neutral, in which information about the anion and its corresponding neutral may be extracted. The energy difference from the negative ion to its corresponding neutral at their respective optimized geometries, i.e., a ground-to-ground state transition, is defined as the adiabatic electron affinity (EA_a). This is not to be confused with the vertical electron affinity, EA_v, which is the energy difference between the neutral and its anion surfaces at the equilibrium geometry of the neutral. The energy transition between the anion and its corresponding neutral at the optimized geometry of the anion is then defined as the vertical detachment energy (VDE). Generally, $VDE \geq EA_a \geq EA_v$, and these differences between the anion and its corresponding neutral are suggestive in the spectrum. Sharp, narrow peaks indicative of little geometrical difference between the anion and its corresponding neutral is when the VDE is essentially equal to the EA_a. While on the other hand, the broadening of peaks

indicates significant structural differences and shows in the VDE being much larger than the EA_a.

The hemispherical electron energy analyzer operates on principle that voltages can be applied to two hemispheres, creating a pass energy across the two allows only electrons with a particular kinetic energy to pass through undeflected. For the photoelectron spectrum to maintain a constant resolution throughout the full spectral range (typically 30 meV), a series of input optics sit directly above the analyzer to prepare the electrons of the particular kinetic energy with the pass energy needed. The electrons which are allowed to pass through the analyzer undeflected are detected by a Ceratron electron multiplier.

The majority of the anions described here were generated and their photoelectron spectra obtained with this continuous source and photoelectron spectrometer. This includes the parent, solvated and modified nucleic acid bases described in **Chapter 1**, the anions formed from electron induced proton transfer in **Chapter 2**, the anions of the alkoxides in **Chapter 3**, and the anions of several novel aromatic systems in **Chapter 5**. The exception is **Chapter 4** in which the metal and metal oxide systems were generated in a pulsed photoelectron spectrometer or by the Fourier-Transform ion cyclotron resonance (FT-ICR) mass spectrometer described in more detail in the chapter's corresponding introduction.

REFERENCES

1. Cellota, R. J.; Bennett, R. A.; Hall, J. L. *J. Chem. Phys*. **1974**, *60*, 1740.
2. J. V. Coe, Ph.D. Thesis, The Johns Hopkins University, 1986.
3. J. T. Snodgrass, Ph.D. Thesis, The Johns Hopkins University, 1986.
4. C. B. Freidhoff, Ph.D. Thesis, The Johns Hopkins University, 1987.
5. K. M. McHugh, Ph.D. Thesis, The Johns Hopkins University, 1988.
6. T. P. Lippa, Ph.D. Thesis, The Johns Hopkins University, 1998.
7. J. M. Nilles, Ph.D. Thesis, The Johns Hopkins University, 2003.
8. J. Chen, Ph.D. Thesis, The Johns Hopkins University, 2012.

CHAPTER 1

The main topic of this chapter covers our experimental studies involving the parent and solvated anions of nucleic acid bases (NABs), as well as the parent anions of modified nucleobases.

Parent and Solvated Anions of Nucleic Acid Bases

When ionizing radiation interacts with a living cell, reactive species such as electrons and hydroxyl radicals are formed, wherein the nucleobases in DNA provide trapping sites for these electrons. This leads to a cascade of mechanisms involving nucleobase radical anions and ultimately to radiation-induced mutagenesis. Thus, the study of NAB anions relevance towards biological studies and the extent of their electron binding, that is their electron affinities, have remained of interest.[1] The electron affinities of NABs are most easily studied in isolation, i.e. experiments performed in the gas-phase. To further extrapolate information on the electron affinities of the anion systems studied, two different types of molecular anions are observed: dipole-bound anions and valence bound anions.

Adamowicz et al. had predicted that nucleic acid bases possess large dipole moments (~5 D) which make them excellent candidates for forming dipole-bound (DB) anions.[2-4] A dipole moment of the neutral molecule exceeding at least 2.5 D[5-8] is known to bind an excess electron to form the dipole-bound anion. Early photoelectron spectra of NAB anions were recorded by Weinkauf et al.[9] and our group.[10] These dipole-bound anions display unique spectral signatures of a sharp, narrow peak with a small electron affinity (EA), meaning there is little structural difference between the anion formed and its corresponding neutral. This is because the excess electron becomes trapped in the diffuse dipole-bound state of the molecule early in the attachment process. DB anions are often referred to as "doorway" states for the well known conventional or valence-bound anions.[10-13] In this case, the excess electron is attracted to the positive atomic/molecular core and the electron goes into a bonding, anti-bonding, or non-bonding molecular orbital. This results in a broad band spectral signature due to the large structural difference between the produced anion and its corresponding neutral.

We also observed the unique case in which both DB and valence anion spectral signatures were present in the same spectrum when using the rare gas xenon as the solvent.[10] The co-existence of DB and the valence anions appear to be strongly coupled with each other; they effectively form a single state that is a superposition of both DB and valence anion states and shift together upon increased solvation. So far little is known behind their co-existence, yet knowledge of our previous studies allowed for further work involving this DB to valence anion transformation. The question then arose of what happens when other solvents are used with nucleobases involving this DB-to-valence transition.

Section **1.1** presents studies of the DB parent anions of the uracil (U^-), thymine (T^-), 1,3 dimethyluracil (1,3-DMU^-), and 1-methylcytosine (1-MC^-) nucleobases as well as the valence anions of these molecules when solvated by water. This is followed by studying the interesting spectral features associated with DB and valence anions when these systems are solvated by a particular number of rare gases (Ar, Kr, Xe) and nonpolar (CH_4, C_2H_6) molecules.

Modified Uracil Nucleobases

The second part of this chapter presents the photoelectron spectra of modified uracil nucleic acid bases. These types of analogues have attracted significant attention due to their usefulness as therapeutic agents and in pharmaceutical applications. Section **1.2** describes the valence anion system of 6-azauracil, known to inhibit the function of some enzymes.[14-16] This is a modified uracil at the 6- position where the C-H group is replaced with a nitrogen atom. Lastly, section **1.3** discusses our work on the 5-substituted uracils, 5-thiocyanouracil (5-SCNU) and 5-cyanouracil (5-CNU). These analogues are useful as substrates for thymidine kinase,[17] which is required for many antiviral drugs to work effectively. These systems are compared on how effectively each uracil derivative undergoes dissociation upon electron attachment based on the substituent at the 5-position; this being a key requirement as an effective radiosensitizer.

REFERENCES

1. Sevilla, M. D.; Baker, D.; Yan, M.; Summerfield, S. R. *J. Chem Phys*. **1991**, *95*, 3409.
2. Oyler, N. A.; Adamowicz, L. *J. Phys. Chem.* **1993**, *97*, 11122.
3. Oyler, N. A.; Adamowicz, L. *Chem. Phys. Lett.* **1994**, *219*, 223.
4. Desfrancois, C.; Abdoul-Carime, H.; Carles, S.; Periquet, V.; Schermann, J. P.; Smith, D. M. A.; Adamowicz, L. *J. Chem. Phys.* **1999**, *110*, 11876.
5. Fermi, E.; Teller, E. *Physical Review* **1947**, *72*, 399.
6. Crawford, O. H.; Dalgarno, A. *Chem. Phys. Lett.* **1967**, *1*, 23.
7. W.R, G. *Chem. Phys. Lett.* **1970**, *5*, 393.
8. Garrett, W. R. *Physical Review A* **1971**, *3*, 961.
9. Schiedt, J.; Weinkauf, R.; Neumark, D. M.; Schlag, E. W. *Chem. Phys.* **1998**, *239*, 511.
10. Hendricks, J. H.; Lyapustina, S. A.; de, C. H. L.; Bowen, K. H. *J. Chem. Phys.* **1998**, *108*, 8.
11. Compton, R. N.; Carman, H. S., Jr.; Desfrancois, C.; Abdoul-Carmine, H.; Schermann, J. P.; Hendricks, J. H.; Lyapustina, S. A.; Bowen, K. H. *J. Chem. Phys.* **1996**, *105*, 3472.
12. Lecomte, F.; Carles, S.; Desfrancois, C.; Johnson, M. A. *J. Chem. Phys.* **2000**, *113*, 10973.
13. Desfrancois, C.; Periquet, V.; Lyapustina, S. A.; Lippa, T. P.; Robinson, D. W.; Bowen, K. H.; Nonaka, H.; Compton, R. N. *J. Chem. Phys.* **1999**, *111*, 4569.
14. Exinger, F.; Lacroute, F. *Curr. Genet*. **1992**, *22*, 9.

15. Nakanishi, T.; Nakano, A.; Nomura, K.; Sekimizu, K.; Natori, S. J. *Biol. Chem.* **1992**, *267*, 13200.

16. Reines, D. Methods *Enzymol*. **2003**, *371*, 284.

17. van Rompay, A. R.; Norda, A.; Linden, K.; Johansson, M.; Karlsson, A. *Mol. Pharmacol.* **2001**, *59*, 1181.

Section 1.1. Photoelectron Spectroscopic Studies of Water Molecule, Rare Gas Atom and Nonpolar Molecule-Solvated Nucleobase Anions

Jing Chen, Angela Buonaugurio, Svetlana A. Lyapustina, Jay H. Hendricks, Helen L. de Clercq, Dean W. Robinson, and Kit H. Bowen

Department of Chemistry, Johns Hopkins University, Baltimore, Maryland 21218, USA

ABSTRACT

Gas-phase nucleobase anions [uracil- (U^-), thymine- (T^-), 1-3 dimethyluracil- (1,3-DMU^-), and 1-methylcytosine- (1-MC^-)] and their complexes with various solvents, $U^-(H_2O)_{n=1-12}$, $U^-(D_2O)_{n=1-2}$, $U^-(Ar)_{n=1-3}$, $U^-(Kr)_{n=1-2}$, $U^-(Xe)_{n=1-3}$, $T^-(Ar)_{n=1-4}$, $T^-(Kr)_{n=1-3}$, $T^-(Xe)_{n=1-4}$, $T^-(CH_4)_{n=1-2}$, $T^-(C_2H_6)_{n=1-3}$, $DMU^-(H_2O)_{n=1-7}$, $DMU^-(Ar)_{n=1-2}$, $DMU^-(Kr)_{n=1,3,4}$, $DMU^-(Xe)n=_{2-5}$, 1-$MC^-(H_2O)$, and Adenine$^-(Xe)_{n=2-4}$ were studied by means of negative ion photoelectron spectroscopy. All of the bare nucleobase anions studied are dipole-bound (DB), and all of their hydrated anions are valence. The spectra of U^-, $U^-(Ar)_{1,2}$ and $U^-(Kr)$ continue to display the DB anion features only. Upon the solvation of more rare gas atoms, the spectra of $U^-(Ar)_3$, $U^-(Kr)_2$, and $U^-(Xe)_{1-3}$ not only retain the DB signatures but also exhibit the valence anion features. Moreover, the DB

and the valence features simultaneously shift together to higher electron binding energies (EBEs) with increasing numbers of rare gas solvent atoms. Therefore, the co-existing DB and valence bound anions appear to be strongly coupled with each other, i.e. they effectively form a single state that is a superposition of both DB and valence anion states. The "onset size" of the xenon, krypton, and argon solvents for the co-appearance of the two anionic states in both U and T series is one, two, and three, respectively. In addition, a minimum of one ethane molecule or two methane molecules are required to induce the coupling between the two states in T series. Thus, the nucleobase anion – non-polar solvent interaction tracks with the summed polarizability of the non-polar solvent. With better Franck-Condon overlap between the origins of the nucleobase-$(Rg)_n$ (Rg: rare gas) valence anion and the neutral nucleobase$(Rg)_n$ than between those of the nucleobase-$(H_2O)_n$ valence anion and the neutral nucleobase$(H_2O)_n$, the extrapolation of the adiabatic valence electron affinities (AEA_vs), measured from the nucleobase-$(Rg)_n$ valence anions, should lead to significantly improved estimations of the AEA_v values of canonical, molecular nucleobases. AEA_v (U) = 36 ± 22 meV, AEA_v (T) = 32 ± 16 meV, AEA_v (1,3-DMU) = -34 ± 24 meV, and AEA_v (A) = -47 ± 44 meV, are our best recommended extrapolated AEAv values from our experiments. Both the DB and the valence anions of 1,3-$DMU^-(Xe)_1$, 1,3-$DMU^-(Kr)_2$, and 1,3-$DMU^-(Ar)_3$ are completely absent in both the mass spectra and the PES. Beyond these "holes", their PES display similar behavior to the U and T series. The extrapolated AEA_v and AEA_{DB} values for these missing species are at or very close to zero, which may explain why they were not seen. The spectra of $A^-(Xe)_{2\text{-}4}$ follow the same trend as the 1,3-$DMU^-(Xe)_{2\text{-}4}$ series. Neither the parent molecular A^- anion nor $A^-(Xe)_1$ anion was observed in the experiment.

INTRODUCTION

Interest in the interaction of electrons with nucleic acid bases (nucleobases), and thus in the electron affinity values of neutral nucleobases, is motivated by a desire to better understand: (1) mechanisms of radiation damage to DNA, e.g. Sanche's finding that very low energy electrons can cause single and even double strand breaks in DNA[1]; (2) migration of photolytically-generated excess electrons in DNA; and (3) potential for electron damage to nucleobase candidates in primitive, evolutionary environments.

In this context, the determination of electron affinities of DNA and RNA bases is of great significance. The attachment of an excess electron to a polar molecule can produce two different types of anions[2,3]: a valence anion and a dipole-bound (DB) anion. Valence anions bind excess electrons strongly in well-defined molecular orbitals, leading to considerably different molecular structures from those of their neutral precursors. In contrast, DB electrons are weakly bound primarily by electrostatic charge-dipole interactions. Consequently, a DB electron affects the intramolecular structural parameters much less than that of a valence electron. The critical dipole moment for binding an excess electron depends on the molecule moment of inertia,[4-7] but as a rule of thumb, a value of 2.5 D is often adopted.[4]

Despite significant experimental efforts, the valence adiabatic electron affinities (AEA_vs) of DNA bases are still not very well established.[3] For many years, the only experimental evidence for nucleobase anions came from electron spin resonance studies in the condensed phase (valence anions) and electron transmission spectroscopy[8,9] of nucleobase vapors (temporary anion states). In more recent times, there have been indirect measurements of AEA_vs of nucleobases in the gas phase. For example, the

existence of a valence state of the gas-phase uracil (U^-) anion has been observed by Schermann et al. using Rydberg electron transfer spectroscopy.[10] Valence bound anions were prepared by attaching electrons to uracil-argon clusters followed by the evaporation of the argon atoms. The author concluded that AEA_v of U (30-60 meV[10]) is smaller than the DB adiabatic electron affinity (AEA_{DB}) of U (93 meV[11]). They supported this conclusion with DFT calculations which provided a positive AEA_v value of 70 meV.[10] Weinkauf et al.[12] obtained an AEA_v value of 0.15 ± 0.12 eV for U, and 0.12 ± 0.12 eV for thymine (T) from the extrapolation of the AEA_v values of their corresponding hydrated series. Eustis et al.[13] pointed out that these AEA_v values were overestimations of the true AEA_v values. Desfrancois et al.[14] and Sanche et al.[15] suggested roughly zero AEA_v values for both U and T. So far theories[10,16-24] have concluded that the valence anions of the biologically-relevant nucleobases are either slightly stable or unstable relative to their neutral counterparts. In other words, the AEA_vs of nucleobases are either slightly positive or slightly negative, with the predicted AEA_v order being U > T > C > A > G (A: adenine; G: guanine). Only U and T were clearly predicted to have positive AEA_v values, with C being a toss-up.

Taking note of the large dipole moments of nucleobases (4-5 D),[25,26] theories predicted stable, ground state, dipole bound states of nucleobase anions,[27-31] and they were subsequently observed in both anion photoelectron spectroscopic (PES) experiments by ourselves[11,32] and Weinkauf et al.,[12] and in Rydberg electron transfer experiments by Schermann.[10,33] Only the DB anions of U and T were observed. The influence of N-methylation on the AEA_{DB} of U and T has been studied both theoretically[28,29] and experimentally by Rydberg electron transfer spectroscopy.[28] The

change of molecular size with N-methylation leads to a reduction of the electron affinity, which is consistent with our results in this paper.

During the course of electron attachment to polar molecules to form their valence anionic states, DB anions may serve as intermediaries. For this reason, they are sometimes referred to as "doorway" or "stepping stone" states.[34-36] Bowen et al.[32] reported an observation of a transformation from a DB state to a valence state due to solvation effects. Surprisingly, a single molecule of water was found to be sufficient for the DB-to-valence transition. This conclusion was verified in another PES experiment reported by Weinkauf et al.[12] The valence form is stabilized by the interaction with water since the excess electron density of the valence U^- anion is much higher than that of the DB anion, and the water interaction is stronger with a more compact electron distribution. Bowen et al.[32] further performed PES experiments with weaker noble gas solvents observing DB anions in $U^-(Ar)_1$ and $U^-(Kr)_1$ clusters, and a coexistence of both DB and valence anions in the $U^-(Xe)_{1-3}$ system. Their later observation raised the question of DB and valence coupling (coexistence), known in the case of the nitromethane molecule.[34] In addition, Kim et al.[37,38] reported the co-existence of both anionic states in the PES of $(pyridine)_4^-$ and $(pyridine)_3^-(H_2O)_1$ anions. Schermann et al.[10] also reported their simultaneous observation of both valence and DB states of free non-solvated uracil. However, except for the coexistence and marching-together of both DB and valence anions in the $U^-(Xe)_{1-3}$ system reported by our group,[32] none of these studies had direct evidences of coupling between the two anionic states.

Here, we present our experimental results pertaining to the influence of solvation on the affinity of nucleobases towards an electron. We set out a few questions in this

report: (a) Is the observed phenomenon unique to uracil or is it present in other nucleobase anions as well? (b) What is the relationship between the DB and the valence forms in the anion species where both anionic states are present [e.g. $U^-(Xe)$]? (c) Can we estimate the electron affinity of the valence state of nucleobases using measured electron binding energies? (d) Will the valence state take over as more xenon atoms are added to nucleobase$^-$(Xe)? In the following sections, we will address these questions based on the results obtained through the study of gas-phase nucleobase anions and their solvated cluster anions using negative ion photoelectron spectroscopy.

EXPERIMENTAL METHODS

Negative ion photoelectron spectroscopy is conducted by crossing a mass-selected beam of negative ions with a fixed-frequency photon beam and energy-analyzing the resultant photodetached electrons. The photodetachment process is governed by the relationship $h\nu = EBE + EKE$, where $h\nu$ is the photon energy, EBE is the electron binding energy or the transition energy needed to take the anion to a particular vibrational state of its neutral counterpart, and EKE is the electron kinetic energy.

Anion complexes were generated in a supersonic expansion nozzle-ion source, where the samples of interest (All nucleobase compounds were of the highest commercially available purity) were placed in a stagnation chamber, heated to 140 – 170°C and co-expanded with 40 – 60 psig argon gas (or a mixture gas of 85% argon/15% other gas) through a 15 μm orifice into ~10^{-4} torr vacuum. Negative ions were formed by injecting low energy electrons from a negatively biased thoriated-iridium filament into the expanding jet, where a microplasma was formed in the presence of a weak external

magnetic field. These anions were then extracted, collimated, and transferred into the flight tube of a 90° magnetic sector mass spectrometer with a typical mass resolution of ~400. The mass-selected anions of interest were then crossed with the intracavity laser beam of an argon ion laser, and the photodetached electrons were energy-analyzed in a hemispherical electron energy analyzer with a resolution of 30 meV. The photoelectron spectra reported here were all recorded with ~180 circulating watts of 2.540 eV photons and calibrated against the well known PES of O^- anion.[39] A detailed description of this apparatus has been described previously.[40]

RESULTS AND DISCUSSION

Molecular Nucleobase Anions: U^-, T^-, 1,3-DMU^-, and 1-MC^-. The PES Signature of a DB Anion

DB anions exhibit a distinctive photoelectron spectral signature, characterized by a single, strong, narrow feature at very low EBEs and by several much lower intensity features at slightly higher EBEs.[11,41] These spectra are unique, that is, they are unlike those of any other anionic species we have encountered. The photoelectron spectra of DB anions are exemplified by our previously reported[11] spectrum of the U^- anion, an important reference species in the present study (see Figure 1.1.1). The dominant peak in this spectrum is essentially due to the origin transition between the ground state of the U^- anion and its corresponding neutral. The fact that its EBE is so small indicates that the excess electron is bound very weakly, while the unusual narrowness of this peak (almost instrumentally limited) imply that the structure of the anion and its corresponding neutral

are very similar. The much weaker intensity features lying to slightly higher EBE are due to the vibrations of neutral U. The peak maximum in this spectrum corresponds to the vertical detachment energy (VDE) of the anion. The VDE of the U^- anion was measured to be 93 ± 7 meV. As mentioned above, the spectrum of the U^- anion strongly implies that the U^- anion has essentially the same structure as its neutral (see Figure 1.1.2). Under these circumstances, the VDE is either equal to or just slightly larger than the AEA_{DB} in value, and thus the AEA_{DB} of U is near 93 meV, in good agreement with the calculations of Adamowicz and coworkers.[27]

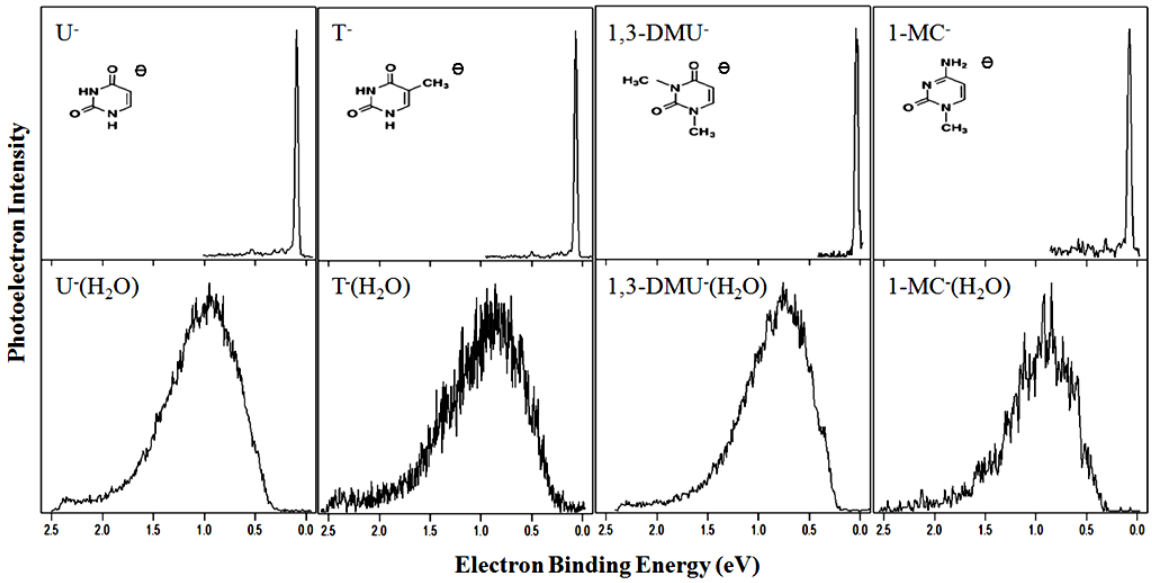

Figure 1.1.1. Photoelectron spectra of the four nucleobase anions: U^-, T^-, 1,3-DMU^-, and 1-MC^- (top row), and their corresponding monohydrate anions: $U^-(H_2O)$, $T^-(H_2O)$, $DMU^-(H_2O)$, and $MC^-(H_2O)$ (bottom row).

The general description given above holds for all DB anions considered here. In particular, it is applicable for DB anions of other nucleobases, namely, T^-, 1,3-DMU^-,

and 1-MC$^-$ (see Figure 1.1.1).[51] All of these display a prominent narrow feature at low EBE and a set of very low intensity vibrational features spaced from the main peak by the energies corresponding the vibrations of their respective neutral molecules. Corresponding VDEs measured from the positions of the main peaks are presented in Table 1.1.1 along with the calculated dipole moments and calculated AEA_{DB} in each case.

Table 1.1.1. Experimental and calculated dipole moments, polarizabilities, and AEA_{DB} of U, T, 1,3-DMU, A, and 1-MC.

Species	Dipole Moment (D)		Polarizability (Å^3)		VDE ≈AEA_{DB} (meV)	
	Expt.	Theory	Expt.	Theory	Expt.	Theory
U	4.16 ± 0.04[42]	4.6[42]		10.09[43]	85 ± 15[10]	86[27]
		5.07[26]			93±7(ours)[11]	
					86 ± 8[12]	
T	4.13 ± 0.03[42]	4.4[42]	11.2[44]	11.3[43]	70 ± 20[28]	88[26]
		4.94[26]	11.2[44]		69±7(ours)[11]	51[20]
					62 ± 8[12]	
1,3-DMU	4.16[42]	4.3[42]			40 ± 20[28]	26[28]
		4.61[46]			37±9(ours)[47]	
A		2.50[48]	13.1[44]	13.1[43]	11[49]	12 ± 6[49]
			13.10[45]			
1-MC		7.56[50]			78 ± 7[51]	56[28]

Results presented in Table 1.1.1 show that the electronic structures of the molecular nucleobase anions are largely determined by the permanent dipole field of these molecules. Their valence monomer anions, if they are stable at all, must be less stable than their DB anions since our supersonic expansion ion source produces anions in their lowest ground electronic states. For example, in the case of such systems as nitromethane[34] and nitrobenzene[36] in which both states are available but the valence form is the ground state and the DB is the excited state of the anion, only the lower energy (valence) state was observed. When the stabilities of the two states coincide, both of them are observed, as demonstrated by our results presented later in this report [e.g. $U^-(Xe)$]. Therefore, the stability of the valence states of U^-, T^-, 1,3-DMU^-, and 1-MC^- must be less than that of their corresponding DB anions.

The PES presented in Figure 1.1.1 and described above clearly identifies DB anions as a separate and unique class of stable anions, where major attributes of electron binding are governed by the interactions of the excess electron with the dipole field. A quantitative look at these spectra, though, reveals that the phenomenon of dipole binding is perhaps more involved than it was thought initially. For example, at the first-order approximation, the excess charge stabilization in these anions must come primarily from the charge-permanent dipole and charge-induced dipole interactions. In other words, if a molecule possesses the dipole moment μ and polarizability α, its EBE should be roughly proportional to μ and α in accordance with the simple electrostatic equation:

$$EBE = -\mu e^2/r^2 - \alpha/r^3$$

Therefore, a straightforward correlation could be expected between the μ and α of the neutral molecule and its EBE. However, the results collected in Table 1.1.1 show that

this simple rule is not always obeyed. For instance, U and T have a similar μ, and T has the higher α of the two, yet the AEA_{DB} of T is lower than that of U. Another example is 1-MC. Both of its μ and α values are higher than those of U, but its EBE is lower.

Overall, from the data in Table 1.1.1, one can draw two interesting conclusions. First, the general agreement between calculated and experimental values for electron binding shows that the current theoretical treatments of this problem are adequate for the most part. Second, there is no direct correlation between the magnitude of the dipole moment and the strength of electron binding, which suggests that there are some other factors at play that yet need to be recognized.

Another important consideration concerns the comparison of the EBEs for different tautomeric forms of the same compound, which have different μ values but practically the same α values. The DB anions studied in the present experiments were most likely formed by attaching the excess electron to the tautomers identified by structures indicated in Figure 1.1.1, because these were experimentally shown to be the most stable, ground state tautomers for these compounds.[52] (The tautomers shown in Figure 1.1.1 are of the lowest energy as established by X-ray crystallography, and in solutions, for example, by NMR technique in deuterated DMSO.[53] In addition, the diketo form of U was shown to be the most stable configuration in the gas phase by means of high resolution IR spectroscopy of neutral beams.[54] The diketo form of T was confirmed to be the ground state tautomer according to nitrogen-14 nuclear quadrupole resonance study of polycrystalline samples.[55] In 1,3-DMU, both of the nitrogens that could potentially be involved in tautomerization are protected by methyl groups. In 1-MC, the most labile proton of cytosine is replaced by a methyl group).[56] Moreover, given that in

each case only one single peak was observed with a width that is essentially limited by the instrumental resolution, the molecular beams that we produced must have contained only these major tautomers. The only alternative would be for the EBEs of other tautomers to have been the same as that of the primary tautomer ± 0.02 eV, an unlikely possibility given their different dipole moments. Nevertheless, the effect of tautomerization on the electron binding properties was investigated by theory to some extent. Remarkably, the results of ab initio calculations are sometimes counterintuitive. For T, the dioxo and 4-hydroxy tautomers were predicted[26] to have AEA_{DB} values of 88 meV and 60 meV, respectively, despite a significant increase in the calculated dipole moment from 4.94 D in dioxo to 5.78 D in 4-hydroxy tautomer. However, in the case of guanine (G),[57] the predicted AEA_{DB} values for the oxo-amino and hydroxy-amino forms (0.034 eV and 0.00038 eV) are in line with their calculated dipole moments (7.4 D and 3.3 D), although again, both of the predicted AEA_{DB} values are surprisingly small in view of the large dipole moment of G relative to the corresponding values of the system investigated in this report. As an explanation for this behavior, Oyler and Adamowicz[26] proposed that some valence character may be mixed in with the DB orbital, and the extent of this balance between the valence and dipole binding will determine relative stabilities of anions. In fact, the contour plot[27] of the molecular orbital occupied by the excess electron in a DB anion of U, as well as some other DB anions [e.g. $(HF)^{2-}$[58,59]] show that while the major part of the orbital is situated outside of the molecular frame, some portion of the electron density is present on the molecule itself, which is an attribute of a valence anion. These examples show that physical foundations of DB theory have

already gone a long way and the current picture is much more sophisticated than the original notion.

Singly Hydrated Nucleobase Anions: $X^-(H_2O)$ (X = U, 1,3-DMU, 1-MC), and $U^-(D_2O)$. The Appearance of the Valence States.

We now turn to the issue of the electronic state of nucleobase anions when they experience condensed phase-like interactions. Naturally, the condensed phase environment with the most relevance to biological problems is that provided by water. Therefore, we conducted a series of experiments on hydrated nucleobase anions, adding one water molecule at a time, and recording the photoelectron spectra of the resultant cluster anions, looking for the appearance of the valence state. As shown at the bottom row of Figure 1.1.1, broad, unresolved, Franck-Condon envelopes appear in the PES of the hydrated nucleobase anions, indicative of a substantial structural difference between the anions and the corresponding neutrals (see Figure 1.1.2). Evidently, the valence anion state emerges as soon as only one water molecule interacts with the molecular nucleobase anions.

To confirm these observations, a number of control experiments were performed. Proton NMR analysis confirmed that the U sample in our chamber did not undergo any chemical reorganization in the presence of water and is a result of the high temperatures and high pressures applied within the source. The photoelectron spectrum of 1,3-$DMU^-(H_2O)$ anion is analogous to that of $U^-(H_2O)$ anion rule out the possibility that the cluster anion we observed might have been a tautomeric form of $U^-(H_2O)$, because both of the potential tautomerization sites are protected by the methyl group in the DMU case.

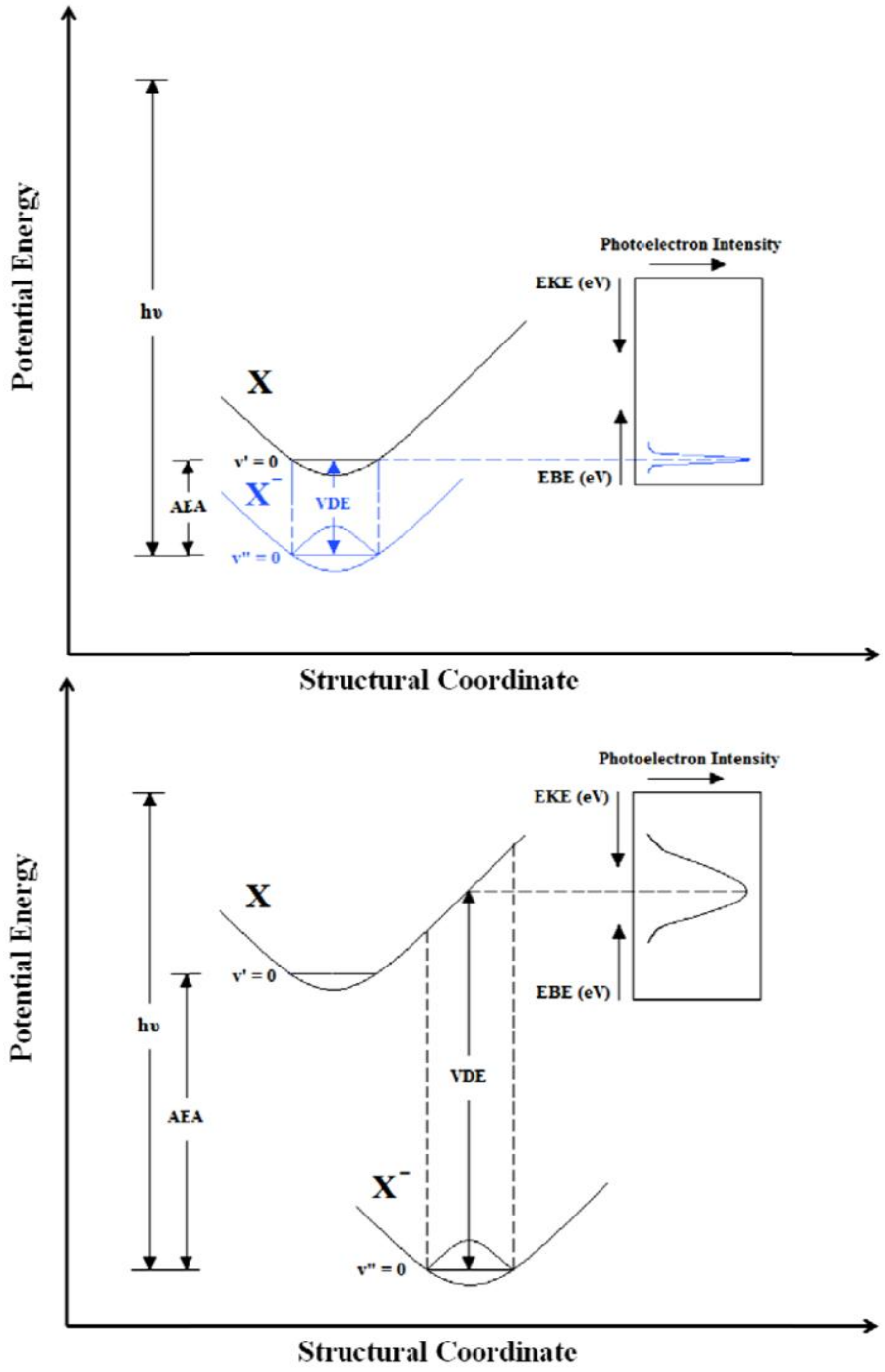

Figure 1.1.2. Diagram showing the relationships between the VDE and AEA in the resulting photoelectron spectrum of a dipole-bound anion (upper trace) and a valence anion (lower trace).

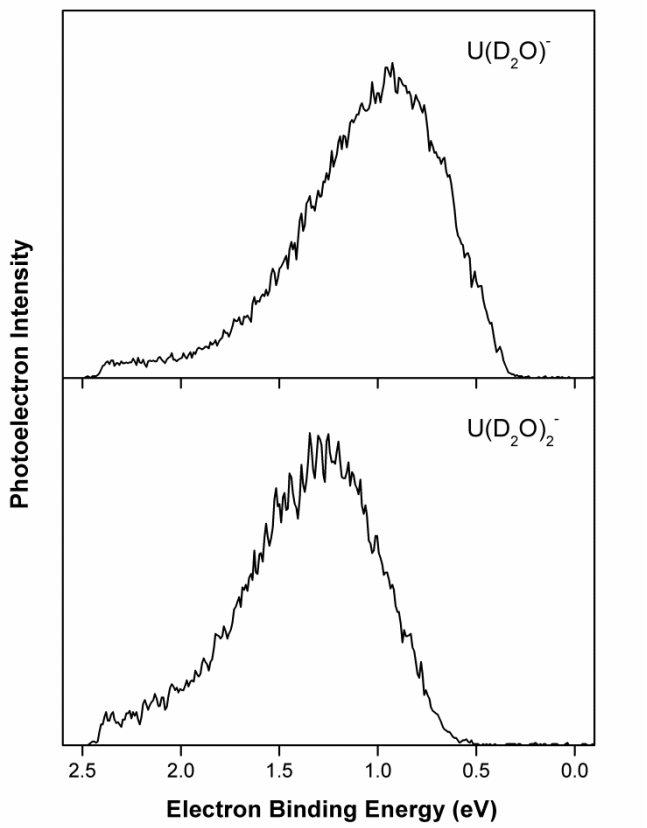

Figure 1.1.3. Photoelectron spectra of heavy water molecule-solvated uracil anions, $U^{-}(D_2O)$ and $U^{-}(D_2O)_2$.

The photoelectron spectra of $T^{-}(H_2O)$ and 1-$MC^{-}(H_2O)$ anions also give a valence anion type signature, underscoring the generality of the phenomenon. The spectrum of $U^{-}(D_2O)$ is nearly identical to that of $U^{-}(H_2O)$ (see Figure 1.1.3).

Multiply Hydrated Nucleobase Anions: $U^{-}(H_2O)_n$, $U^{-}(D_2O)_n$, and $DMU^{-}(H_2O)_n$.

The spectra presented in Figure 1.1.4 and Figure 1.1.5 provides insight into the energetics and structures of these water solvated nucleobase anions. Each series of

spectra shows the same photoelectron signature being shifted to successively higher EBEs as the number of water molecules per cluster increases. The corresponding VDEs, stepwise stabilization energies ΔSE(n) = VDE(n) – VDE (n-1) are listed in Table 1.1.2.

Table 1.1.2. The VDEs and stepwise stabilization energies ΔSE(n) = VDE(n) – VDE (n-1) of $U^-(H_2O)_n$, $U^-(D_2O)_n$, 1,3-$DMU^-(H_2O)_n$ and 1-$MC^-(H_2O)$. The error bar for VDE is ± 0.02 eV.

System	VDE (eV)	ΔSE (eV)	System	VDE (eV)	ΔSE (eV)
$U^-(H_2O)$	0.93		**1,3-$DMU^-(H_2O)$**	0.74	
$U^-(H_2O)_2$	1.26	0.33	**1,3-$DMU^-(H_2O)_2$**	1.05	0.31
$U^-(H_2O)_3$	1.49	0.23	**1,3-$DMU^-(H_2O)_3$**	1.30	0.25
$U^-(H_2O)_4$	1.69	0.20	**1,3-$DMU^-(H_2O)_4$**	1.50	0.20
$U^-(H_2O)_5$	1.88	0.19	**1,3-$DMU^-(H_2O)_5$**	1.66	0.16
$U^-(H_2O)_6$	2.01	0.13	**1,3-$DMU^-(H_2O)_6$**	1.80	0.14
$U^-(H_2O)_7$	2.10	0.09	**1,3-$DMU^-(H_2O)_7$**	1.94	0.14
$U^-(H_2O)_8$	2.18	0.08			
$U^-(H_2O)_9$	2.25	0.07			
$U^-(D_2O)$	0.93		**1-$MC^-(H_2O)$**	0.85	
$U^-(D_2O)_2$	1.26	0.33			

The error bar for VDE determination is ± 0.02 eV and is mainly due to the uncertainty of fitting the peak to an asymmetric Gaussian.

In addition to the PES of $U^{-}(H_2O)_n$, $U^{-}(D_2O)_n$, and 1,3-$DMU^{-}(H_2O)_n$ (Figure 1.1.3 to 1.1.5), the mass spectra of $U^{-}(H_2O)_n$ cluster anions and 1,3-$DMU^{-}(H_2O)_n$ cluster anions (Figures 1.2.6 and 1.2.7) reveal that while the intensity of the parent DB anion in either case is extremely low, the electron attachment to hydrated nucleobases produces cluster anions in abundance, with n = 2 as the preferred cluster size for both $U^{-}(H_2O)_n$ and $DMU^{-}(H_2O)_n$. The small intensity peaks in these mass spectra are neat water cluster anions $(H_2O)_n^{-}$.

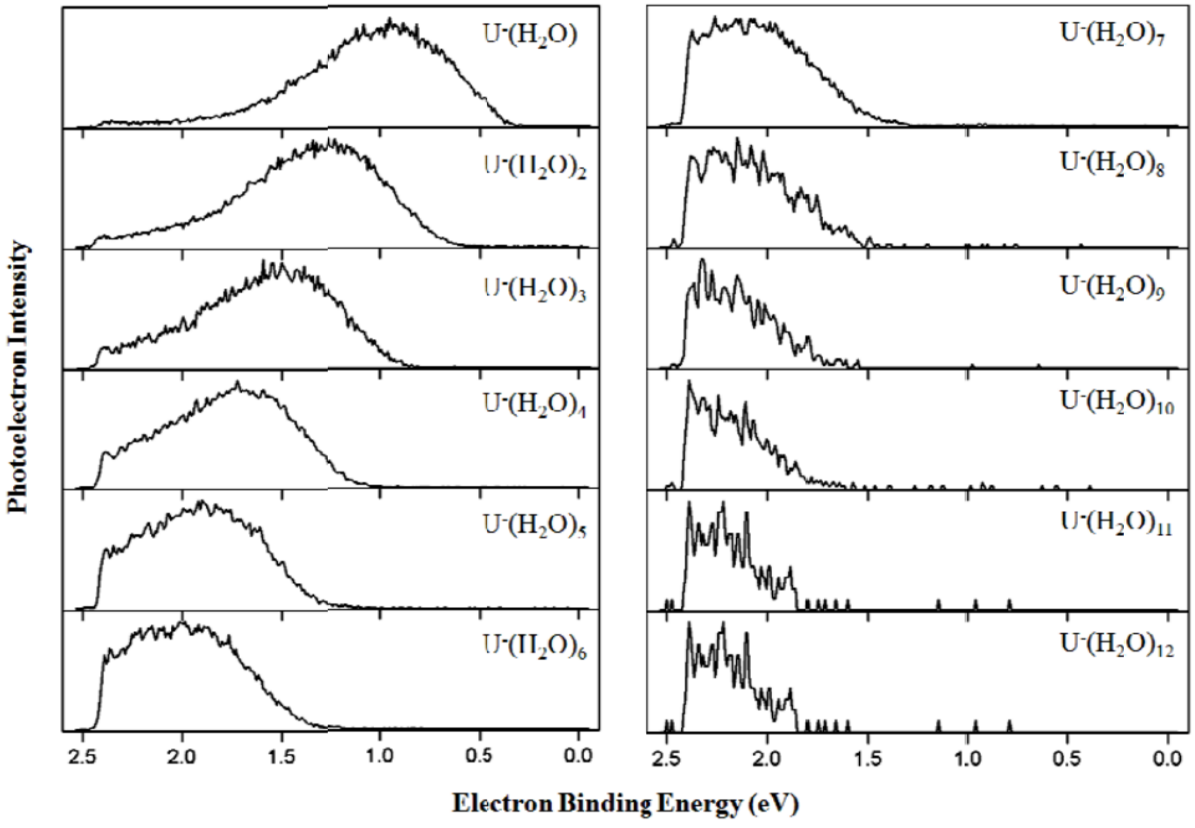

Figure 1.1.4. Photoelectron spectra of water molecule-solvated uracil anions, $U^{-}(H_2O)_{1\text{-}12}$.

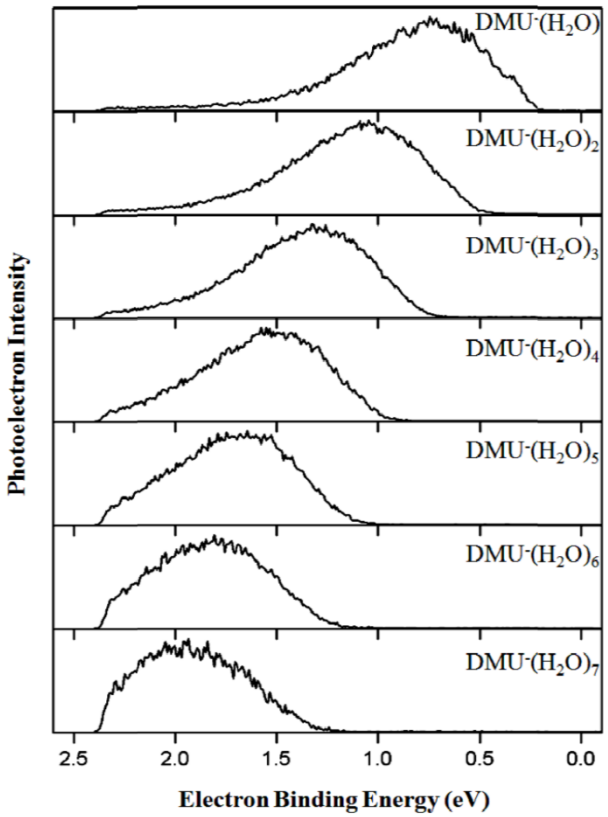

Figure 1.1.5. Photoelectron spectra of water molecule-solvated 1,3-dimethyluracil anions, 1,3-$DMU^{-}(H_2O)_{1\text{-}7}$.

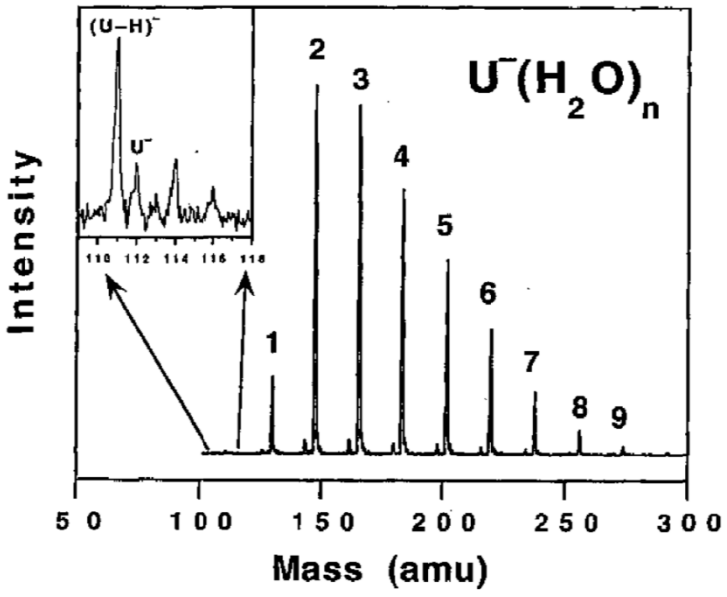

Figure 1.1.6. Mass spectrum of water molecule-solvated uracil anions, $U^{-}(H_2O)_n$.

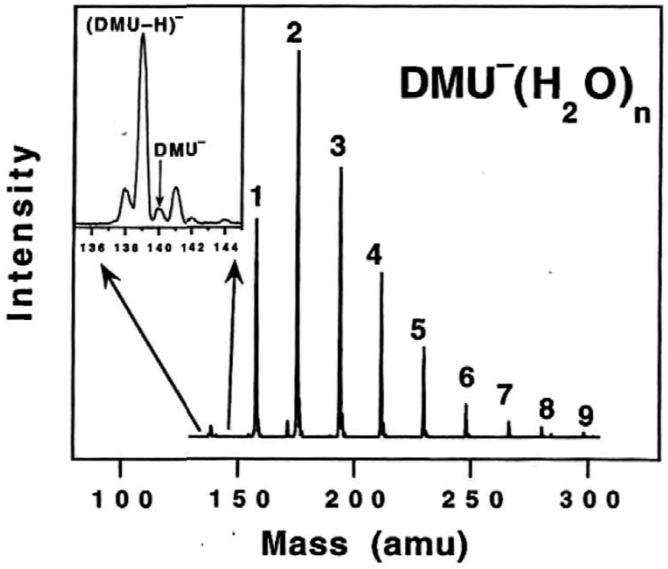

Figure 1.1.7. Mass spectrum of water molecule-solvated 1,3-dimethyluracil anions, 1,3-$DMU^{-}(H_2O)_n$.

Rare Gas or Nonpolar Molecule-Solvated Nucleobase Anions: $X^{-}(Rg)_n$ (X= U, T, 1, 3-DMU, A; Rg = Ar, Kr, Xe), $T^{-}(CH_4)_n$, and $T^{-}(C_2H_6)_n$.

Coupling of the DB and valence anionic states

Since the interaction of one water molecule with the nucleobase anions was enough to make the valence state energetically more stable than the DB state, the effect of weaker solvents in hopes of seeing a gradual transition was explored.

The spectra of U^{-}, $U^{-}(Ar)_{1\text{-}2}$ and $U^{-}(Kr)_1$ continue to display the DB anion features only (see Figure 1.1.8), and the EBE was increased only marginally (see Table 1.1.3). Upon the solvation of more rare gas atoms, dramatic effects were observed: the spectra of $U^{-}(Ar)_3$, $U^{-}(Kr)_2$, and $U^{-}(Xe)_{1\text{-}3}$ not only retain the DB signatures but

also exhibit the valence anion features; in other words, the DB and the valence anions appear together in these spectra (Figure 1.1.8) . For the DB feature, the $VDE_{DB} \approx AEA_{DB}$,

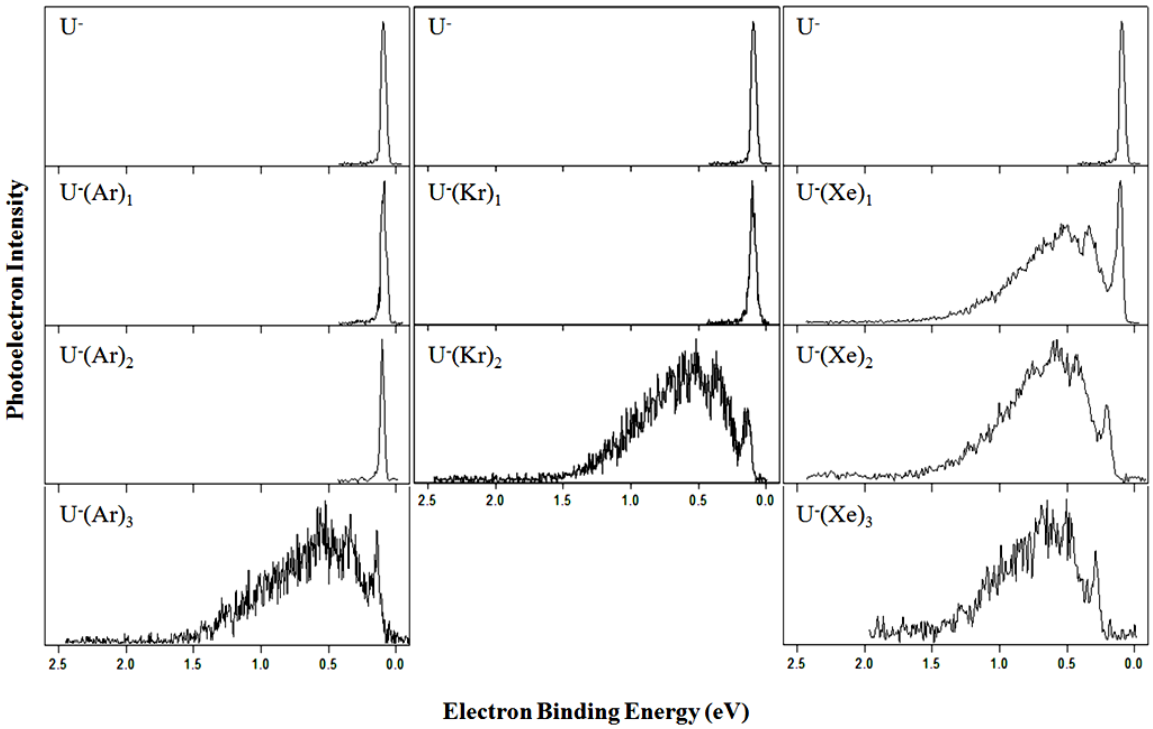

Figure 1.1.8. Photoelectron spectra of the U^- anion and its solvation series with argon, krypton, and xenon atoms, i.e., $U^-(Ar)_{1\text{-}3}$, $U^-(Kr)_{1\text{-}2}$, and $U^-(Xe)_{1\text{-}3}$. The peak centers for these spectra are listed in Table 1.1.3.

as previously discussed. For the valence form, there is clearly a substantial structural difference between the anion and its neutral (as evidenced by the broad width of its partially resolved vibrational progression), and thus, $VDE_V > AEA_V$. The AEA_V lies at the low EBE edge of this feature, that is, essentially at the same EBE as the VDE_{DB}. A schematic illustration of the neutral and anionic (both DB and valence) potential wells of $U(Xe)_1$ and $U(H_2O)_1$ is shown in Figure 1.1.9.

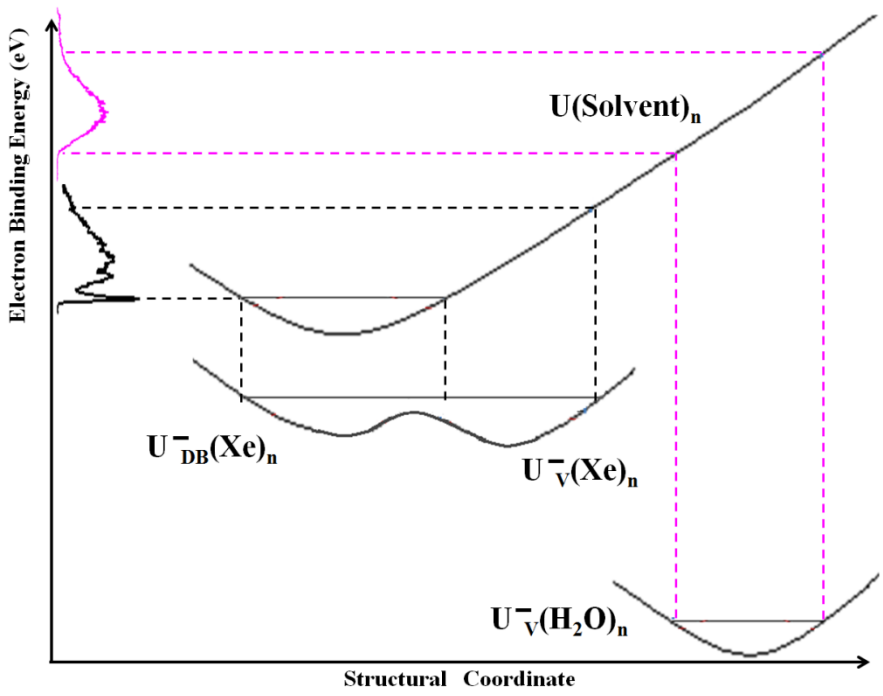

Figure 1.1.9. Illustration of the neutral and anionic (both DB and valence) potential wells of $U(Xe)_n$ and $U(H2O)_n$ clusters.

Initially, we assumed that the two anionic features in these spectra were due to two separate (distinct) species: a DB and a valence anion which, by coincidence, have the similar energy relative to the corresponding neutral complex. Because the DB anions have much more diffuse charge densities than their valence anion counterparts, it is expected that the sequential solvation energies of the two anionic states should differ dramatically. However, this is clearly not the case; in the spectra of $U^-(Ar)_3$, $U^-(Kr)_2$, and $U^-(Xe)_{1\text{-}3}$ (Figure 1.1.8), the DB and the valence features simultaneously shift together to higher EBEs with increasing numbers of rare gas solvent atoms. Therefore,

Table 1.1.3. EBEs of the main peaks where $VDE_{DB} = AEA_{DB}$. $VDE_{1,2}$ and $EBE_{1,2,3}$ are EBEs of DB and valence peaks in the order of increasing EBE values, respectively.

Anion Species	DB Anion Spectral Features (eV)		Valence Anion Spectral Features (eV)		
	VDE1	VDE2	EBE1	EBE2	EBE3
U^-	0.093 ± 0.010				
$U^-(Ar)1$	0.093 ± 0.010				
$U^-(Ar)2$	0.103 ± 0.009				
$U^-(Ar)3$	0.142 ± 0.015		0.35 ± 0.03	0.54 ± 0.03	
$U^-(Kr)1$	0.102 ± 0.009				
$U^-(Kr)2$	0.144 ± 0.020		0.35 ± 0.02	0.54 ± 0.04	
$U^-(Xe)1$	0.111 ± 0.012		0.32 ± 0.02	0.51 ± 0.03	0.68 ± 0.03
$U^-(Xe)2$	0.208 ± 0.013		0.41 ± 0.02	0.60 ± 0.03	0.76 ± 0.03
$U^-(Xe)3$	0.289 ± 0.010		0.49 ± 0.03	0.68 ± 0.03	0.84 ± 0.03
T^-	0.069 ± 0.007				
$T^-(Ar)1$	0.069 ± 0.008				
$T^-(Ar)2$	0.073 ± 0.009				
$T^-(Ar)3$	0.121 ± 0.015		0.32 ± 0.03	0.51 ± 0.03	0.69 ± 0.04
$T^-(Ar)4$	0.163 ± 0.013		0.36 ± 0.02	0.55 ± 0.03	0.73 ± 0.02
$T^-(Kr)1$	0.073 ± 0.008				
$T^-(Kr)2$	0.069 ± 0.010	0.144 ± 0.015	0.34 ± 0.01	0.53 ± 0.03	
$T^-(Kr)3$	0.169 ± 0.015		0.37 ± 0.02	0.56 ± 0.03	0.73 ± 0.03
$T^-(Xe)1$	0.063 ± 0.008	0.131 ± 0.010	0.31 ± 0.02	0.50 ± 0.03	0.68 ± 0.03
$T^-(Xe)2$	0.193 ± 0.017		0.40 ± 0.03	0.59 ± 0.03	
$T^-(Xe)3$	0.274 ± 0.013		0.48 ± 0.02	0.68 ± 0.03	0.87 ± 0.03
$T^-(Xe)4$	0.324 ± 0.015		0.52 ± 0.03	0.70 ± 0.03	0.88 ± 0.03
$T^-(CH4)1$	0.074 ± 0.007				
$T^-(CH4)2$	0.153 ± 0.015		0.35 ± 0.03	0.54 ± 0.03	0.70 ± 0.03
$T^-(C_2H_6)1$	0.062 ± 0.007	0.142 ± 0.015	0.34 ± 0.02	0.53 ± 0.02	0.69 ± 0.03
$T^-(C_2H_6)2$	0.243 ± 0.030		0.44 ± 0.03	0.62 ± 0.03	
$T^-(C_2H_6)3$	0.325 ± 0.030		0.54 ± 0.04	0.74 ± 0.03	
1,3-DMU^-	0.037 ± 0.009				
1,3-$DMU^-(Ar)1$	0.043 ± 0.009				
1,3-$DMU^-(Ar)2$	0.053 ± 0.010				
1,3-$DMU^-(Kr)1$	0.046 ± 0.009				
1,3-$DMU^-(Kr)3$	0.085 ± 0.013		0.30 ± 0.01	0.47 ± 0.03	0.63 ± 0.03
1,3-$DMU^-(Kr)4$	0.125 ± 0.012		0.32 ± 0.02	0.52 ± 0.03	0.69 ± 0.02
1,3-$DMU^-(Xe)2$	0.112 ± 0.010		0.32 ± 0.02	0.51 ± 0.03	
1,3-$DMU^-(Xe)3$	0.182 ± 0.015		0.39 ± 0.02	0.57 ± 0.03	0.74 ± 0.03
1,3-$DMU^-(Xe)4$	0.252 ± 0.017		0.46 ± 0.02	0.63 ± 0.03	
1,3-$DMU^-(Xe)5$	0.312 ± 0.017		0.53 ± 0.02	0.72 ± 0.03	
A^-					
$A^-(Xe)2$	0.091 ± 0.020		0.28 ± 0.02	0.47 ± 0.03	
$A^-(Xe)3$	0.166 ± 0.010		0.36 ± 0.02	0.55 ± 0.03	
$A^-(Xe)4$	0.234 ± 0.010		0.42 ± 0.02	0.59 ± 0.03	

instead of being two separate anionic states, the co-existing DB and valence anions appear to be strongly coupled with each other, i.e. they effectively form a single state that is a superposition of both DB and valence anions states.

There have been several other studies that also indicated the coexistence of DB and valence anionic states. Weinkauf et al.[12] reported the co-appearance of DB and the valence anionic features in the PES of $U^-(H_2O)_{2,4}$, $C^-(H_2O)_{2,4}$, and $T^-(H_2O)_{2,4}$. In these cases, the two anionic states do not belong to the same anion species. The DB features come from the molecular nucleobase anions U^-, C^-, and T^-, which are the photodissociation products of $U^-(H_2O)_{2,4}$, $C^-(H_2O)_{2,4}$, and $T^-(H_2O)_{2,4}$, respectively. In addition, Kim et al.[37,38] reported the co-existence of both anionic states in the PES of $(pyridine)_4^-$ and $(pyridine)_3^-(H_2O)_1$ anions. Again, however, there was no direct evidence of coupling between the two anionic states. (In Kim's experiments, the DB and valence bands were not overlapping, and they were clearly separated by an energy window of over 0.1 eV. Moreover, upon the addition of more pyridine molecules to the $(pyridine)_4^-$ anion, the valence band was shifting to the blue, while the position of the DB feature remained the same.[38] The conclusion of the authors was that in the $(pyridine)_4^-$ anion, the two anionic states are separated by a substantial energy barrier, and therefore remain essentially uncoupled.) As far as our knowledge goes, we have the single evidence so far for the DB and the valence anionic states co-appearing and marching together simultaneously upon the same solvation, i.e. strong coupling.

"Everything" tracks with polarizability.

Interesting patterns were observed when comparing the spectra of the nucleobase anions solvated by several different rare gas atoms (see Figure 1.1.10 and 1.1.11). The co- existence of the two anionic states in both the U and T series first occurs (i.e., "onset size") with one xenon, two krypton, or three argon atoms. Note that one xenon, two krypton, or three argon atoms give the same total (summed) polarizability (see Table 1.1.4). Therefore, the co-existence of the two anionic states tracks with the summed polarizability of the rare gas solvents. The following paragraph suggests an explanation for this observation.

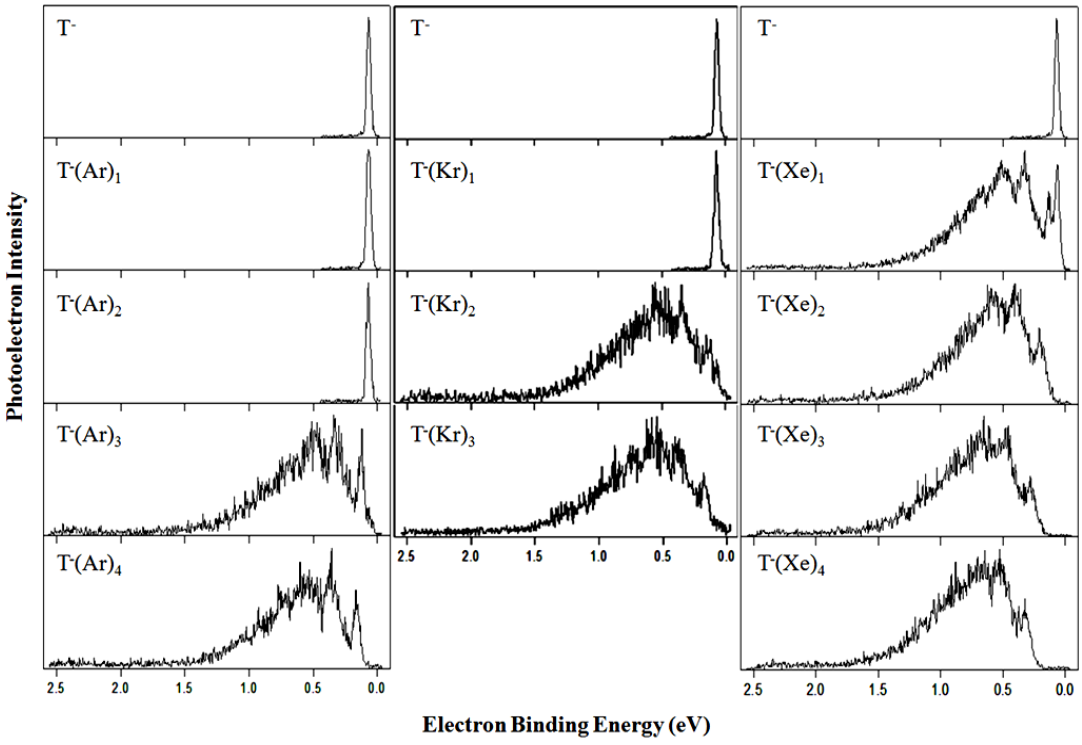

Figure 1.1.10. Photoelectron spectra of the T^- anion, and its solvation series with argon, krypton, and xenon atoms, i.e., $T^-(Ar)_{1\text{-}4}$, $T^-(Kr)_{1\text{-}3}$ and $T^-(Xe)_{1\text{-}4}$. The peak centers for these spectra are listed in Table 1.1.3.

Table 1.1.4. Summed polarizabilities (Σα) of the solvents.

Number of Solvents	$\Sigma[\alpha(Ar)_n]$ ($Å^3$)	$\Sigma[\alpha(Kr)_n]$ ($Å^3$)	$\Sigma[\alpha(Xe)_n]$ ($Å^3$)	$\Sigma[\alpha(CH_4)_n]$ ($Å^3$)	$\Sigma[\alpha(C_2H_6)_n]$ ($Å^3$)
1	1.64	2.48	4.04	2.59	4.47
2	3.28	4.96	8.08	5.18	8.94
3	4.92	7.44	12.12	7.77	13.41
4	6.56	9.92	16.16	10.36	17.88
5	8.20	12.4	20.2	12.95	22.35

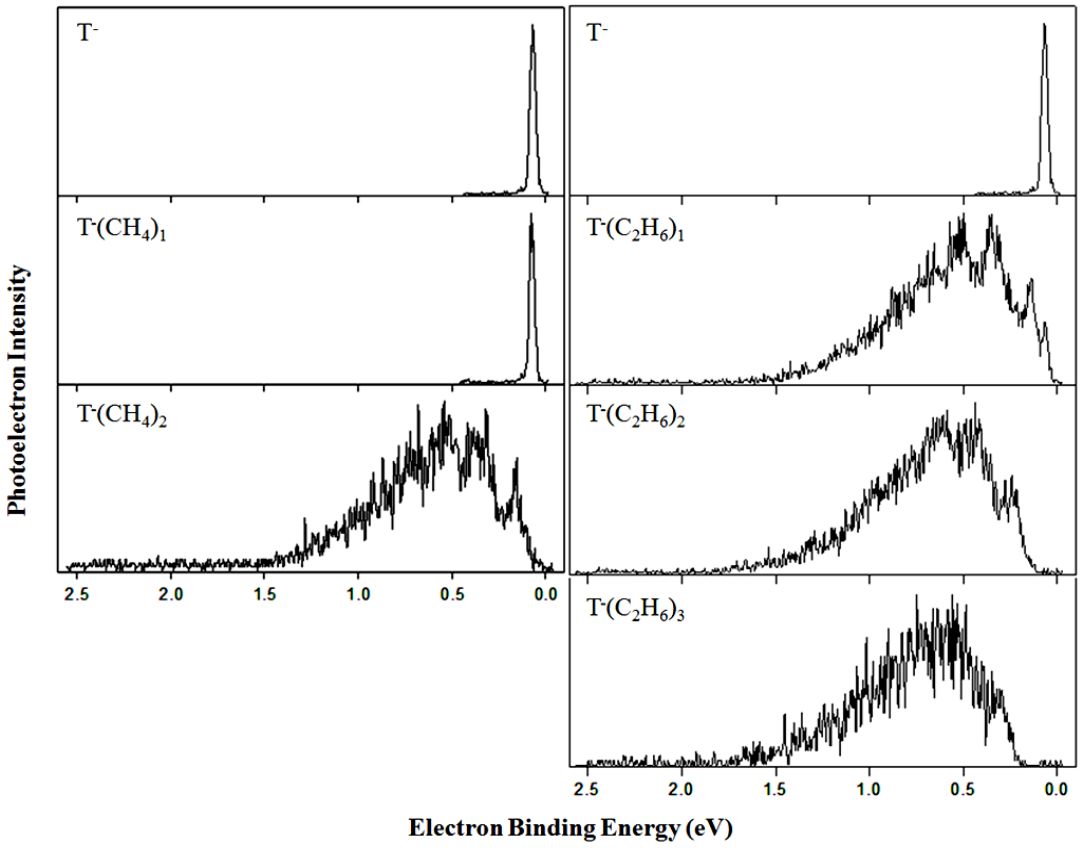

Figure 1.1.11. Photoelectron spectra of the T^- anion, and its solvation series with methane and ethane molecules, i.e., $T^-(CH_4)_{1,2}$ and $T^-(C_2H_6)_{1\text{-}3}$. The peak centers for these spectra are listed in Table 1.1.3.

When rare gas atoms are used as solvents, the main term in the stabilization energy (SE) is due to the ion-induced dipole interactions. It is, therefore, proportional to the total polarizability of the rare gas atoms (i.e. $\Sigma\alpha$), and inversely proportional to the third power of the distance (r) between the solvent and the center of the charge distribution, or the charge density on the anion:

$$SE \sim \Sigma\alpha/r^3$$

The nearly linear dependence of the total stabilization energy [e.g. $AEA(U(Rg)_n - AEA(U)]$ on $\Sigma\alpha$ of the rare gas solvents can been seen in Figure 1.1.12. It demonstrates that a more localized molecular orbital (valence) enjoys stronger interaction with the solvent, which helps explain why the valence anion becomes the more stable species with increasing solvation.

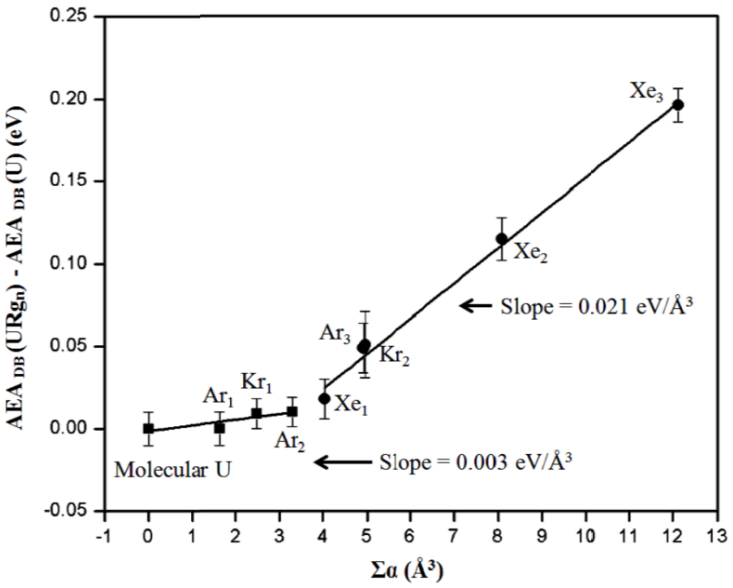

Figure 1.1.12. Total stabilization energies of U^- anion as it interacts with rare gas solvents versus the total polarizability of the solvents, $\Sigma\alpha$.

With this correlation in place, we then asked a question: would non-polar molecules other than rare gas atoms show solvation effects that also track with polarizability? If so, because methane and krypton have very similar polarizabilities, as do ethane and xenon (see Table 1.1.4), then the "onset size" would be two for methane (same as krypton), and one for ethane (same as xenon). In support of this statement, Figure 1.1.11 showed that at least two methane or one ethane molecules are required to induce the coupling between the DB and valence anionic states. Thus, the solvation effects of these non-polar molecules continue to track with the polarizabilities of these molecules and their sums as well.

Now, consider the spectral behavior of 1,3-DMU^- anion solvated by rare gas atoms, which at first sight seemed quite odd (see Figure 1.1.13). Whereas the co-existent DB and valence anion states start appearing with one xenon, two krypton, and three argon atoms in the PES of rare gas-solvated U and T anions, species with these numbers of rare gas solvents are completely absent in both the mass spectra and the PES of rare gas- solvated 1,3-DMU^- anions. Even the DB anions of $DMU^-(Xe)_1$, $DMU^-(Kr)_2$, and $DMU^-(Ar)_3$ are missing. Beyond these "holes", the expected ions continue to be seen in the mass spectra, and their PES display similar behavior to the U and T series. A rationalization for the appearance of these "holes" in the spectral data will be presented later in this paper.

The spectra of $A^-(Xe)_{2\text{-}4}$ (Figure 1.1.14) follow the same trend as the 1,3-$DMU^-(Xe)_{2\text{-}4}$ spectra. Neither the parent molecular A^- anion nor $A^-(Xe)_1$ anion was observed in the experiment.

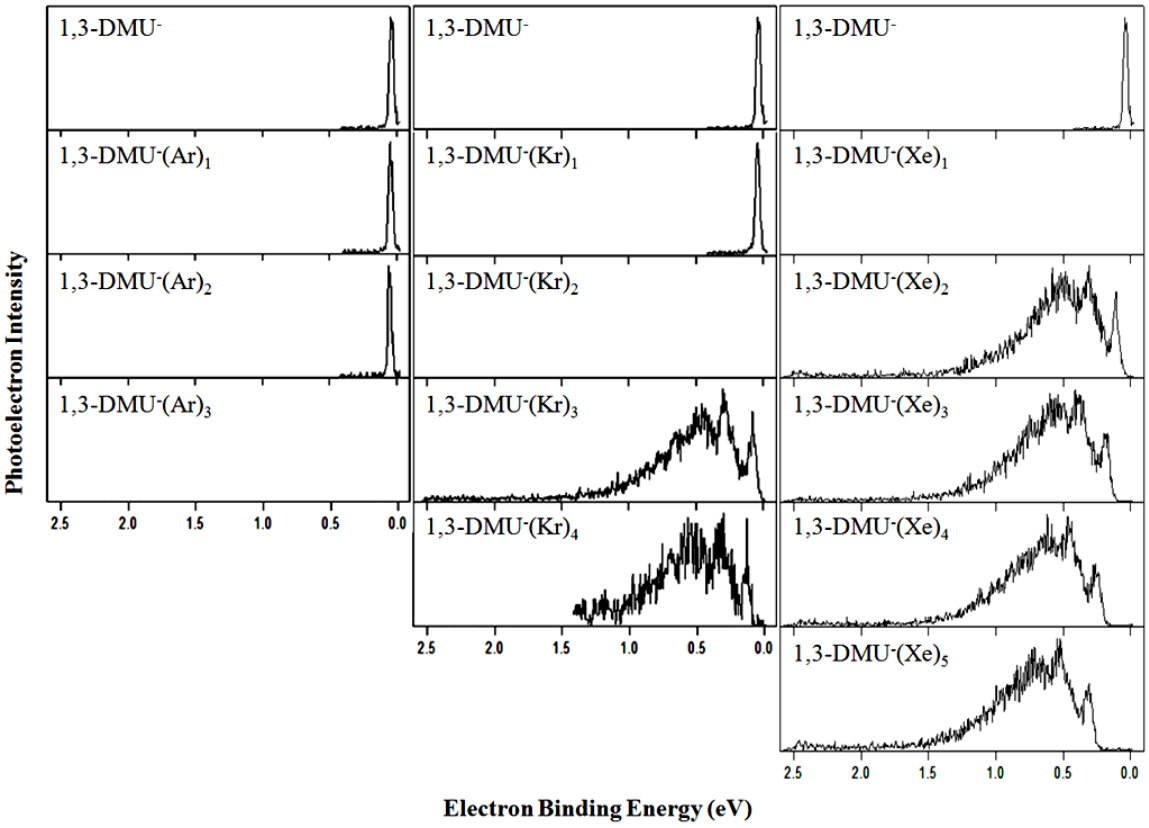

Figure 1.1.13. Photoelectron spectra of the 1,3-DMU$^-$ anion, and its solvation series with argon, krypton, and xenon atoms, i.e., 1,3-DMU$^-$(Ar)$_{1,2}$, 1,3-DMU$^-$(Kr)$_{1,3,4}$, and 1,3-DMU$^-$(Xe)$_{2\text{-}5}$. The peak centers for these spectra were listed in Table 1.1.3.

Notably, only T$^-$(Xe)$_1$, T$^-$(C$_2$H$_6$)$_1$, and T$^-$(Kr)$_2$ spectra exhibit double peaks for the DB anionic states of the compounds, a feature that do not appear in any of the other spectra (Figure 1.1.10 and 1.1.11). Literature data suggested that the canonical thymine tautomer is far more stable than any other T tautomers.[60-63] Therefore, it is unlikely that the double DB peak features are results of different T tautomers. We suspect that it is the isomers of the DB anions of T$^-$(Xe)$_1$, T$^-$(C$_2$H$_6$)$_1$, and T$^-$(Kr)$_2$

that contribute to their double DB peak features. Moreover, the summed polarizability of one xenon atom, one ethane molecule, or two krypton atoms are similar (see Table 1.1.4); thus, the appearance of the DB anion isomers tracks with the summed polarizability of the solvents as well.

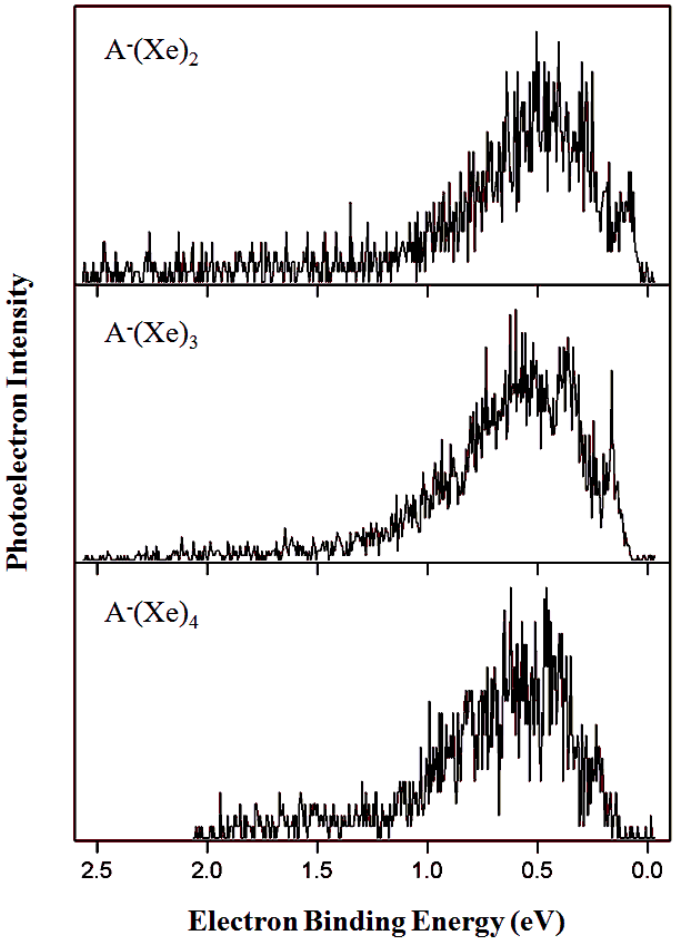

Figure 1.1.14**.** Photoelectron spectra of the A^- anion solvation series with two to four xenon atoms, i.e., $A^-(Xe)_{2\text{-}4}$. The peak centers for these spectra were listed in Table 1.1.3.

Furthermore, two or three "robust" peaks (vibrational features) constantly appear in every valence anion spectra band throughout Figures 1.1.8, 1.1.10, 1.1.11, 1.1.13, and 1.1.14. The spacing between the adjacent peaks in these valence bands reveals the vibrational structure of the corresponding neutral molecular nucleobase. A few calculations indicated that the neutral nucleobases are planar, whereas their anionic counterparts are buckled, with the C=C bonds most distorted upon the electron attachment.[20-23,64,65] Indeed, the measured vibrational frequency values (converted from the peak spacings) from our spectra match very well with the literature vibrational frequency values[54,66-77] of C=C stretch in the molecular nucleobases (see Table 1.1.5).

Table 1.1.5. The vibrational frequency values of C=C stretch in the neutral nucleobases extracted from our spectra and from literatures.[54,66-78]

Species	($EBE_3 - EBE_2$) (eV)	($EBE_2 - EBE_1$) (eV)	($EBE_1 - AEA_v$) (eV)	Literatures (eV)
U	~0.16	~0.19	~0.20	~0.20
T	~0.18	~0.19	~0.21	~0.21
1.3-DMU	~0.17	~0.19	~0.21	~0.21
A		~0.19	~0.19	~0.19

Estimation of AEA_vs of molecular nucleobases.

Can we estimate the AEA_v of the molecular nucleobases by extrapolating our data? This was tried in the past using hydrated nucleobase anion data both by Weinkauf et al.[12] and by us.[13] However, due to the lack of Franck-Condon overlap between the origins of the hydrated nucleobase anions and the origins of their corresponding hydrated nucleobase neutrals, these results were over-estimations of the AEA_v of the nucleobases.[13]

Since the interaction of a water molecule with a nucleobase anion is significantly

stronger than the interaction of a rare gas atom with the same nucleobase anion,[32] the structural difference between the nucleobase valence anion chromophore in the nucleobase$^-$(Rg)$_n$ (Rg: rare gas) valence anion and the nucleobase moiety in the neutral nucleobase(Rg)$_n$ is presumably considerably smaller than the structural difference between the nucleobase valence anion chromophore in the nucleobase$^-$(H$_2$O)$_n$ valence anion and the nucleobase moiety in neutral nucleobase(H$_2$O)$_n$. Thus, one expects better Franck-Condon overlap between the origins of the nucleobase$^-$(Rg)$_n$ valence anion and the neutral nucleobase(Rg)$_n$ than between those of the nucleobase$^-$ (H$_2$O)$_n$ valence anion and the neutral nucleobase(H$_2$O)$_n$. Extrapolation of the AEA$_v$ value, measured from the PES of the nucleobase$^-$(Rg)$_n$ valence anions, should lead to significantly improved estimations of the AEA$_v$ values of canonical, molecular nucleobases.

To obtain the AEA$_v$ values, we extrapolated the low EBE side of the valence bands to the baseline of the spectra. The resulting extrapolated values were found to be essentially the same as the AEA values of their DB peaks, i.e., AEA$_v$ ≈ AEA$_{DB}$. Take U$^-$(Xe)$_1$ spectrum for example (see Figure 1.1.15), the crossing point (~0.12 eV) was designated as the AEA$_v$ value of U$^-$(Xe)$_1$, which is very close to its AEA$_{DB}$ value (~0.111 eV).

With all the AEA$_v$ values in hand (Table 1.1.6), we considered two different methods for extrapolating these values to eventually obtain the AEA$_v$ values of the canonical, molecular nucleobases (see Figure 1.1.16). In method (a), we plotted the AEA$_v$ values versus the number of rare gas atoms (n). The data within each nucleobase series in Figure 1.1.16 (a) all appear to have a close-to-linear relationship,

although the actual plots are curves dropping faster to the left. As a result, the intercept values of the least squares linear fit of these data only give approximate AEA_v values of the nucleobases. The same situation exists in method (b), where we plotted the AEA_v values versus the summed polarizabilities of rare gases (Σα). However in this case, we were able to use much more data points in the plot than method (a). Therefore, method (b) is likely to give more

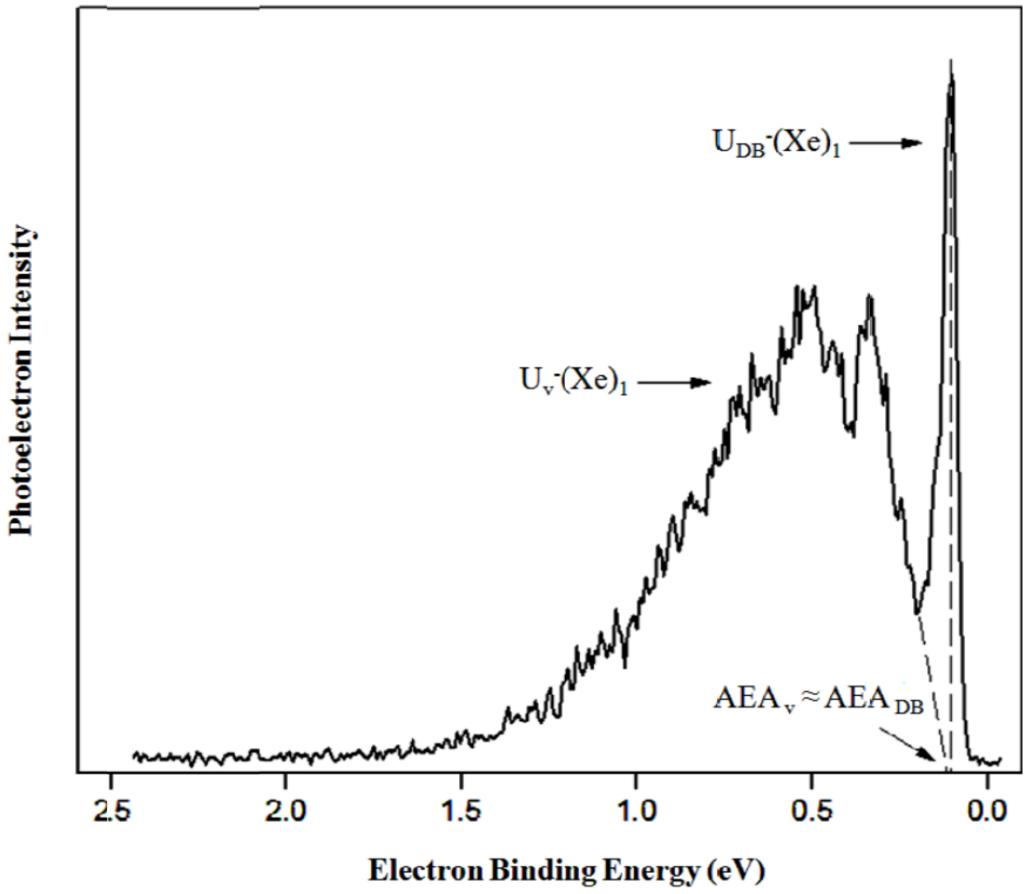

Figure 1.1.15. Illustration of the extrapolation of the AEA_v of $U^-(Xe)_1$ anion, and its AEA_{DB} from the PES of $U^-(Xe)_1$ anion.

accurate AEA_v values than method (a).

The extrapolated AEA_v values using both methods and the recommended theoretical AEA_v values.[20,22,24,79] were listed in Table 1.1.7. After considering the amount of experimental data being used, and the comparison with the theoretical values, we recommend that AEA_v(U) = 36 ± 22 meV, AEA_v(T) = 32 ± 16 meV, AEA_v(1,3-DMU) = -34 ± 24 meV, and AEA_v(A) = -47 ± 44 meV, from our method (b), are the best estimated AEA_v values of the four molecular nucleobases from our experiments.

Lastly, we also extrapolated the AEA_v values of the three missing valence anions of 1,3-DMU$(Rg)_n$ species by using method (b). Recall that in the spectra of 1,3-DMU$^-(Rg)_n$ series, the DB features exhibit the same shifting trend/pace as the valence features upon solvation (see Figure 1.1.13 and 1.1.17). Therefore, we applied the same extrapolation method to estimate the AEA_{DB} and AEA_v values of the three missing DB and valence 1,3-DMU$^-(Rg)_n$ anions. One can see that both of their AEA_v and AEA_{DB} values are at or very close to zero (see Figure 1.1.17), which may explain why the three 1,3-DMU$^-(Rg)_n$ anions are absent in the spectra. However, why this was the case is still not clear yet.

Will the valence state take over as more xenon atoms are added to the Nucleobase(Xe)$^-$ system?

When solvated by more and more xenon atoms, the valence feature maintains while the DB feature seems to be weaker but still pertains in the PES of U$^-(Xe)_n$, T$^-(Xe)_n$, and 1,3-DMU$^-(Xe)_n$ (see Figure 1.1.18). A question is naturally brought up at this point: Will the valence state take over as more xenon atoms are adding to the nucleobase$^-$(Xe) anion system? More experiments and investigations are needed to

answer this question.

Table 1.1.6. Extrapolated valence electron affinity (AEA_v) values from the spectra.

Anion Species	AEA_v (eV)
$U^-(Ar)_3$	0.14 ± 0.02
$U^-(Kr)_2$	0.14 ± 0.02
$U^-(Xe)_1$	0.12 ± 0.02
$U^-(Xe)_2$	0.21 ± 0.02
$U^-(Xe)_3$	0.29 ± 0.02
$T^-(Ar)_3$	0.12 ± 0.02
$T^-(Ar)_4$	0.16 ± 0.02
$T^-(Kr)_2$	0.12 ± 0.02
$T^-(Kr)_3$	0.17 ± 0.02
$T^-(Xe)_1$	0.10 ± 0.02
$T^-(Xe)_2$	0.19 ± 0.02
$T^-(Xe)_3$	0.27 ± 0.02
$T^-(Xe)_4$	0.32 ± 0.02
$T^-(CH_4)_2$	0.15 ± 0.02
$T^-(C_2H_6)_1$	0.14 ± 0.02
$T^-(C_2H_6)_2$	0.24 ± 0.03
$T^-(C_2H_6)_3$	0.33 ± 0.03
1,3-$DMU^-(Kr)_3$	0.09 ± 0.02
1,3-$DMU^-(Kr)_4$	0.13 ± 0.02
1,3-$DMU^-(Xe)_2$	0.11 ± 0.02
1,3-$DMU^-(Xe)_3$	0.18 ± 0.02
1,3-$DMU^-(Xe)_4$	0.25 ± 0.02
1,3-$DMU^-(Xe)_5$	0.31 ± 0.02
$A^-(Xe)_2$	0.09 ± 0.02
$A^-(Xe)_3$	0.17 ± 0.02
$A^-(Xe)_4$	0.23 ± 0.02

Table 1.1.7. Our extrapolated valence electron affinity (AEA_v) values of canonical nucleobases and comparison with their most widely accepted theoretical AEA_v values.

Species	AEA_v (meV) Method (a) AEA_v vs. n	AEA_v (meV) Method (b) AEA_v vs. $\Sigma\alpha$	AEA_v (meV) Theory
U	37 ± 31	36 ± 22	40 (Gutowski et al.)[22]
T	35 ± 24	32 ± 16	20 (Svozil et al.)[20]
1,3-DMU	-22 ± 33	-34 ± 24	-37 (Sevilla et al.)[79]
A	-47 ± 44	-47 ± 44	-350 (Sevilla et al.)[24]

SUMMARY

We have used negative ion photoelectron spectroscopy to investigate the effects of solvation (environment) on the electronic structure and energetic of several nucleobase anions. In a series of molecular beams experiments, it was shown on a molecular level how various solvents, including water molecules and rare gas atoms, affect the electron affinity of these nucleobase anions, and how these solvents condition the stability of the valence form of these anions. More importantly, these studies suggest that the co-existing DB and valence anions are strongly coupled states, that is, they effectively form single states which can be seen as superpositions of both the DB and valence anion states; and the extrapolation of the spectral data provides the best experimentally-based estimations to date of the AEA_vs for several canonical nucleobases.

REFERENCES

1. Sanche, L. *Mass Spectrometry Reviews* **2002**, *21*, 349.
2. Simons, J.; Jordan, K. D. *Chem. Rev.* **1987**, *87*, 535.
3. Svozil, D.; Jungwirth, P.; Havlas, Z. *Collect. Czech. Chem. Commun.* **2004**, *69*, 1395.
4. Crawford, O. H.; Dalgarno, A. *Chem. Phys. Lett.* **1967**, *1*, 23.
5. W.R, G. *Chemical Physics Letters* **1970**, *5*, 393.
6. Garrett, W. R. *Physical Review A* **1971**, *3*, 961.
7. Fermi, E.; Teller, E. *Physical Review* **1947**, *72*, 399.
8. Jordan, K. D.; Burrow, P. D. *Chem. Rev.* **1987**, *87*, 557.
9. Aflatooni, K.; Gallup, G. A.; Burrow, P. D. *J. Phys. Chem. A* **1998**, *102*, 6205.
10. Desfrancois, C.; Periquet, V.; Bouteiller, Y.; Schermann, J. P. *J. Phys. Chem. A* **1998**, *102*, 1274.
11. Hendricks, J. H.; Lyapustina, S. A.; de, C. H. L.; Snodgrass, J. T.; Bowen, K. H. *J. Chem. Phys.* **1996**, *104*, 7788.
12. Schiedt, J.; Weinkauf, R.; Neumark, D. M.; Schlag, E. W. *Chem. Phys.* **1998**, *239*, 511.
13. Eustis, S.; Wang, D.; Lyapustina, S.; Bowen, K. H. *J. Chem. Phys.* **2007**, *127*, 224309/1.
14. Periquet, V.; Moreau, A.; Carles, S.; Schermann, J. P.; Desfrancois, C. *J. Electron Spectrosc. Relat. Phenom.* **2000**, *106*, 141.
15. Boudaiffa, B.; Cloutier, P.; Hunting, D.; Huels, M. A.; Sanche, L. *Science* **2000**, *287*, 1658.

16. Sevilla, M. D.; Besler, B.; Colson, A. O. *J. Phys. Chem.* **1994**, *98*, 2215.

17. Sevilla, M. D.; Besler, B.; Colson, A.-O. *J. Phys. Chem.* **1995**, *99*, 1060.

18. Wesolowski, S. S.; Leininger, M. L.; Pentchev, P. N.; Schaefer, H. F., III. *J. Am. Chem. Soc.* **2001**, *123*, 4023.

19. Li, X.; Cai, Z.; Sevilla, M. D. *J. Phys. Chem. A* **2002**, *106*, 1596.

20. Svozil, D.; Frigato, T.; Havlas, Z.; Jungwirth, P. *Phys. Chem. Chem. Phys.* **2005**, *7*, 840.

21. Kim, S.; Schaefer, H. F., III. *J. Chem. Phys.* **2006**, *125*, 144305/1.

22. Bachorz, R. A.; Klopper, W.; Gutowski, M. *J. Chem. Phys.* **2007**, *126*, 085101/1.

23. Dedikova, P.; Demovic, L.; Pitonak, M.; Neogrady, P.; Urban, M. *Chem. Phys. Lett.* **2009**, *481*, 107.

24. Kumar, A.; Sevilla, M. D. *Wiley Ser. React. Intermed. Chem. Biol.* **2009**, *2*, 1.

25. Sponer, J.; Leszczynski, J.; Hobza, P. *Biopolymers* **2001**, *61*, 3.

26. Oyler, N. A.; Adamowicz, L. *Chem. Phys. Lett.* **1994**, *219*, 223.

27. Oyler, N. A.; Adamowicz, L. *J. Phys. Chem.* **1993**, *97*, 11122.

28. Desfrancois, C.; Abdoul-Carime, H.; Carles, S.; Periquet, V.; Schermann, J. P.; Smith, D. M. A.; Adamowicz, L. *J. Chem. Phys.* **1999**, *110*, 11876.

29. Smith, D. M. A.; Smets, J.; Elkadi, Y.; Adamowicz, L. *J. Phys. Chem. A* **1997**, *101*, 8123.

30. Gutowski, M.; Skurski, P. *Recent Res. Dev. Phys. Chem.* **1999**, *3*, 245.

31. Gutowski, M.; Dabkowska, I.; Rak, J.; Xu, S.; Nilles, J. M.; Radisic, D.; Bowen, K. H., Jr. *Eur. Phys. J. D* **2002**, *20*, 431.

32. Hendricks, J. H.; Lyapustina, S. A.; de, C. H. L.; Bowen, K. H. *J. Chem. Phys.* **1998**, *108*, 8.

33. Desfrancois, C.; Abdoul-Carime, H.; Schermann, J. P. *J. Chem. Phys.* **1996**, *104*, 7792.

34. Compton, R. N.; Carman, H. S., Jr.; Desfrancois, C.; Abdoul-Carmine, H.; Schermann, J. P.; Hendricks, J. H.; Lyapustina, S. A.; Bowen, K. H. *J. Chem. Phys.* **1996**, *105*, 3472.

35. Lecomte, F.; Carles, S.; Desfrancois, C.; Johnson, M. A. *The Journal of Chemical Physics* **2000**, *113*, 10973.

36. Desfrancois, C.; Periquet, V.; Lyapustina, S. A.; Lippa, T. P.; Robinson, D. W.; Bowen, K. H.; Nonaka, H.; Compton, R. N. *J. Chem. Phys.* **1999**, *111*, 4569.

37. Han, S. Y.; Kim, J. H.; Song, J. K.; Kim, S. K. *J. Chem. Phys.* **1998**, *109*, 9656.

38. Han, S. Y.; Song, J. K.; Kim, J. H.; Oh, H. B.; Kim, S. K. *J. Chem. Phys.* **1999**, *111*, 4041.

39. Neumark, D. M.; Lykke, K. R.; Andersen, T.; Lineberger, W. C. *Phys. Rev. A: Gen. Phys.* **1985**, *32*, 1890.

40. Coe, J. V.; Snodgrass, J. T.; Freidhoff, C. B.; McHugh, K. M.; Bowen, K. H. *J. Chem. Phys.* **1986**, *84*, 618.

41. Hendricks, J. H.; De, C. H. L.; Lyapustina, S. A.; Fancher, C. A.; Lippa, T. P.; Collins, J. M.; Arnold, S. T.; Lee, G. H.; Bowen, K. H. *Front. Sci. Ser.* **1996**, *16*, 321.

42. Kulakowska, I.; Geller, M.; Lesyng, B.; Wierzchowski, K. L. *Biochim.*

Biophys. Acta, Nucleic Acids Protein Synth. **1974**, *361*, 119.

43. Basch, H.; Garmer, D. R.; Jasien, P. G.; Krauss, M.; Stevens, W. J. *Chem. Phys. Lett.* **1989**, *163*, 514.

44. Böttcher, C. J. F.; Rip, A. *Theory of electric polarization*, 2d ed. completely rev. ed.; Elsevier Scientific Pub. Co.: Amsterdam, 1973.

45. Miller, K. J. *J. Am. Chem. Soc.* **1990**, *112*, 8533.

46. Adamowicz, L. *Private comminication.*

47. Chen, J.; Buonaugurio A.; et al. *This work.*

48. Abdoul-Carime, H.; Desfrancois, C. *Eur. Phys. J. D* **1998**, *2*, 149.

49. Carles, S.; Lecomte, F.; Schermann, J. P.; Desfrancois, C. *J. Phys. Chem. A* **2000**, *104*, 10662.

50. Kulakowska, I.; Geller, M.; Lesyng, B.; Bolewska, K.; Wierzchowski, K. I. *Biochim. Biophys. Acta, Nucleic Acids Protein Synth.* **1975**, *407*, 420.

51. Hendricks, J. H.; Lyapustina, S. A.; De, C. H. L.; Bowen, K. H. *PhD. Dissertation (unpubished results)* **1996**, 109.

52. Katritzky, A. R.; Boulton, A. J.; Editors *Advances in Heterocyclic Chemistry, Vol. 18*; Academic, 1975.

53. Kokko, J. P.; Goldstein, H. H.; Mandell, L. *J. Am. Chem. Soc.* **1961**, *83*, 2909.

54. Viant, M. R.; Fellers, R. S.; McLaughlin, R. P.; Saykally, R. J. *J. Chem. Phys.* **1995**, *103*, 9502.

55. Subbarao, S. N.; Bray, P. J. *J. Chem. Phys.* **1977**, *67*, 1085.

56. Szczesniak, M.; Szczepaniak, K.; Kwiatkowski, J. S.; KuBulat, K.; Person, W.

B. *J. Am. Chem. Soc.* **1988**, *110*, 8319.

57. Roehrig, G. H.; Oyler, N. A.; Adamowicz, L. *Chem. Phys. Lett.* **1994**, *225*, 265.

58. Gutowski, M.; Skurski, P. *J. Chem. Phys.* **1997**, *107*, 2968.

59. Gutowski, M.; Jordan, K. D.; Skurski, P. *J. Phys. Chem. A* **1998**, *102*, 2624.

60. Buda, A.; Sygula, A. *J. Mol. Struct.: THEOCHEM* **1983**, *9*, 255.

61. Scanlan, M. J.; Hillier, I. H. *J. Am. Chem. Soc.* **1984**, *106*, 3737.

62. Sorarrain, O. M.; Castro, E. A. *Chem. Phys. Lett.* **1973**, *19*, 422.

63. Boldeskul, A. I.; Sokhodub, L. F. *Biopolim. Kletka* **1997**, *13*, 185.

64. Dolgounitcheva, O.; Zakrzewski, V. G.; Ortiz, J. V. *Chem. Phys. Lett.* **1999**, *307*, 220.

65. Bachorz, R. A.; Rak, J.; Gutowski, M. *Phys. Chem. Chem. Phys.* **2005**, *7*, 2116.

66. Wierzchowski, K. L.; Litonska, E.; Shugar, D. *J. Am. Chem. Soc.* **1965**, *87*, 4621.

67. Susi, H.; Ard, J. S.; Purcell, J. M. *Spectrochim. Acta, Part A* **1973**, *29*, 725.

68. Lippert, B. *J. Raman Spectrosc.* **1980**, *9*, 324.

69. Radchenko, E. D.; Plokhotnichenko, A. M.; Sheina, G. G.; Blagoi, Y. P. *Biofizika* **1983**, *28*, 923.

70. Szczesniak, M.; Nowak, M. J.; Rostkowska, H.; Szczepaniak, K.; Person, W. B.; Shugar, D. *J. Am. Chem. Soc.* **1983**, *105*, 5969.

71. Barnes, A. J.; Stuckey, M. A.; Le, G. L. *Spectrochim. Acta, Part A* **1984**, *40A*, 419.

72. Maltese, M.; Passerini, S.; Nunziante-Cesaro, S.; Dobos, S.; Harsanyi, L. *J. Mol. Struct.* **1984**, *116*, 49.

73. Szczesniak, M.; Nowak, M. J.; Szczepaniak, K.; Chin, S.; Scott, I.; Person, W. B. *Spectrochim. Acta, Part A* **1985**, *41A*, 223.

74. Nowak, M. J. *J. Mol. Struct.* **1989**, *193*, 35.

75. Graindourze, M.; Smets, J.; Zeegers-Huyskens, T.; Maes, G. *J. Mol. Struct.* **1990**, *222*, 345.

76. Leś, A.; Adamowicz, L.; Nowak, M. J.; Lapinski, L. *Spectrochim. Acta, Part A* **1992**, *48*, 1385.

77. Colarusso, P.; Zhang, K. Q.; Guo, B.; Bernath, P. F. *Chem. Phys. Lett.* **1997**, *269*, 39.

78. Mohamed, T. A.; Shabaan, I. A.; Zoghaib, W. M.; Husband, J.; Farag, R. S.; Alajhaz, A. E.-N. M. A. *J. Mol. Struct.* **2009**, *938*, 263.

79. Sevilla, M. D. *Private communications*

Section 1.2. Photoelectron Spectroscopy of the 6-Azauracil Anion

Jing Chen,[†] Angela Buonaugurio,[†] Olga Dolgounitcheva,[‡] V. G. Zakrzewski,[‡] Kit H. Bowen,[*,†] and J. V. Ortiz[*,‡]

[†]*Department of Chemistry, Johns Hopkins University, Baltimore, Maryland 21218, United States*

[‡]*Department of Chemistry and Biochemistry, Auburn University, Auburn, Alabama 36849, United States*

ABSTRACT

We report the photoelectron spectrum of the 6-azauracil anion. The spectrum is dominated by a broad band exhibiting a maximum at an electron binding energy (EBE) of 1.2 eV. This spectral pattern is indicative of a valence anion. Our calculations were carried out using ab initio electron propagator and other many-body methods. Comparison of the anion and corresponding neutral of 6-azauracil with those of uracil shows that substituting a nitrogen atom for C−H at the C6 position of uracil gives rise to significant changes in the electronic structure of 6-azauracil versus that of uracil. The adiabatic electron affinity (AEA) of the canonical 6-azauracil tautomer is substantially larger than that of canonical uracil. Among the five tautomeric, 6-azauracil anions studied computationally, the canonical structure was found to be the most stable. The vertical detachment energies (VDE) of the canonical, valence-bound anion of 6-azauracil and its closest "very-rare" tautomer have been calculated. Electron propagator calculations on the canonical anion yield a VDE value that is in close agreement with the experimentally determined VDE value of 1.2 eV. The AEA value of 6-azauracil, assessed at the

CCSD(T) level of theory to be 0.5 eV, corresponds with the EBE value of the onset of the experimental spectrum.

*Corresponding authors: email: ortiz@auburn.edu, kbowen@jhu.edu

INTRODUCTION

Substituted nucleobases have received significant attention due to their use as therapeutic agents.[1-6] Both halo-nucleobases and thio-nucleobases, for example, have possible roles in the treatment of cancer.[7-13] It has been shown that halo- nucleobases may aid in increasing the radiosensitivity of tumor cells. Thio-substituted nucleobases, on the other hand, may provide milder, safer alternatives to current methods of cancer therapy. Likewise, nucleobases in which a C−H group has been substituted by a nitrogen atom may result in compounds with pharmacologically interesting properties.[14-20] Specifically, 6-azauracil is known to inhibit the function of some enzymes[14-16] and many microorganisms.[14,17-20]

The 6-azauracil molecule differs from uracil in only one respect: the substitution of a nitrogen atom for a C−H group at uracil's C6 position. Neutral 6-azauracil has been studied extensively; many experimental and theoretical studies have revealed its structural, chemical, and spectroscopic properties.[21-35] In contrast, there is a scarcity of data on the 6-azauracil anion. Studying this anion should elucidate the interaction of 6-azauracil with excess electrons, and this may be relevant to the compound's radio-therapeutic properties. Indeed, previous studies have found both sulfur and halogen modifications of uracil to give rise to significant changes in its electronic structure.[36,37] The objective of the present study is to investigate the influence of N-substitution at the C6 position of uracil on its resulting electrophilic properties. This was revealed through the differing characteristics of the uracil versus the 6-azauracil negative ions.

EXPERIMENTAL AND COMPUTATIONAL METHODS

Photoelectron Spectroscopy

Negative ion photoelectron spectroscopy is conducted by crossing a mass-selected beam of negative ions with a fixed-frequency photon beam and energy-analyzing the resultant photodetached electrons. The photodetachment process is governed by the relationship $h\nu = EBE + EKE$, where $h\nu$ is the photon energy, EBE is the electron binding energy, i.e., the transition energy between the anion and a particular vibronic state of its neutral counterpart, and EKE is the electron kinetic energy.

Negative ions of 6-azauracil were formed in a supersonic expansion nozzle-ion source, where 6-azauracil powder was placed in a stagnation chamber, heated to ~100°C, and co-expanded with ~50 psig argon gas through a 20 μm orifice into $\sim 10^{-4}$ torr vacuum. Negative ions were formed by injecting low energy electrons from a negatively biased, thoriated-iridium filament into the expanding jet, where a microplasma was formed in the presence of a weak external magnetic field. These anions were then extracted, collimated, and transferred into the flight tube of a 90° magnetic sector mass spectrometer with a typical mass resolution of ~ 400. The mass-selected anions of interest were then crossed with the intracavity laser beam of an argon ion laser, and the photodetached electrons energy-analyzed in a hemispherical electron energy analyzer having a resolution of ~ 30 meV. The photoelectron spectrum reported here was recorded with 2.540 eV photons, and it was calibrated against the photoelectron spectrum of the O^- anion.[38] Detailed descriptions of this apparatus have been described previously.[39]

Theoretical Calculations

All calculations were performed with the Gaussian-09 suite of programs.[40] Geometric structures of neutral 6-azauracil and isomeric anions were optimized with the MP2/6-311++G(2df,2p) method.[41–43] Because we were interested only in valence-bound anions, a conventional (canonical) anion and four so-called "very-rare" anionic tautomers were the subjects of the current investigation. These tautomers are denoted as:

- N1→N6 where a proton is transferred from N1 to N6
- N1→C5 where a proton is transferred from N1 to C5
- N3→N6 where a proton is transferred from N3 to N6
- N3→C5 where a proton is transferred from N3 to C5

Structures resulting from proton transfer from either imino group to a carboxylic oxygen were not taken into account. Minima on the potential energy surface were verified by harmonic frequencies. Zero-point corrections were obtained in these calculations. Total energies of all species under consideration were obtained at higher levels of theory: coupled-cluster singles and doubles (CCSD)[44] as well as CCSD with perturbative triples corrections[45] or CCSD(T). Vertical electron binding (detachment) energies were obtained with electron propagator calculations in various quasi-particle approximations.[46,47] The OVGF renormalization schemes A, B, and C,[48,49] the P3[50,51] and P3+[52] methods were employed to get correlation and relaxation corrections to Koopmans's (KT) results. The same 6-311++G(2df,2p) basis was used.

RESULTS AND DISCUSSION

Photoelectron Spectrum

The photoelectron spectrum of 6-azauracil anion is presented in Figure 1.2.1. The spectrum exhibits a broad peak centered at EBE = 1.2 eV (its vertical detachment energy, VDE), with its width at baseline extending from EBE = 0.6 to 1.9 eV. By comparing the photoelectron spectrum of the 6-azauracil anion with that of the dipole-bound anion of uracil,[53] it is clear that the 6-azauracil anion studied here is not a dipole-bound anion; it is

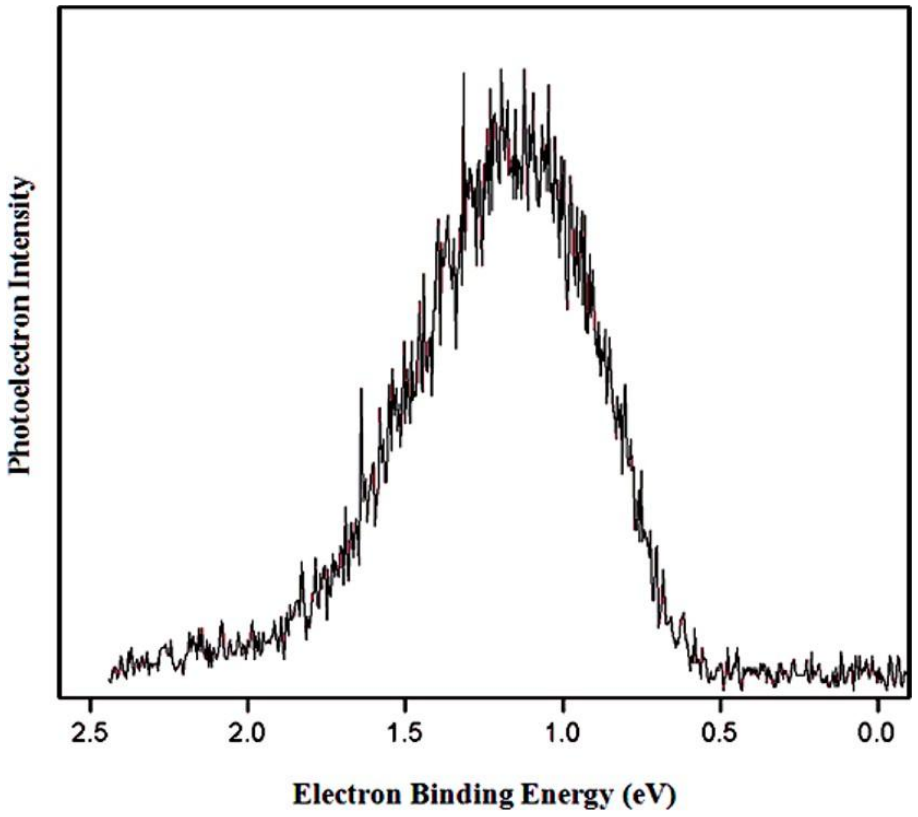

Figure 1.2.1. Photoelectron spectrum of the 6-azauracil anion recorded with 2.540 eV photons. The resolution of the spectrum is ~30 meV.

in fact a valence-bound anion. The more pertinent question is whether the broad band exhibited in the spectrum of the 6-azauracil anion is indicative of the canonical or one of the other tautomers of the 6-azauracil anion. To answer this question, we rely on the calculations presented in the following Computational Section.

Theoretical Calculations

Relative energies of tautomeric, valence-bound anions of 6-azauracil are presented in Table 1.2.1. VDE values for its two most stable anions are presented in Table 1.2.2. The atomic numbering scheme is given in Figure 1.2.2.

Table 1.2.1. Relative energies (kcal/mol) of tautomeric, valence-bound 6-azauracil anions.

tautomers	ΔE_{UMP2}	ΔE_{PUMP2}	ΔE_{UMP2}+ZPE
canonical	0	0	0
N1→N6	2.94	4.24	3.20
N3→C5	4.79	6.32	5.08
N1→C5	6.81	7.57	6.77
N3→N6	22.90	24.15	22.72

Table 1.2.2. VDE (eV) values of 6-azauracil anions.

tautomers	ΔCCSD	ΔCCSD(T)	OVGF	P3	P3+	Expt.
canonical	0.96	0.85	1.03 (A) 1.01 (B) 1.17 (C)	1.33	1.23	1.2
N1→N6	1.80	1.60	1.70 (A) 1.65 (B) 1.84 (C)	2.02	1.89	If present, this transition would lie on the far edge of the spectrum.

Vertical and Adiabatic Electron Affinities of 6-Azauracil. Optimization of the 6-azauracil parent (neutral) molecule revealed a minimum corresponding to a planar, C_s structure. This system was capable of accepting an electron into its a″ virtual molecular orbital (which was not the LUMO). Vertical electron attachment energies (vertical electron affinities) of 0.16 and 0.11 eV were obtained at the CCSD and CCSD(T) single point level of computations, respectively. The canonical, ^{2}A″ anion was optimized with UMP2. A planar structure was obtained. Harmonic frequencies calculations confirmed a minimum for this structure. Being planar, the valence-bound anion of 6-azauracil differs significantly from the corresponding, canonical anions of uracil, cytosine, and the thiouracils, all of which are significantly puckered.[36,54,55] The adiabatic electron affinity (AEA) of 6-azauracil was calculated at the CCSD(T) level of theory as a difference between the total energies of the neutral and its anion. The calculated value of 0.50 eV is in accord with the onset of the experimental spectrum (~0.6 eV, see Figure 1.2.1). Although the true AEA may be slightly higher in energy than the EBE of the onset, due to the likely presence of hot bands in the spectrum, the agreement between our experiment and our calculations is quite good.

Relative Stabilities of 6-Azauracil Tautomeric Anions. "Very-rare" isomers of the uracil valence anion arise when one of the imino group's protons is transferred to either the C5 or C6 atoms of the pyrimidinic ring. One such isomer was found to be responsible for the peak observed in the experimental photoelectron spectrum of the uracil anion.[56,57] Thus, in the current study, four "very-rare" tautomers of 6-azauracil anions were considered to determine whether any of these had been observed in the

photoelectron spectrum of the 6-azauracil anion. Geometry optimizations of these anions revealed four minima corresponding to structures of C_1 symmetry. Ring puckering was found in all of these anions. Relative energy data in Table 1.2.1 show that the canonical, $^2A''$ valence-bound anion is the lowest energy structure and very likely corresponds to the global minimum on the potential energy surface. The N1→N6 tautomer is about 3 kcal/mol higher in energy than the canonical anion. Three other isomeric anions are less stable and are excluded from further consideration.

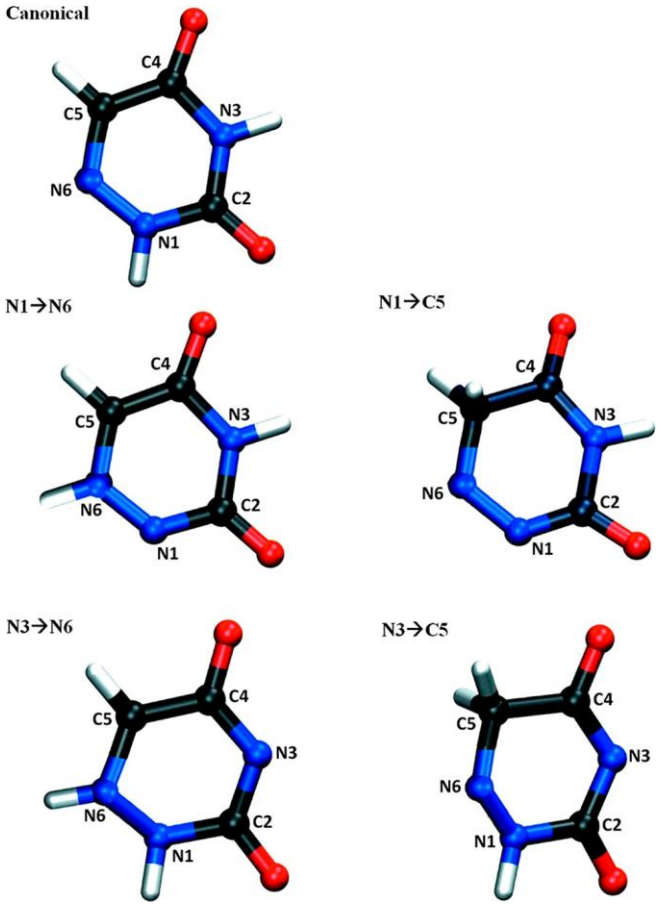

Figure 1.2.2. Atomic numbering scheme for neutral 6-azauracil.

Vertical Detachment Energies and the Assignment of the Photoelectron Spectrum. Table 1.2.2 shows the VDE values of two 6-azauracil valence-bound anions obtained with many-body methods. For the canonical anion, most of the results are in reasonably good agreement with the experimentally determined VDE value of 1.2 eV, with the P3+ value being in excellent agreement. The VDE values obtained for the N1→N6 tautomer are about 0.7 eV larger, i.e., at EBE ~ 1.9 eV. These values lie at the far edge of the observed spectral band, and no separate peak for this tautomeric anion's photodetachment transition was observed.

CONCLUSION

A broad band centered at EBE = 1.2 eV (its VDE value) was observed in the photoelectron spectrum of the 6-azauracil anion. The spectrum was assigned on the basis of ab initio, many-body calculations. The canonical, valence-bound 6-azauracil anion of C_s symmetry was found to be solely responsible for the experimental peak. The calculated AEA value of 0.5 eV is consistent with the onset of the experimental band at EBE = 0.6 eV. Moreover, the calculated and measured VDE values of the 6-azauracil anion are in excellent agreement. These conclusions contrast with uracil, whose most stable anion was calculated to be its "N1→C5" rare tautomer and not its canonical form.[56,57] Although the AEA value of canonical 6-azauracil is +0.5 eV, the AEA value of canonical uracil is only slightly positive, at +40 meV.[56,58] Clearly, the replacement of a C−H group at C6 of uracil with a nitrogen atom significantly changes the electronic structure of the uracil anion relative to that of the 6-azauracil anion, switching the order

of stabilities between rare tautomer and canonical forms. The valence anion of 6-azauracil is much more than an N-substituted uracil valence anion.

ACKNOWLEDGEMENTS

This material is based upon experimental work supported by the National Science Foundation under grant number, CHE-1111693 (KHB). O.D., V.G.Z., and J.V.O. acknowledge support from the National Science Foundation through grant CHE-0809199 to Auburn University.

REFERENCES

1. Saenger, W. *Principles of Nucleic Acid Structure*; Springer-Verlag: Berlin, 1984.
2. Osman, R.; Topiol, S.; Rubenstein, L.; Weinstein, H. *Mol. Pharmacol*. **1987**, *32*, 699−705.
3. Mars, U.; Larsson, B. S. *Pigm. Cell Res*. **1995**, *8*, 194−201.
4. Wang, Z.; Rana, T. M. *Biochemistry* **1996**, *35*, 6491−6499.
5. Wetmore, S. D.; Boyd, R. J.; Eriksson, L. A. *Chem. Phys. Lett*. **2001**, *343*, 151−158.
6. Esposito, V.; Randazzo, A.; Piccialli, G.; Petraccone, L.; Giancola, C.; Mayol, L. *Org. Biomol. Chem.* **2004**, *2*, 313−318.
7. Zamenhof, S.; De, G. R.; Greer, S. *Nature* **1958**, *181*, 827−829.
8. Dewey, W. C.; Sedita, B. A.; Humphrey, R. M. *Science* **1966**, *152*, 519−521.
9. Hutchinson, F. Q. *Rev. Biophys*. **1973**, *6*, 201−246.
10. Lawrence, T. S.; Davis, M. A.; Maybaum, J.; Stetson, P. L.; Ensminger, W. D. *Radiat. Res*. **1990**, *123*, 192−198.
11. Sugiyama, H.; Tsutsumi, Y.; Saito, I. *J. Am. Chem. Soc*. **1990**, *112*, 6720−6721.
12. Chen, T.; Cook, G. P.; Koppisch, A. T.; Greenberg, M. M. *J. Am. Chem. Soc*. **2000**, *122*, 3861−3866.
13. Zhang, X.; Xu, Y.-Z. *Molecules* **2011**, *16*, 5655−5664.
14. Exinger, F.; Lacroute, F. *Curr. Genet*. **1992**, *22*, 9−11.
15. Nakanishi, T.; Nakano, A.; Nomura, K.; Sekimizu, K.; Natori, S. *J. Biol. Chem*. **1992**, *267*, 13200−13204.
16. Reines, D. *Methods Enzymol*. **2003**, *371*, 284−292.

17. Handschumacher, R. E.; Welch, A. D. *Cancer Res*. **1956**, *16*, 965−969.

18. Handschumacher, R. E. J. *Biol. Chem*. **1960**, *235*, 2917−2919.

19. Jund, R.; Lacroute, F. *J. Bacteriol*. **1970**, *102*, 607−615.

20. Matsuno, T.; Okada, Y.; Kobayashi, N. *Chikusan no Kenkyu* **1998**, *52*, 1105−1115.

21. Seibert, W. *Chem. Ber.* **1947**, *80*, 494−502.

22. Falco, E. A.; Pappas, E.; Hitchings, G. H. *J. Am. Chem. Soc*. **1956**, *78*, 1938−1941.

23. Grundmann, C. J.; Schroeder, H.; Ratz, R. F. W. *J. Org. Chem*. **1958**, *23*, 1522−1524.

24. Cristescu, C.; Marcus, *J. Pharmazie* **1961**, *16*, 135−137.

25. Hrebabecky, H.; Beranek, J. *Collect. Czech. Chem. Commun*. **1975**, *40*, 2364−2377.

26. Lovelette, C. A. J. *Heterocycl. Chem*. **1979**, *16*, 1649−1650.

27. Farkas, J. *Collect. Czech. Chem. Commun*. **1983**, *48*, 2676−2681.

28. Sheldrick, W. S.; Neumann, D. *Inorg. Chim. Acta* **1994**, *223*, 131−137.

29. Novozhenyuk, M. L.; Lampeka, R. D. *Dopov. Nats. Akad. Nauk Ukr*. **2004**, *8*, 152−157.

30. Al-Awadi, N. A.; Ibrahim, Y. A.; Dib, H. H.; Ibrahim, M. R.; George, B. J.; Abdallah, M. R. *Tetrahedron* **2006**, *62*, 6214−6221.

31. Habibi-Khorassani, M.; Maghsoodlou, M. T.; Ebrahimi, A.; Kazemian, M. A.; Zakarianejad, M. *Phosphorus, Sulfur Silicon Relat. Elem*. **2009**, *184*, 2959−2979.

32. Zahradnik, R.; Koutecky, J.; Jonas, J.; Gut, J. *Collect. Czech. Chem. Commun*. **1963**, *28*, 1499−1506.

33. Lifshitz, C.; Bergmann, E. D.; Pullman, B. *Tetrahedron Lett*. **1967**, *46*, 4583−4586.

34. Fulara, J.; Nowak, M. J.; Lapinski, L.; Les, A.; Adamowicz, L. *Spectrochim. Acta, Part A* **1991**, *47A*, 595−613.

35. Frysova, I.; Otyepka, M.; Slouka, J.; Hlavac, J. *Acta Univ. Palacki. Olomuc., Fac. Rerum Nat., Chem*. **2004**, *43*, 73−79.

36. Dolgounitcheva, O.; Zakrzewski, V. G.; Ortiz, J. V. *J. Chem. Phys*. **2011**, *134*, 074301−074305.

37. Li, X.; Chen, J.; Bowen, K. H. *J. Chem. Phys*. **2011**, *134*, 074301−074304.

38. Neumark, D. M.; Lykke, K. R.; Andersen, T.; Lineberger, W. C. *Phys. Rev. A: Gen. Phys.* **1985**, *32*, 1890−1892.

39. Coe, J. V.; Snodgrass, J. T.; Freidhoff, C. B.; McHugh, K. M.; Bowen, K. H. *J. Chem. Phys.* **1986**, *84*, 618−625.

40. Frisch, M. J.; Trucks, G. W.; Schlegel, H. B.; Scuseria, G. E.; Robb, M. A.; Cheeseman, J. R.; Scalmani, G.; Barone, V.; Mennucci, B.; Petersson, G. A.; et al. *Gaussian-09*, G09RevB.01; Gaussian Inc.: Wallingford, CT, 2010.

41. Krishnan, R.; Binkley, J. S.; Seeger, R.; Pople, J. A. *J. Chem. Phys.* **1980**, *72*, 650−654.

42. Clark, T.; Chandrasekhar, J.; Spitznagel, G. W.; Schleyer, P. v. R. *J. Comput. Chem*. **1983**, *4*, 294−301.

43. Frisch, M. J.; Pople, J. A.; Binkley, J. S. *J. Chem. Phys*. **1984**, *80*, 3265−3269.

44. Purvis, G. D., III; Bartlett, R. J. *J. Chem. Phys*. **1982**, *76*, 1910−1918.

45. Raghavachari, K.; Trucks, G. W.; Pople, J. A.; Head-Gordon, M. *Chem. Phys. Lett*. **1989**, *157*, 479−483.

46. Linderberg, J.; hrn, Y. *Propagators in Quantum Chemistry*, 2nd ed.; Wiley-Interscience, Hoboken, NJ, 2004.

47. Zakrzewski, V. G.; Dolgounitcheva, O.; Zakjevskii, A. V.; Ortiz, J. V. *Annu. Rep. Comput. Chem*. **2010**, *6*, 79−94.

48. von Niessen, W.; Schirmer, J.; Cederbaum, L. S. *Comput. Phys. Rep*. **1984**, *1*, 57−125.

49. Ortiz, J. V. *Computational Chemistry: Reviews of Current Trends*; Leszczynski, J., Eds.; World Scientific: Singapore, 1997; Vol. 2, pp 1−61.

50. Ortiz, J. V. *J. Chem. Phys*. **1996**, *104*, 7599−7605.

51. Ferreira, A. M.; Seabra, G.; Dolgounitcheva, O.; Zakrzewski, V. G.; Ortiz, J. V. Quantum-Mechanical Prediction of Thermochemical Data. *Understanding Chemical Reactivity*; Cioslowski, J., Eds.; Kluwer: Dordrecht, The Netherlands, 2001; Vol. 22.

52. Ortiz, J. V. *Int. J. Quantum Chem*. **2005**, *105*, 803−808.

53. Hendricks, J. H.; Lyapustina, S. A.; de, C. H. L.; Snodgrass, J. T.; Bowen, K. H. *J. Chem. Phys*. **1996**, *104*, 7788−7791.

54. Dolgounitcheva, O.; Zakrzewski, V. G.; Ortiz, J. V. *Chem. Phys. Lett*. **1999**, *307*, 220−226.

55. Dolgounitcheva, O.; Zakrzewski, V. G.; Ortiz, J. V. *J. Phys. Chem. A* **2001**, *105*, 8782−8786.

56. Bachorz, R. A.; Klopper, W.; Gutowski, M. *J. Chem. Phys.* **2007**, *126*, 085101−085107.

57. Bachorz, R. A.; Klopper, W.; Gutowski, M.; Li, X.; Bowen, K. H. *J. Chem. Phys*. **2008**, *129*, 054309.

58. Desfrancois, C.; Periquet, V.; Bouteiller, Y.; Schermann, J. P. *J. Phys. Chem. A* **1998**, *102*, 1274−1278.

Section 1.3. How to Find Out Whether a 5-Substituted Uracil Could Be a Potential DNA Radiosensitizer

Lidia Chomicz,[†] Magdalena Zdrowowicz,[†] Franciszek Kasprzykowski,[†] Janusz Rak,[*,†] Angela Buonaugurio,[‡] Yi Wang,[‡] and Kit H. Bowen[*,‡]

[†] , , , - *sk, Poland*

[‡]*Department of Chemistry, Johns Hopkins University, Baltimore, Maryland 21218, United States*

ABSTRACT

Incorporated into genomic DNA, 5-substituted uracils could be employed in human cancer radiotherapy if they could be sensitized to dissociate upon reaction with hydrated electrons. Using the B3LYP/6-31++G(d,p) method, we calculate electron affinities and energy profiles related to the dissociation of the respective anions for a series of uracil derivatives. We demonstrate that for a uracil analogue to be an efficient electron acceptor the uracil substituent has to possess significant electron-withdrawing power. On the other hand, in order to ensure effective dissociation of the anion, the chemical bond holding together the substituent and uracil residue should be relatively weak. Our theoretical predictions are in excellent agreement with the results of our negative ion photoelectron spectroscopy experiments. We propose two new potential sensitizers that seem to possess the required properties, although they have never been tested in radiobiological experiments.

*Corresponding authors: email: janusz@raptor.chem.univ.gda.pl, kbowen@jhu.edu

INTRODUCTION

Radiotherapy (RT) is the most common curative and palliative modality in human cancer treatments. Above fifty percent of all cancer patients receive RT at some point during their management.[1] However, it is worth emphasizing that ionizing radiation (IR) employed in RT is cytotoxic not only toward the cancer but also to normal cells, considering the target irradiated volume always includes a substantial amount of normal tissue. Hence, effective radiotherapy is unavoidably associated with a risk for early and late side-effects, including the development of a secondary cancer.[1] Furthermore, efficient repair mechanisms in cells lessen the therapeutic effects of gamma/X-ray radiation. Finally, cancer cells usually suffer from hypoxia, and it has been demonstrated that well-oxygenated cells are more radiosensitive than hypoxic ones.[2,3] The abovementioned facts call for introducing into clinical practice substances that could specifically sensitize tumor cells to the action of γ/X-rays. This, as a consequence, should diminish the magnitude of therapeutic doses that would save normal cells as well as help to circumvent the hypoxic conditions and repair machinery of cancer cells.

As far as cell death by ionizing radiation is concerned, the DNA molecule is the most important target. Although IR deposits its energy randomly damaging all molecules within the cell, there are multiple copies of most molecules, and many of them undergo a continuous and rapid turnover that limits the destroying effects of IR. On the other hand, there are only two copies of DNA per cell, its turnover is very limited, and the molecule itself is crucial for all cellular functions. Indeed with eukaryotic cells that contain their DNA in the nucleus, little lethal damage is observed as long as IR is absorbed by the

membrane or cytoplasm. However, there is a dramatic increase in cellular death in instances where the ionizing radiation reaches the nucleus.[4]

IR interacts with DNA either directly causing its ionizations/excitations or indirectly via the products of radiolysis of the molecules present in an environment. In the cell, which contains 70−80% water, the indirect action of IR far exceeds the direct effects. Namely, water radiolysis results in the hydroxyl and hydrogen radicals as well as in hydrated electrons. Studies with scavenger molecules indicate that almost all indirect DNA damage is due to attack by the highly reactive hydroxyl radicals (OH•). The reducing counterparts of OH•, i.e., hydrated electrons, although generated by the ionizing radiation in the amount similar to that of hydroxyl radicals,[5] are nevertheless relatively ineffective, especially at inducing DNA strand breaks[6] (DSBs belong to the most lethal damage, and their number generated in the DNA of X-ray irradiated cells correlates with the cell death[7]). This situation may, however, change dramatically provided that modified nucleosides of sufficient electron affinity are incorporated into cellular DNA. Additionally, in order to be effective radiosensitizers, these nucleosides must easily decompose upon electron attachment (by dissociative electron attachment), leaving behind reactive radicals in DNA that in secondary steps may produce strand breaks.

Uracil analogues, notably 5-bromouracil (5-BrU), can be used by a cell for DNA biosynthesis almost as easily as thymine and has long been recognized as a radiosensitizing agent with potential clinical applications.[8−10] Indeed, *in vitro* 5-BrU labeled cells are 2−3 fold more radiosensitive than the nonlabeled ones.[11] The sensitization mechanism is likely related to the rapid reaction of 5-bromo-2′-deoxyuridine (5-BrdU) with hydrated electrons, which has recently been studied by time-resolved

femtosecond laser spectroscopy.[12–14] The primary anions formed as a result of electron attachment to 5-BrdU undergo bromide anion elimination with a tiny kinetic barrier,[15,16] yielding the highly reactive uridine-5-yl radical. If the latter species is produced in DNA, then a secondary hydrogen atom transfer from either the sugar of the nucleoside radical or adjacent nucleoside can ultimately lead to a single bond break.

Although 5-BrU effectively radiosensitizes cell lines in vitro, one of the most extensive phase III clinical trials proved no increased survival related to 5-BrdU administration in radiotherapy for various astrocytomas and malignant gliomas.[17] Moreover, the range of radiosensitizers currently employed in clinical practice is quite narrow.[18] Taking this into account, a further search for potential radiosensitizers seems to be fully justified.

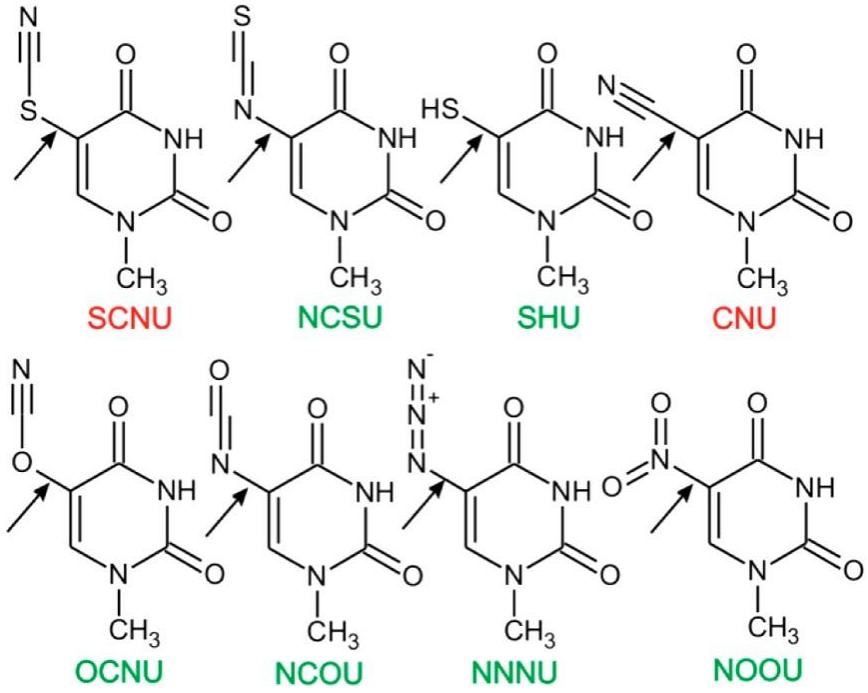

Figure 1.3.1. 5-substituted 1-methyl-uracil derivatives studied with corresponding name abbreviations.

In this Communication we study the propensity of 5-substituted uracils to undergo dissociation by an excess electron. Our choice of uracil derivatives is based on their usefulness as substrates for thymidine kinase[19] – a prerequisite for their incorporation into DNA under the cellular environment. We chose 5-substituted uracils since the 5 site of uracil can be easily modified chemically,[20] and this is the site not involved in the complementary hydrogen bonds responsible for the stability of double helix. For a series of 5-substituted uracil derivatives (see Figure 1.3.1) electron affinities and energy profiles related to their electron-induced degradation were calculated at the DFT level both in aqueous solution and in the gas phase (see Figure 1.3.2 and 1.3.S3).

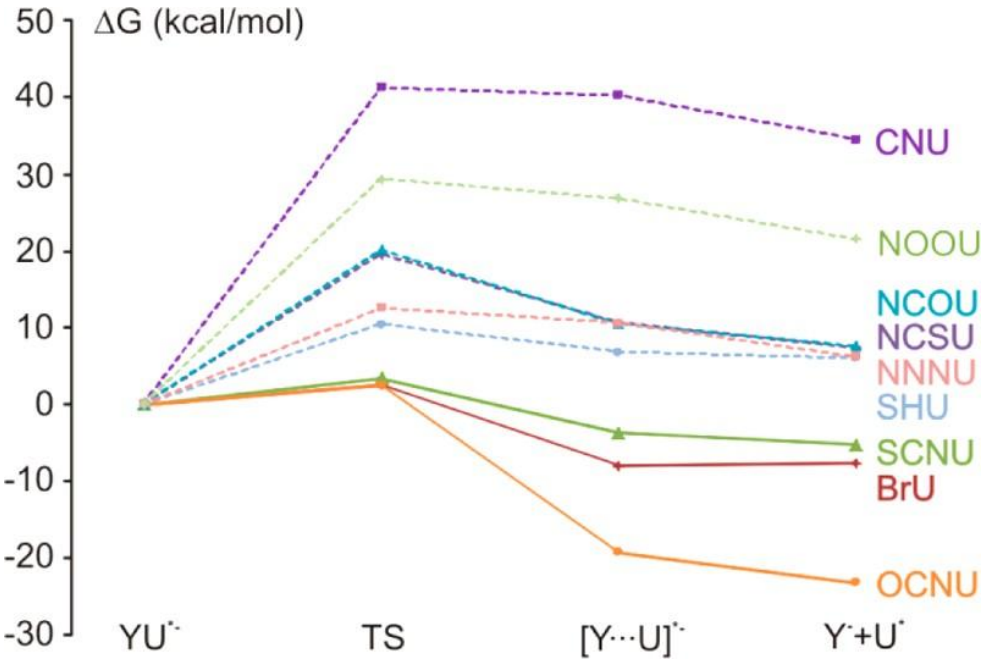

Figure 1.3.2. Free enthalpy profiles for electron induced degradation of 5-substituted modified uracils, in aqueous solution.

For two derivatives – one forming a stable valence anion and another one that undergoes dissociative electron attachment – the quantum chemical computational results were compared to those originating from our anion photoelectron spectroscopy (PES) experiments. The excellent accordance between the calculated and PES characteristics confirms the reliability of the quantum chemical model employed. Our studies suggest that the 5-SCNU and 5-OCNU derivatives that have never been examined in radiobiological experiments so far, could be potential radiosensitizers and should be tested in *in vitro* trials with cell lines.

To model the electrophilic properties of the 5-substituted uracils and the reactivity of their anions, we applied the density functional theory method with Becke's three-parameter hybrid functional (B3LYP)[21,22] and the 6-31++G(d,p) basis set[23,24] to the gas-phase calculations and additionally the polarizable continuum model (PCM)[25–27] of the solvent for the aqueous solution. To mimic the sugar-binding sites present in a nucleoside, the uracil derivatives are methylated at site 1 (see Figure 1.3.1). The adiabatic electron affinity (AEA) is defined as the difference in the electronic free enthalpies of the neutral and the respective anion radical at their corresponding fully relaxed structures. Vertical detachment energies (VDEs) were calculated as the difference between the electronic energies of the neutral and the anion radical at the geometry of the fully relaxed anion radical.

As mentioned above, a substituted uracil having radiosensitizing properties should be (i) a substantially better electron acceptor than thymine, and (ii) its anion should easily decompose giving the uracil-5-yl radical. In order to demonstrate how the substituent at the 5 position of the uracil ring influences electrophilic properties of the studied system,

we chose a series of nine substituents differing by their electron withdrawing properties (see Figure 1.3.1). As the strongest electrophile we used the nitro group, with the Hammett inductive constant, σ_I, of 0.65, considered to have nearly maximal electron-withdrawing power, while as the weakest we used the thiol function with σ_I of 0.3.[28] Hence, the substituents studied here are characterized by a positive value of the Hammett constant, which indicates they should bind an excess electron stronger than the unsubstituted uracil. Indeed, the AEA values gathered in Table 1.3.1 confirm such a conclusion. While the electron affinity of the hydrated uracil calculated at the same level of theory amounts to only 1.94 eV,[29] the respective values

Table 1.3.1. AEA and VDE of 5-substituted 1-methyl-uracil derivatives calculated in an aqueous solution.

YU	AEA[a,b]	VDE[b]
BrU[30]	2.48	2.74
CNU	2.83	3.18
SCNU	2.70	3.07
NCSU	2.73	3.86
NCOU	2.40	2.78
OCNU	2.62	3.07
SHU	2.26	2.66
NNNU	2.38	2.77
NOOU	3.55	3.81

[a]In the free enthalpy scale. [b]In eV.

for the 5-substituted uracils are substantially larger. The AEA value for the analogue substituted with the weakest electrophile, −SH, amounts to 2.26 eV, while that for the strongest, $-NO_2$, is as much as 3.55 eV (see Table 1.3.1).

The stabilities of particular anions, formed as a result of electron attachment to a given derivative, with respect to the process of vertical electron detachment, vary in a way similar to that observed for the adiabatic stabilities, i.e., VDE is the smallest for the −SH substituent and the second largest for the $-NO_2$ (see Table 1.3.1).

The electron affinity value of a modified nucleoside incorporated into the biopolymer is a crucial factor in effectively radiosensitizing DNA due to its interaction with a hydrated electron. However, a large electron affinity is not necessarily the only requirement for its radiosensitizing properties. For example, despite the largest electron adiabatic affinity and vertical stability of its anion (see Table 1.3.1), 5-nitrouracil is not a promising candidate for a DNA radiosensitizer. As indicated by Figure 1.3.2 and the thermodynamic and kinetic characteristics gathered in Table 1.3.2, dissociation of the NOOU anion leading to the reactive uracil-5-yl radical is rather unfavorable.

The reaction of NOOU is associated with the activation barrier of 29.3 kcal/mol, while the ΔG_{SP} is positive and amounts to as much as 21.5 kcal/mol (Table 1.3.2). This shows that after electron attachment to NOOU, the uracil-5-yl radical will not form at all (see Figure 1.3.2). The characteristics of ΔG^* and ΔG_{SP} are quite similar for the second most stable anion, i.e. that originating from 5-cyanouracil. The dissociation of the CNU anion is even more difficult than that of NOOU, i.e., the activation barrier is equal to 41.2 kcal/mol, while ΔG_{SP} amounts to 34.5 kcal/mol (Table 1.3.2). This again prevents the formation of the uracil-5-yl radical from the CNU anion (see Figure 1.3.2).

Table 1.3.2. Thermodynamic and kinetic characteristics for degradation of uracil methyl derivatives in aqueous solution (kcal/mol).

YU	$YU^{*-} \rightarrow [Y....U]^{*-}$		$YU^{*-} \rightarrow Y^{-} + U^{*}$	$YU + e \rightarrow Y^{-} + U^{*}$
	ΔG_{PC}	ΔG^{*}	ΔG_{SP}	ΔG_{total}
BrU[30]	-8.0	2.5	-7.7	-65.0
CNU	40.2	41.2	34.5	-30.8
SCNU	-3.7	3.4	-5.2	-67.5
NCSU	10.5	19.5	7.4	-55.5
NCOU	10.5	20.1	7.6	-47.8
OCNU	-19.3	2.5	-23.3	-83.7
SHU	6.8	10.4	6.0	-46.0
NNNU	10.6	12.5	6.2	-48.8
NOOU	26.8	29.3	21.5	-60.4

Thus, in order to assess the usefulness of the studied derivative, one should also take into account the chemical bond strength that connects a substituent to the C5 carbon of uracil as well as the electron affinity of the radical fragment, Y•, in addition to the stability of the substituted uracil anion. Note that the AEAs of CNU and OCNU differ by only 5 kcal/mol (0.21 eV, see Table 1.3.1) while the respective ΔG_{SP} free energies by as much as 57.8 kcal/mol (see Table 1.3.2). Consequently, despite the fact that both CNU (AEA = 2.83 eV) and OCNU (AEA = 2.62 eV) should attach an electron (cf. BrU has an AEA of only 2.48 eV that sensitizes modified DNA to hydrated electrons), only the latter

compound may act as a radiosensitizer since its electron-induced dissociation is associated with a negligible activation barrier (2.5 kcal/mol; Table 1.3.2) and an exceptionally favorable ΔG_{SP} stimulus (−23.3 kcal/mol; Table 1.3.2). As the AEAs of OCNU and CNU differ by only ca. 5 kcal/mol, the advantageous dissociation thermodynamics of the $OCNU^-$ anion has to be a consequence of much weaker bond strength between the substituent and uracil moiety in the former case. Indeed, the B3LYP/6-31++G(d,p) dissociation free energies, YU → Y• + U•, for OCNU and CNU are equal to 58 and 124 kcal/mol, respectively.

For strengthening our quantum modeling, we also employed the use of negative ion photoelectron spectroscopy (PES, for details see Supporting Information). With this powerful experimental technique, we confirmed the quantum chemically predicted behavior of two compounds, SCNU and CNU, differing in their potential radiosensitizing properties. As indicated by Figure 1.3.2, CNU belongs to the group of nonsensitizing species whose electron-induced dissociation is accompanied by substantial activation barriers and unfavorable thermodynamics. On the other hand, SCNU can be considered as a potential radiosensitizer (as BrU and OCNU; Figure 1.3.2) whose dissociation proceeds with a negligible activation barrier and negative thermodynamic stimulus. The PES experiment was carried out for nonmethylated CNU and SCNU since the former compound was accessible commercially. The nonmethylated form of SCNU was synthesized (for details see Supporting Information).

The PES spectrum recorded for 5-cyanouracil (CNU(-Me)) depicted in Figure 1.3.3 demonstrates that, in accordance with our QM model (see Figure 1.3.2), CNU(-Me) forms a stable valence anion in the gas phase. The VDE read from the spectrum (the

maximum value of photoelectron signal) is 1.55 eV. The B3LYP VDE calculated for CNU(-Me) is equal to 1.69 eV. However, it is known that the VDE values for nucleobase anions are overestimated at the B3LYP level by ca. 0.20 eV, as was determined by the difference between the VDEs of valence uracil anion calculated at the B3LYP/6-31++G and CCSD(T)/aug-cc-pVDZ levels.[31] It is worth noticing that the value of this increment is pretty close to corrections found within recent benchmark studies, where it was demonstrated that AEAs and VDEs of the isolated uracil and its complexes with water were larger than the respective CCSD(T) values by 0.2−0.3 eV.[32,33]

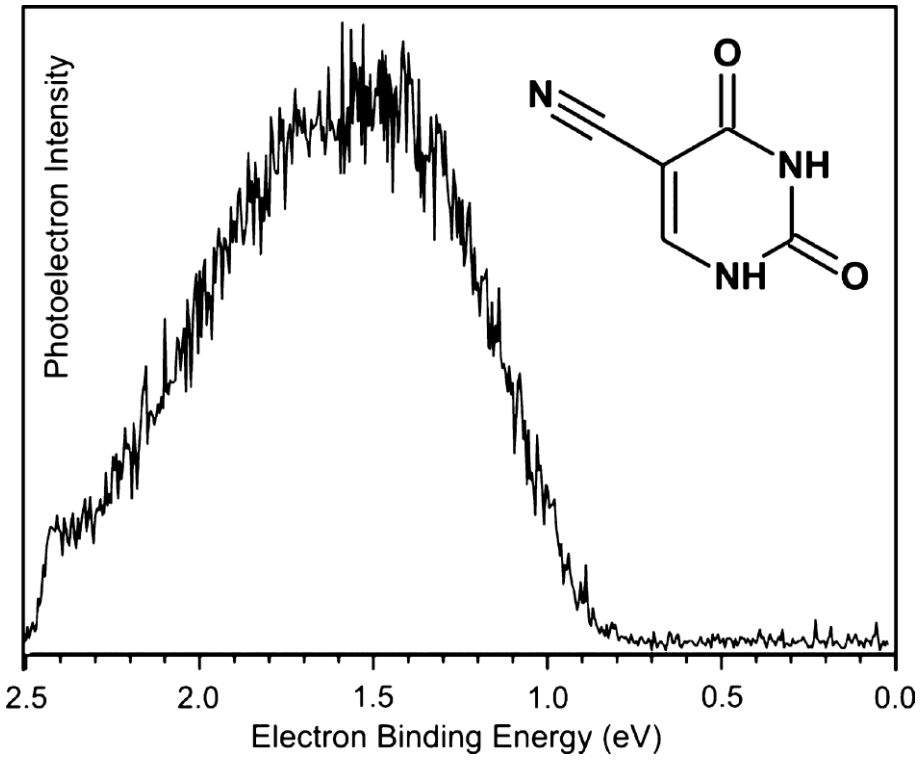

Figure 1.3.3. 5-Cyanouracil photoelectron spectrum recorded with 2.540 eV photons.

Applying the increment of 0.2 eV,[31] one obtains 1.49 eV as a theoretical VDE, which thereafter agrees well with the experimental value. Similarly, the experimental

AEA (the electron binding energy value at 10% of the maximal photoelectron intensity) is estimated to be 0.95 eV, while the theoretical value is equal to 1.02 eV. Moreover, as indicated by the mass spectrum of CNU(-Me) recorded during the PES experiment (see Figure 1.3.4B) there are no significant amounts of CN^- present (beyond background) and only the parent CNU(-Me) anion is observed, this being in full agreement with our theoretical predictions (Figure 1.3.2 and Table 1.3.2).

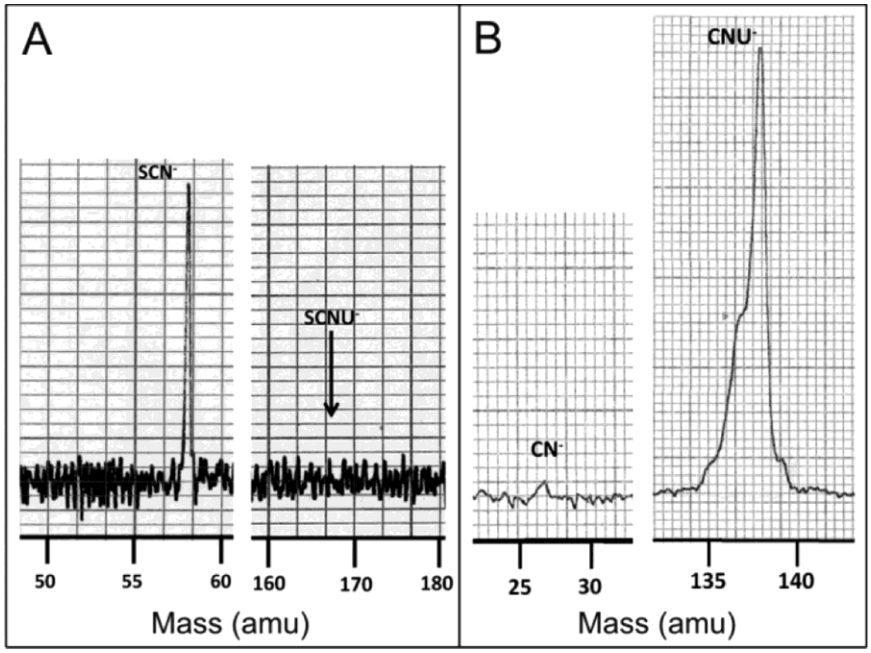

Figure 1.3.4. Anionic mass spectra for SCNU(-Me) (A) and CNU(-Me) (B), each pair of mass spectra having been recorded on the same signal intensity scales.

The behavior of SCNU(-Me), belonging to the group of potential radiosensitizers, is completely different. We were unable to observe any of the parent anion, $[SCNU(-Me)]^-$, while the mass originating from the SCN^- parent anion had a strong signal intensity (Figure 1.3.4A). This again is in complete agreement with the QM model.

In summary, we presented a protocol that should enable a potential uracil-based DNA radiosensitizer that utilizes hydrated electrons to be assessed. Efficient sensitizers should be modified with a substituent excreting a substantial electron-withdrawing effect in order to ensure uracil anion stability that will make electron transfer to modified DNA possible from hydrated electrons. What is even more important, the chemical bond connecting a substituent to the uracil residue cannot be too strong. Otherwise, the kinetic barrier and thermodynamics related to electron-induced dissociation will prevent dissociation. The results of PES experiments carried out for two derivatives, one being a sensitizer and the other resistant to the electron-induced cleavage of the Y−U bond, are in full agreement with our theoretical investigations. The limited search for new DNA radiosensitizers, comprising only eight analogues, yielded two potential candidates, 5-thiocyanato- and 5-cyanatouracil, which have never been tested in radiobiological experiments.

ACKNOWLEDGEMENTS

This work was supported by the Polish National Science Center (NCN) under the Grant No. 2012/07/N/ST5/01877 (M.Z.), by the National Science Foundation under Grant No. CHE-1111693 (K.H.B.) and by the system project "InnoDoktorant−Scholarships for PhD students, Vth edition". Project is co-financed by the European Union in the frame of the European Social Fund (L.C.). Calculations have been carried out in Wroclaw Center for Networking and Supercomputing, Grant No. 209 (L.C.).

REFERENCES

1. Joiner, M., van der Kogel, A. *Basic Clinical Radiobiology*; Hodder Arnold: London, 2009.
2. Da u, A.; Denekamp, J. New Insights into Factors Influencing the Clinically Relevant Oxygen Enhancement Ratio. *Radiother. Oncol*. **1998**, *46*, 269−277.
3. Oronsky, B. T.; Knox, S. J.; Scicinski, J. Six Degrees of Separation: The Oxygen Effect in the Development of Radiosensitizers. *Transl. Oncol*. **2011**, *4*, 189−198.
4. Warters, R. L.; Hofer, K. G. Radionuclide Toxicity in Cultured Mammalian Cells: Elucidation of the Primary Target of Radiation Damage. *Curr. Top. Radiat. Res. Q*. **1977**, *69*, 348−358.
5. von Sonntag, C. *The Chemical Basis of Radiation Biology*; Taylor and Francis: London, 1987.
6. Michael, B. D.; O'Neill, P. A Sting in the Tail of Electron Tracks. *Science* **2000**, *287*, 1603−1604.
7. Peters, G. *Deoxynucleoside Analogs in Cancer Therapy*; Humana Press Inc.: Totowa, NJ, 2006.
8. Djordjevic, B.; Szybalski, W. Genetics of Human Cell Lines III. Incorporation of 5-Bromo- and 5-Iododeoxyuridine into the Deoxyribonucleic Acid of Human Cells and Its Effect on Radiation Sensitivity. *J. Exp. Med*. **1960**, *112*, 509−531.
9. Erickson, R. L.; Szybalski, W. Molecular Radiobiology of Human Cell Lines: V. Comparative Radiosensitizing Properties of 5-Halodeoxycytidines and 5-Halodeoxyuridines. *Radiat. Res*. **1963**, *20*, 252−262.

10. Cramer, J. W.; Prusoff, W. H.; Welch, A. D.; Sartorelli, A. C.; Delmore, I. W.; von Essen, C. F.; Chang, P. K. Studies on the Biochemical Pharmacology of 5-IODO-2′-deoxycytidine *in vitro and in vivo. Biochem. Pharmacol*. **1962**, *11*, 761−768.
11. Brust, D.; Feden, J.; Farnsworth, J.; Amir, C.; Broaddus, W. C; Valerie, K. Radiosensitization of Rat Glioma with Bromodeoxycytidine and Adenovirus Expressing Herpes Simplex Virus-Thymidine Kinase Delivered by Slow, Rate-Controlled Positive Pressure Infusion. *Cancer Gene Ther*. **2000**, *7*, 778−788.
12. Wang, C. R.; Hu, A.; Lu, Q.-B. Direct Observation of the Transition State of Ultrafast Electron Transfer Reaction of a Radiosensitizing Drug Bromodeoxyuridine. *J. Chem. Phys*. **2006**, *124*, 241102.
13. Wang, C. R.; Lu, Q. B. Real-Time Observation of a Molecular Reaction Mechanism of Aqueous 5-Halo-2′-deoxyuridines under UV/Ionizing Radiation. *Angew. Chem., Int. Ed.* **2007**, *46*, 6316−6320.
14. Wang, C. R.; Lu, Q. B. Molecular Mechanism of the DNA Sequence Selectivity of 5-Halo-2′-deoxyuridines as Potential Radiosensitizers. *J. Am. Chem. Soc.* **2010**, *132*, 14710−14713.
15. Wetmore, S. D.; Boyd, R. J.; Eriksson, L. A. A Theoretical Study of 5-Halouracils: Electron Affinities, Ionization Potentials and Dissociation of the Related Anions. *Chem. Phys. Lett*. **2001**, *343*, 151−158.
16. Li, X.; Sanche, L.; Sevilla, M. D. Dehalogenation of 5-Halouracils after Low Energy Electron Attachment: A Density Functional Theory Investigation. *J. Phys. Chem. A* **2002**, *106*, 11248−11253.

17. Prados, M. D.; Scott, C.; Sandler, H.; Buckner, J. C.; Phillips, T.; Schultz, Ch.; Urtasun, R.; Davis, R.; Gulin, P.; Cascino, T.; et al. A Phase 3 Randomized Study of Radiotherapy Plus Procarbazine, CCNU, and Vincristine (PCV) with or without BUdR for the Treatment of Anaplastic Astrocytoma: A Preliminary Report of RTOG 9404. *Int. J. Radiat. Oncol. Biol. Phys*. **1999**, *45*, 1109−1115.
18. Choy, H. *Chemoradiation in Cancer Therapy; Humana Press Inc*.: Totowa, NJ, 2011.
19. van Rompay, A. R.; Norda, A.; Linden, K.; Johansson, M.; Karlsson, A. Phosphorylation of Uridine and Cytidine Nucleoside Analogs by Two Human Uridine-Cytidine Kinases. *Mol. Pharmacol*. **2001**, *59*, 1181−1186.
20. Ressner, E. C.; Fraher, P.; Edelman, M. S.; Mertes, M. P. Synthesis of 5-Substituted Uracil Derivatives. *J. Med. Chem*. **1976**, *19*, 194−196.
21. Becke, A. D. Density-Functional Exchange-Energy Approximation with Correct Asymptotic Behavior. *Phys. Rev. A* **1988**, *38*, 3098−3100.
22. Becke, A. D. Density-Functional Thermochemistry. III. The Role of Exact Exchange. *J. Chem. Phys.* **1993**, *98*, 5648−5652.
23. Ditchfield, R.; Hehre, W. J.; Pople, J. A. Self-Consistent Molecular-Orbital Methods. IX. An Extended Gaussian-Type Basis for Molecular-Orbital Studies of Organic Molecules. *J. Chem. Phys*. **1971**, *54*, 724−728.
24. Hehre, W. J.; Ditchfield, R.; Pople, J. A. Self-Consistent Molecular Orbital Methods. XII. Further Extensions of Gaussian-Type Basis Sets for Use in Molecular Orbital Studies of Organic Molecules. *J. Chem. Phys*. **1972**, *56*, 2257−2261.

25. Miertu , S.; Scrocco, E.; Tomasi. Electrostatic Interaction of a Solute with a Continuum. A Direct Utilization of Ab Initio Molecular Potentials for the Prevision of Solvent Effects. *J. Chem. Phys*. **1981**, *55*, 117−129.
26. Miertu , S.; Tomasi. Approximate Evaluations of the Electrostatic Free Energy and Internal Energy Changes in Solution Processes. *J. Chem. Phys*. **1982**, *65*, 239−245.
27. Cossi, M.; Barone, V.; Cammi, R.; Tomasi. Ab Initio Study of Solvated Molecules: A New Implementation of the Polarizable Continuum Model. *J. Chem. Phys. Lett*. **1996**, *255*, 327−335.
28. Hansch, C.; Leo, A.; Taft, R. W. A Survey of Hammett Substituent Constants and Resonance and Field Parameters. *Chem. Rev*. **1991**, *97*, 165−195.
29. Mazurkiewicz, K.; Bachorz, R. A.; Gutowski, M.; Rak, J. On the Unusual Stability of Valence Anions of Thymine Based on Very Rare Tautomers: A Computational Study. *J. Phys. Chem. B* **2006**, *110*, 24696−24707.
30. Chomicz, L.; Rak, J.; Storoniak, P. Electron-Induced Elimination of the Bromide Anion from Brominated Nucleobases. A Computational Study. *J. Phys. Chem. B* **2012**, *116*, 5612−5619.
31. Gutowski, M.; Dąbkowska, I.; Rak, J.; Xu, S.; Nilles, J. M.; Radisic, D.; Bowen, K. H., Jr. Barrier-Free Intermolecular Proton Transfer in the Uracil−Glycine Complex Induced by Excess Electron Attachment. *Eur. Phys. J. D* **2002**, *20*, 431−439.

32. Ded kov , P.; Neogr dy, P.; Urban, M. Electron Affinities of Small Uracil−Water Complexes: A Comparison of Benchmark CCSD(T) Calculations with DFT. *J. Phys. Chem. A* **2011**, *115*, 2350−2358.
33. Melicher k, M.; Pa teka, L. F.; Neogr dy, P.; Urban, M. Electron Affinities of Uracil: Microsolvation Effects and Polarizable Continuum Model. *J. Phys. Chem. A* **2012**, *116*, 2343−2351.

SUPPORTING INFORMATION

A. General procedure for synthesis of 5-thiocyanatouracil.

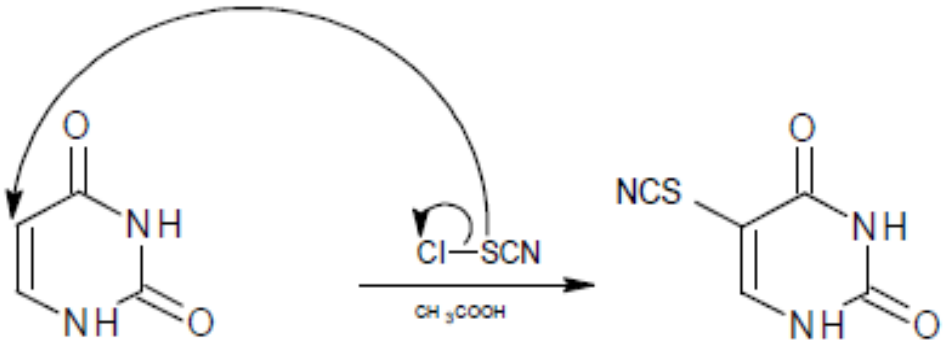

Figure 1.3.S1. Scheme of synthesis of 5-thiocyanatouracil (5-SCNU).

Dried KSCN was used in the preparation of ClSCN and the Cl_2 gas was passed through a $CaCl_2$ trap prior to use. Acetic acid (CH_3COOH) was dried by distillation and freezing. Dried fine powder of KSCN (5.35 g, 55 mmol) was added to an ice-cold solution of Cl_2 (3.55 g, 50 mmol) in dry CH_3COOH (300 ml). The resulting suspension was stirred for 1.5 hour at room temperature. Uracil **(**0.672 g, 6 mmol) was added to a solution of ClSCN in HOAc and the resulting mixture was stirred at room temperature for 2 hour. Cyclohexene (15 ml) was added and stirring continued for 20 min. After filtration, the solution was evaporated under vacuum to give a residue which was extracted with hot water. The extract was purified with semi-preparative HPLC. The HPLC purification was performed on a Schimadzu SPD-10A system with a UV detector, which was set at 260 nm. A 10 mm x 250 mm Gemini reverse-phase C18 column (5Dm in particle size and 110 A in pore size) (Phenomenex) with a mobile phase consisting of

deionized water, acetonitrile (Sigma-Aldrich, Poland) and 1% formic acid (POCH S.A., Poland) (pH 2.55; 87.7:2:10.3, v/v/v) was used. The flow rate was set at 4 ml/min. The resulting product was a white-yellowish powder. IR (KBr) 2973, 2814, 2159, 1701, 1656, 1477, 1435, 1351, 1244, 1186, 1009, 870, 781, 551, 453; Anal. ($C_{16}H_{13}NO_2$): calculated C, 35.5; H, 1.79; N, 24.84; S, 18.96 found C, 35.58; H, 1.83; N, 24.50; S, 18.66; Purity (HPLC): 99.8% t_R= 5.897 min (see Figure 1.3.S2); ESI-MS $[M-H]^-$ =167.9 (MW = 169.16) (see Figure 1.3.S3).

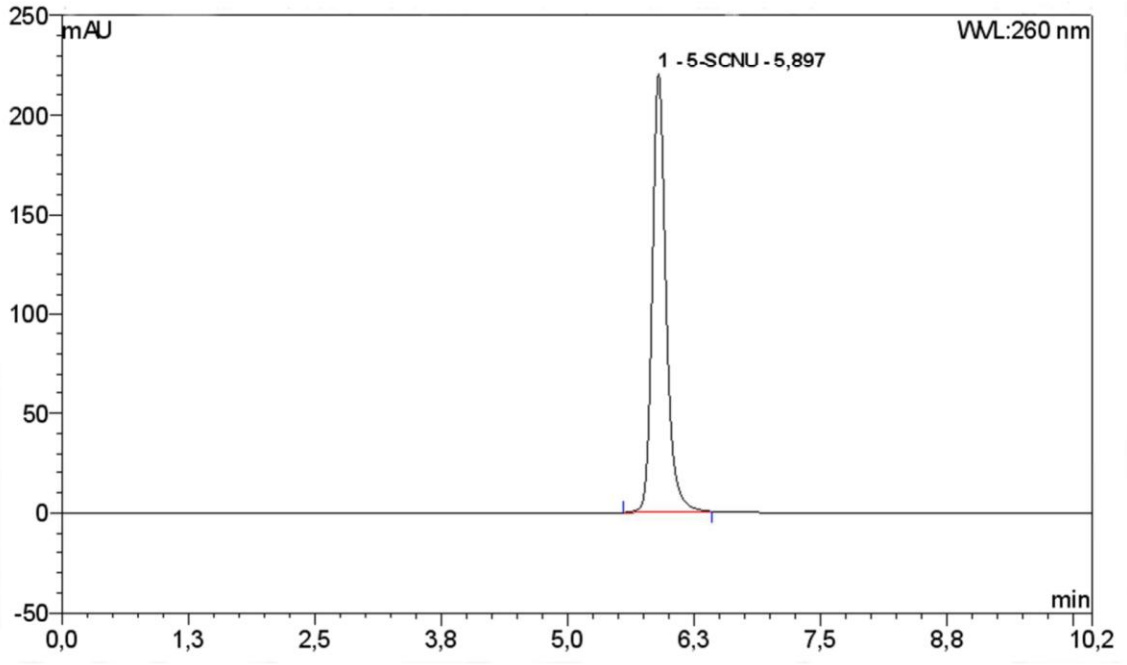

Figure 1.3.S2. Chromatogram of 5-thiocyanatouracil after purification (conditions: Dionex UltiMate 3000 System with Diode Array Detector; column-Phenomenex Gemini C18; elution- 100% A= 0,1% HCOOH, 2% ACN in water; flow-4ml/min; detection-260 nm).

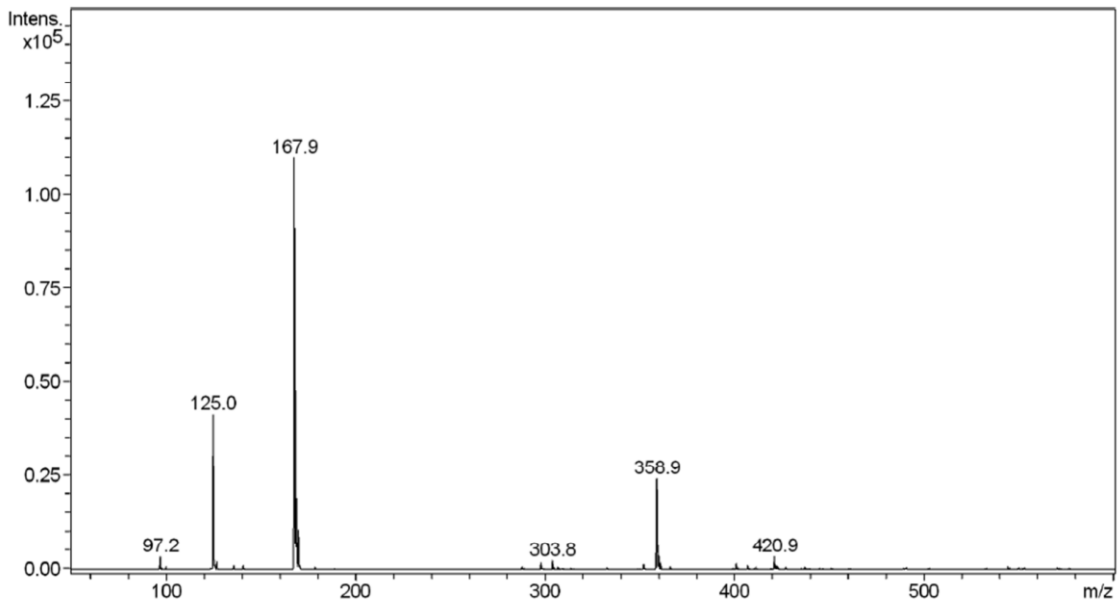

Figure 1.3.S3. Mass spectrum of 5- thiocyanatouracil after purification (ESI-MS, HCTultra ion-trap mass spectrometer, the analysis was conducted in the negative ion mode).

B. Computational details and additional computational results.

All the geometries were fully optimized without any geometrical constraints, and the analysis of harmonic frequencies demonstrated that all of them were geometrically stable (all force constants were positive) or first-order saddle points (all but one force constant positive). The energies of particular reactions (ΔEs) were calculated as the differences between the electronic energies of substrates and products, while the Gibbs free energies of these reactions (ΔGs) were ΔEs corrected for zero-point vibration terms, thermal contributions to energy, the pV term, and the entropy term. These terms were calculated in the rigid rotor-harmonic oscillator approximation for T = 298 K and p = 1 atm. To calculate ΔG for the solvated systems, the same correction terms were applied to

the solute as were used for calculating the gas-phase free energies. All quantum chemical calculations were carried out with GAUSSIAN09.[1]

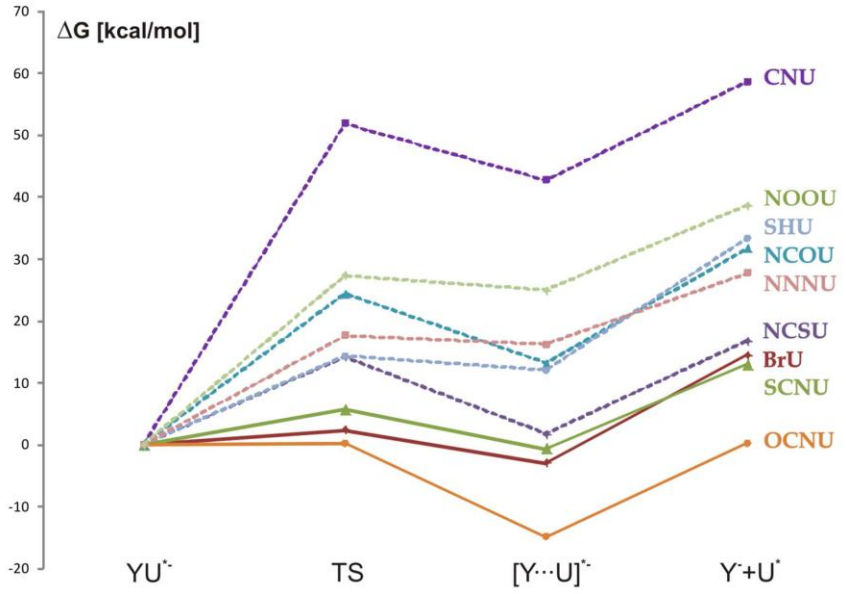

Figure 1.3.S4. Electron induced degradation of 5-substituted uracils free enthalpy profiles, gas phase.

Table 1.3.S1. Adiabatic electron affinity (AEA) and vertical detachment energy (VDE) of 5-substituted 1-methyluracil calculated in the gas phase.

YU	AEA[a] [kcal/mol]	VDE [eV]
BrU[b]	16.0	1.02
CNU	27.0	1.59
SCNU	26.6	1.57
NCSU	14.8	1.75
NCOU	15.6	1.12
OCNU	24.2	1.58
SHU	10.6	0.87
NNNU	16.1	1.07
NOOU	40.6	1.94

[a]in the free enthalpy scale, [b]data from ref. 20

Table 1.3.S2. Thermodynamic and kinetic characteristics for degradation of uracil methyl derivatives in the gas phase, in kcal/mol.

YU	$YU^{*-} \rightarrow [Y....U]^{*-}$		$YU^{*-} \rightarrow Y- + U^*$	$YU + e \rightarrow Y^- + U^*$
	ΔG	ΔG^*	ΔG	ΔG_{total}
BrU[a]	-3.0	2.4	14.5	-1.5
CNU	42.7	51.8	58.6	31.6
SCNU	-0.7	5.7	12.9	-13.7
NCSU	1.7	14.2	16.7	1.9
NCOU	13.1	24.3	31.7	16.1
OCNU	-14.9	0.2	0.2	-24.1
SHU	12.0	14.2	33.3	22.7
NNNU	16.2	17.6	27.7	11.6
NOOU	24.9	27.3	38.6	-2.0

[a]data from ref. 20

C. Photoelectron spectroscopy experimental details.

Negative ion photoelectron spectroscopy was conducted by crossing a mass-selected beam of parent negative ions with a fixed-frequency photon beam and energy-analyzing the resultant photodetached electrons. The photodetachment process is governed by the relationship hν = EBE + EKE, where hν is the photon energy, EBE is the electron binding energy or the transition energy needed to take the anion to a particular vibrational state of its neutral counterpart, and EKE is the electron kinetic energy. The negative ions were formed in a supersonic expansion nozzle-ion source. Each sample was

placed in the stagnation chamber of the source and heated into the gas phase (~160-180°C for SCNU(-Me); ~180-200°C for CNU(-Me)). Samples were co-expanded with 1 atm of argon gas through a 25 μm orifice into ~10^{-4} torr vacuum. The anions were then formed by injecting low energy electrons from a hot and even more negatively biased, thoriated iridium filament into the expanding jet where the microplasma was formed in the presence of a weak external magnetic field. The anions were extracted, and transported via a series of ion optics through the flight tube of a 90° magnetic sector mass spectrometer with a typical mass resolution of ~400. The mass-selected anions of interest were crossed with an intracavity operated argon ion laser beam, and the resultant photodetached electrons were energy-analyzed in a hemispherical electron energy analyzer with a resolution of ~30 meV. The photoelectron spectrum reported here was recorded with 2.54 eV photons and calibrated against the well-known photoelectron spectrum of the O^- anion.[2]

SUPPLEMENTAL MATERIAL REFERENCES

1. Gaussian 09, Revision B.01, Frisch, M. J.; Trucks, G. W.; Schlegel, H. B.; Scuseria, G. E.; Robb, M. A.; Cheeseman, J. R.; Scalmani, G.; Barone, V.; Mennucci, B.; Petersson, G. A.; Nakatsuji, H.; Caricato, M.; Li, X.; Hratchian, H. P.; Izmaylov, A. F.; Bloino, J.; Zheng, G.; Sonnenberg, J. L.; Hada, M.; Ehara, M.; Toyota, K.; Fukuda, R.; Hasegawa, J.; Ishida, M.; Nakajima, T.; Honda, Y.; Kitao, O.; Nakai, H.; Vreven, T.; Montgomery, Jr., J. A.; Peralta, J. E.; Ogliaro, F.; Bearpark, M.; Heyd, J. J.; Brothers, E.; Kudin, K. N.; Staroverov, V. N.; Kobayashi, R.; Normand, J.; Raghavachari, K.; Rendell, A.; Burant, J. C.; Iyengar, S. S.; Tomasi, J.; Cossi, M.; Rega, N.; Millam, J. M.; Klene, M.; Knox, J. E.; Cross, J. B.; Bakken, V.; Adamo, C.; Jaramillo, J.; Gomperts, R.; Stratmann, R. E.; Yazyev, O.; Austin, A. J.; Cammi, R.; Pomelli, C.; Ochterski, J. W.; Martin, R. L.; Morokuma, K.; Zakrzewski, V. G.; Voth, G. A.; Salvador, P.; Dannenberg, J. J.; Dapprich, S.; Daniels, A. D.; Farkas, O.; Foresman, J. B.; Ortiz, J. V.; Cioslowski, J.; Fox, D. J. Gaussian, Inc., Wallingford CT, 2009.
2. Neumark, D. M.; Lykke, K. R.; Andersen, T.; Lineberger, W. C. Laser photodetachment measurement of the electron affinity of atomic oxygen. *Phys. Rev. A: Gen. Phys.* **1985**, *32*, 1890.

CHAPTER 2

Section 2.1. Intramolecular Proton Transfer in Acetoacetic Acid Induced by a π* Excess Electron

Section 2.2. Remarkable Electrophilicity of the Oxalic Acid Monomer Anion: A Photoelectron Spectroscopy and Theoretical Study

Section 2.3. Electron-Induced Proton Transfer from HCl to the Superbase 1,8-Bis(dimethylamino)naphthalene

This chapter presents several systems in which upon addition of an excess electron, intramolecular or intermolecular proton transfer may occur within a complex. This phenomenon may also be referred to as electron-induced proton transfer (EIPT) and is fundamental to energetic conversion in chemical and biological processes. Examples of where intramolecular tautomerization and intermolecular proton transfer are involved include breakage of single and double strands of DNA, reactions within acid-base chemistry, and photosynthesis. Regardless if the proton transfer occurs as an intramolecular or intermolecular process, changes in the electronic structure of the system is the result. Thus, the study of particular gas-phase anions as model systems allows for a better understanding of such processes that occur in the condensed phase.

Sections **2.1** and **2.2** introduce the complexes acetoacetic acid and oxalic acid, respectively, which undergo intramolecular tautomerization upon attachment of an excess electron. In both cases, the proximity of a carboxylate group to either a keto or another carboxylate group enhances the electrophilicity of the molecule. This allows the excess electron to bind on the π* valence orbital and thus change the localization of a proton in

the complex. Section **2.4** introduces an interesting system involving intermolecular proton transfer between an acid and a base. By introducing an excess electron under isolation, i.e. in the gas-phase, the proton of HCl transfers to the superbase 1,8-bis(dimethylamino)naphthalene and forms the anion of the ionic salt. This system is an extension to earlier studies of the ammonia-HX (X=Cl, Br, I) series but replaces ammonia with a much stronger base. The obtained photoelectron spectrum is compared to the spectra of the ammonia-HX series.

Section 2.1 Intramolecular Proton Transfer in Acetoacetic Acid Induced by a π* Excess Electron

Zibo G. Keolopile,[*, †] Maciej Gutowski,[*, †] Angela Buonaugurio,[‡] Evan Collins,[‡] Xinxing Zhang,[‡] Jeremy Erb,[‡] Thomas Lectka,[‡] Kit Bowen,[‡] and Michael Allan[§]

[†]*Institute of Chemical Sciences, School of Engineering and Physical Sciences, Heriot-Watt University, Edinburgh, Scotland, EH14 4AS, UK*

[‡]*Department of Chemistry, Johns Hopkins University, Baltimore, Maryland 21218, USA*

[§]*Department of Chemistry, University of Fribourg, chemin du Musée 9, 1700 Fribourg, Switzerland*

ABSTRACT

Acetoacetic acid (AA), equipped with neighboring carboxylic and keto groups, is a promising system for studies of intramolecular proton transfer. The results of our computational search for the most stable tautomers and conformers of the neutral and anionic AA allowed to guide and interpret the parallel anion photoelectron and electron energy-loss spectroscopy measurements. We identified several conformers of the canonical neutral AA within a narrow energy range of 1 kcal/mol. The conformer with the intramolecular hydrogen bond, and thus susceptible to intramolecular carboxylic-to-keto proton transfer, proved to be the third most stable and the most polar, with a dipole moment of 5.4 D. The polar neutral conformer supports a dipole-bound anion with an electron vertical detachment energy of 57 meV. The valence anions of AA all exist in the enol form. The distinct global minimum is more stable than other minima by more than

12 kcal/mol. It is supported by a short intramolecular hydrogen bond between the enol and carboxylate groups. The valence anion is characterized by a significant electron vertical detachment energy of 2.38 eV, but a modest adiabatic electron affinity of 0.33 eV. The inherent instability of AA with respect to acetone and CO_2 is suppressed in the valence anionic state. The valence anion was identified in photoelectron spectroscopy experiments and the measured electron vertical detachment energy of 2.30 eV is very good agreement with our computational predictions. We conclude that binding an excess electron in a π^* valence orbital changes localization of the proton in AA. The results of electron energy-loss spectroscopy demonstrate that AA is able to quasithermalize electrons attached into the lowest π^* resonance at about 0.5 eV, but with an efficiency much lower than the that of the dimer of formic acid and thus does not provide evidence for an ultrarapid proton transfer capable of competing with the spontaneous electron detachment. Our computational results allow rationalizing these experimental findings in terms of the co-existence of various conformers of AA. Only one, and not the most stable, conformer is prearranged for intramolecular proton transfer, and it is not present in the target gas with sufficient density. This conclusion is confirmed by our vibrational spectrum, recorded by electron energy-loss spectroscopy. All other low-lying conformers undergo electron autodetachment with or without vibrational excitations, but are unable to relax to the enol structure on a timescale fast enough to compete with autodetachment.

*Corresponding authors: email: keolopilezg@mopipi.ub.bw, m.gutowski@hw.ac.uk

INTRODUCTION

The phenomenon of proton transfer is coupled with the electronic structure of the molecules involved. In particular, an excess electron can drive the redistribution of protons.[1] Proton motion coupled with electron transfer has been identified long ago as the basic mechanism of bioenergetic conversion.[2] Recent experimental and theoretical research on electron-driven processes has been primarily driven by two factors: (i) damage of DNA and RNA by low-energy electrons[3] and (ii) the potential of electron beam lithography to fabricate the next generation of micro- and nano-electromechanical devices.[4]

Recent experimental gas phase studies on electron electron-induced proton transfer in fragments of DNA and proteins[1,5] have been hampered by low vapor pressure of these molecules. This motivated us to identify model systems in which analogous fundamental chemical physics processes take place, but which display a larger vapor pressure than typical biomolecules. When dealing with intermolecular proton transfer induced by a π excess electron we suggested that the dimer of formic acid may serve as a model system.[6] It displays many similarities with intermolecular proton transfer in anionic complexes of nucleic acid bases with weak acids. Similarly, a hydrogen bonded complex of ammonia and hydrogen chloride may serve as a model system for intermolecular proton transfer induced by a σ excess electron.[7]

The electron-induced proton transfer in formic acid dimer (scheme in Figure 2.1.1) was invoked to interpret differences in the results of electron energy loss spectroscopy experiments on the monomer and dimer of formic acid.[8] The yield of very low energy electrons was found to be 20x stronger in the dimer than in the monomer. The

dramatic increase in the efficiency of the dimer to quasithermalize electrons arriving in the 1-2 eV energy range and captured in the lowest π* shape resonance was interpreted in terms of rapid intermolecular proton transfer that quenches the fast autodetachment channel. It was concluded that the phenomenon of electron-driven proton transfer can be ubiquitous and it may be responsible for rapid slowing down of excess electrons.

The relaxed anion of the formic acid dimer has recently been experimentally characterized using Ar-tagged vibrational predissociation and electron autodetachment spectroscopies.[9] These results confirmed that excess electron attachment leads to a rapid barrier-free transfer of one of the protons across the H-bonded bridge. The study corroborated that the relaxed anion of formic acid dimer is composed of a largely intact formate anion attached to the dihydroxymethyl radical through a symmetrical, double O-H bonded bridge.

Less information is available on intramolecular proton transfer induced by an excess electron and the results are available primarily for low-vapor pressure molecules, e.g., nucleotides.[10] For example, the anion photoelectron spectrum of 2'-deoxyadenosine-5'-monophosphate[10] has been interpreted through intramolecular proton transfer from a hydroxyl group of the phosphate to the N3 position of the adenine.[11] Fundamental studies of intramolecular proton transfer induced by an excess electron would benefit from model systems with well defined intramolecular hydrogen bonds and vapor pressures significantly larger than those in biomolecules.

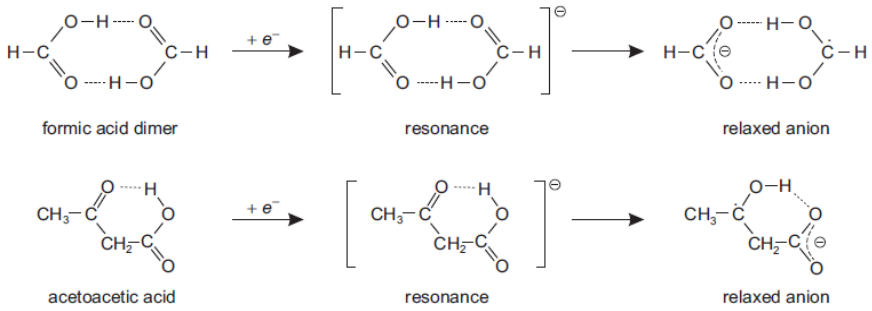

Figure 2.1.1. The electron-induced intermolecular proton transfer in the formic acid dimer (top), and the analogous intramolecular proton transfer in the acetoacetic acid (bottom). In both cases the vertical electron attachment leads to a (shape) resonance, with the excess electron in the lowest π* orbital, which can then relax by an ultrarapid proton transfer, in competition with the very fast spontaneous electron detachment.

Here we present computational and experimental results on the neutral and anionic acetoacetic acid (AA) (Figures 2.1.1 and 2.1.2). Upon formation of the proper conformer, the neighboring carboxylic and keto group engage in an intramolecular hydrogen bond providing a bridge for the intramolecular proton transfer. AA is the simplest beta-keto acid and is thermodynamically unstable with respect to decomposition to acetone and CO_2. However, the experimental half-life of 140 minutes has been reported for a water solution of AA at 37°C.[12] Thus the molecule can be probed experimentally provided care is taken to operate at low temperatures. Some computational information is available on the ketonic decarboxylation of AA.[13–15] Huang et al.[13] reported a two step process of unimolecular decarboxylation with barriers of 25.7 and 55.9 kcal/mol at the MP2/6 31G* level of theory.

Our computational study is focused on the tautomers and conformers of the neutral and anionic AA. The anion photoelectron spectroscopy measurements allow probing bound anionic states of AA and verify computational predictions. The electron energy loss spectroscopy measurements provide a vibrational spectrum of the neutral AA target and the vertical electron attachment energies for the (unrelaxed) π*-states (resonances) of the AA^- anion. Based on the past experience with the dimer of formic acid,[8] particular attention is paid to the possibility of quasithermalization of electrons captured in the lowest π* shape resonance, which would be indicative of an ultrarapid proton transfer.

COMPUTATIONAL METHODS

The tautomers and conformers of neutral and anionic AA were explored using our in-house tool, PESST.[16] Only two tautomers were considered, the canonical keto tautomer and a zwitterionic enol tautomer resulting from proton transfer from O2 to O1, both shown in Figure 2.1.2. The keto tautomer supports a dipole-bound anionic state. The enol tautomer supports a strongly bound valence anion in addition to the dipole bound anion. Henceforth we will use DB and VB to refer to the dipole and valence-bound anions, respectively. The conformational space of keto was explored through systematic rotations around bonds *α, β, γ,* and *η*, see Figure 2.1.2, while *ε* replaces *α* for enol.

When probing the conformational space of the keto tautomer (*keto*), the bond *α* was rotated with a step size of 180°. The bonds *β* and *γ* were rotated with a step size of 60° each whereas *η* was fixed at 0° and 60°. All combinations of these rotatable bonds *α, β, γ,* and *η* resulted in 144 initial structures for screening purposes. When probing the

conformational space of the enol tautomer (*enol*), γ and η were rotated with a step-size of 60° and 180°, respectively, and β was kept fixed at 0° and 90° and η fixed at 0° and 60° yielding 42 initial structures.

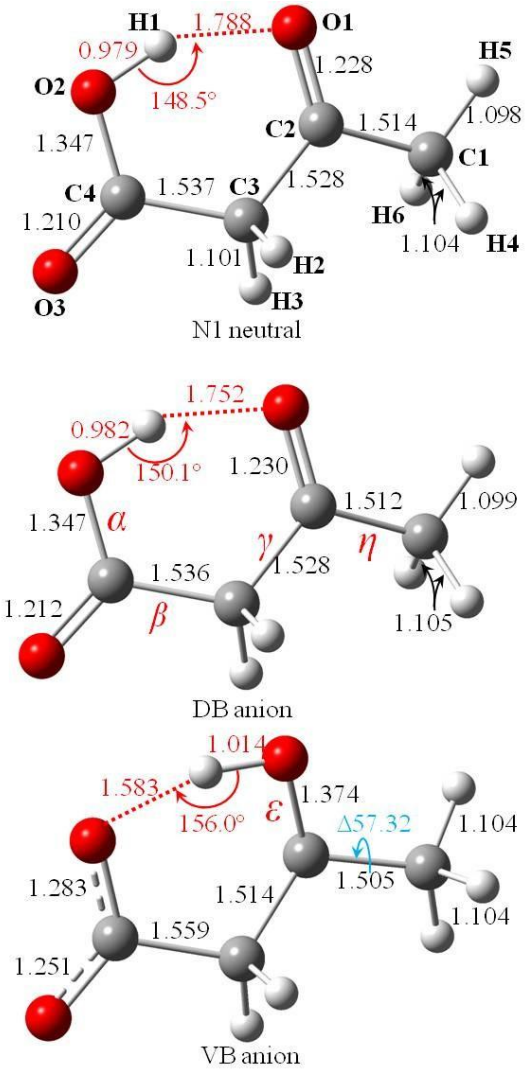

Figure 2.1.2. Molecular structures of AA considered in this study. The principal geometrical parameters (in Å) were characterized at CCSD/ADZ + DF level of theory. Bonds α, β, γ, η, and ε were rotated for conformational searches. The change (Δ) in the O1–C2–C1–H5 dihedral angle (blue) from the N1 to VB geometry is in ° (deg).

Electronic structure calculations for dipole-bound anions require basis sets with very diffuse basis functions. In this study, we used the standard Dunning's aug-cc-pVDZ (ADZ)[17,18] basis set supplemented with extra diffuse basis functions centered on the carbon of (-CH_3). The exponents α_n of these basis functions were determined through: $\alpha_n = \frac{\alpha 0}{q^n}$, n = 1, 2,…, initiated from the lowest exponent $\alpha_0$of the *s-, p-* or *d*-functions in the standard ADZ basis set, and advanced with q = 3.2.[19] We limited the extra diffuse set to 5 *s*-, 5 *p*-, and 2 *d*-functions based on the values of the LCAO coefficients of the singly occupied molecular orbital in the dipole-bound state calculated at the geometry of the neutral.[20,21] This procedure led to the lowest exponents of 1.3256 x10^{-4} au, 1.1421 x 10^{-4} au and 1.4437 x 10^{-2} au for the *s*-, *p*- and *d*-symmetries, respectively. We will use a label DF for these additional diffuse functions and ADZ+DF for the combined basis set. The dipole moment of the neutral increases upon the intra-molecular proton transfer from O2 to O1, thus the above set of additional diffuse functions should be sufficient for all geometries considered.

The initial structures of the neutral and valence anions of acetoacetic acid were pre-screened at the density functional level of theory with the B3LYP exchange-correlation functional.[22–25] All minima were re-optimized at the coupled-cluster singles and doubles[26] (CCSD) level of theory; harmonic frequencies were calculated at the same level. The minimum energy structures contained within an energy range of 10 kcal/mol were subjected to single-point coupled-cluster calculations with single, double and noniterative triple excitations[27] (CCSD(T)). Thus our most accurate energies of the neutral and anionic systems are based on the CCSD(T) electronic energies and zero-point vibrational energies determined at the CCSD level, both obtained with the ADZ+DF

basis set. We identified several low-lying conformers of the neutral *keto* AA and the energy barriers separating them. The search for transition states was performed in two stages. First, we constructed the energy profiles (MP2 or B3LYP) for rotations around α or β by performing partial geometry optimizations for several fixed values of the selected dihedral angle. The geometries associated with maxima on these profiles were used as starting geometries for transition state searches using the Berny algorithm.[28–30] We also considered the decomposition of neutral AA into CO_2 and 2-hydroxy-propylene (the latter further transforms to acetone, see Figure 2.1.3).

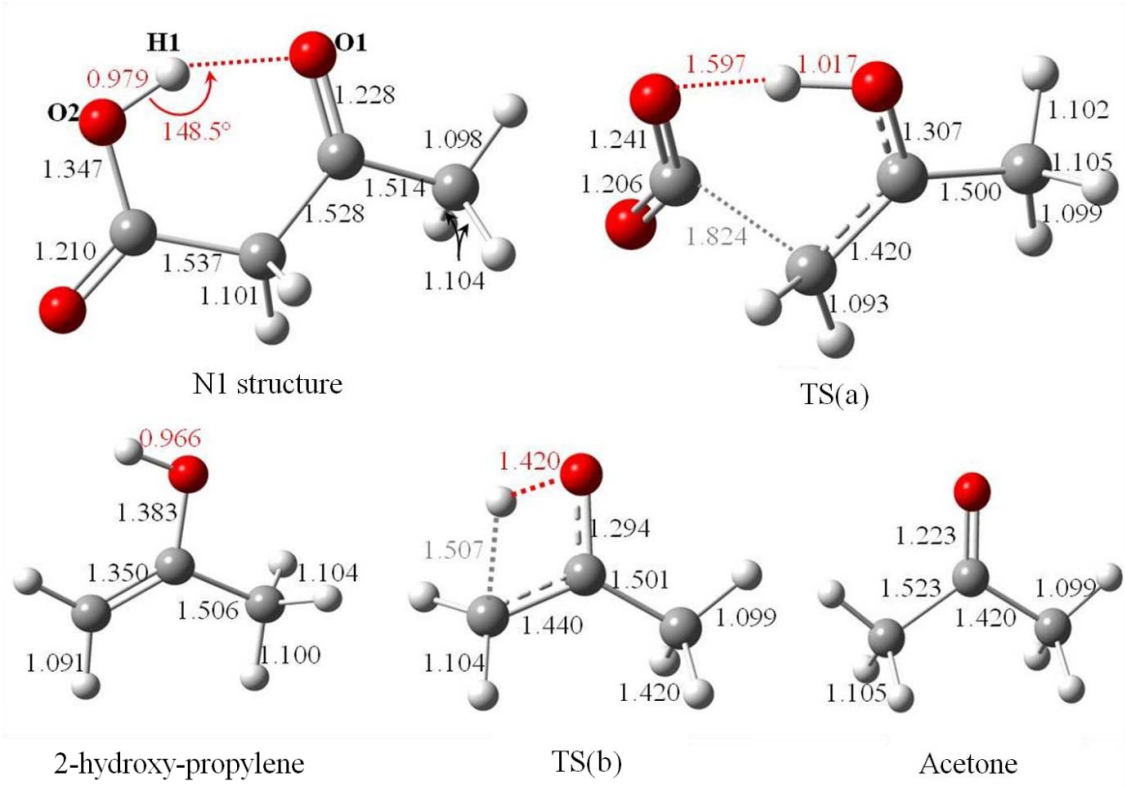

Figure 2.1.3. The unimolecular decomposition path of AA characterized at the CCSD/ADZ level of theory. The bond H1 – O1 was scanned and the transition states TS(a) and TS(b) illustrate the unimolecular decomposition path.

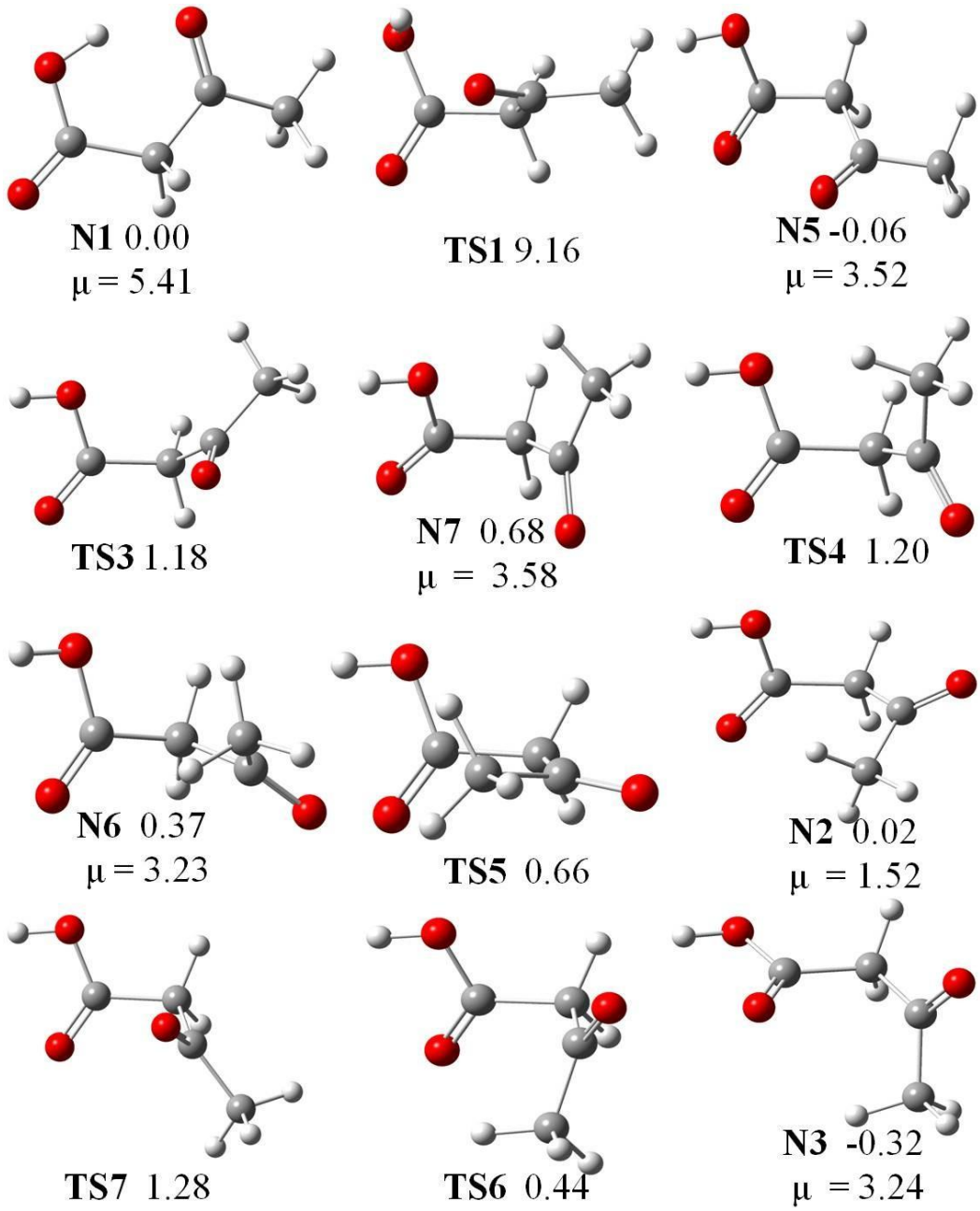

Figure 2.1.4. The low-lying neutral conformers of AA with the interconnecting barriers separating them. The relative energies (in kcal/mol) were obtained at the CCSD(T)/ADZ level of theory and corrected for MP2/ADZ zero-point vibration energies; the dipole moments μ are in Debye.

The N1 conformer of neutral AA (see Figure 2.1.4) was the most promising candidate for supporting a dipole-bound anionic state: (i) it is the most stable neutral conformer in terms of electronic energy, (ii) its dipole moment of 5.4 D exceeds dipole moments of other low-energy conformers by 1.8 D. Thus our discussion of the dipole-bound anionic state is limited to this conformer, though we also consider evolution of this anionic state along the proton transfer coordinate.

The vertical excess electron binding energies were calculated it two ways. In "indirect" approaches, the energy of the anion was subtracted from the energy of the neutral and the procedure was executed at the SCF, MP2, CCSD, and CCSD(T) levels of theory. The vertical excess electron binding energy can be also calculated "directly". Here we used the Electron Propagator Theory (EPT) method with the P3 propagator[31] applicable to both electron detachment and attachment processes in which the frozen-orbitals, single-determinant picture of Koopmans' theorem (KT)[32] is valid. One can calculate the vertical excess electron binding energy as either electron affinity (EA) of the neutral or ionization potential (IP) of the anion. We will use *EPT* to refer to third-order electron binding energies. In order to illustrate the evolution of the DB and VB, anionic states as a function of intramolecular proton transfer, we constructed λ-1 intermediate structures. By using the same set of geometric variables β_k (inter-atomic distances, angles and dihedral angles, k = 1,…,3*N*-6), we define the set of intermediate structures as:

$$\beta_k^m = \beta_k^i + m\delta_k \qquad m = 1..., \lambda\text{-}1 \tag{1a}$$

$$\delta_k = \frac{\beta_k^f - \beta_k^i}{\lambda}, \tag{1b}$$

where β_k^f and β_k^i are the values of the k^{th} variable for the final (VB) and initial (DB) structure, respectively.

The energy of the anion M^- at a geometry G can be written as;

$$E_{M^-}(G) = E_M(G_M) + \Delta E_M(G) - EBE(G), \quad (2)$$

where $E_M(G_M)$ is the energy of the neutral M at its optimal geometry G_M,

$$\Delta E_M(G) = E_M(G) - E_M(G_M) \quad (3)$$

represents an increase of the energy of the neutral M associated with its geometrical deformation from G_M to G, and $EBE(G)$ is the vertical electron binding energy at the geometry G:

$$EBE(G) = E_M(G) - E_M(G) \quad (4)$$

The values of EBE are positive for vertically bound anionic states and negative for resonances. The electron vertical attachment energy (VAE) is equivalent to $EBE(G_M)$. The electron vertical detachment energy (VDE) is equivalent to $EBE(G_{M^-})$ and the electronic part of the adiabatic electron affinity is defined as:

$$AEA = E_M(G_M) - E_{M^-}(G_{M^-}), \quad (5)$$

where G_{M^-} is the optimal geometry on the anion of M. Notice that

$$AEA = -\Delta E_M(G_{M^-}) + \mathrm{EBE}(G_{M^-}) = -\Delta E_M(G_{M^-}) + VDE \quad (6)$$

Further extensions of this notation are needed for AA, which supports a valence and dipole-bound anions. In this study we will characterize three characteristic molecular structures. In addition to G_M we will consider $G_{M^-_{dbs}}$ and $G_{M^-_{VB}}$ which are the lowest

energy structures for the dipole- and valence-bound anions of *M*, respectively. The labels of VAE, VDE and AEA will be supplemented with a subscript dbs or VB to discriminate between the two anionic states. We will also consider the quantity:

$$\Delta E_{VB\rightarrow b} = E_{M^-_{dbs}}(G_{M^-_{VB}}) - E_{M^-_{VB}}(G_{M^-_{VB}}), \quad (7)$$

which is the vertical excitation energy from the valence to the dipole-bound anion at the optimal geometry of the G_{VB}^-. This quantity might be important in future experiments on the anion of acetoacetic acid.

All electronic structure calculations reported in this study were performed with the Gaussian 2009 package.[33] The orbitals occupied by an excess electron were generated with the Visual Molecular Dynamics[34] package and the contour values used in the plots were calculated with the OpenCubeMan[35] tool using a fraction of electron (F_e) density equal to 0.6. The GaussView[36] package was used to draw molecular structures.

EXPERIMENTAL METHODS

Synthesis of Acetoacetic Acid

Our synthesis followed the protocol described in Ref. 37. Sodium hydroxide (0.16 mol) was added to aqueous ethyl acetoacetate (0.15 mol) on ice. The reaction was stirred and allowed to react overnight. The resulting solution was saturated with ammonium sulfate. Sulfuric acid was then used to acidify the solution. The solution was extracted three times with diethyl ether (200 ml) and dried over magnesium sulfate. After removing the ether using a rotary evaporator and drying using a rotary vacuum pump, a yellowish gel of acetoacetic acid was obtained. Since batches of acetoacetic acid were readily subject to decomposition, care was taken to ensure that the solutions did not become

warmer than 30°C, and they were utilized in photoelectron and electron energy loss spectroscopy experiments as quickly as possible.

Photoelectron Spectroscopy

In the first approach, the anions of acetoacetic acid were generated with a nozzle-ion source and their photoelectron spectra were measured with a continuous anion photoelectron apparatus.[38] In the second approach, the anions were generated with a photo-induced electron emission, pulsed source and their photoelectron spectra were measured with a pulsed anion photoelectron apparatus.[39] In both instruments, anion photoelectron spectroscopy was conducted by crossing a mass-selected negative ion beam with a fixed energy photon beam and energy analyzing the resultant photodetached electrons. This technique is governed by the energy conserving relationship, hv = EKE + EBE, where hv is the photon energy, EKE is the measured electron kinetic energy, and EBE is the electron binding energy.

Continuous Anion Photoelectron Spectrometer

In this type of anion photoelectron spectrometer, the ion source and all of the other components operate continuously.[38] The ion source was a biased (–500 V), supersonic expansion nozzle-ion source, in which acetoacetic acid samples were placed inside its stagnation chamber. There, due to the warming of the source by the adjacent hot filament, some of the sample evaporated and was expanded through a 25 μm diameter nozzle orifice into ~10^{-4} torr vacuum by argon gas which was maintained at a pressure of 1–2 atm in the stagnation chamber. Anions were formed by injecting low energy electrons from a hot, even more negatively-biased, thoriated iridium filament into the expanding jet, where a weak external magnetic field helped to form a microplasma. The

nascent anions were then extracted from this region and mass-selected by a 90° magnetic sector, mass spectrometer with a mass resolution of ~ 400. Upon mass-selection, the beam of acetoacetic acid parent anions was crossed with an argon ion laser beam (operated intra-cavity), where electrons were photodetached. These were then energy-analyzed by a hemispherical electron energy analyzer having a resolution of 30 meV. Photoelectron spectra were recorded with 2.540 eV photons and calibrated against the well-known photoelectron spectrum of O^-.[40]

Pulsed Anion Photoelectron Spectrometer

In this type of anion photoelectron spectrometer, the ion source and all of the other components operate in a pulsed mode.[39] Anions were generated by the interaction of laser generated photoelectrons with a pulsed jet of helium gas containing a small amount of acetoacetic acid vapor. The photoelectrons were produced by pulsed laser irradiation (Nd:YAG laser operating at 2.33 eV/photon) of a rotating, translating copper rod which was mounted inside a grounded housing having a laser beam entrance port, a pulsed gas valve, and an exit nozzle. A small amount of acetoacetic acid sample was placed inside the pulsed gas valve and together with 4 atm. of helium gas, its vapor was expanded in synchronization with the laser pulses. The resulting anions were entrained in the ensuing jet which itself was directed through a skimmer and a subsequent differential pumping chamber into the Wiley-McLaren extraction plates of a linear, time of flight mass spectrometer (mass resolution 2,000). After mass selection by a mass gate and deceleration via a momentum decelerator, the anions of interest were irradiated by a second pulsed laser beam (Nd:YAG laser operating at 3.49 eV/photon) which photodetached electrons from them. The photodetached electrons were then energy

analyzed by a magnetic bottle, electron energy analyzer with a resolution of 35 meV at EKE = 1 eV. The photoelectron spectrum was calibrated against the well-known atomic lines of Cu^-.[41]

Electron Energy Loss Spectroscopy

The electron-impact spectrometer used in this study has been described in the work on the formic acid dimer[8] and references cited therein. It uses hemispherical analyzers to prepare a beam with a narrow electron energy spread and to analyze energies of the scattered electrons. The measurements were performed at a scattering angle of 135°. The sample was kept in ice and evaporated through a needle valve to a 0.25 mm diameter effusive nozzle kept at 30°C. The resolution was about 20 meV in the energy-loss mode.

COMPUTATIONAL RESULTS

Neutral AA

Our results indicate that the neutral AA supports minima for the *keto* tautomer only (Figure 2.1.4). Our attempts to identify an *enol* minimum energy structure with H1 bound to O1 failed: the H1 proton either transferred back to O2 or the molecule broke into 2-hydroxyl-propylene and CO_2 (Figure 2.1.3). Notice that the proton-transferred structure, with the H1 proton bound to O1, is the global minimum for the anion of AA (the bottom part of Figure 2.1.2).

The low-lying minimum energy structures of the canonical neutral (N1 – N7) and transition states that separate the minima (TS1 – TS7) are illustrated in Figure 2.1.4 and a simplified landscape of the potential energy surface is illustrated in Figure 2.1.5. The

stationary points exist in two enantiomeric forms. One could anticipate the N1 conformer to be uniquely stable due to the intramolecular O2H1⋯O1 hydrogen bond, but the relative energies listed in Figure 2.1.4 indicate that N1 is not necessarily the most stable conformer. There are at least five neutral conformers within a narrow energy range of 1 kcal/mol. N1 is unique not so much in its stability but in the energy barrier (TS1 at 9.2 kcal/mol) that separates it from N5 and the remaining conformers. This barrier can be associated with breaking of the intramolecular hydrogen bond. The barriers separating the conformers N2 –N7 are much smaller and do not exceed 1.1 kcal/mol.

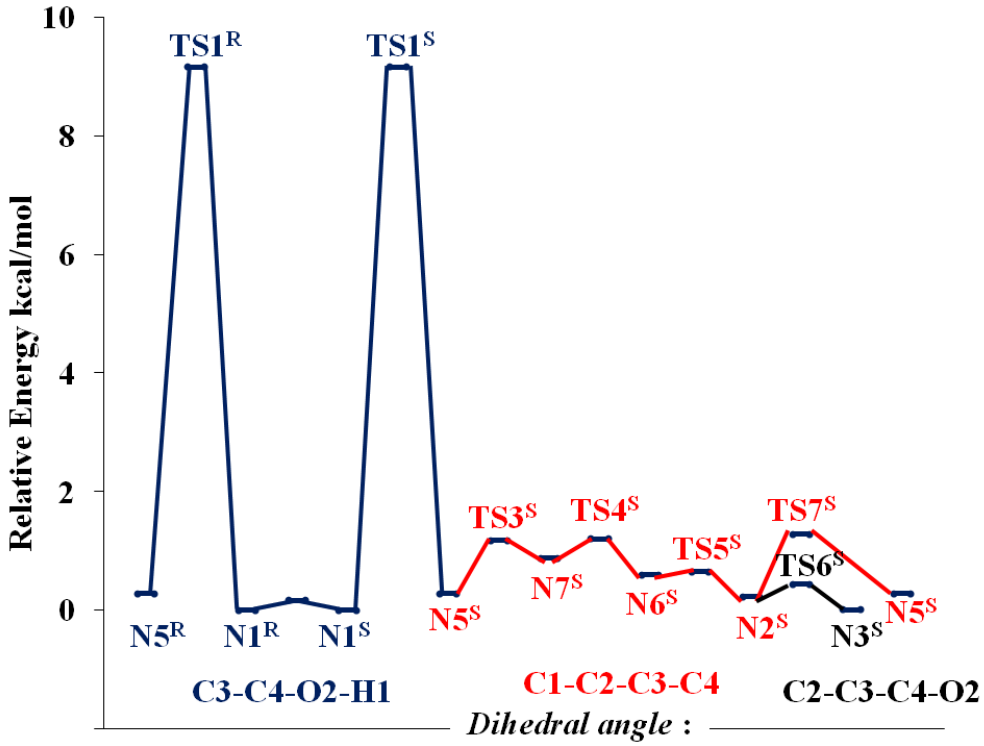

Figure 2.1.5. Energy profile connecting the neutral structures of AA. The energies (in kcal/mol) were calculated at the CCSD(T)/ADZ level using the CCSD/ADZ geometries.

There are at least two factors that oppose the stabilizing effect of the intramolecular hydrogen bond in N1. First, N1 is the most polar conformer, with a dipole moment exceeding 5.4 D. The remaining conformers have dipole moments smaller by more than 1.8 D. High polarity typically increases electronic energy of a neutral molecule by raising the energy of the highest occupied orbital. Second, formation of the O2H1···O1 hydrogen bond is associated with intramolecular strain. The results obtained with the Amber[42] force field confirm this hypothesis. The sum of the angle bending, torsional and bond stretching terms is larger in N1 than in e.g., N5, by ca. 2.8 kcal/mol, an energy term comparable with the stabilizing effect of the hydrogen bond.

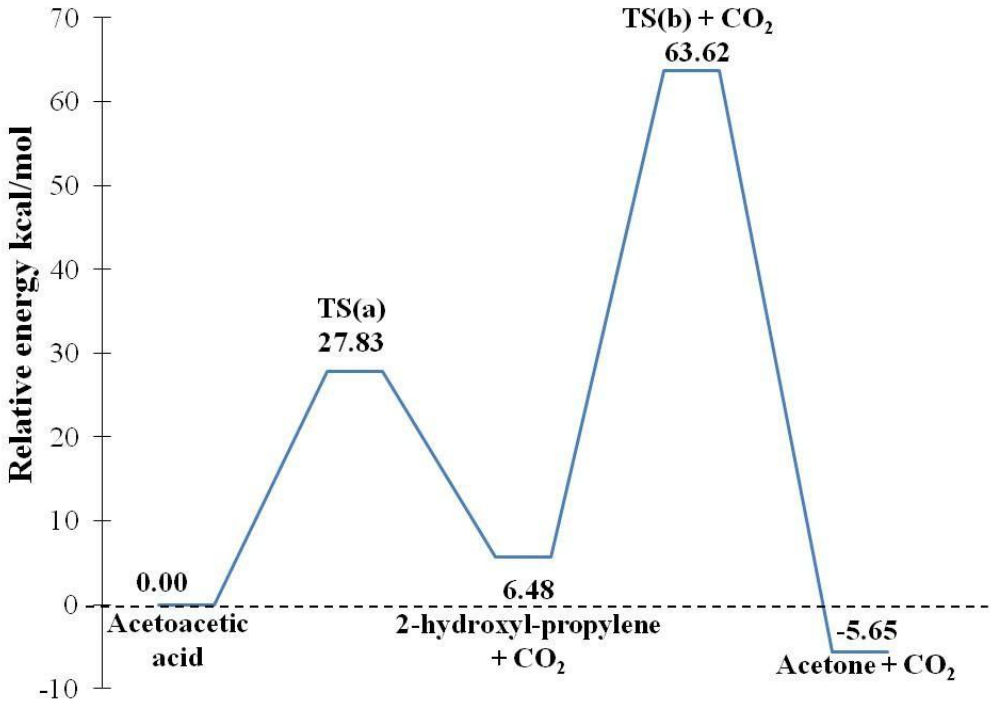

Figure 2.1.6. Dissociation energy profile of neutral AA. The relative energies were computed at CCSD(T)/ADZ level of theory using CCSD/ADZ optimal geometries.

The neutral AA is unstable with respect to the decomposition to acetone and CO_2 (Figure 2.1.6). The products are stable, with respect to the reactant by 5.7 kcal/mol in terms of electronic energies corrected for zero-point vibrations. The entropic effects will further enhance the stability of products. Here we consider only unimolecular decomposition channels. The first step of decomposition is associated with intramolecular proton transfer and leads to CO_2 plus 2-hydroxyl propylene. The barrier height (TS(a) in Figures 2.1.3 and 2.1.6) is 27.8 kcal/mol and is comparable with the previous MP2 value of 25.7 kcal/mol.[13] The unimolecular transformation of 2-hydroxyl propylene to acetone encounters a high barrier of 57.1 kcal/mol (the past MP2 result was 55.9 kcal/mol[13]). The decomposition of AA in the liquid phase is not limited to unimolecular channels and is expected to proceed with lower barriers. The thermodynamic instability of AA is consistent with experimental findings.[12]

Anionic AA

Neutral molecules with dipole moments exceeding 1.625 D can bind an excess electron.[43] N1 is the most promising conformer to host a dipole-bound anionic state in view of its competitive stability and dominant polarity (μ = 5.4 D). In addition to the dipole-bound state, AA can support a valence anion.

An overview of anionic states of AA is presented in Figure 2.1.7 using a set of geometries defined by Eq. 1. This series of geometries connects the dipole-bound minimum based on the N1 structure of the neutral with the minimum of the valence-bound anion. The potential energy curve of the neutral is repulsive upon transferring the

proton from O2 to O1. The dipole moment of the neutral increases, upon proton transfer, from 5.4 D at the minimum of the neutral to 10.0 D at the minimum of the valence anion.

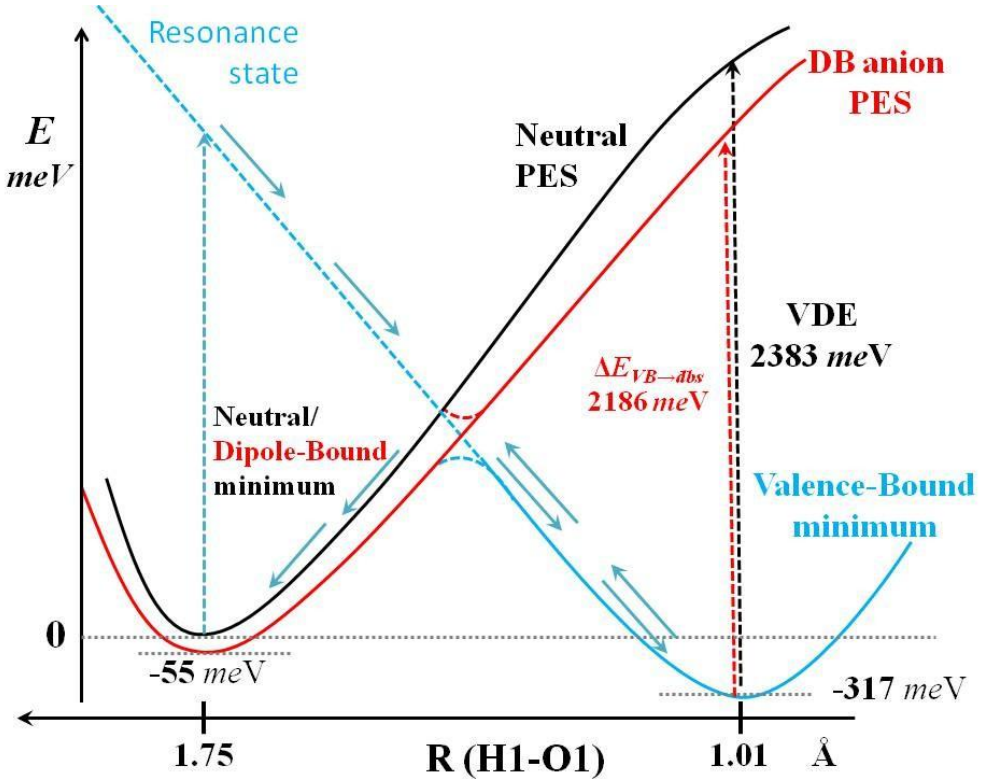

Figure 2.1.7. Energy profile depicting the neutral, dipole-bound and valence anionic potential energy surfaces of AA. The energies (meV) computed at the CCSD(T)/ADZ+DF level.

Thus, the dipole-bound anion remains bound upon proton transfer. The valence anion is unbound at the minimum energy structure of the neutral; it can be probed as a resonance state with a very short finite lifetime in the electron energy loss experiments. The energy of the resonance quickly decreases upon intramolecular proton transfer, crosses the potential energy surface of the neutral, and undergoes an avoided crossing with the

dipole-bound anion. With the proton transferred from O2 to O1, the valence anion supports a minimum characterized by a significant electron vertical detachment energy of

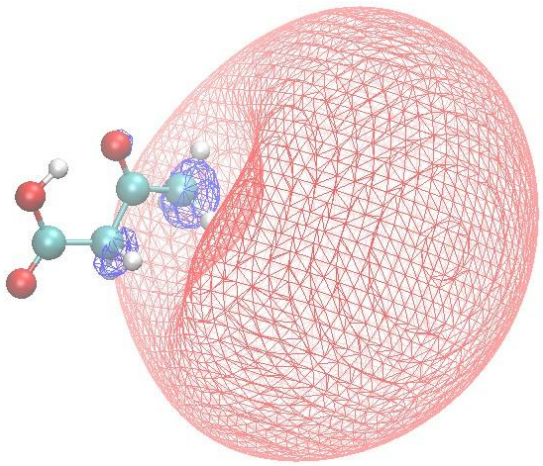

(a) Dipole bound

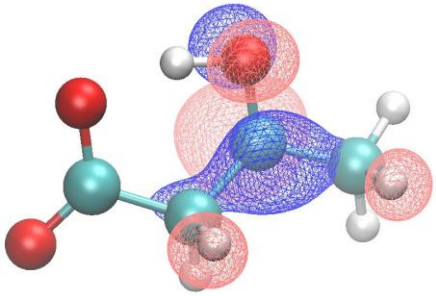

(b) Valence bound

Figure 2.1.8. The orbital occupied by an excess electron in the DB and VB anions of AA. The plots were generated using VMD with contour values calculated using the OpenCubeMan package from 60% of electron density of these respective orbitals.

2383 meV. The valence anion is adiabatically bound with respect to the neutral by 317 meV (in terms of electronic energies). We re-emphasize that the dipole-bound anion remains bound at the minimum of the valence-bound anion and the electron excitation energy from the valence- to dipole-bound state is 2186 meV. The singly-occupied molecular orbitals in the dipole-bound and valence anions, each at its minimum energy structure, are illustrated in Figure 2.1.8. The former orbital is very diffuse and localized on the positive pole of the molecular dipole, which proves to be a hydrophobic group CH_3. The latter is a p orbital localized around the C2 atom, with bonding interactions involving the neighboring carbon atoms and an antibonding interaction between C2 and O1.

The minimum energy structure of dipole-bound anion differs from the neutral by shortening the O1···H1 distance by 0.036 Å, increasing the O1–H1–O2 angle by 1.6° and an elongation of the O2···H1 distance by 0.003 Å, see Figure 2.1.2. Overall it is a small step towards proton transfer, a nascent zwitterionization. The dipole moment of the neutral increases by 0.16 D upon these geometrical distortions, a typical increase for dipole-bound anionic states.

The vertical electron binding energies for the dipole-bound anionic state, obtained with indirect and direct methods, are reported in Table 2.1.1 for the minimum energy geometries of N1, and dipole- and valence-bound anions. The "indirect" electron binding energies are reported at the SCF and correlated levels of theory. The SCF contribution represents only 46-65% of the CCSD(T) results, illustrating the role of electron correlati-

Table 2.1.1. Vertical electron binding energies (meV) of the dipole-bound anionic state at the G_M, $G_{M^-_{dbs}}$ and the $G_{M^-_{VB}}$ geometries using the CCSD/ADZ+DF optimal geometries.

Method		EBE		
		G_M	$G_{M^-_{dbs}}$	$G_{M^-_{VB}}$
Indirect	SCF	24.06	26.89	127.68
	MP2	32.81	36.31	217.72
	CCSD	52.34	56.59	196.85
	CCSD(T)	52.19	56.55	197.04
Direct EA	KT	21.59	24.33	113.30
	EPT	43.63	47.46	245.07
Direct IP	KT	26.32	29.78	135.79
	EPT	45.27	50.45	247.84

on effects in dipole-bound anionic states. The differences between the CCSD and CCSD(T) results do not exceed 0.2 meV suggesting methodological saturation of our results. The electron binding energies obtained in "direct" approaches start from the Koopmans' theorem estimations, thus they neglect orbital relaxation and electron correlation effects. The differences between the KT and SCF "indirect" results are small indicating that orbital relaxation effects are relatively small for the dipole-bound anionic state. The EPT results are in good agreement with the "indirect" CCSD(T) results, further confirming the reliability of electron binding energies for this anionic state. Various estimations of adiabatic electron affinity for this anionic state are reported in Table 2.1.2. The CCSD(T) electronic energy result of 54.56 meV is methodologically converged and the zero-point vibrational correction further stabilizes the anion by 2.63 meV. This dipole-bound anion is amenable to experimental investigations using Rydberg electron transfer methods.[44] Probing this anionic state in anion photoelectron spectroscopy

Table 2.1.2. Adiabatic electron affinities (meV) of the DB and VB anions calculated at different levels of theory with the CCSD optimal geometries. All calculations with the ADZ+DF basis set.

	AEA (electronic)				ΔE_{vib}	*AEA*
	HF	MP2	CCSD	CCSD(T)	CCSD	CCSD(T)
DB	8.60	38.88	54.15	54.56	2.63	57.19
VB	-182.80	286.26	289.55	317.02	17.27	334.29

experiments[45] might be more problematic due to the possibility of collapsing to the global minimum of valence anion (Figure 2.1.7). Finally, the decomposition of electronic component of AEA into the $\Delta E_M(G_{M^-})$ and VDE terms (Eq. 6, Table 2.1.3), illustrates a very small geometrical distortion of the molecular framework upon the excess electron attachment and the dominant role of VDE.

Table 2.1.3. The electronic component (CCSD(T)/ADZ+DF) of AEA (meV) decomposed into the $\Delta E_M(G_{M^-})$ term and VDE.

	$\Delta E_M(G_{M^-})$	*VDE*	*AEA*
DB	-1.99	56.55	54.56
VB	-2065.69	2382.71	317.02

In contrast to the neutral AA, which supports several low-lying minimum energy structures, the valence anion of AA supports one distinct global minimum illustrated in the bottom of Figure 2.1.2. The other local minima were less stable by

more than 12 kcal/mol, and are characterized in the supporting information. The H1 proton is bound to O1 and the O1H1···O2 hydrogen bond is very short, R(H1O2)=1.583 Å, in the global minimum structure of valence anion. The intramolecular hydrogen bond is more linear than in the neutral or dipole-bound anion by 6–8°. When compared with the N1 neutral, there is a significant elongation of the C2O1 distance by 0.146 A and a shortening of C4O2 by 0.064 Å, consistent with a redistribution of double bonds upon tautomerization. Finally, the CH_3 group is rotated by ca. 58° in comparison with N1. The values of electron VDE obtained using "indirect" methods (including SCF) and "direct" EPT span a reasonably narrow range of 2300–2600 meV (Table 2.1.4).

Table 2.1.4. The values of VDE (meV) for the valence anion of AA.

Method		VDE
Indirect	SCF	2400.48
	MP2	2347.34
	CCSD	2482.36
	CCSD(T)	2382.71
Direct EA	KT	713.43
	EPT	2304.34
Direct IP	KT	4200.09
	EPT	2602.50

The KT(EA) value is only 713 meV while the KT(IP) value is 4200 meV, demonstrating that orbital relaxation effects are critically important for this anionic state. Electron correlation effects, on the other hand, do not contribute much to the VDE value. The anion should be readily formed in common experimental sources, because its adiabatic electron affinity is modest but positive, 334 meV after inclusion of the zero-

point vibrational correction (Table 2.1.2). The value of electronic contribution to AEA can be analyzed in terms of Eq. 6 (Table 2.1.3). The proton transfer from O2 to O1 is accompanied by a significant increase of the energy of the neutral ($\Delta E_M(G_{M_{VB}^-})$=2066 meV). This energy increase is, however, outweighed by the VDE of 2383 meV. The modest electronic contribution to AEA of 317 meV results from cancellation of the $\Delta E_M(G_{M_{VB}^-})$ and VDE terms. Thus the situation is different than in the dipole-bound anion, for which the ΔE_M ($G_{M_{dbs}^-}$) term was small in comparison with the VDE value. The anion of AA supports more than one bound electronic state at the geometry $G_{M_{VB}^-}$. The electronic excitation energy from the valence to dipole-bound state is 2186 meV. In future experiments, one might want to probe the molecular dynamics of AA^- upon this electronic excitation.

Contrary to our experience with the neutral AA (Figures 2.1.3 and 2.1.6), we did not witness any propensity of the valence anion of AA to unimolecular decomposition. The decomposition products CO_2 plus acetone are thermodynamically less stable than AA^-, and the AEA of CO_2 is negative.[46] Acetone, with a dipole moment of 2.91 D, supports only a very weakly bound state (AEA < 2 meV).[47] Unless other decomposition channels prove to be thermodynamically favorable, we suggest that AA can be stabilized with respect to the spontaneous decomposition12 through formation of the valence anion. Whether such an anion can exist in condense phases will be considered in our future studies.

EXPERIMENTAL RESULTS

Photoelectron Spectroscopy Results for AA^- and $(AA)_2^-$

Parent anions of AA were prepared using two rather different source environments. Figure 2.1.9 presents a representative mass spectrum of the anions produced.

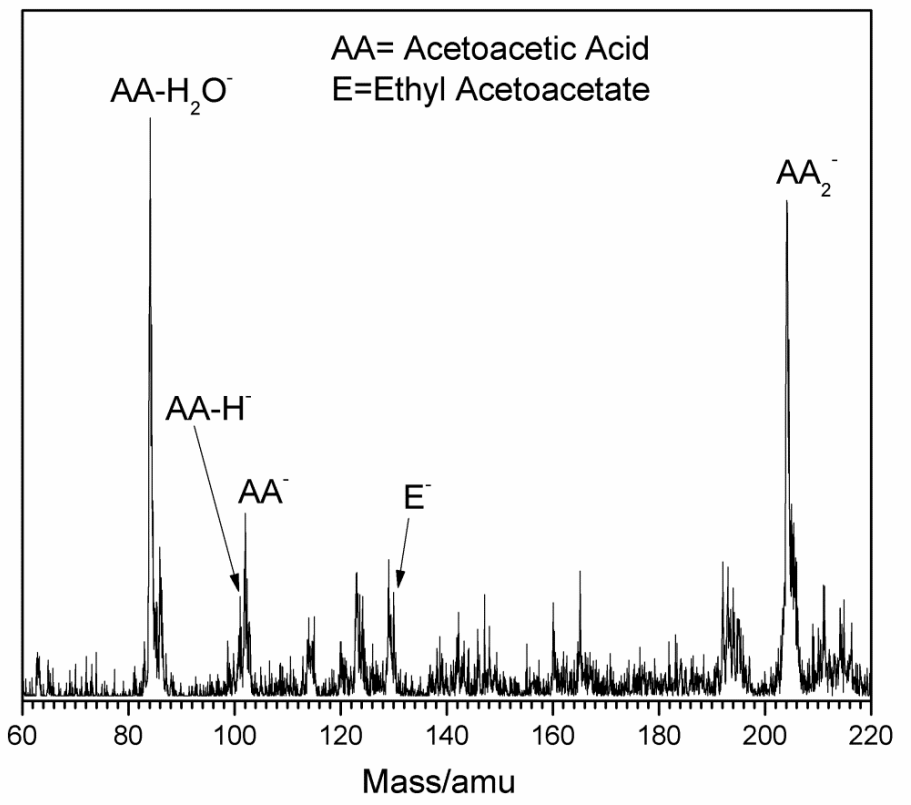

Figure 2.1.9. Mass spectrum of anions observed in these experiments.

The photoelectron spectrum of the AA parent anion measured on the continuous photoelectron spectrometer is presented in Figure 2.1.10. This spectrum consists of a broad, featureless band with an onset at EBE ~1.2 eV and an intensity maximum at EBE

2.04 eV. This latter quantity corresponds to the VDE of the AA parent anion. The calculated adiabatic electron affinity of 0.33 eV is much smaller than the onset indicating that the 0-0 transition has a very small intensity. The calculated VDE of 2.38 eV is larger by 0.34 eV than the measured intensity maximum. The source of this discrepancy will be analyzed further on.

The photoelectron spectrum of the AA parent anion measured on the pulsed photoelectron spectrometer is presented in Figure 2.1.11. This spectrum also consists of a broad, featureless band with an onset at EBE 1.2 eV but with an intensity maximum at EBE 2.30 eV. This latter quantity again corresponds to the VDE of the AA parent anion. The value of VDE is in excellent agreement with the calculated value of 2.38 eV.

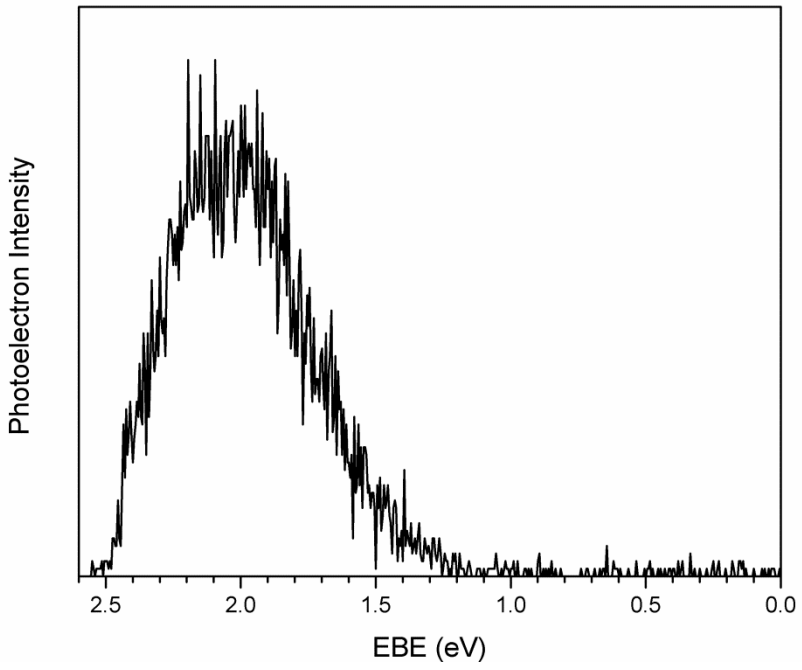

Figure 2.1.10. Photoelectron spectrum of the AA parent anion recorded with 2.540 eV photons on the continuous photoelectron spectrometer.

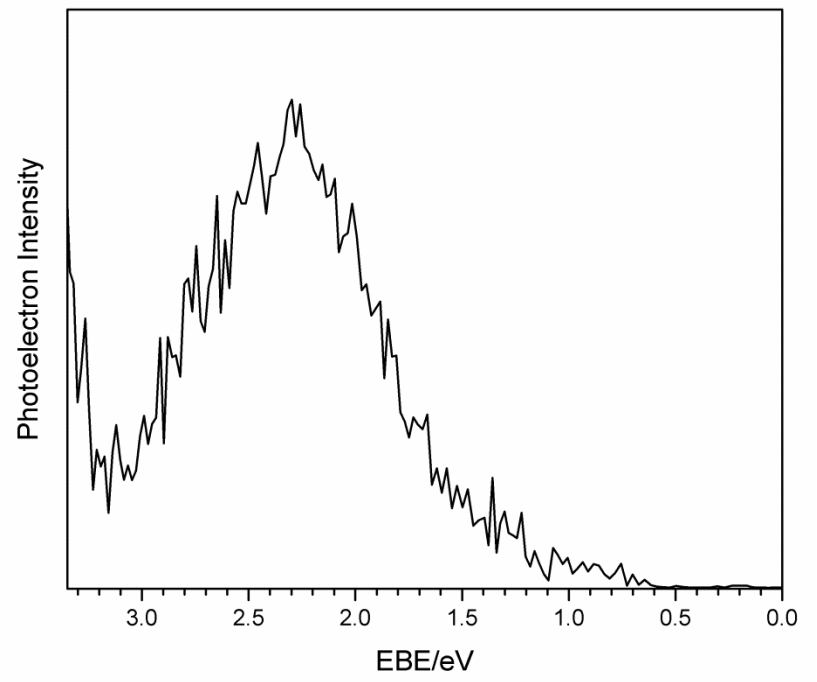

Figure 2.1.11. Photoelectron spectrum of the parent AA parent anion recorded with 3.49 eV photons on the pulsed photoelectron apparatus.

For the most part the two photoelectron spectra are the same, indicating that both source environments produced the same AA parent anion species. The main difference lies in the slightly different VDE values obtained on different apparatus. The difference between the two measured VDE values is no doubt due to the electron transmission function roll-off inherent for low kinetic energy (high EBE) electrons. This effect would come into play more strongly for a lower versus a higher photon energy, since a lower photon energy puts more of the spectrum in the low EKE region of the spectrum. On the continuous apparatus, whose photon energy was limited to 2.540 eV/photon, this had the effect of cutting into the still rising, photoelectron intensity at the top of the peak, making its intensity maximum appear to occur at a slightly lower EBE value. By contrast, the

pulsed apparatus, which utilized a photon energy of 3.49 eV/photon, was not significantly affected in this way. Thus, we believe that the better value for the VDE of the AA parent anion is 2.30 eV, as predicted by theory.

Electron Energy Loss Spectroscopy Results for AA

The processes induced by the attachment of an electron are suitably visualized by the diagram in Figure 2.1.7. Vertical electron attachment, indicated by the vertical blue dashed arrow, transfers the nuclear wave packet to the repulsive part of the valence anion potential surface – a resonance because it is subject to a spontaneous electron detachment. The present discussion concentrates on the lowest shape (i.e., not core excited) resonance with temporary occupation of the π_1^* orbital. The nuclear wave packet then starts to relax by sliding down the repulsive surface, in competition with rapid autodetachment. Detachment of the partially relaxed anion leads to vibrationally excited final state of the neutral molecule. Since the detachment rate can be assumed to be faster than the relaxation (because of absence of boomerang structure in the spectra), this process leads to (i) excitation of primarily low quanta of the vibration, and (ii) pronounced selectivity with respect to the modes, with those modes being primarily excited along which the anion potential has a large slope at the point of attachment. This process has been termed 'specific' vibrational excitation[48] and gives rise to the sharp vibrational peaks on the left side of the spectra in Figure 2.1.12. A (generally small) fraction of the nuclear wave packet 'survives' till it reaches portions of the potential surface where the detachment is slow or the ion is even bound, allowing intramolecular vibrational redistribution (IVR) which 'wipes out' the initial mode specificity, leading to

the excitation of a quasicontinuum of high-lying vibrational levels, accompanied by detachment of a very slow electron. This process has been termed 'unspecific' vibrational

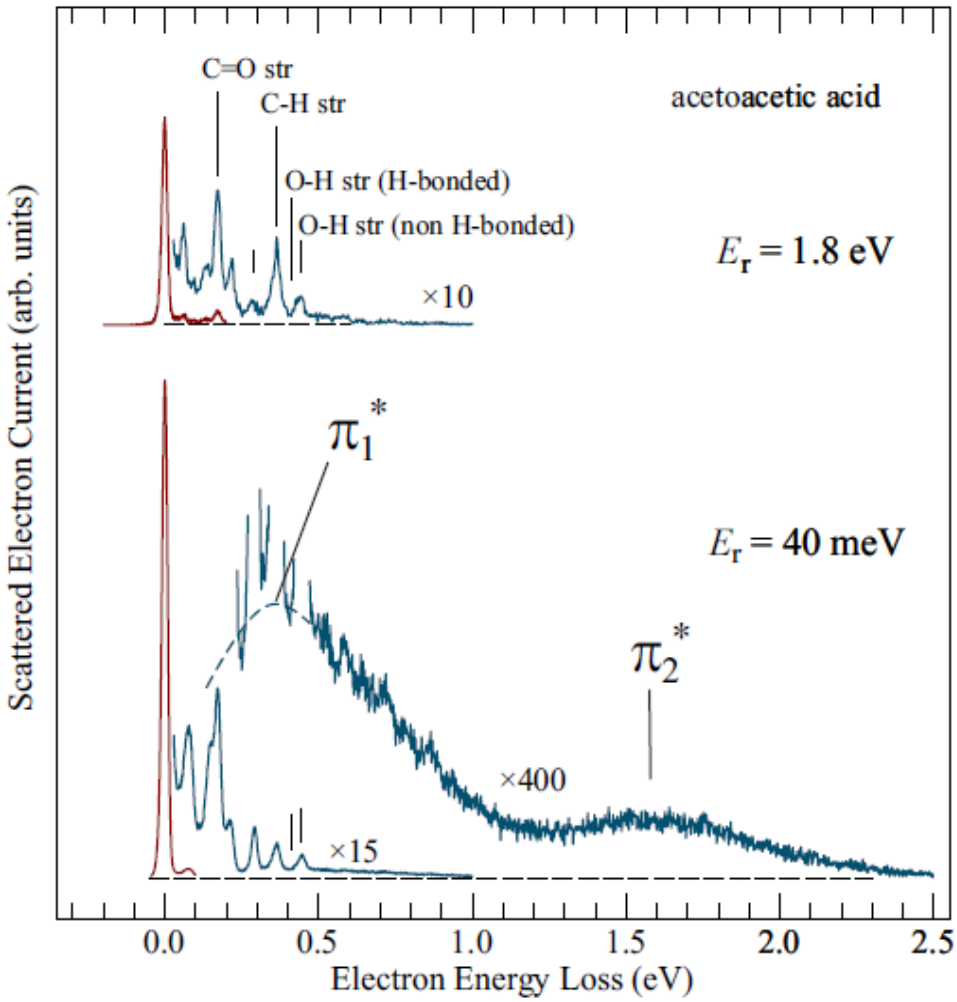

Figure 2.1.12. Spectra showing the yields of electrons with the specified residual electron energies E_r, plotted as a function of the electron energy-loss.

excitation[48] and gives rise to the structureless humps in the lower spectrum in Figure 2.1.12. One could also term the detachment in the initial phases of the relaxation 'nearly vertical' and in the later phases, after IVR, 'nearly horizontal'. The latter process gives

rise to the capacity of the resonances to quasithermalize the incident electrons. The 'unspecific' vibrational excitation and the corresponding humps in the spectra showing the yield of very slow electrons, at incident electron energies corresponding to resonances, are found in all more than diatomic molecules.[48] The effect is usually weak but becomes more pronounced for large molecules. The two humps in the lower spectrum in Figure 2.1.12 indicate a π_1^* (LUMO) resonance at 0.4 eV and a π_2^* (LUMO-1) resonance at 1.6 eV.

An interesting effect was observed in the acetic acid dimer where the 'unspecific' vibrational excitation band in the yield of quasithermal electrons was anomalously large, 20× larger than in the monomer.[8] It was interpreted as a manifestation of a very fast intramolecular proton (or hydrogen) transfer in the resonance, which increased the competitiveness of the relaxation towards the prompt detachment, thus increasing the yield of the unspecific process.

It may be noted as a side remark that stretching of the O−H bond in the formic acid monomer yields $HCOO^-$+ H (dissociative electron attachment, DEA), the mechanism of which we studied recently.[49] The intra-complex (in the case of AA the intramolecular) proton transfer may be viewed as a 'frustrated' DEA.

The question posed here is whether an anomalously high intensity of the 'unspecific' vibrational excitation hump, linked to intramolecular proton transfer, is also observed in AA. The spectra in Figure 2.1.12 show that a hump is indeed observed, but to decide whether it may be called anomalously high requires at least an approximate quantitative consideration. For this purpose we determined the ratio of the signals integrated under the discrete narrow vibrational peaks (representative for the weakly

relaxed specific process) and the structureless hump (representative for the fully relaxed unspecific process). A visual extrapolation of the structureless band to low energies was required, as indicated by a dashed curve in Figure 2.1.12. The result is that the integral under the structureless band is about 3× less than the integral under the narrow structures. This can be compared to the formic acid dimer where the integral under the structureless band is about 3× larger than the integral under the narrow structures. The ratio in AA is only marginally larger than that in the formic acid monomer, where the integral under the structureless band is about 6× smaller than the integral under the narrow structures.

The capacity of the π_1^* resonance in AA to quasithermalize electrons is thus not large enough to provide positive evidence for an intramolecular proton transfer fast enough to compete with autodetachment. The anion photoelectron spectra and the calculations show beyond doubt that the equilibrium structure of the valence anion is proton-transferred, however. The combined evidence thus indicates that the electron-induced transfer occurs, but slower than in formic acid dimer, so that it does not efficiently compete with the fast autodetachment. The reason may be that only a fraction of the target AA is in the H-bonded conformation suitable for proton transfer. This is indicated by the computational evidence detailed above, and also by the discrete vibrational energy-loss spectra on the left side of both traces in Figure 2.1.12, where nearly no intensity is observed for H-bonded O−H stretch.

SUMMARY

We performed search for the most stable tautomers and conformers of the

neutral and anionic acetoacetic acid using a potential energy surface scanning tool (PESST).[16] We identified several conformers of the canonical neutral within a narrow energy range of 1 kcal/mol. The conformer with the intramolecular hydrogen bond, and thus susceptible to intramolecular carboxylic-to-keto proton transfer, proved to be the third most stable and the most polar, with a dipole moment of 5.4 D. This polar conformer is separated from other conformers by a relatively high barrier exceeding 9 kcal/mol. The barriers separating other conformers are much smaller and do not exceed 1.1 kcal/mol. The neutral acetoacetic acid was found unstable by 5.7 kcal/mol with respect to acetone and CO_2.

The polar neutral conformer supports a dipole-bound anion with an electron vertical detachment energy of 57 meV. The dipole-bound anion remains bound upon the intramolecular carboxylic- to-keto proton transfer but its energy increases steadily and we failed to identify a minimum for the zwitterionic enol structure.

The valence anions of acetoacetic acid all exist in the enol form. The distinct global minimum is more stable than other minima by more than 12 kcal/mol. It is supported by a short (H···O distance of 1.58 Å) intramolecular hydrogen bond between the enol and carboxylate groups. We conclude that binding an excess electron on a π^* valence orbital changes localization of the proton in acetoacetic acid. The valence anion is characterized by a significant electron vertical detachment energy of 2383 meV, but a modest adiabatic electron affinity of 334 meV. The electronic excitation energy from the valence to dipole-bound state is 2186 meV. Thus the dynamics of the anion excited to the repulsive wall of the dipole-bound state can be explored in future experiments. The valence anion of acetoacetic acid is stable, in terms of electronic energies corrected for

zero-point vibrations, with respect to acetone and the anion of CO_2.

Parent anions of acetoacetic acid were successfully prepared using two different source environments. The photoelectron spectra obtained on the continuous and pulsed photoelectron spectrometers were obtained with 2.540 and 3.49 eV photons, respectively. The PES spectra consist of a broad, featureless band with an onset at electron binding energy of ca. 1.2 eV. The intensity maxima on the continuous and pulsed photoelectron spectrometers differ by 0.26 eV (2.04 vs. 2.30 eV). Only the latter is in good agreement with the computed VDE of 2.38 eV. The difference between the two measured VDE values is due to the electron transmission function roll-off inherent to low kinetic energy electrons. The calculated adiabatic electron affinity of 0.33 eV is much smaller that the onset of the spectra indicating that the 0-0 transition has a very small intensity. The reported spectra do not provide evidence for the dipole-bound anion. The photoelectron spectrum of the parent dimer anion of acetoacetic acid shows a vertical detachment energy at 1.7 eV, thus considerably lower than that of the monomer, indicating that the additional monomer is not simply solvating the monomeric anion.

The electron-energy loss spectra do show a broad structureless band in the yield of quasithermalized electrons (40 meV) following an attachment of an electron into the π_1^* resonance. This band indicates a rapid IVR process in the resonance, but in contrast to the formic acid dimer case the band is not anomalously strong and thus does not provide evidence of the IVR process being promoted by an ultrafast proton transfer in the resonance. We explain it as a consequence of the fact that only the N1-conformer, with an intermolecular hydrogen bond, is susceptible to an intramolecular proton transfer fast enough to compete with the very fast autodetachment, and that, contrary to

initial chemical intuition, this conformer is present in only small fraction in the target gas of the energy-loss experiment. Evidence for the low population comes from the calculation and from the near-absence of the H-bonded O−H stretch in the energy-loss spectra. This conclusion implies that AA^- is formed in the microplasma sources of the photoelectron spectrometers by a mechanism more complex than a simple electron attachment to AA followed by a rapid proton transfer. An intervention of a third body is required.

In the future, we will study the strength of coupling between the dipole- and valence-bound anionic states in the avoided crossing region (Figure 2.1.7). We will also explore the chemical nature of parent anions of the dimer of acetoacetic acid, of ethyl acetoacetate, and of dehydrated acetoacetic acid. All these species were observed in the anion mass spectrum (Figure 2.1.9). Finally, we will consider stability of the valence anion of AA in condense phases.

ACKNOWLEDGEMENTS

Z.G.K. was supported by the fellowship from the University of Botswana (UB). This research used resources of the National Energy Research Scientific Computing Center, which is supported by the Office of Science of the U.S. Department of Energy under Contract No. DE-AC02-05CH11231. This material is based (in part; to KHB) on experimental work which was supported by the (US) National Science Foundation through grant number, CHE-1360692. This research is part of project No. 200020-144367/1 of the Swiss National Science Foundation and of the COST Action CM1301 CELINA.

REFERENCES

1. Kumar, A.; Sevilla, M. D. *Chemical Reviews* **2010**, *110*, 7002–7023.
2. Chang, C. J.; Chang, M. C.; Damrauer, N. H.; Nocera, D. G. *Biochimica et Biophysica Acta (BBA) - Bioenergetics* **2004**, *1655*, 13 – 28.
3. Sanche, L. *The European Physical Journal D - Atomic, Molecular, Optical and Plasma Physics* **2005**, *35*, 367–390.
4. McCord, M. A.; Rooks, M. J. In *SPIE Handbook of Microlithography, Micromachining and Microfabrication*; Rai-Choudhury, P., Ed.; Cornell NanoScale Science & Technology Facility 2000; Vol. 1.
5. Xu, S.; Zheng, W.; Radisic, D.; Kit H. Bowen, J. *J. Chem. Phys.* **2005**, *122*, 091103.
6. Bachorz, R. A.; Harańczyk, M.; Dabkowska, I.; Rak, J.; Gutowski, M. *J. Chem. Phys.* **2005**, *122*, 204304.
7. Eustis, S. N.; Radisic, D.; Bowen, K. H.; Bachorz, R. A.; Haranczyk, M.; Schenter, G. K.; Gutowski, M. *Science* **2008**, *319*, 936–939.
8. Allan, M. *Phys. Rev. Lett.* **2007**, *98*, 123201.
9. Gerardi, H. K.; DeBlase, A. F.; Leavitt, C. M.; Su, X.; Jordan, K. D.; McCoy, A. B.; Johnson, M. A. *J. Chem. Phys.* **2012**, *136*, 134318.
10. Stokes, S. T.; Grubisic, A.; Li, X.; Ko, Y. J.; Bowen, K. H. *J. Chem. Phys.* **2008**, *128*, 044314.

11. Kobylecka, M.; Gu, J.; Rak, J.; Leszczynski, J. *J. Chem. Phys.* **2008**, *128*, 044315.

12. Hay, R. W.; Bond, M. A. *Aust. J. Chem.* **1967**, *20*, 1823–1828.

13. Huang, C.-L.; Wu, C.-C.; Lien, M.-H. *J. Phys. Chem. A* **1997**, *101*, 7867– 7873.

14. Pedersen, K. J. *J. Am. Chem. Soc.* **1929**, *51*, 2098–2107.

15. Hoz, S.; Kresge, A. J. *J. Phys. Org. Chem.* **1997**, *10*, 182–186.

16. Keolopile, Z. G.; Gutowski, M.; Haranczyk, M. *J. Chem. Theory Comput.,* **2013**, *9*, 4374-4381.

17. Dunning, Jr., T. H. *J. Chem. Phys.* **1989**, *90*, 1007–1023.

18. Kendall, R. A.; Dunning, Jr., T. H.; Harrison, R. J. *J. Chem. Phys.* **1992**, *96*, 6796–6806.

19. Gutowski, M.; Simons, J. *J. Chem. Phys.* **1990**, *93*, 3874–3880.

20. Gutowski, M.; Jordan, K. D.; Skurski, P. *J. Phys. Chem. A* **1998**, *102*, 2624–2633.

21. Skurski, P.; Gutowski, M.; Simons, J. *International Journal of Quantum Chemistry* **2000**, *80*, 1024–1038.

22. Becke, A. D. *J. Chem. Phys.* **1993**, *98*, 5648–5652.

23. Lee, C.; Yang, W.; Parr, R. G. *Phys. Rev. B* **1988**, *37*, 785–789.

24. Vosko, S. H.; Wilk, L.; Nusair, M. *Canadian Journal of Physics* **1980**, *58*, 1200–1211.

25. Stephens, P. J.; Devlin, F. J.; Chabalowski, C. F.; Frisch, M. J. *J. Phys. Chem.* **1994**, *98*, 11623-11627.

26. Purvis-III, G. D.; Bartlett, R. J. *J. Chem. Phys.* **1982**, *76*, 1910–1918.

27. Bartlett, R. J.; Musiał, M. *Rev. Mod. Phys.* **2007**, *79*, 291–352.

28. Schlegel, H. B. *J. Comp. Chem.* **1982**, *3*, 214–218.

29. Schlegel, H. B. *Theor. Chem. Acc.* **1984**, *66*, 333–340.

30. Simons, J.; Jørgensen, P.; Taylor, H.; Ozment, J. *J. Phys. Chem.* **1983**, *87*, 2745–2753.

31. von Niessen, W.; Schirmer, J.; Cederbaum, L. *Computer Physics Reports* **1984**, *1*, 57 – 125.

32. Koopmans, T. *Physica* **1934**, *1*, 104 – 113.

33. Frisch, M. J. et al. Gaussian 09 Revision A.1. 2009.

34. Humphrey, W.; Dalke, A.; Schulten, K. *J. Mol. Graph.* **1996**, *14*, 33–8, 27–8.

35. Haranczyk, M.; Gutowski, M. *J. Chem. Theory Comput.* **2008**, *4*, 689– 693.

36. Dennington, R.; Keith, T.; Millam, J. GaussView Version 5. Semichem Inc. Shawnee Mission KS 2009.

37. Krueger, R. C. *J. Am. Chem. Soc.* **1952**, *74*, 5536–5536.

38. Coe, J. V.; Snodgrass, J. T.; Freidhoff, C. B.; McHugh, K. M.; Bowen, K. H. *J. Chem. Phys.* **1986**, *84*, 618–625.

39. Gerhards, M.; Thomas, O. C.; Nilles, J. M.; Zheng, W.-J.; Bowen, J., K. H. *J. Chem. Phys.* **2002**, *116*, 10247–10252.

40. Neumark, D. M.; Lykke, K. R.; Andersen, T.; Lineberger, W. C. *Phys. Rev. A* **1985**, *32*, 1890–1892.

41. Ho, J.; Ervin, K. M.; Lineberger, W. C. *J. Chem. Phys.* **1990**, *93*, 6987– 7002.

42. Cornell, W. D.; Cieplak, P.; Bayly, C. I.; Gould, I. R.; Merz, K. M.; Ferguson, D. M.; Spellmeyer, D. C.; Fox, T.; Caldwell, J. W.; Kollman, P. A. *J. Am. Chem. Soc.* **1995**, *117*, 5179–5197.

43. Simons, J. *J. Phys. Chem. A* **2008**, *112*, 6401–6511.

44. Desfrancois, C.; Carles, S.; Schermann, J. P. *Chem. Rev.* **2000**, *100*, 3943–3962.

45. Castleman, A. W.; Bowen, K. H. *J. Phys. Chem.* **1996**, *100*, 12911– 12944.

46. Gutsev, G. L.; Bartlett, R. J.; Compton, R. N. *J. Chem. Phys.* **1998**, *108*, 6756–6762.

47. Desfrancois, C.; Carles, S.; Schermann, J. P. *Chem. Rev*. **2000**, *100*, 3943-3962.

48. Allan, M. *J. Electron Spectrosc. Relat. Phenom.* **1989**, *48*, 219.

49. Janečková, R.; Kubala, D.; May, O.; Fedor, J.; Allan, M. *Phys. Rev. Lett.* **2013**, *111*, 213201.

SUPPLEMENTAL MATERIAL

Table 2.1.S1. The relative electronic energies (kcal/mol) of canonical conformers of neutral acetoacetic acid calculated at different levels of theory followed by their dipole moments calculated at MP2/ADZ level of theory. Single point CCSD(T) energy calculation on CCSD optimal geometries.

Str.	ADZ					
	E_{elect}^{MP2}	$E_{elect}^{MP2}+E_{0,vib}^{MP2}$	E_{elec}^{CCSD}	$E_{elec}^{CCSD(T)}$	$E_{elec}^{CCSD(T)}+E_{0,vib}^{MP2}$	μ^{CCSD}
N1	0.00	0.00	0.00	0.00	0.00	5.41
N2	0.03	-0.17	-0.04	0.23	0.03	1.52
N3	0.04	-0.29	-0.41	0.01	-0.32	3.24
N4	0.10	0.04	-	-	-	-
N5	0.24	-0.10	-0.13	0.28	-0.06	3.52
N6	0.43	0.20	0.36	0.60	0.37	3.23
N7	0.74	0.54	0.55	0.88	0.68	3.58

Table 2.1.S2. The dipole moments of the neutral (N) at HF, MP2 and CCSD level of theory at the three representative geometries; (i) optimal geometry of N, (G_M), (ii) optimal geometry of DB, ($G_{M_{dbs}^-}$), (iii) optimal geometry of VB, ($G_{M_{VB}^-}$). All the geometries were optimized at the CCSD/ADZ+DF level.

Neutral @ Geometry	Dipole Moments, μ		
	HF	MP2	CCSD
N	5.63	5.42	5.41
$N^{(MP2)}$	6.5	5.42	5.54
N @ G_M	6.01	5.31	5.41
DBA	5.71	5.59	5.57
$DBA^{(MP2)}$	6.32	5.59	5.70
N @ $G_{M_{dbs}^-}$	6.18	5.47	5.57
VBA	11.09	9.69	10.00
$VBA^{(MP2)}$	10.72	9.69	9.85
N @ $G_{M_{VB}^-}$	10.87	9.84	10.00

Table 2.1.S3. Contributions from components of the force fields to N1, N3, and N5 energies calculated using Amber, UFF and Dreiding force fields implemented on Gaussian suite of programs.

FF-comp	Amber		
	N1	N3	N5
Bond Stretching	1.3976	0.8843	0.954
Angle Bending	3.5055	1.8546	1.6753
Improper Torsion	0.0419	0.0074	0.0009
Torsional Angle	1.955	0.7796	1.4466
Van der Waals	2.2484	1.1863	1.769
Charge-Charge	-18.9634	-22.9145	-18.3529
Total	-18.9634	-18.202	-12.5068

Table 2.1.S4. The relative electronic energies (kcal/mol) of valence anions of acetoacetic acid calculated at different levels of theory.

Str.	6-311G*		ADZ+ DF			
	E_{elec}^{B3LYP}	$E_{elect}^{B3LYP}+E_{0,vib}^{B3LYP}$	E_{elec}^{B3LYP}	$E_{elect}^{B3LYP}+E_{0,vib}^{B3LYP}$	E_{elec}^{MP2}	$E_{elect}^{MP2}+E_{0,vib}^{MP2}$
VB1	0.00	0.00	0.00	0.00	0.00	0.00
VB2	14.87	14.56	13.56	13.50	12.65	12.56
VB3	16.73	16.36	15.33	15.14	15.87	15.68

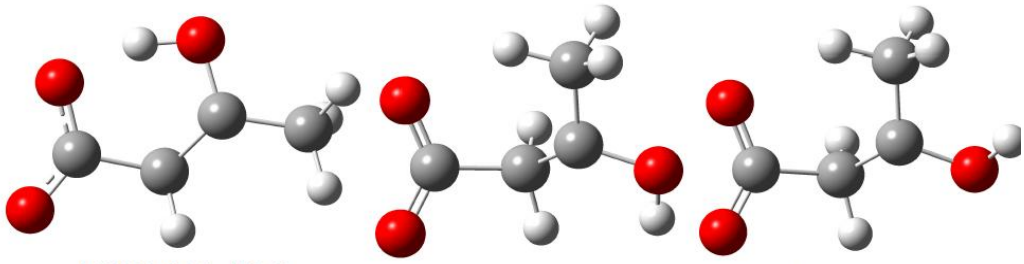

Figure 2.1.S1. The principal geometrical parameters (the C1-C2-C3-C4 dihedral angle in °) and the relative energies (in kcal/mol) of the structures considered in this study, with respect to N1 structure, characterized at MP2/ADZ + DF level of theory.

Table 2.1.S5. Incremental electronic binding energies of the dipole bound anionic state at G_M, $G_{M^-_{dbs}}$, and $G_{M^-_{VB}}$ and geometries using the CCSD/ADZ+DF optimal geometries.

Method	EBE		
	G_M	$G_{M^-_{dbs}}$	$G_{M^-_{VB}}$
KT(EA)	21.77	24.22	113.47
ΔE_{bind}^{SCF}	2.30	2.68	14.21
$\Delta E_{bind}^{MP2-disp}$	24.32	26.69	172.36
$\Delta E_{bind}^{MP2-no-disp}$	-15.57	-17.27	-82.32
ΔE_{bind}^{CCSD}	19.52	20.27	-20.87
ΔE_{bind}^{T}	-0.15	-0.04	0.19
Total	52.19	56.55	197.04

Table 2.1.S6. Cartesian coordinates of N1 neutral, DB anion and VB anion. Optimal CCSD/ADZ+DF geometries.

	N1 Neutral		
C	2.516605	-0.648014	-0.164126
C	1.211565	0.093479	0.037571
O	1.153675	1.319670	0.001508
C	-0.021125	-0.764763	0.316302
C	-1.404072	-0.176482	-0.005698
O	-1.514892	1.165542	-0.016913
O	-2.354505	-0.900934	-0.197982
H	-0.618422	1.551878	0.063044
H	0.056655	-1.735423	-0.197071
H	-0.012395	-0.985494	1.401474
H	2.664376	-1.383781	0.645036
H	2.464521	-1.209737	-1.113638
H	3.353198	0.063007	-0.196045

	DB				**VB** anion		
C	2.528004	-0.637843	-0.134706	C	2.511211	-0.655154	-0.074065
C	1.212397	0.090863	0.024596	C	1.147644	-0.034892	-0.222404
O	1.141073	1.318560	-0.006574	O	1.132583	1.317090	0.021988
C	-0.019652	-0.780706	0.265877	C	-0.065077	-0.805140	0.256521
C	-1.405710	-0.177533	-0.005056	C	-1.433281	-0.102430	0.001885
O	-1.503532	1.166336	-0.000845	O	-1.405513	1.180419	0.029601
O	-2.373320	-0.887120	-0.175374	O	-2.430087	-0.838424	-0.166454
H	-0.596109	1.536352	0.061769	H	0.139806	1.518589	0.058054
H	0.057258	-1.721840	-0.300587	H	-0.089964	-1.811827	-0.193167
H	0.003643	-1.067548	1.336289	H	0.002606	-0.947620	1.364299
H	2.662289	-1.361688	0.689045	H	2.818750	-0.697998	0.998761
H	2.509216	-1.215975	-1.075889	H	2.519055	-1.687175	-0.467913
H	3.359697	0.079805	-0.152549	H	3.270896	-0.060956	-0.612740

Section 2.2 Remarkable Electrophilicity of the Oxalic Acid Monomer: An Anion Photoelectron Spectroscopy and Theoretical Study

Angela Buonaugurio,[†] Jacob Graham,[†] Allyson Buytendyk,[†] Kit H. Bowen[†*]

[†]*Department of Chemistry, Johns Hopkins University, Baltimore, Maryland 21218, USA*

Matthew R. Ryder,[§] Zibo G. Keolopile,[§‡*] Maciej Haranczyk,[&] Maciej Gutowski[§*]

[§]*Institute of Chemical Sciences, School of Engineering and Physical Sciences, Heriot-Watt University, Edinburgh, Scotland, EH14 4AS, UK*

[‡]*Department of Physics, University of Botswana, Private Bag 0022, Gaborone, Botswana*

[&]*Computational Research Division, Lawrence Berkeley National Laboratory, One Cyclotron Road, MS 50F-1650, Berkeley, CA 94720, USA*

ABSTRACT

Our experimental and computational results demonstrate an unusual electrophilicity of oxalic acid (OA), the simplest dicarboxylic acid. The monomer is characterized by an adiabatic electron affinity and electron vertical detachment energy (VDE) of 0.72 and 1.08 eV (± 0.05 eV), respectively. The electrophilicity results primarily from the bonding carbon-carbon interaction in the singly occupied molecular orbital of the anion, but it is further enhanced by intramolecular hydrogen bonds. The well-resolved structure in the photoelectron spectrum is reproduced theoretically, based on Franck-Condon factors for the vibronic anion → neutral transitions.

*Corresponding authors: email: m.gutowski@hw.ac.uk, kbowen@jhu.edu, keolopilezg@mopipi.ub.bw

INTRODUCTION

Stable, closed-shell organic molecules with heteroatoms, such as monocarboxylic acids (formic, acetic), nucleic acid bases and amino acids, usually do not support bound valence anionic states in the neighborhood of the optimal geometry of the neutral species.[1] These molecules still support metastable (resonant) anionic states, with finite lifetimes and energies higher than the energy of the neutral,[2-4] but they are not able to permanently bind an excess electron in a valence orbital. The electrophilicity of these molecules is typically enhanced upon specific geometric distortions, including tautomerizations.[5,6] In consequence, valence anionic states are frequently characterized by positive values of electron vertical detachment energies (VDE), while adiabatic electron affinities (AEA) of the corresponding neutrals might remain negative (CO_2[5]), approach zero (canonical uracil[7]), or settle at positive values (unconventional tautomers of guanine[8,9] and adenine,[10] nucleotides[11,12]). Here we report a significant electrophilicity of the oxalic acid (OA) monomer. It is the simplest dicarboxylic acid, see Figure 2.2.1, which may be viewed as a product of condensation of two formic acid molecules (with the release of H_2). Let us reemphasize that the formic acid monomer does not support a bound valence anionic state.

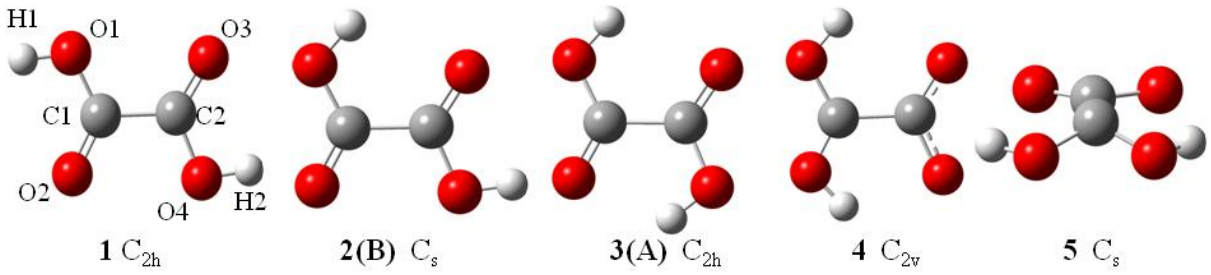

Figure 2.2.1. Conformers and tautomers of the oxalic acid monomer. The naming scheme for atoms is shown for **1**.

The neutral OA molecule can exist in three conformational forms (structures **1-3** in Figure 2.2.1); it also has a local minimum for a "rare tautomer" (structure **4**). These minimum energy structures differ in the extent of intramolecular hydrogen bonding; this phenomenon attracted attention of many experimental[13-19] and computational[20-25] groups. Indeed, the gas phase structure of the neutral OA monomer has been studied by electron diffraction,[13] infrared and Raman spectroscopy,[13,14] matrix-isolation,[15-17] UV absorption,[18] microwave spectroscopy,[19] and theoretically at various levels of theory.[20-25] Here we report a photoelectron spectrum (PES) of the OA monomer anion, which unravels a significant electrophilicity of the neutral; where the main features extend from 0.5 to 2.5 eV (Figure 2.2.2). Our computational results provide an interpretation of this well-resolved photoelectron spectrum.

COMPUTATIONAL AND EXPERIMENTAL METHODS

Theoretical Calculations

The minimum energy structures and harmonic frequencies for **1-5** of OA and OA^- were determined at the CCSD level of theory[26] and single-point energies were determined at the CCSD(T) level.[26] Initial calculations were performed with the aug-cc-pVDZ[27] (ADZ) basis set. For the most stable neutral and anionic structure **3**, the calculations were repeated with the aug-cc-pVTZ[27] (ATZ) basis set. The electronic structure calculations have been carried out with the Gaussian 09[28] and Molpro[29] codes. Molecular structures and orbitals were plotted with the GMolden program.[30]

The Franck-Condon (FC) factors, i.e., the squares of overlap integrals between vibrational wave functions for the anionic and neutral OA, were calculated in harmonic

approximation with molecular structures and Hessians determined at the CCSD/ATZ level. Both geometrical equilibrium parameters as well as curvatures are affected by excess electron attachment and the resulting FC factors may contribute to vibrational structure in the photoelectron spectrum. The polyatomic FC factors were calculated using the recursion relations of Doktorov.[31,32] The simulations were performed for different temperatures of the anionic beam (25 K < T < 300 K). The energy of the 0-0 transition was determined from the CCSD(T)/ATZ electronic energies and the CCSD/ATZ zero-point harmonic frequencies. The intensity for the 0-0 transition was normalized to 1 and all other intensities were scaled accordingly. The calculated FC factors were convoluted with Lorentzian line shapes (full width at half maximum = 218 cm^{-1}) and the simulated spectrum is presented in Figure 2.2.2.

Photoelectron Spectroscopy

Negative ion photoelectron spectroscopy is conducted by crossing a mass-selected beam of parent negative ions with a fixed-frequency photon beam and energy-analyzing the resultant photodetached electrons. This process is governed by the energy conserving relationship $h\nu = EKE + EBE$, where $h\nu$ is the photon energy, EKE is the measured electron kinetic energy, and EBE is the electron binding energy. OA anions were generated in a biased (-500V) supersonic expansion nozzle-ion source, in which the OA sample was heated between 80-100 °C and co-expanded with approximately several atmospheres of argon gas through a 10 μm diameter nozzle. Low energy electrons were injected directly into the expanding jet by a hot and even more negatively biased thoriated iridium filament, in the presence of a weak external magnetic field where the microplasma was formed. The anions were then extracted and transported by an ion

optics series through a 90° magnetic sector, mass spectrometer with a typical mass resolution of ~400. The mass-selected OA anion beam was then crossed with an intracavity run argon ion laser beam. The resultant photodetached electrons were energy-analyzed in a hemispherical electron energy analyzer with a resolution of ~30 meV. The photoelectron spectrum reported here was recorded with 2.540 eV photons (488 nm) and calibrated against the well-known photoelectron spectrum of the O^- anion.[33]

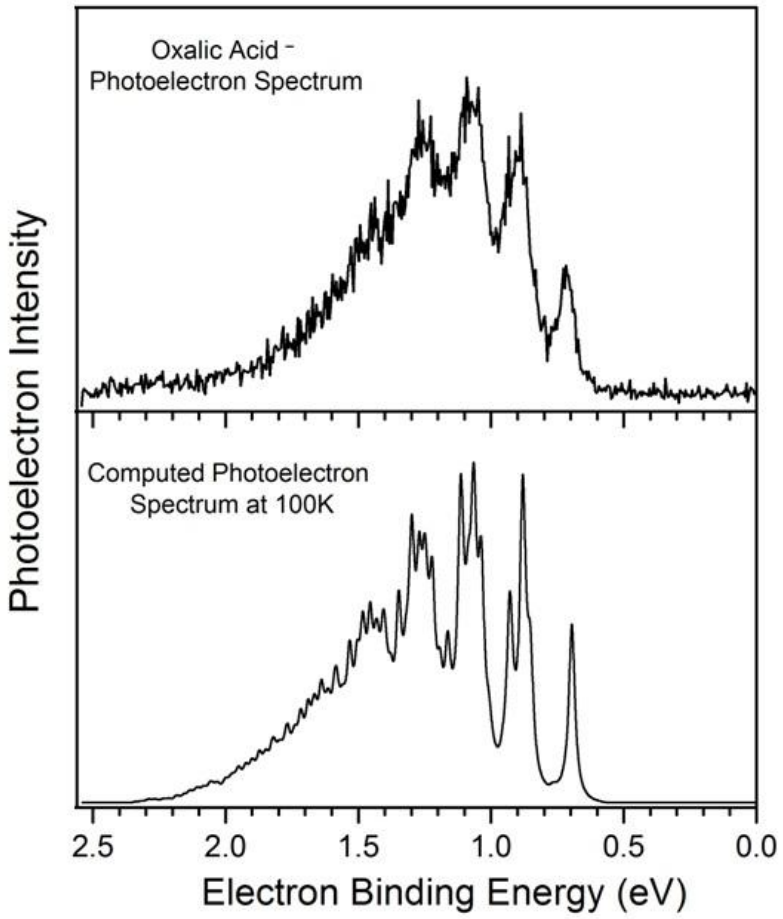

Figure 2.2.2. (Upper trace) Photoelectron spectrum of OA^- recorded with 2.540 eV photons. (Lower trace) Computed spectrum based on the CCSD(T)/ATZ electronic energies and CCSD/ATZ geometries and hessians.

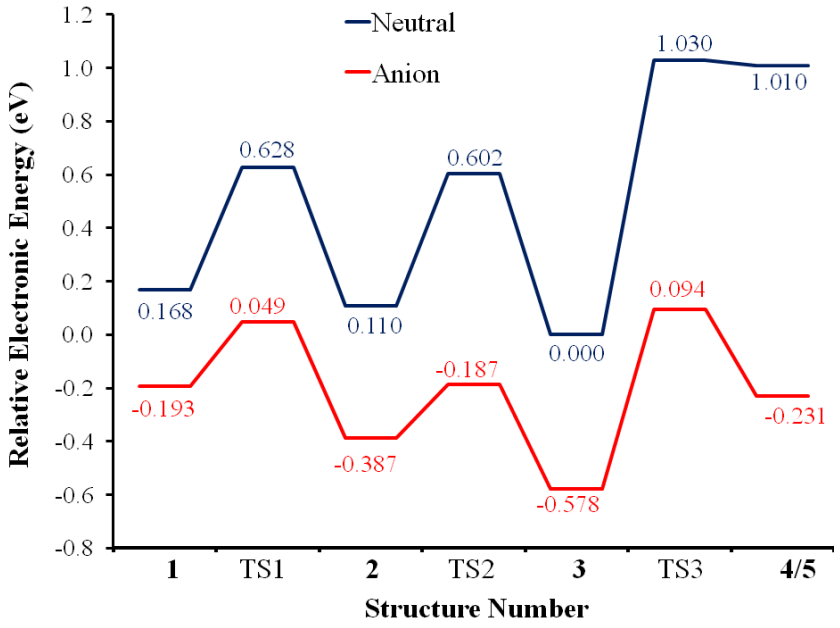

Figure 2.2.3. Energetics of stationary points (minima and transition states) on the potential energy surface of the neutral and anionic monomer of oxalic acid, where the zero of energy is set to the energy of the neutral **3**.

The OA monomer supports a bound valence anionic state: all anionic minima (**1**-**3**, and **5**) are more stable than the most stable neutral **3** by a few tenths of an eV. **3** is the most stable anionic conformer (Figure 2.2.3). The barriers separating conformers **1**-**3** are smaller for the valence anion than for the neutral. The tautomer **4** is strongly stabilized by the excess electron attachment. The molecular framework for the anion lowers symmetry from C_{2v} (structure **4**, with an imaginary frequency for a b_1 mode) to C_s (structure **5**) and the CCSD(T) barrier for **5** → **3** becomes 0.325 eV, thus one order of magnitude larger than the barrier **4** → **3** for the neutral. Thus, the anion **5** may be sufficiently long-lived to be observed in experimental conditions.

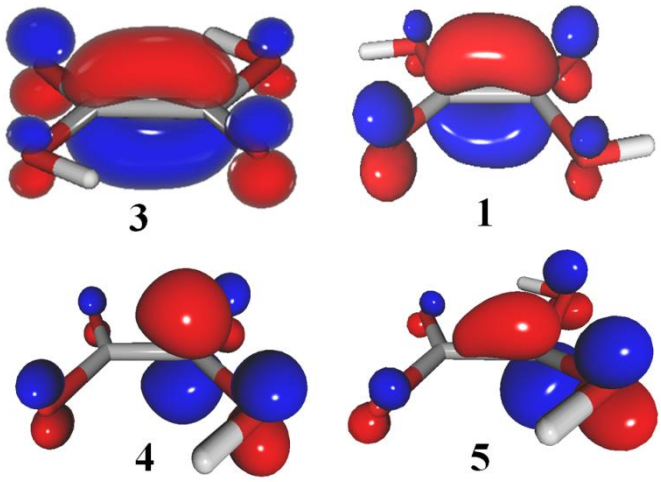

Figure 2.2.4. The SOMO of anionic OA structures plotted with a contour value of 0.1 au.

Which factors contribute to the stability of valence anions of the OA monomer? The singly occupied molecular orbital (SOMO) is of π symmetry (Figure 2.2.4). The SOMO is characterized by a bonding C-C interaction and antibonding C-O interactions, which is clearly illustrated for the C_{2h} structures **3** and **1**. A similar pattern holds for **4** and **5**, though the carbon atoms are not equivalent due to lower symmetries. We believe that the unique electrophilicity of OA results primarily from the proximity of the carboxylic groups, which allows for the bonding C-C interaction in the SOMO.

There are also secondary factors that contribute to the stability of valence anions of OA. The CCSD(T) values of VDE (Figure 2.2.5a) increase from **1** to **3** demonstrating that intramolecular hydrogen bonding stabilizes the anion. An even greater increase of VDE is brought by intramolecular proton transfer as the value of VDE increases by 0.605 eV from **3** to **4**. Finally, a buckling of the molecular framework further increases the value of VDE (**4** → **5**) by 0.591 eV.

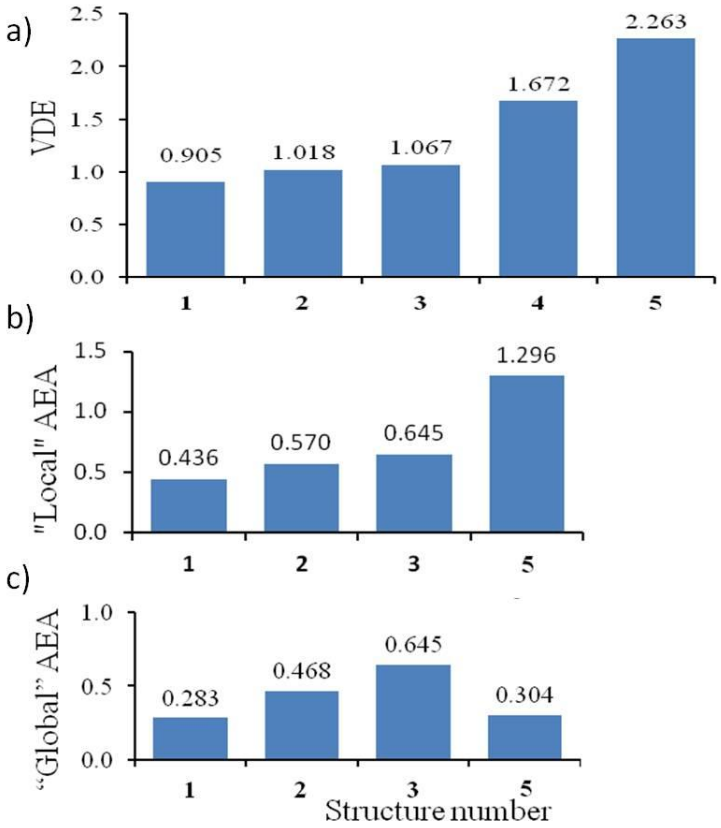

Figure 2.2.5. Excess electron binding energies (eV) for the oxalic acid monomer. (a) The VDE values are reported. The AEA values are reported with respect to (b) the corresponding neutral ("Local" AEA), and (c) the most stable neutral **3** ("Global" AEA).

The buckling of molecular frameworks upon binding an excess electron on a π* orbital is a common phenomenon in valence anions of nucleic acid bases.[6] In the case of the most stable valence anion of OA, **3**, the framework remains unbuckled and the C_{2h} symmetry is maintained. Notice, however, that the buckling mode of b_g symmetry is softer by 201.7 cm^{-1} for the anion than for the neutral (Table 2.2.1).

It requires the intramolecular proton transfer (**3** → **4**) to change the sign of the curvature of the buckling mode. Upon intramolecular proton transfer the unpaired electron becomes localized on the $C(OH)_2$ fragment (bottom of Figure 2.2.4) and the C

Table 2.2.1. Nature of vibrational modes and harmonic frequencies, calculated at the CCSD/ATZ level for structure **3.** The "buckling" mode in bold, the modes contributing primarily to the vibronic structure reported in Figure 2.2.2 are underlined.

Mode	Symmetry	Nature	Frequency (cm^{-1})	
			Neutral	Anion
1	$\mathbf{a}_u$	C-C Rotation	122.7	190.0
2	$\mathbf{b}_u$	C-C-O Bend	269.4	255.0
3	$\mathbf{a}_u$	Buckling	481.5	403.5
4	$\mathbf{a}_g$	C-C Stretch	418.6	411.8
5	$\mathbf{a}_g$	C-C-O Bend	572.7	603.5
6	$\mathbf{b}_u$	C-C-O Bend	683.3	612.6
7	$\mathbf{b}_g$	C-O(H) Rotation	686.5	615.9
8	$\mathbf{a}_u$	C-O(H) Rotation	691.2	633.3
9	$\mathbf{b}_g$	**Buckling**	**855.5**	**653.8**
10	$\mathbf{a}_g$	C-C Stretch	848.1	836.3
11	$\mathbf{b}_u$	C-O(H) Stretch	1233.5	1082.5
12	$\mathbf{a}_g$	C-O-H Bend	1262.1	1278.5
13	$\mathbf{b}_u$	C-O-H Bend	1368.4	1322.6
14	$\mathbf{a}_g$	C-O(H) Stretch	1490.3	1424.2
15	$\mathbf{b}_u$	C=O Stretch	1894.8	1628.2
16	$\mathbf{a}_g$	C=O Stretch	1884.5	1780.1
17	$\mathbf{b}_u$	O-H Stretch	3737.4	3732.6
18	$\mathbf{a}_g$	O-H Stretch	3733.6	3735.9

atom forms an apex of the buckled structure (Figure 2.2.1). The stationary point, **4**, is a transition state for the valence anion and the b_1 mode has an imaginary frequency of ~300*i* cm^{-1}.This mode morphs into a' symmetry mode of **5** with a frequency of ~800cm^{-1}.

The electron binding energies (VDE, AEA) are summarized in Figure 2.2.5. The AEA values are corrected for the energies of zero-point vibrations and are reported with respect to the corresponding neutral ("Local" AEA, Figure 2.2.5b), and the most stable neutral **3** ("Global" AEA, Figure 2.2.5c). For each structure, we report significant differences between the VDE and "Local" AEA values, which must be associated with

geometric distortions, such as changes of bond lengths and angles, upon binding an excess electron. These will be critical for the discussion of the PES spectrum of OA^-. Notice that the "Global" AEA values (Figure 2.2.5c) remain positive for all structures.

The experimental PES spectrum of OA^- is presented in black in Figure 2.2.2 (upper trace). It spreads from ca. 0.5 to 2.5 eV, with well-defined peaks at 0.72, 0.90, 1.08, 1.27, and 1.40 eV (± 0.05 eV). In view of the fact that the anionic minimum **3** is more stable than other minima by more than 0.2 eV (Figure 3), we focused our attention on FC factors for the structure **3** anion→neutral vibronic transitions, and we assumed that contributions from other anionic structures to the experimental PES spectrum are less probable. Two observations support this assumption: (i) the position of the highest peak in the experimental spectrum (1.08 ± 0.05 eV) coincides with the calculated value of VDE for **3** of 1.13 eV, and (ii) the position of the first peak in the spectrum at 0.72 ± 0.05 eV coincides with the calculated value of AEA for **3** of 0.70 eV.

The calculated FC factors and signal intensities are presented in Table 2.2.S3 of the SI[34] and the resulting computed spectrum is presented in Figure 2.2.2 (lower trace). The best match with the experimental spectrum was found for T=100 K. A very good agreement between the computed and experimental spectra suggests that the experimental anionic beam is indeed dominated by the most stable anionic structure **3**. Notice, however, a nonzero photoelectron intensity at approximately 2.2-2.3 eV, where the computed spectrum has no intensity. This weak feature might result from a small fraction of structure **5** in the anionic beam, with the calculated VDE of 2.26 eV (Figure 2.2.5a).

Table 2.2.2. Geometric parameters for the neutral and anionic structure **3** at the CCSD/ATZ level.

Parameter	Neutral	Anion
C1-C2	1.538	1.422
C1-O1	1.321	1.382
C1=O2	1.200	1.253
O1-H1	0.970	0.969
H1...O4	2.118	2.099
C2-C1-O1	113.58	113.94
C2-C1=O2	121.20	125.41
C1-O1-H1	107.19	102.70

Further analysis of harmonic frequencies (Table 2.2.1) and geometric parameters (Table 2.2.2) of the neutral and anion of **3** is needed to understand the origin of the vibronic structure reported in Figure 2.2.2 and Table 2.2.S3. The C-C bond contracts and the C-O bonds elongate upon excess electron attachment. These are significant distortions, exceeding 0.05 Å. In addition, the C-C=O and C-O-H angles expand and contract, respectively, by 4-5°. The geometric distortion from the anion to the neutral can be accomplished by displacements along the fully symmetric modes 10, 12, 14 and 16. These are C-O or C-C stretching modes with the exception of 12, which is a C-O-H bending mode (Table 2.2.1). The geometric changes are consistent with the nature of the SOMO in the anion, which is bonding in the C-C region and antibonding in the C-O regions (Figure 2.2.4). The C-O stretching modes 14 and 16 are strongly red-shifted upon an excess electron attachment by 66 and 104 cm^{-1} respectively (Table 2.2.1). Finally, perusal of the data from Table S3 confirms that the largest FC factors are associated with the 0-0 transition at 0.72 eV, and vibrational excitations involving the modes 12, 14 and

16, which are responsible for the developments of PES peaks at 0.90, 1.08, 1.27, and 1.40 eV (± 0.05 eV).

CONCLUDING REMARKS

The oxalic acid monomer displays electrophilicity uncharacteristic for most simple organic molecules. It supports a bound valence anion in the neighborhood of the global C_{2h} minimum of the neutral. The bound valence anion is characterized by an AEA of 0.72 eV and a VDE of 1.10 eV (± 0.05 eV). The unique electrophilicity of OA results primarily from the proximity of the carboxylic groups, which allows for the bonding C-C interaction in the SOMO of the anion. The intramolecular hydrogen bonding also contributes to the overall stability of the anion. The PES of OA^{-} can be modeled based on the calculated AEA value of OA and the intensities of vibronic transitions given by Franck-Condon factors.

ACKNOWLEDGEMENTS

This material is based, in part, upon experimental work supported by the (US) National Science Foundation under grant number, CHE-1360692 (KHB). Z.G.K. was supported by the fellowship from the University of Botswana. This research was supported in part (to M.H.) by the U. S. Department of Energy under contract DE-AC02-05CH11231. This research used resources of the National Energy Research Scientific Computing Center, which is supported by the Office of Science of the U.S. Department of Energy under Contract No. DE-AC02-05CH11231.

REFERENCES

1. NIST webbook, Standard Reference Database 69 http://webbook.nist.gov/chemistry/, *May 2012*.
2. Allan, M. *Phys. Rev. Lett.* **2007**, *98*, 123201.
3. Aflatooni, K.; Gallup, G. A.; Burrow, P. D. *J. Phys. Chem. A* **1998**, *102*, 6205.
4. Scheer, A. M.; Mozejko, P.; Gallup, G. A.; Burrow, P. D. *J. Chem. phys.* **2007**, *126*, 174301.
5. Gutsev, G. L.; Bartlett, R. J.; Compton, R. N. *J.Chem. Phys.* **1998**, *108*, 6756.
6. Li, X.; Bowen, K. H.; Haranczyk, M.; Bachorz, R. A.; Mazurkiewicz, K.; Rak, J.; Gutowski, M. *J. Chem. Phys.* **2007**, *127*, 174309/1.
7. Bachorz, R. A.; Klopper, W.; Gutowski, M. *J. Chem. Phys.* **2007**, *126*, 085101.
8. Haranczyk, M.; Gutowski, M. *Angew. Chem. Int. Ed.* **2005**, *44*, 6585.
9. Haranczyk, M.; Gutowski, M.; Li, X. A.; Bowen, K. H. *J. Phys. Chem. B* **2007**, *111*, 14073.
10. Haranczyk, M.; Gutowski, M.; Li, X.; Bowen, K. H. *P. Natl. Acad. Sci. USA* **2007**, *104*, 4804.
11. Stokes, S. T.; Grubisic, A.; Li, X.; Ko, Y. J.; Bowen, K. H. *J. Chem. Phys.* **2008**, *128*, 044314.
12. Kobylecka, M.; Gu, J.; Rak, J.; Leszczynski, J. *J. Chem. Phys.* **2008**, *128*, 044315.
13. Nahlovsk.Z; Nahlovsk.B; Strand, T. G. *Acta Chem. Scand.* **1970**, *24*, 2617.
14. Stace, B. C.; Oralratm.C *J. Mol. Struct.* **1973**, *18*, 339.
15. Redington, R. L.; Redington, T. E. *J. Mol. Struct.* **1978**, *48*, 165.
16. Nieminen, J.; Rasanen, M.; Murto, J. *J. Phys. Chem-Us* **1992**, *96*, 5303.

17. Macoas, E. M. S.; Fausto, R.; Pettersson, M.; Khriachtchev, L.; Rasanen, M. *J. Phys. Chem. A* **2000**, *104*, 6956.

18. Back, R. A. *Can. J. Chem.* **1984**, *62*, 1414.

19. Godfrey, P. D.; Mirabella, M. J.; Brown, R. D. *J. Phys. Chem. A* **2000**, *104*, 258.

20. Chen, C.; Shyu, S. F. *Int. J. Quantum Chem.* **2000**, *76*, 541.

21. Vanalsenoy, C.; Klimkowski, V. J.; Schafer, L. *Theochem-J. Mol. Struct.* **1984**, *18*, 321.

22. Raabe, G. *Z Naturforsch. A* **2002**, *57*, 961.

23. Mohajeri, A.; Shakerin, N. *J. Mol. Struct-Theochem* **2004**, *711*, 167.

24. Chang, J. G.; Chen, H. T.; Xu, S. C.; Lin, M. C. *J. Phys. Chem. A* **2007**, *111*, 6789.

25. Buemi, G. *J. Phys. Org. Chem.* **2009**, *22*, 933.

26. Bartlett, R. J.; Musial, M. *Rev. Mod. Phys.* **2007**, *79*, 291.

27. Kendall, R. A.; Dunning, T. H.; Harrison, R. J. *J. Chem. Phys.* **1992**, *96*, 6796.

28. Frisch, M. J. T., G. W.; Schlegel, H. B.; Scuseria, G. E.; Robb, M. A.; Cheeseman, J. R.; Scalmani, G.; Barone, V.; Mennucci, B.; Petersson, G. A.; Nakatsuji, H.; Caricato, M.; Li, X.; Hratchian, H. P.; Izmaylov, A. F.; Bloino, J.; Zheng, G.; Sonnenberg, J. L.; Hada, M.; Ehara, M.; Toyota, K.; Fukuda, R.; Hasegawa, J.; Ishida, M.; Nakajima, T.; Honda, Y.; Kitao, O.; Nakai, H.; Vreven, T.; Montgomery, Jr., J. A.; Peralta, J. E.; Ogliaro, F.; Bearpark, M.; Heyd, J. J.; Brothers, E.; Kudin, K. N.; Staroverov, V. N.; Kobayashi, R.; Normand, J.; Raghavachari, K.; Rendell, A.; Burant, J. C.; Iyengar, S. S.; Tomasi, J.; Cossi, M.; Rega, N.; Millam, J. M.; Klene, M.; Knox, J. E.; Cross, J. B.; Bakken, V.; Adamo,

C.; Jaramillo, J.; Gomperts, R.; Stratmann, R. E.; Yazyev, O.; Austin, A. J.; Cammi, R.; Pomelli, C.; Ochterski, J. W.; Martin, R. L.; Morokuma, K.; Zakrzewski, V. G.; Voth, G. A.; Salvador, P.; Dannenberg, J. J.; Dapprich, S.; Daniels, A. D.; Farkas, Ö.; Foresman, J. B.; Ortiz, J. V.; Cioslowski, J.; Fox, D. J. *Gaussian, Inc., Wallingford CT* **2009**.

29. Werner, H.-J.; Knowles, P. J.; Knizia, G.; Manby, F. R.; Schütz, M.; Celani, P.; Korona, T.; Lindh, R.; Mitrushenkov, A.; Rauhut, G.; Shamasundar, K. R.; Adler, T. B.; Amos, R. D.; Bernhardsson, A.; Berning, A.; Cooper, D. L.; Deegan, M. J. O.; Dobbyn, A. J.; Eckert, F.; Goll, E.; Hampel, C.; Hesselmann, A.; Hetzer, G.; Hrenar, T.; Jansen, G.; Köppl, C.; Liu, Y.; Lloyd, A. W.; Mata, R. A.; May, A. J.; McNicholas, S. J.; Meyer, W.; Mura, M. E.; Nicklass, A.; O'Neill, D. P.; Palmieri, P.; Pflüger, K.; Pitzer, R.; Reiher, M.; Shiozaki, T.; Stoll, H.; Stone, A. J.; Tarroni, R.; Thorsteinsson, T.; Wang, M; Wolf, A. *Molpro, version 2010.1, Cardiff, UK, Editon edn., 2011.* **2010**.
30. Schaftenaar, G.; Noordik, J. H. *J. Comput. Aid Mol. Des.* **2000**, *14*, 123.
31. Doktorov, E. V.; Malkin, I. A.; Manko, V. I. *J. Mol. Spectrosc.* **1975**, *56*, 1.
32. Yang, D. S.; Zgierski, M. Z.; Rayner, D. M.; Hackett, P. A.; Martinez, A.; Salahub, D. R.; Roy, P. N.; Carrington, T. *J. Chem. Phys.* **1995**, *103*, 5335.
33. Neumark, D. M.; Lykke, K. R.; Andersen, T.; Lineberger, W. C. *Phys. Rev. A* **1985**, *32*, 1890.

SUPPLEMENTAL MATERIAL

Table 2.2.S1. The CCSD/ADZ structures for the neutral and anion of oxalic acid. The geometrical parameters (in Å) for the neutral and anion in black and blue, respectively. All structures are minima but the anionic **4**, which is a transition state.

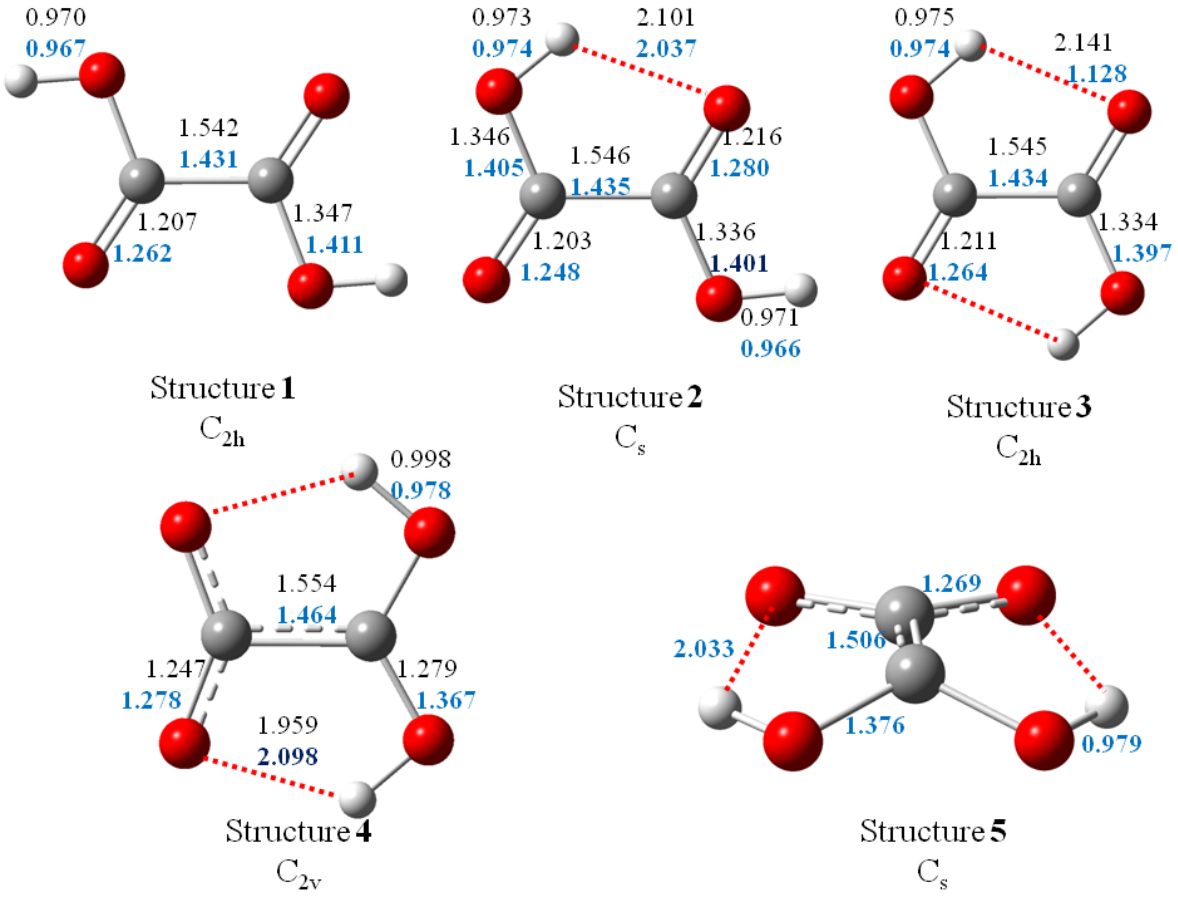

Structure	Neutral	Anion
1	C 0.000000 0.000000 0.000000 O 0.000000 0.000000 1.347237 O 0.982973 0.000000 -0.701148 C -1.445226 0.000000 -0.538566 O -1.445226 0.000000 -1.885803 O -2.428199 0.000000 0.162582 H -2.375931 0.000000 -2.160378 H 0.930705 0.000000 1.621812	C 0.000000 0.000000 0.000000 O 0.000000 0.000000 1.410901 O 1.111248 0.000000 -0.598095 C -1.315462 0.000000 -0.564242 O -1.315462 0.000000 -1.975143 O -2.426710 0.000000 0.033853 H -2.263433 0.000000 -2.164223 H 0.947971 0.000000 1.599980
2	C 0.000000 0.000000 0.000000 C 0.000000 0.000000 1.545546 O 1.038406 0.000000 2.178347 O 1.248928 0.000000 -0.502446 O -0.999174 0.000000 -0.669697 O -1.230807 0.000000 2.065282 H -1.134011 0.000000 3.031641 H 1.868349 0.000000 0.248091	C 0.000000 0.000000 0.000000 C 0.000000 0.000000 1.435223 O 1.054823 0.000000 2.160888 O 1.307705 0.000000 -0.513327 O -0.968228 0.000000 -0.787615 O -1.253784 0.000000 2.060719 H -1.010901 0.000000 2.996169 H 1.858923 0.000000 0.289720
3	C 0.000000 0.000000 0.000000 C 0.000000 0.000000 1.545275 O 1.035141 0.000000 2.173612 O 1.220308 0.000000 -0.539951 O -1.035141 0.000000 -0.628337 O -1.220308 0.000000 2.085226 H 1.858435 0.000000 0.196827 H -1.858435 0.000000	C 0.000000 0.000000 0.000000 C 0.000000 0.000000 1.433856 O 1.029863 0.000000 2.167474 O 1.275118 0.000000 -0.570281 O -1.029863 0.000000 -0.733618 O -1.275118 0.000000 2.004137 H 1.859498 0.000000 0.208324 H -1.859498 0.000000 1.225532

	1.348448	
4	C 0.000000 0.000000 0.000000 O 0.000000 0.000000 1.279197 O 1.091336 0.000000 -0.667331 C -1.355194 0.000000 -0.759816 O -2.311569 0.000000 0.039809 O -1.171901 0.000000 -1.992883 H -0.978854 0.000000 1.475342 H 0.748027 0.000000 -1.604757	C 0.000000 0.000000 0.000000 O 0.000000 0.000000 1.367353 O 1.229188 0.000000 -0.598958 C -1.241769 0.000000 -0.776275 O -2.312542 0.000000 -0.078220 O -1.083271 0.000000 -2.044626 H -0.965073 0.000000 1.530236 H 0.952871 0.000000 -1.537864
5	N/A	C 0.000000 0.000000 0.000000 O 0.000000 0.000000 1.376150 O 1.255539 0.000000 -0.563393 C -1.039949 0.856719 -0.673194 O -2.030448 1.163356 0.058656 O -0.777753 1.163360 -1.876500 H -0.880453 0.393846 1.547854 H 1.051739 0.393847 -1.436974

Table 2.2.S2. The CCSD/ADZ structures of the neutral and anionic transition states TS1-TS3 of oxalic acid. The geometrical parameters are in Å, °.

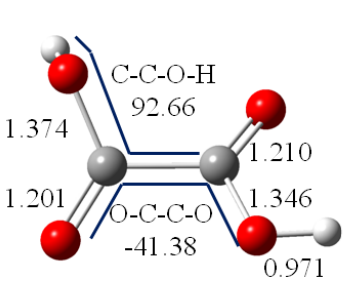

Neutral TS1

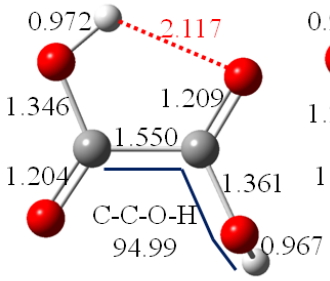

Neutral TS2

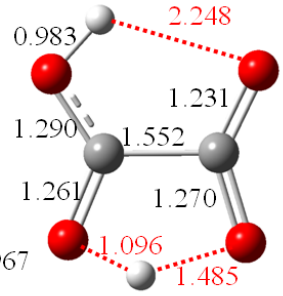

Neutral TS3

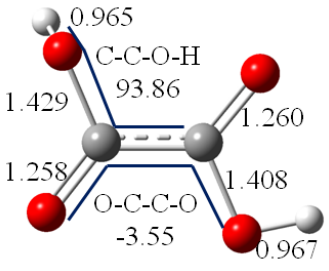

Anion TS1

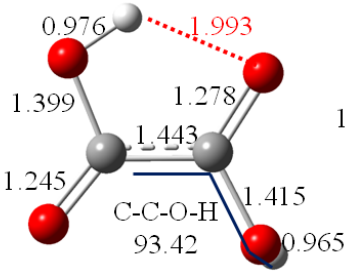

Anion TS2

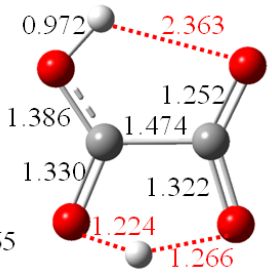

Anion TS3

Structures	Neutral	Anion
TS1	C 0.000000 0.000000 0.000000 O 0.000000 0.000000 1.373996 O 0.985759 0.000000 -0.686448 C -1.419965 -0.000149 -0.591831 O -1.523351 0.824962 -1.649875 O -2.300484 -0.708814 -0.160060 H -2.430969 0.741564 -1.985418 H 0.042112 -0.904733 1.712862	C 0.000000 0.000000 0.000000 O 0.000000 0.000000 1.408050 O 1.114021 0.000000 -0.587928 C -1.318245 -0.015025 -0.568172 O -1.324339 0.069034 -1.995016 O -2.410541 -0.089681 0.051494 H -1.353796 -0.837411 -2.324055 H 0.947453 0.006284 1.599989
TS2	C 0.000000 0.000000 0.000000 C 0.000000 0.000000 1.549845 O 1.043819 0.000000 2.159779	C 0.000000 0.000000 0.000000 C 0.000000 0.000000 1.443090 O 1.073719 0.000000 2.136488 O 1.301271 0.060228 -0.509984 O -0.961679 -0.056090 -

	O 1.233182 0.142139 -0.521457 O -0.997214 -0.141800 -0.659399 O -1.232208 0.060222 2.125433 H -1.560480 -0.822281 2.344851 H 1.862902 0.197293 0.217327	0.788631 O -1.262529 -0.005839 2.082589 H -1.484004 -0.928737 2.258687 H 1.844836 0.076291 0.300128
TS3	C 0.000000 0.000000 0.000000 C 0.000000 0.000000 1.552249 O 1.160651 0.000000 2.044199 O 1.218865 0.000000 -0.356721 O -1.104011 0.000000 -0.545348 O -1.083242 0.000000 2.253218 H 1.651146 0.000000 1.063933 H -1.808702 0.000000 1.589434	C 0.000000 0.000000 0.000000 O 0.000000 0.000000 1.385725 O 1.145824 0.000000 -0.675211 C -1.069921 0.685586 -0.747712 O -2.183348 0.983202 -0.259642 O -0.608299 0.913655 -1.965371 H -0.904350 0.283476 1.599776 H 0.527920 0.476839 -1.618668

Table 2.2.S3. Franck-Condon factors and signal intensities for the anion → neutral vibronic transitions based on the most stable conformers of OA and OA^- (structure **3**).

Peak	Assignment	Position (cm^{-1})	Rel. FC factor	Signal
1	1_0^0	5612.612	1	1
2	$1_0^1 1_1^0$	5545.326	0.950	0.062
3	$1_0^1 12_0^1 1_1^0$	6807.456	0.595	0.039
4	$1_0^1 12_0^1 14_0^1 1_1^0$	8297.722	0.977	0.063
5	$1_0^1 12_0^1 14_0^2 1_1^0$	9787.988	0.810	0.053
6	$1_0^1 12_0^1 14_0^3 1_1^0$	11278.253	0.453	0.029
7	$1_0^1 12_0^1 16_0^1 1_1^0$	8691.909	0.542	0.035
8	$1_0^2 14_0^1$	7348.336	0.038	0.038
9	$1_0^2 14_0^2$	8838.602	0.031	0.031
10	$1_0^1 14_0^1 1_1^0$	7035.592	1.537	0.100
11	$1_0^1 14_0^2 1_1^0$	8525.858	1.257	0.082
12	$1_0^1 14_0^3 1_1^0$	10016.124	0.693	0.045
15	$1_0^1 14_0^1 16_0^2 1_1^0$	10804.497	0.669	0.043
16	$1_0^1 14_0^2 16_0^1 1_1^0$	10410.310	1.031	0.067
17	$1_0^1 14_0^2 16_0^2 1_1^0$	12294.762	0.480	0.031
18	$1_0^1 14_0^3 16_0^1 1_1^0$	11900.576	0.530	0.034
19	$1_0^1 16_0^1 1_1^0$	7429.779	0.893	0.058
20	$1_0^1 16_0^2 1_1^0$	9314.231	0.471	0.031
21	$2_0^1 14_0^1 2_1^0$	7117.246	1.607	0.041
22	$2_0^1 14_0^2 2_1^0$	8607.512	1.315	0.034
23	$2_0^1 14_0^1 16_0^1 2_1^0$	9001.698	1.412	0.036
24	$2_0^1 14_0^2 16_0^1 2_1^0$	10491.964	1.078	0.027
25	5_0^1	6185.324	0.031	0.031
26	$5_0^1 12_0^1 14_0^1$	8937.719	0.033	0.033
27	$5_0^1 14_0^1$	7675.590	0.049	0.049
28	$5_0^1 14_0^2$	9165.855	0.039	0.039
29	$5_0^1 14_0^1 16_0^1$	9560.042	0.052	0.052
30	$5_0^1 14_0^1 16_0^2$	11444.494	0.030	0.030
31	$5_0^1 14_0^2 16_0^1$	11050.308	0.039	0.039
32	$5_0^1 16_0^1$	8069.776	0.034	0.034
33	$10_0^1 12_0^1 14_0^2$	10703.411	0.027	0.027
34	12_0^1	6874.742	0.626	0.626
35	12_0^2	8136.872	0.198	0.198
38	$12_0^1 14_0^2$	9855.273	0.852	0.852
39	$12_0^1 14_0^3$	11345.539	0.476	0.476
40	$12_0^1 14_0^4$	12835.805	0.202	0.202
41	$12_0^1 14_0^5$	14326.070	0.069	0.069
42	$12_0^2 14_0^1$	9627.138	0.330	0.330
43	$12_0^2 14_0^2$	11117.403	0.277	0.277
44	$12_0^2 14_0^3$	12607.669	0.157	0.157
45	$12_0^2 14_0^4$	14097.935	0.067	0.067
46	$12_0^3 14_0^1$	10889.267	0.071	0.071
47	$12_0^3 14_0^2$	12379.533	0.061	0.061
48	$12_0^3 14_0^3$	13869.799	0.035	0.035
49	$12_0^1 14_0^1 16_0^1$	10249.460	0.875	0.875
50	$12_0^1 14_0^1 16_0^2$	12133.912	0.422	0.422
51	$12_0^1 14_0^1 16_0^3$	14018.365	0.150	0.150
52	$12_0^1 14_0^1 16_0^4$	15902.817	0.044	0.044
53	$12_0^1 14_0^2 16_0^1$	11739.726	0.677	0.677
54	$12_0^1 14_0^2 16_0^2$	13624.178	0.306	0.306
55	$12_0^1 14_0^2 16_0^3$	15508.630	0.103	0.103
56	$12_0^1 14_0^2 16_0^4$	17393.083	0.028	0.028
57	$12_0^1 14_0^3 16_0^1$	13229.991	0.353	0.353
58	$12_0^1 14_0^3 16_0^2$	15114.444	0.150	0.150
59	$12_0^1 14_0^3 16_0^3$	16998.896	0.047	0.047
60	$12_0^1 14_0^4 16_0^1$	14720.257	0.139	0.139
61	$12_0^1 14_0^4 16_0^2$	16604.709	0.055	0.055
62	$12_0^2 14_0^1 16_0^1$	11511.590	0.272	0.272
63	$12_0^2 14_0^1 16_0^2$	13396.042	0.127	0.127
64	$12_0^2 14_0^1 16_0^3$	15280.494	0.044	0.044
65	$12_0^2 14_0^2 16_0^1$	13001.856	0.213	0.213

66	$12_0^2 14_0^2 16_0^2$	14886.308	0.094	0.094
67	$12_0^2 14_0^2 16_0^3$	16770.760	0.031	0.031
68	$12_0^2 14_0^3 16_0^1$	14492.121	0.113	0.113
69	$12_0^2 14_0^3 16_0^2$	16376.573	0.046	0.046
70	$12_0^2 14_0^4 16_0^1$	15982.387	0.045	0.045
71	$12_0^3 14_0^1 16_0^1$	12773.720	0.057	0.057
72	$12_0^3 14_0^2 16_0^1$	14263.985	0.045	0.045
73	$12_0^1 16_0^1$	8759.194	0.570	0.570
74	$12_0^1 16_0^2$	10643.647	0.292	0.292
75	$12_0^1 16_0^3$	12528.099	0.110	0.110
76	$12_0^1 16_0^4$	14412.551	0.034	0.034
77	$12_0^2 16_0^1$	10021.324	0.175	0.175
78	$12_0^2 16_0^2$	11905.776	0.087	0.087
79	$12_0^2 16_0^3$	13790.229	0.032	0.032
80	$12_0^3 16_0^1$	11283.454	0.036	0.036
81	14_0^1	7102.878	1.618	1.618
82	14_0^2	8593.144	1.323	1.323
83	14_0^3	10083.409	0.729	0.729
84	14_0^4	11573.675	0.305	0.305
85	14_0^5	13063.941	0.103	0.103
86	14_0^6	14554.206	0.029	0.029
87	$14_0^1 16_0^1$	8987.330	1.421	1.421
88	$14_0^1 16_0^2$	10871.782	0.704	0.704
89	$14_0^1 16_0^3$	12756.235	0.257	0.257
90	$14_0^1 16_0^4$	14640.687	0.077	0.077
91	$14_0^2 16_0^1$	10477.596	1.085	1.085
92	$14_0^2 16_0^2$	12362.048	0.505	0.505
93	$14_0^2 16_0^3$	14246.501	0.174	0.174
94	$14_0^2 16_0^4$	16130.953	0.049	0.049
95	$14_0^3 16_0^1$	11967.862	0.558	0.558
96	$14_0^3 16_0^2$	13852.314	0.243	0.243
97	$14_0^3 16_0^3$	15736.766	0.079	0.079
98	$14_0^4 16_0^1$	13458.127	0.217	0.217
99	$14_0^4 16_0^2$	15342.580	0.089	0.089
100	$14_0^4 16_0^3$	17227.032	0.027	0.027
101	$14_0^5 16_0^1$	14948.393	0.068	0.068
102	16_0^1	7497.064	0.940	0.940
103	16_0^2	9381.517	0.495	0.495
104	16_0^3	11265.969	0.192	0.192
105	16_0^4	13150.421	0.061	0.061

Section 2.3. Electron-Induced Proton Transfer from HCl to the Superbase 1,8-Bis(dimethylamino)naphthalene

Angela Buonaugurio, Jacob Graham, Allyson Buytendyk, Yi Wang, and Kit H. Bowen

Department of Chemistry, Johns Hopkins University, Baltimore, Maryland 21218, USA

ABSTRACT

The technique of negative ion photoelectron spectroscopy was used to investigate electron-induced proton transfer from the hydrochloric acid to the superbase 1,8-bis(dimethylamino)naphthalene (DMAN). The photoelectron spectrum of $DMAN(HCl)^-$ was recorded and the EA_a and VDE measured to be ~0.90 eV and 1.12 ± 0.05 eV, respectively. The neutral and anion optimized geometries were calculated using DFT theory, identifying two stationary neutral ground state structures **N1** and **N2**, and one anion ground state structure, **A**. The VDE and the EA_a of calculated structure **N2** were found to be in very good agreement with experimental data. Similar trends are observed when comparing the DMAN(HCl) complex to previously studied acid-base systems NH_3-HX (X= Cl, Br, I). Thus, under isolation, the DMAN(HCl) complex exists as the hydrogen bonded DMAN···HCl and only upon addition of an electron does proton transfer occur, forming the anion ionic salt $[DMANH^+Cl^-]^-$.

INTRODUCTION

Electron-driven acid base chemistry has been of wide interest considering mechanisms involving electron induced proton transfer are fundamental to all chemical and biological processes. Previously we had posed the question of how an acid and a base fundamentally interact using the acid-base pair of ammonia and hydrogen chloride.[1] We concluded that under isolation, the acid-base pair does not spontaneously proton transfer and takes the form of a hydrogen-bonded, $NH_3\cdots HCl$ complex. Upon addition of an excess electron to the ammonia-HCl system, proton transfer then occurs, and the system takes the form of the ionic molecule, $NH4^+Cl^-$. This study was extended to the remaining hydrogen halides[2] and the same results determined that proton transfer does not spontaneously occur with one molecule of ammonia and one molecule of HX as it does so readily in the bulk, but instead requires perturbation from an outside environmental component, i.e. an electron.

However, say instead we replace the moderate base ammonia with a stronger base, i.e. a so called superbase, to react with a hydrogen halide. The most well-known representative of the superbases, is 1,8-bis(dimethylamino)naphthalene (DMAN) with its exceptionally high basicity strength (pKa= 12.1[3]) and gas phase proton affinity (1030.1 kJ/mol[4]). Here we present the study of the electron induced proton transfer from HCl to the superbase 1,8-bis(dimethylamino)naphthalene.

The physical properties of DMAN are in direct relation to the close proximity of the two dimethylamino substituents and its bi-dentate type coordination. This discovery was first made by Alder[5] in adding two nitrogen atoms of close proximity and N-methylation, there is a resulting sharing of a proton to form a strong intramolecular

hydrogen bond, thereby inevitably forming a proton sponge cation of $[NHN]^+$. Yet, the mechanism for the phenomena of proton transfer remains unclear. The crystal structure[6] and thermochemical properties[7,8] of DMAN have been well characterized. Additional information has been queried from IR spectroscopy[9,10] and ESCA and solid-state NMR spectroscopy.[11] Ab initio studies have calculated optimized structures of the neutral,[12,13] emphasizing relief strain importance, and therefore protonation is preferred. Fluorescence spectroscopy further revealed that the proton sponge can adopt two conformations in the electronic ground state, differing slightly in energy (~ 4.7 kcal/mol).[13]

However, many experiments performed in the condensed phase leads to characterization complications due to the presence of counterions and solvent interactions. These difficulties make gas phase studies of particular interest because solvent complications are avoided to directly probe a molecule or cluster. Herein, the spectroscopic properties of the 1,8-bis(dimethylamino)naphthalene hydrogen halide ionic salt under isolation, i.e. in the gas phase, is presented.

METHODS

Experimental

Negative ion photoelectron spectroscopy is conducted by crossing a mass-selected beam of negative ions with a fixed-frequency photon beam and energy-analyzing the resultant photodetached electrons. The photodetachment process is governed by the relationship, $h\nu$ = EBE + EKE, where $h\nu$ is the photon energy, EBE is the electron binding energy, and EKE is the measured electron kinetic energy. Cluster anions were generated using two different analytical apparatus. The first approach utilized a supersonic expansion nozzle ion source and the photoelectron spectrum measured with a

continuous anion photoelectron apparatus.[14] The second approach utilized a laser vaporization and oven source and the mass spectrum obtained with a pulsed anion photoelectron apparatus.[15]

For the continuous apparatus, the DMAN sample was placed in the stagnation chamber of the source, heated to between 180-200°C and co-expanded with 1-2 atm of argon gas through a 25 μm diameter nozzle into 10^{-4} torr vacuum. A HCl/argon (10%/90%) mixture at a few torr flowed from a small tube into the expansion region immediately outside the nozzle, also referred to as the "pick-up" line. The stagnation chamber and nozzle were biased at -500 V, while relatively low energy electrons were injected directly into the expanding jet by an even more negatively-biased filament, in the presence of weak axial magnetic fields to enhance the stability of the microplasma. The resultant anions were then extracted and transported by a series of ion optics through a 90° magnetic sector, the mass analyzer and selector with a mass resolution of ~400. The selected anions of interest were then photodetached with ~200 W of 488 nm (2.540 eV) photons from an argon ion laser, which was operated intracavity. The photodetached electrons were then energy analyzed with a hemispherical energy analyzer having a resolution of 30 meV. The photoelectron spectrum was calibrated against the photoelectron spectrum of O^-.[16]

For the pulsed apparatus, the DMAN sample was placed in a small oven (~50-80°C) attached to the front of the pulsed valve, where helium (~60 psi) was expanded over the sample in a vacuum chamber (10^{-5} torr). Just outside the orifice of the oven, low-energy electrons were produced by laser/photoemission from a pulsed Nd:YAG laser

beam (10 Hz, 532 nm) striking a translating, rotating silver rod. The anions were then pulse-extracted into the mass spectrometer.

Computational

DFT calculations were conducted by applying Becke's three-parameter hybrid functional (B3LYP)[17-19] using the Gaussian 09[20] software package to determine the electron affinity (EA) value of the salt and the vertical detachment energy (VDE) of the anion of the ionic complex. All geometries of the anion and its corresponding neutral, were fully optimized without any geometrical constraints with the 6-311+G(d,p)[21] basis set.

RESULTS

Experimental

Photodetachment is a fast process, where the essentially instantaneous Franck-Condon overlap of anion and neutral wavefunctions is reflected in the vertical detachment energy, VDE. The VDE is the EBE of the maxima in the broadened photoelectron spectral profile, and as such, it is a well-defined quantity. When there is Franck-Condon overlap between the lowest vibrational level of the anion (v") and the lowest vibrational level its corresponding neutral (v'), the photoelectron spectrum carries information about the adiabatic (thermodynamic) electron affinity of the neutral species. When the spectral profile is vibrationally resolved, an assignment of the spectrum can identify the v"=0 → v'=0 transition. For this transition, its EBE value is equal to the

adiabatic electron affinity, EA_a. When the profile is unresolved, however, the determination of EA_a is more approximate. If the anion were to be cold, i.e., if only v"=0 were occupied, then the low EBE threshold value of the spectrum would equal the EA_a value. But since anions are generated with finite internal temperatures, the first few vibrational levels of anions may also occupied, leading to some degree of photoelectron intensity at EBE values less than that corresponding to the EA_a, i.e., hot bands.

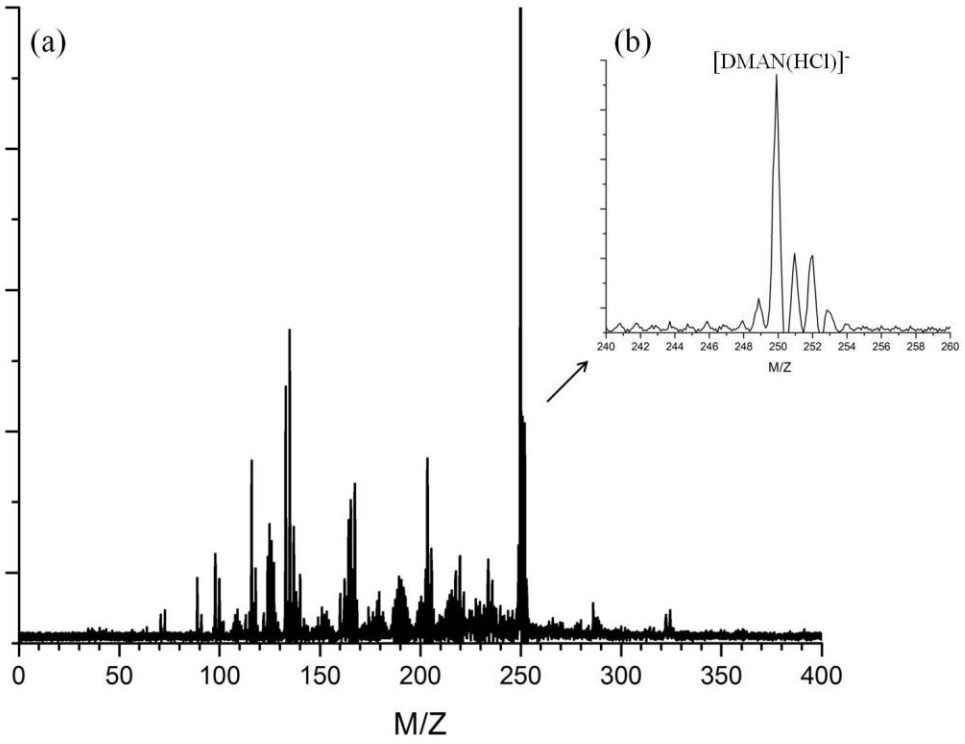

Figure 2.3.1. (a) Typical anion mass spectrum obtained using the pulsed photoelectron apparatus, in which the highest intensity peak showing the $DMAN(HCl)^-$ parent anion. (b) The inset shows selected magnified portion of the spectrum showing the $DMAN(HCl)^-$ anion appearing at several mass peaks associated with the isotope pattern. The highest signal intensity is observed for $DMAN(H^{35}Cl)^-$ at m/z= 250.31 amu.

Figure 2.3.1 represents the typical anions produced when forming the anion $DMAN(HCl)^{-}$, recorded on the pulsed source apparatus. In both the continuous and pulsed source apparatus mass spectra, there was no evidence of the $DMAN^{-}$ parent anion. Note, that under specific source conditions the $DMAN(HCl)^{-}$ anion peak associated with isotope ^{35}Cl is the strongest signal intensity.

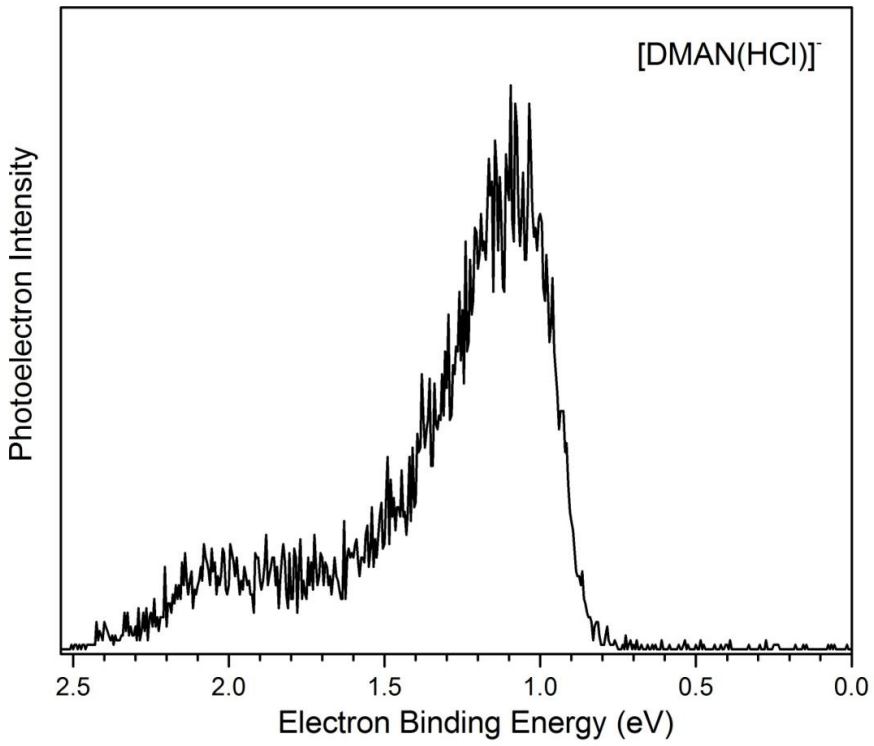

Figure 2.3.2**.** Photoelectron spectrum of the DMAN(HCl) ionic salt recorded with 2.540 eV photons on the continuous photoelectron apparatus.

The photoelectron spectrum of the 1:1 anion of the ionic salt $DMAN(HCl)^{-}$measured on the continuous source apparatus is presented in Figure 2.3.2. The spectrum may be characterized as a broad and vibrationally unresolved band with a

maximum at 1.12 ± 0.05 eV. This is taken as the VDE of the anion complex. In addition, there appears to be another feature, albeit at a much lower intensity, in the range of 1.8 to 2.3 eV. This may be an indication of several anionic structures of $DMAN(HCl)^-$ coexisting in the gas phase under experimental conditions due to the large size of DMAN and the constant oscillation and rotation of the dimethylamino groups.

Computational

Geometry Optimizations, VDE and EA_a

Our theoretical calculations started with the geometry optimization of the neutral DMAN···HCl complex, and a stationary point was found, labeled **N1** in Figure 2.3.3. As DFT methods generally underestimate reaction barrier heights[22] and no proton transfer is observed in the neutral calculations, we can tentatively claim that no proton transfer occurs in the isolated, neutral DMAN···HCl complex. This is analogous to the ammonia-HX series.[1,2] The geometry optimization was then calculated for the anion species, and a stationary point was found, which was observed to undergo proton transfer and form the anion ionic salt. The electron induced proton transfer anionic complex is labeled **A**. Figure 2.3.3 also illustrates the energetic relationship between **N1** and **A**, referring to the adiabatic electron affinity of **N1**. This value was computed to be 1.22 eV, which is much higher than the estimated EA_a of 0.90 ± 0.05 eV from the experimental spectrum. However, the calculated VDE of the **A** complex at 1.16 eV is in excellent agreement with the first band feature observed at 1.12 ± 0.05 eV.

Upon re-optimization of the anion complex as a neutral species, a new proton transferred complex was found. This new stationary point is shown in Figure 2.3.3 as **N2**.

The adiabatic energy difference between **N2** and **A** corresponds to 0.98 eV and in this case matches very well with our experimental EA_a of ~ 0.90 ± 0.05 eV. From this one could conclude that although we do not believe the isolated DMAN···HCl undergoes proton transfer in isolation, it does exhibit a neutral proton transferred state and our experimental observations correspond to transitions between the electron induced proton transfer anion and the neutral proton transfer complex.

For the optimized anion complex, **A**, to be observed the neutral complex must undergo a transition state then form the optimized neutral complex **N2**. But for this to happen there must be enough energy in the system succeed the barrier between the non-proton transfer (**N1**) and the proton transfer (**N2**) potential wells, in addition to the 0.24 eV difference between the bottom of their potential wells. This scenario may be compared to better understanding how the transitioning from gas-phase to condensed phase reactions in bulk occurs. At what point does addition of a solvent lower the transition state to a point where the reaction may proceed from **N1** to **N2**.

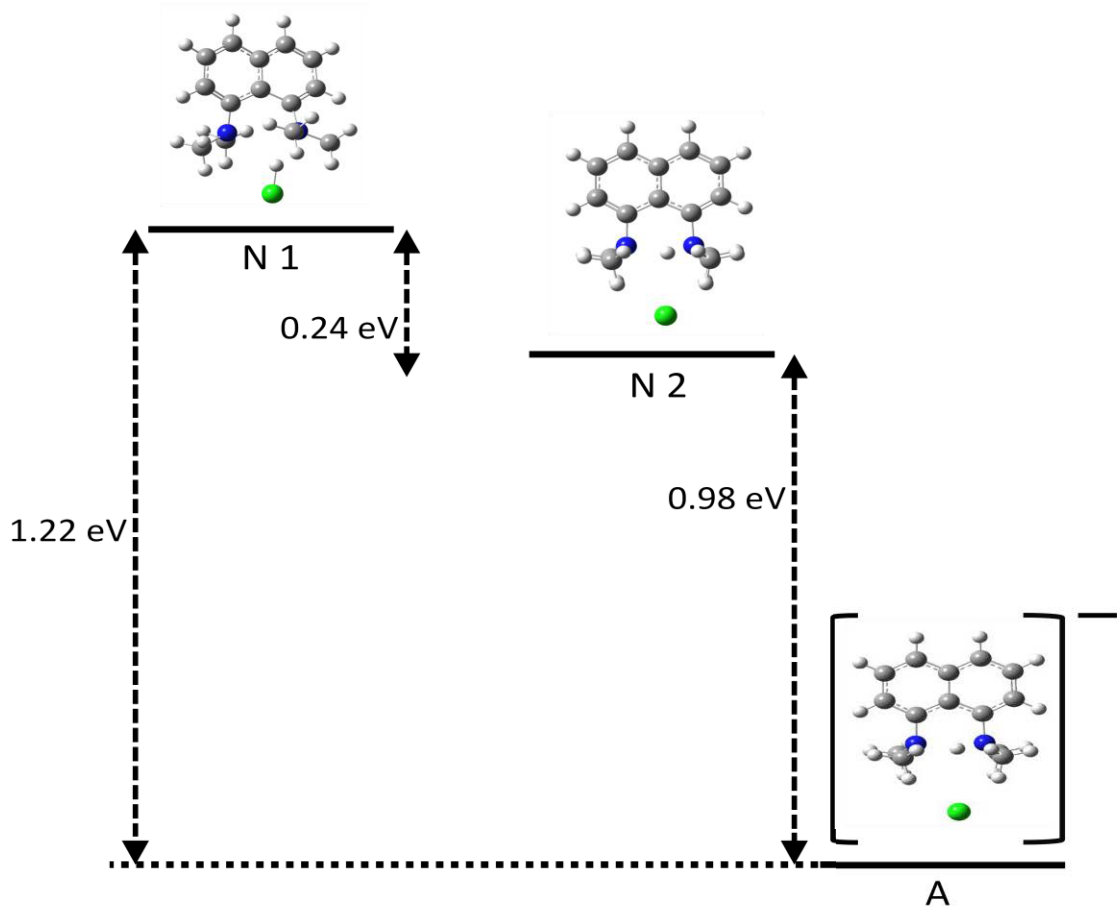

Figure 2.3.3. Schematic diagram of the optimized structures calculated for this system which includes: **N1** the optimized structure of the neutral complex, **N2** the optimized neutral complex starting from the proton transferred anion, and **A** the optimized anion complex. An undetermined barrier separates the non-proton transfer (**N1**) and proton transfer (**N2**) complexes, and the EA_a that best fits the photoelectron spectrum obtained is that from **A** to the **N2** structure of 0.98 eV.

Bond lengths

The hydrogen chloride bond length in the neutral complex is close, albeit slightly elongated, to that of a free hydrogen halide. The distance from either nitrogen of DMAN

to the proton of the hydrogen chloride is substantially larger than a nitrogen-hydrogen bond in a free ammonium cation. Therefore, the hydrogen chloride in the neutral complex is determined to be covalently bonded and noncovalently bonded to either trimethylamine group of DMAN.

Upon addition of an excess electron and formation of the anion complex, the distance between one of the nitrogens of the trimethylamine moiety is very close to that observed of an ammonium cation. The distance between the proton and chlorine atoms is significantly increases and is much larger than a free hydrogen chloride. This identifies that in the anion complex, the proton has been completely transferred, covalently bonding to one of the nitrogens and dissociated from the chloride anion. This is clearly illustrated in Figure 2.3.4, and in addition, shows that the excess electron is localized on the π* orbital of DMAN. The bond distances for all the structures are listed in Table 2.3.1.

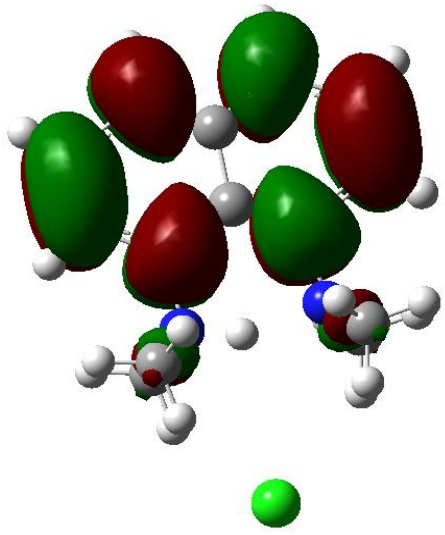

Figure 2.3.4. Highest occupied molecular orbital of the optimized anion complex of DMAN(HCl) showing that the excess electron is localized on the π* orbital of the 1,8-bis(dimethylamino)naphthalene.

Table 2.3.1. Bond distances comparing that of the free neutral molecules of HCl, NH_3, the ionic salt $NH_4^+Cl^-$, to those of the optimized **N1**, **N2**, and **A** structures involving HCl and DMAN.

	Bond Distances (Å)		
System	**H-Cl**	**N-H 1**	**N-H 2**
Free HCl	1.275 [a)]		
Free NH_3		1.012 [a)]	
Free $NH_4^+Cl^-$		1.220 [a)]	
N1	1.341	1.873	2.547
N2	2.825	1.083	1.654
A	3.186	1.085	1.617

[a)] CRC Handbook of Chemistry and Physics 87th Ed. 2006-7

DISCUSSION

For proton transfer in the neutral complexes to approach spontaneity in the NH_3-HX series, the stabilization of the excess electron with forming the anionic ionic complex grows with increasing halogen size. This makes the electron-induced proton transfer increasingly exothermic, and is explained as the dominant trend contribution.[1,2] The increased stabilization occurs with decreasing dipole moment of the neutral complex, $NH_3\cdots HX$, and with a corresponding increase in dipole moment of the neutral ionic complex, $NH_4^+Cl^-$. The dipole moments of DMAN$\cdots$HCl and $DMANH^+Cl^-$ fit into this trend with the series as expected, with the exception being that it is the base that grows in size rather than the halogen. For the decreasing dipole moment of the neutral complex, the trend goes from 4.31, 4.20, 3.74 to 2.14 D for $NH_3\cdots HCl$, $NH_3\cdots HBr$, $NH_3\cdots HI$, to DMAN$\cdots$HCl, respectively. For the increasing dipole moment of the neutral ionic complex, the trend goes from 10.01, 10.95, 11.69 to 11.78 D for $NH_4^+Cl^-$, $NH_4^+Br^-$, $NH_4^+I^-$, to $DMANH^+Cl^-$, respectively. In other words, proton transfer is made as a

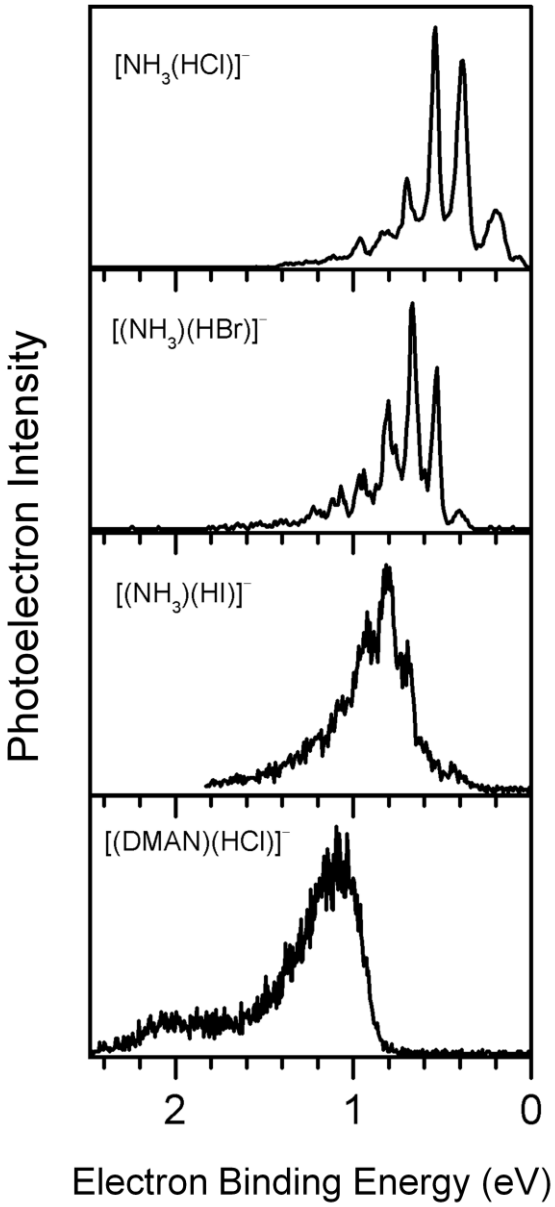

Figure 2.3.5. Photoelectron spectra of the DMAN(HCl)$^-$ anion with respect to the electron induced proton transfer $NH_3(HX)$, X= Cl, Br, I series in order of increasing EBE. The experimental and calculated EA_a and VDEs of each system are in Table 2.3.2.

favorable process upon addition of an excess electron because of the stabilization of the electron due to the increased dipole moment of the ionic complex versus the hydrogen-bonded system.

A stronger case that anion complex of DMAN(HCl) is in fact the anion of the ionic salt complex may be built by comparing the photoelectron spectrum to the NH_3-HCl series. First, observation of the photoelectron spectra in Figure 2.3.4 shows that there are trend similarities, as should be expected. The VDEs show an increasing trend while there is a decreasing trend in vibrational progressions from NH_3-HCl to DMAN-HCl. These trends gradually and consistently change through the series, as shown in the EA_as and VDEs in Table 2.3.2. In particular, the lack of vibrationally resolved features of the

Table 2.3.2. Experimental Adiabatic Electron Affinities (EA_a) and Vertical Detachment Energies (VDE) for the anion and corresponding neutral DMAN(HCl) system compared to NH_3(HX) series.

		Expt EA_a	Theo EA_a	Expt VDE	Theo VDE
$NH_3\cdots HCl$		0.075	0.068		
	$(NH_4^+Cl^-)^-$			0.540	0.52
$NH_3\cdots HBr$		0.28	0.26		
	$(NH_4^+Br^-)^-$			0.65	0.67
$NH_3\cdots HI$		0.45	0.47		
	$(NH_4^+I^-)^-$			0.81	0.77
DMAN$\cdots$HCl		0.90	0.98		
	$(DMANH^+Cl^-)^-$			1.12	1.16

DMAN-HCl system may be due to the drastic changes in the molecule structure from strain relief accessed by rotation of the dialkylamino groups upon protonation.

SUMMARY

We have used negative ion photoelectron spectroscopy to obtain the spectrum for the anion of the ionic salt, $DMAN(HCl)^-$. The EA_a and VDE were measured to be ~ 0.90(± 0.05) and 1.12(± 0.05) eV, respectively. Ab initio calculations identified the optimized geometry for two neutral structures, **N1** and **N2**, and the anion complex, **A**, in which the VDE is in excellent agreement and the calculated EA_a of **N2** matches well with the experimental value. The same comparisons reflected in the experimental and theoretical results from the previously studied[1,2] the ammonia hydrogen halide series may also be applied to DMAN(HCl). The formation of their anion salts, differ in their vibrational structure within the spectra due to shuttling proton motions within the systems.

ACKNOWLEDGEMENTS

This material is based upon work supported by the National Science Foundation under Grant Number, CHE-1360692 (KHB).

REFERENCES

1. Eustis, S. N.; Radisic, D.; Bowen, K. H.; Bachorz, R. A.; Haranczyk, M.; Schenter, G. K.; Gutowski, M. *Science*, **2008**, *319*, 936.
2. Eustis, S. N.; Whiteside, A.; Wang, D.; Gutowski, M.; Bowen, K. H. *J. Phys. Chem. A*, **2010**, *114*, 1357.
3. Hibbert, F. *J. Chem Soc., Perkin Trans.* **1974**, *2*, 1862.
4. Lou, Y. K.; Saluja, P. P. S.; Kebarle, P.; Alder, R. W. *J. Am. Chem. Soc.* **1978**, *100*, 7328.
5. Alder, R. W.; Bowman, P.S.; Steele, W. R.S.; Winterman, D. R. *J. Chem. Soc., Chem. Commun.* **1968**, *10*, 723.
6. Einspahr, H.; Robert, J. B.; Marsh, R. E.; Roberts, R. D. *Acta Crystallogr*. **1973**, *B29*, 1611.
7. Davalos, J. Z.; Lago, A. F.; Costa, J. C. S.; Santos, L. M. N. B. F.; Gonzalez, J. *J. Chem. Thermodynamics* **2012**, *54*, 346.
8. Howard, S. T. *J. Am. Chem. Soc*. **2000**, *122*, 8238.
9. Grech, E.; Malarski, Z.; Sobczyk, L. *J. Molecular Structure* **1985**, *129*, 35.
10. Brzezinski, B.; Grech, E.; Malarski, Z.; Sobczyk, L. *J. Chem. Soc. Perkin Trans.* **1990**, *86*, 1777.
11. Wozniak, K.; He, H.; Klinowski, J.; Barr, T. L.; Milart, P. *J. Phys. Chem*. **1996**, *100*, 11420.
12. Platts, J. A.; Howard, S. T.; Wozniak, K. *J. Org. Chem.* **1994**, *59*, 4647.
13. Szemik-Hojniak, A.; Zwier, J. M.; Buma, W. J.; Bursi, R.; van der Waals, J. H. *J. Am. Chem. Soc.* **1998**, 120, 4840.

14. Coe, J. V.; Snodgrass, J. T.; Freidhoff, C. B.; McHugh, K. M.; Bowen, K. H. *J. Chem. Phys.* **1986**, *84*, 618.

15. Thomas, O.; Zheng, W. J.; Bowen, K. H. *J. Chem. Phys.* **2001**, *114*, 5514.

16. Neumark, D. M.; Lykke, K. R.; Andersen, T.; Lineberger, W. C. *Phys. Rev. A* **1985**, *32*, 1890.

17. Becke, A. D. *Phys. Rev. A* **1988**, *38*, 3098.

18. Becke, A. D. J. *Chem. Phys*. **1993**, *98*, 5648.

19. Lee, C.; Yang, W.; Parr, R. G. *Phys. Rev. B* **1988**, *37*, 785.

20. Gaussian 09, Revision A.2, Frisch, M. J.; Trucks, G. W.; Schlegel, H. B.; Scuseria, G. E.; Robb, M. A.; Cheeseman, J. R.; Scalmani, G.; Barone, V.; Mennucci, B.; Petersson, G. A.; Nakatsuji, H.; Caricato, M.; Li, X.; Hratchian, H. P.; Izmaylov, A. F.; Bloino, J.; Zheng, G.; Sonnenberg, J. L.; Hada, M.; Ehara, M.; Toyota, K.; Fukuda, R.; Hasegawa, J.; Ishida, M.; Nakajima, T.; Honda, Y.; Kitao, O.; Nakai, H.; Vreven, T.; Montgomery, J. A., Jr.; Peralta, J. E.; Ogliaro, F.; Bearpark, M.; Heyd, J. J.; Brothers, E.; Kudin, K. N.; Staroverov, V. N.; Kobayashi, R.; Normand, J.; Raghavachari, K.; Rendell, A.; Burant, J. C.; Iyengar, S. S.; Tomasi, J.; Cossi, M.; Rega, N.; Millam, N. J.; Klene, M.; Knox, J. E.; Cross, J. B.; Bakken, V.; Adamo, C.; Jaramillo, J.; Gomperts, R.; Stratmann, R. E.; Yazyev, O.; Austin, A. J.; Cammi, R.; Pomelli, C.; Ochterski, J. W.; Martin, R. L.; Morokuma, K.; Zakrzewski, V. G.; Voth, G. A.; Salvador, P.; Dannenberg, J. J.; Dapprich, S.; Daniels, A. D.; Farkas, Ö.; Foresman, J. B.; Ortiz, J. V.; Cioslowski, J.; Fox, D. J. Gaussian, Inc., Wallingford CT, 2009.

21. Krishnan, R.; Binkley, J. S.; Seeger, R.; Pople, J. A. *J. Chem. Phys.* **1980**, *72*, 650.

22. Lynch, B. J.; Fast, P. L.; Harris, M.; Truhlar, D. G. *J. Phys. Chem. A* **2000**, *104*, 4811.

CHAPTER 3

Anion Photoelectron Spectroscopy of the Linear $C_nH_{2n+1}O^-$ (n = 1-9) Alkoxides

Sarah T. Stokes[†]

[†]*Chemistry Department, Towson University, Baltimore, MD, 21204*

John E. Bartmess[§]

[§]*Chemistry Department, University of Tennessee, Knoxville, TN, 37996*

Angela Buonaugurio[‡], Yi Wang[‡], Soren N. Eustis[&], and Kit H. Bowen Jr.[‡]

[‡]*Chemistry Department, Johns Hopkins University, Baltimore, MD, 21218*

[&]*Chemistry Department, Bowdoin College, Brunswick, MA, 04011*

ABSTRACT

The photoelectron spectra of the linear $C_nH_{2n+1}O^-$ alkoxides where n = 1-9 are presented. The first new photoelectron spectrum in the series is that of $C_4H_9O^-$ whose vertical detachment energy (VDE) and electron affinity (EA) are 1.96 eV and 1.85 eV respectively. VDE's and EA's of the longer chain alkoxide ions show a monotonic increase with carbon chain length and are used in conjunction with previously reported gas phase acidities of their corresponding alcohols to determine the O-H bond dissociation energies for these alcohols.

INTRODUCTION

Alkoxide radicals have enjoyed much study as a result of their importance in atmospheric chemistry and also because of their fundamental significance in organic chemistry. This has been especially true for the methoxy and ethoxy radicals; indeed their anion photoelectron spectra alone have been measured on four and three occasions respectively.[1-6] Numerous, hundreds, of other spectroscopic and theoretical studies have been focused on these smaller alkoxides. Comparatively fewer studies have been done on their larger counterparts, especially the 1-alkoxides. Photoelectron and photodetachment studies of higher alkoxides have focused on other isomers, 2-propoxy[2,4], t-butoxy[2,4,7], n-pentoxy[7], as well as some cyclic analogues, c-propoxy, c-butoxy, and c-pentoxy[8,9]. Recently, however, laser induced fluorescence (LIF) and dispersed fluorescence spectra of the 1-alkoxides through n = 10 have been collected[10-19] and a few theoretical studies have calculated electron affinities and simulated photoelectron spectra of the linear alkoxides.[20-23]

Of no less importance, the measurement of the electron affinities of the alkoxides allows for the calculation of O-H bond dissociation energies (BDE's) of the corresponding alcohol; this is done via a thermochemical cycle presented in the discussion below using the gas phase acidities of the alcohol of interest. The measurement of gas phase acidities of the linear alcohols has also occupied some space in the scientific literature especially after the discovery that the gas phase acidities of these alcohols runs exactly opposite to their solution phase acidities.[24-33] Bond dissociation energies for the smaller alcohols have also been measured directly or calculated via this thermochemical cycle.[1,4,31,34] Accurate bond dissociation energies are required to model

combustion processes of alcohols which brings us full circle back to the importance of the alkoxide radicals in atmospheric chemistry.

Here we present our photoelectron spectra (PES) of the linear, 1-alkoxides, $C_nH_{2n+1}O^-$, where n = 1-9. We extract VDE's and EA's from our spectra and where applicable peak positions and splittings are provided. Comparisons to the earlier work of Lineberger and Neumark[1-6] on the smaller alkoxides in this series, n = 1-3 are made to anchor our work. We focus our discussion on three main points: 1) the overall monotonic increase in electron affinities over the entire series of spectra, 2) a closer look at the n=3 and n=4 alkoxides as for 1-propoxy we are able to see a new peak relative to the earlier work of Lineberger[2] and the new PES of 1-butoxy is the largest in the series to retain some vibrational structure in its spectrum, and 3) the calculation of the O-H BDE's using the anion thermochemical cycle.

EXPERIMENTAL METHODS

Negative ion photoelectron spectroscopy was used to measure the electron affinities and vertical detachment energies of several alkoxide radicals and their anions. Anion photoelectron spectroscopy is conducted by crossing a mass-selected beam of negative ions with a fixed-frequency photon beam and energy-analyzing the resultant photodetached electrons. The photodetachment process is governed by the relationship,

$$h\nu = \text{EBE} + \text{EKE} \qquad (1)$$

where $h\nu$ is the photon energy, EBE is the electron binding energy, and EKE is the electron kinetic energy. Essentially, the photon energy is sub-divided into the transition energy needed to take the anion to a particular vibronic state of its neutral counterpart,

i.e., EBE, and the kinetic energy of the electron, i.e., EKE. Figure 3.1 illustrates the energetics of photodetachment transitions. Since photodetachment is a fast process, the essentially instantaneous Franck-Condon overlap of anion and neutral wavefunctions is reflected in the vertical detachment energy, VDE. When the structures of the anion, X^-, and its corresponding neutral, X are different (as in Figure 3.1), the VDE is the EBE of the maxima in the broadened photoelectron spectral profile, and as such, it is a well-defined quantity.

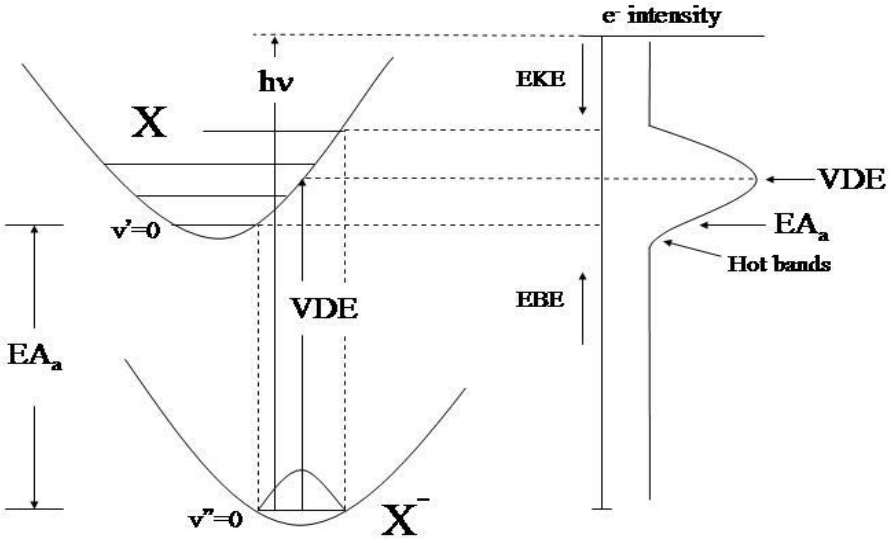

Figure 3.1. Schematic diagram of the energetics of the photodetachment process, $X^- + h\nu \rightarrow X + e^-$, defining EA_a and VDE.

When there is Franck-Condon overlap between the lowest vibrational level of the anion (v″) and the lowest vibrational level its corresponding neutral (v′), the photoelectron spectrum carries information about the adiabatic (thermodynamic) electron

affinity of the neutral species. When the spectral profile is vibrationally resolved, an assignment of the spectrum can identify the v″=0 → v′=0 transition. For this transition, its EBE value is equal to the adiabatic electron affinity, EA_a. When the profile is unresolved, however, the determination of EA_a is more approximate. If the anion were to be cold, i.e., if only v″=0 were occupied, then the low EBE threshold value of the spectrum would equal the EA_a value. But since anions are generated with finite internal temperatures, the first few vibrational levels of anions may also occupied, leading to some degree of photoelectron intensity at EBE values less than that corresponding to the EA_a, i.e., hot bands. Thus, in order to extract reasonable estimates of EA_a values from unresolved photoelectron spectral profiles (bands), we have performed Franck-Condon fittings of our spectra.

The apparatus consists of a source for generating anions, a magnetic sector for mass analysis and mass selection, and argon ion laser operated intra-cavity as the photon source, and a hemispherical electron energy analyzer. The mass analyzer/selector has a mass resolution of ~400, and the electron energy analyzer has a resolution of 30 meV. All photoelectron spectra reported here were recorded with 2.540 eV photons and calibrated against the photoelectron spectrum of O^-.[35] Our apparatus has been described previously.[36]

Selected alkoxide anions were generated in a supersonic expansion, nozzle-ion source which was biased at -500 V. Samples of the alcohols of interest were placed inside the stagnation chamber of the source and heated to temperatures ranging between 30-120°C in order to partially vaporize them. The resulting vapor was then co-expanded with argon (2-3 psig) through a 50 μm orifice into vacuum. Negative ions were formed

by injecting electrons from a biased filament into the expanding jet, where a microplasma was formed with the help of an external magnetic field. Negative ions were then extracted into the beam-line of the apparatus and subsequently mass-selected so that the anions of interest could be photodetached.

RESULTS

The photoelectron spectra of the linear $C_nH_{2n+1}O^-$ alkoxides where n = 1-9 are presented below in Figure 3.2. The first three spectra have been reported in the literature before[1-6] but are presented here to show the progression of the series of alkoxides in its entirety. The first of the new photoelectron spectra, that of $C_4H_9O^-$, shows two definitive peaks in the photoelectron spectrum while spectra of subsequent alkoxides show a single, broad band that moves to progressively higher binding energies as carbon chain length increases. Note that there is a monotonic increase in electron binding energies as one progressively lengthens the alkane tail via the addition of $-CH_2-$ groups. This observation can be quantified primarily using the EA's and VDE's given in Table 3.1. The extraction of these values from the photoelectron spectra required some care particularly for the larger alkoxides as their spectra are unresolved, thus, Franck-Condon fittings were done using the PESCAL 2010 program from Ervin and Lineberger.[37] These fittings are included in Figure 3.2 in the insets next to their respective PES.

Table 3.1. [1]EA's were assigned using Franck Condon fittings as a guide. [2] ΔEA's are the change in EA between adjacent (in terms of n) alkoxides. [3]EA's in kJ/mol will be used in thermochemical calculations presented in Table 3.4. [4]VDE's were found by fitting a Gaussian function to the photoelectron spectra after they were cropped below the FWHM line. [5]ΔVDE's are tabulated similarly to ΔEA's.

Species	EA (eV)[1]	ΔEA (eV)[2]	EA (kJ/mol)[3]	VDE (eV)[4]	ΔVDE (eV)[5]
CH_3O^-	1.578 ± 0.02	--	152 ± 2	1.578	--
$C_2H_5O^-$	1.710 ± 0.02	0.133	165 ± 2	1.755	0.178
$C_3H_7O^-$	1.781 ± 0.02	0.071	172 ± 2	1.921	0.166
$C_4H_9O^-$	1.849 ± 0.02	0.068	178 ± 2	1.920	-0.001
$C_5H_{11}O^-$	1.88 ± 0.05	0.03	181 ± 5	1.944	0.024
$C_6H_{13}O^-$	1.90 ± 0.05	0.02	183 ± 5	1.976	0.032
$C_7H_{15}O^-$	1.92 ± 0.05	0.02	185 ± 5	2.004	0.028
$C_8H_{17}O^-$	1.95 ± 0.05	0.03	188 ± 5	2.031	0.027
$C_9H_{19}O^-$	1.98 ± 0.05	0.03	191 ± 5	2.095	0.064

Great care was taken in the assignment of electron affinities; for the first three alkoxides we were able to compare our spectra with multiple points of reference to the literature. We see that our n = 1-3 photoelectron spectra share the same profile as previously recorded spectra provided differences in resolution are taken into account. Secondly, the electron affinities we find for these three alkoxides are in excellent agreement with those reported by Lineberger and Neumark.[1-6] Finally, these electron affinities are confirmed through FC fittings. These three provide the ground work for assignments of electron affinities for the larger alkoxides. We use the same methodology and extend it to the new systems. While there are no literature PES for these specific isomers of the n = 4-9 alkoxides we are able to make comparisons to other isomers (see below). The electron affinities for the n = 5-9 alkoxides should be expected to have larger error bars associated

with them as a result of the spectra being unresolved. Figure 3.3 plots VDE and EA vs. carbon chain length which shows graphically what can be seen on inspection of the PES which again is the largely monotonic increase in electron binding energy as chain length increases.

DISCUSSION

Comparison to earlier photoelectron studies. Methoxy and Ethoxy alkoxides. The photoelectron spectra of the methoxy and ethoxy anions have each been taken on several previous occasions, each time with higher resolution.[1-6] Our photoelectron spectra have comparatively lower resolution than these latest studies and thus are presented to show the progression of the entire series of n-alkoxides and as a point of comparison to the literature. That being said our photoelectron spectra of these ions broadly match the spectra of Lineberger and Neumark; because of the higher resolution of their spectra they are able to resolve two peaks where often we see only one broader peak, however, the EA and overall peak spacings are in agreement. Peak positions and splittings in the photoelectron spectra of the n = 1 to 4 alkoxides are summarized in Table 3.2; the EA's of the larger alkoxides are also given again for comparison.

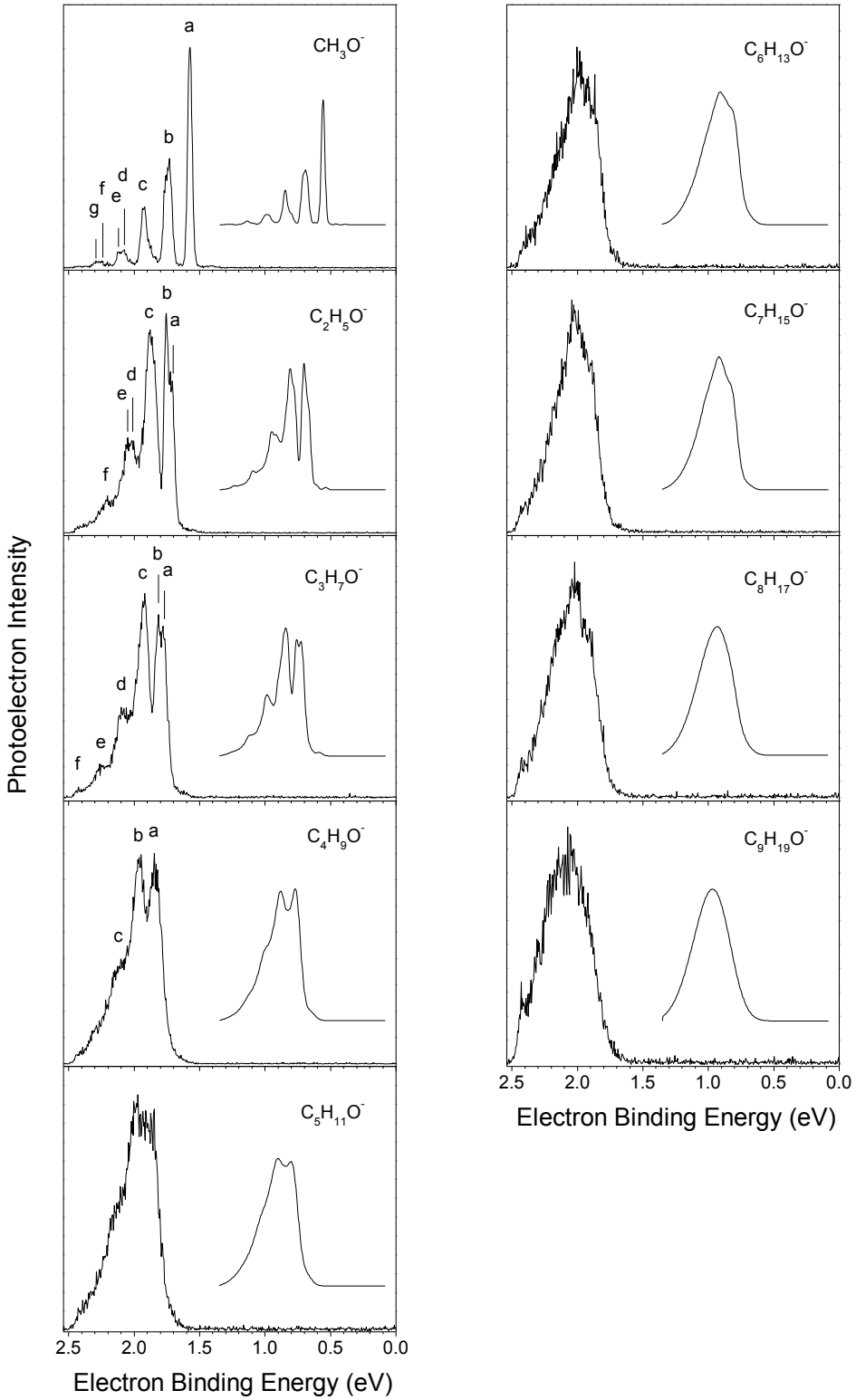

Figure 3.2. Photoelectron spectra of the linear $C_nH_{2n+1}O^-$ alkoxides where n = 1-9 taken with 2.540 eV photons. Franck-Condon fittings are shown in the insets.

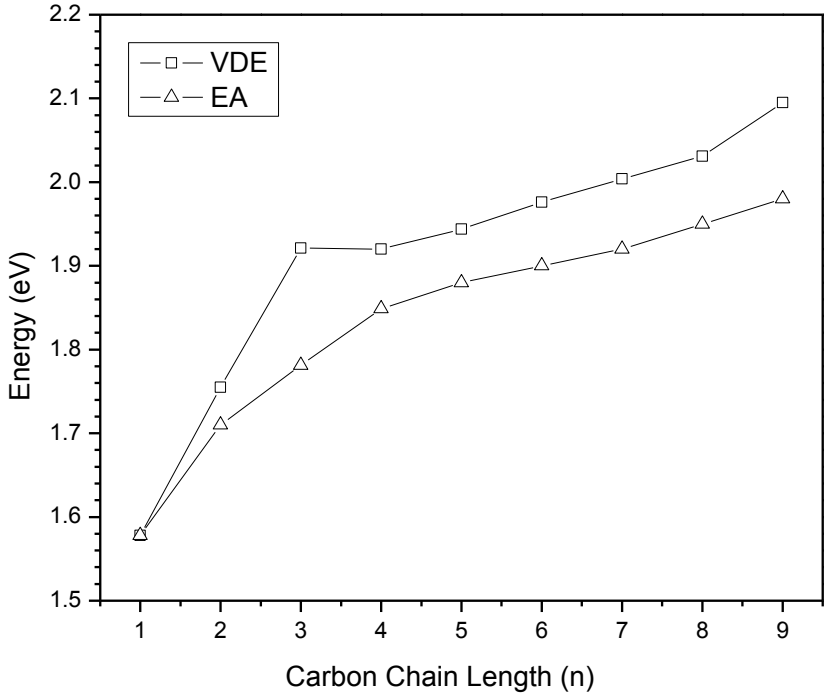

Figure 3.3. VDE's and EA's plotted as a function of the length of the alkane tails of the alkoxides, $C_nH_{2n+1}O^-$. One can see a roughly monotonic increase in these values. This plot essentially summarizes graphically what is presented numerically in Table 3.1.

1-Propoxy. As carbon chain length increases one needs to be cognizant that there are not only two isomers of propoxy, 1-propoxy and 2-propoxy (isopropoxy) separable of course, but also 2 conformers of 1-propoxy, identified as the trans, *T* conformer (C_1-symmetry) and the gauche, *G* conformer (C_s-symmetry) by Miller and coworkers.[16] These conformers are both present in the fluorescence studies of Miller; they are separated in energy by only 20 cm^{-1}. Here we assume both will be present and that our photoelectron spectrum of 1-propoxy will have contributions from both conformers.

Table 3.2. Summary of peak positions and splitting for labeled spectra (n = 1-4); EA's for the larger (n = 5-9) alkoxides are again included for comparison.

Species	Peak Label	Position (eV)	Shift from origin (eV)	Shift from origin (cm^{-1})
CH_3O^-	a, origin	1.578		
	B	1.733	0.155	1250
	C	1.923	0.345	2780
	D	2.077	0.499	4020
	E	2.117	0.539	4350
	F	2.243	0.665	5360
	G	2.293	0.715	5770
$C_2H_5O^-$	a, origin	1.710		
	B	1.755	0.045	360
	C	1.880	0.170	1440
	D	2.020	0.310	2500
	E	2.050	0.340	2740
	F	2.205	0.495	3990
$C_3H_7O^-$	a, origin	1.781		
	B	1.816	0.035	280
	C	1.921	0.140	1130
	D	2.101	0.320	2580
	E	2.256	0.475	3830
	F	2.426	0.645	5200
$C_4H_9O^-$	a, origin	1.849		
	B	1.964	0.115	930
	C	2.104	0.155	1250
$C_5H_{11}O^-$		1.88		
$C_6H_{13}O^-$		1.90		
$C_7H_{15}O^-$		1.92		
$C_8H_{17}O^-$		1.95		
$C_9H_{19}O^-$		1.98		

Multiple conformers will also necessarily be the case for the larger alkoxides as discussed below.

Of the two isomers 2-propoxy is certainly the better studied; to our knowledge the photoelectron spectrum of the 1-propoxy anion has been collected on only one previous occasion by Lineberger and coworkers.[2] Here our PES of this anion has somewhat improved resolution and thus we are able to just resolve two additional peaks, six in total relative to that of the previous study with four features. We see what had been the origin transition at 1.789 eV in the earlier spectrum split into two peaks, 280 cm^{-1} apart labeled *a* and *b* at 1.781 eV and 1.816 eV respectively; thus our assigned EA is, as expected, a bit smaller than that reported by Lineberger and coworkers. Peak positions and spacings are comparable within experimental error to those reported by Lineberger with the exception noted above.

Recent dispersed fluorescence measurements from Miller,[16] allows for two possible assignments for peak b (observed in our spectra 280 cm^{-1} above the origin). The first possible assignment is to the 0_0^0 $\tilde{A} \leftarrow \tilde{X}$ transition, between the ground electronic state of the anion and the first low-lying excited electronic state of the radical. Miller reports the $\tilde{A}$-$\tilde{X}$ energy separation in the radical to be 321 cm^{-1} and 214 cm^{-1} for the 1-propoxy *T* conformer and *G* conformer respectively. The second possible assignment of this peak is to the $\tilde{X} \leftarrow \tilde{X}\ 3_0^1$ vibrational mode, an in-plane CCO bend with a CCC bend contribution to this normal mode. Miller finds this transition at 274 cm^{-1}(*T*) and 302 cm^{-1} (*G*) above the vibrational ground state. We will make the case that we do see the first low-lying electronic state of the neutral for reasons that follow.

Lineberger,[4] in the case of ethoxy, was able to differentiate between anion electronic ground state to neutral electronic ground state transitions ($\tilde{X} \leftarrow \tilde{X}$) and anion electronic ground state to the first electronically excited state of the neutral ($\tilde{A} \leftarrow \tilde{X}$) using photoelectron angular distribution data. Ethoxy's first electronically excited state lies 360 cm^{-1} above the ground electronic state as seen in the angular distribution data has been collected by Lineberger. In the case of 1-propoxy we are unable to conclusively differentiate between the two above possibilities but we think it is likely that we do observe the first electronically excited state of the radical in analogy to the ethoxy radical. One may wonder that we do not make the comparison to 2-propoxy. Lineberger identifies the transition to the first electronically excited state of the radical 1225 cm^{-1} above the origin. This finding is at odds with Miller's later finding of 68 cm^{-1} for the $\tilde{A}$-$\tilde{X}$ energy separation which the calculations of Yarkony confirms.[16,22] Miller finds low-lying electronic excited states of the radicals of 1-propoxy, 2-propoxy, 1-butoxy, and 2-butoxy, thus we are reassured that this transition is seen in our 1-propoxy spectrum and likely our 1-butoxy spectrum though unresolved.

Without photoelectron angular distribution data specifically for 1-propoxy we are unable to decide which peaks can be ascribed to transitions to the ground electronic state of the radical versus the first low lying excited electronic state of the propoxy radical; making definitive assignments is further impeded by the assumed presence of both *T* and *G* conformers.

1-Butoxy and the Higher Alkoxides (n = 4-9). This is the first time the PES of the 1-butoxy anion has been taken; this is also the last alkoxide PES in the series to show any structure in its spectrum and as such its electron affinity, 1.849 eV is still readily

assigned (confirmed also via the FC fitting). The EA we have measured for 1-butoxy is comparable to an experimentally reported EA of Williams and Hamill[38] of 1.90 ± 0.1 eV and to a theoretical value from Li and coworkers of 1.83 eV.[23] The EA of 1-butoxy sits in between that of 1-propoxy, 1.789 ± 0.033 eV and t-butoxy, 1.909 ± 0.004 eV.[2,4] There are 4 isomers of butoxy, 1-butoxy, 2-butoxy (chiral R,S), s-butoxy, and t-butoxy; to our knowledge only the PES of the t-butoxy anion has been taken thus far by Lineberger; the photodetachment spectrum of this ion was taken by Brauman.[4,7]

As mentioned above in the discussion of 1-propoxy multiple conformers may contribute to our photoelectron spectrum of 1-butoxy. Miller[16] identifies five unique conformers of 1-butoxy labeled as T_1T_2, an all trans conformer, G_1G_2, and $G_1'G_2$, two all gauche conformers and G_1T_2 and T_1G_2. In his fluorescence spectra not every conformer is observed only the T_1T_2, G_1T_2 and T_1G_2 conformers are seen; he speculates that this is due to energy considerations and conversion of the all gauche conformations to the hydroxyl butyl radical. Thus we anticipate that our spectrum will include contributions from at least the three conformers Miller observes. We also note that because our source conditions are hotter than those reported by Miller we would expect to have higher energy conformations populated and so we expect our spectra to have contributions from at minimum the number of conformers seen in the fluorescence experiments if not more. As carbon chain length increases the number of possible conformers increases dramatically to 14 for 1-pentoxy, 41 for 1-hexoxy, 122 for 1-heptoxy, 365 for 1-octoxy, and 1094 for 1-nonoxy, however, at least in Miller's fluorescence spectra of the n = 3-7 alkoxides the number of conformers that he observes is still a reasonably small number,

1-hexoxy and 1-heptoxy are dominated by only two conformers, the all trans conformers ($T_1T_2...T_{n-2}$) and the ($G_1T_2...T_{n-2}$) conformer.[16-18]

In the spectrum of $C_4H_9O^-$, peak *b* appears at 1.964 eV giving a splitting of 0.115 eV or 930 cm^{-1}. As was the case in 1-propoxy assigning this transition is precarious owing to the possibility of a low-lying excited electronic state in the neutral as well as contributions from at minimum three conformers.

Photoelectron spectra of 1-pentoxy through 1-nonoxy are also presented for the first time; please see Table 3.1 for EA and VDE assignments for these alkoxides. Comparatively few studies have been done on these larger alkoxides; Brauman and coworkers have taken the photodetachment spectrum of neo-pentoxy[7] another of the many isomers of $C_5H_{11}O$. Brauman reports the EA of neo-pentoxy as 1.93 ± 0.06 eV which, not surprisingly, is similar to our reported EA of n-pentoxy of 1.88 eV. The photodetachment spectra of the linear $C_nH_{2n+1}S^-$ (n = 1-5) have been taken and their EA's assigned by Brauman and coworkers.[39] Theoretical calculations have also tabulated EA's for these alkylthio radicals[40] each of which has a higher EA as compared to the alkoxide radicals but follow the same overall trend with a monotonic increase to higher binding energy as the carbon chain length increases.

Thus far it seems to be the overall case that the electron affinities for the 1-alkoxides are lower than those of their respective structural isomers. Additionally, it also seems to be the case that these 1-alkoxides share more in common with one another than with their respective isomers; we have generally found it more helpful to make comparisons between 1-propoxy and ethoxy or between 1-butoxy and 1-propoxy than to compare 1-propoxy to 2-propoxy or to compare 1-butoxy to 2-butoxy or t-butoxy.

Thermochemistry. The electron affinities extracted from our photoelectron spectra when combined with gas-phase acidities available in the NIST database[41-43] afford the O-H bond dissociation energies (BDE's) of each alcohol via the following cycle:

$$RO - H \rightarrow RO + H \qquad DH^o(RO - H)$$

$$RO + H \rightarrow RO + H^+ + e^- \qquad IE(H)$$

$$RO + H^+ + e^- \rightarrow RO^- + H^+ \qquad -EA(RO)$$

$$RO - H \rightarrow RO^- + H^+ \qquad \Delta H^o_{acid}$$

Which yields:

$$\Delta H^o_{acid} = DH^o(RO - H) + IE(H) - EA(RO) \quad \text{or} \tag{2}$$

$$DH^o(RO - H) = \Delta H^o_{acid} - IE(H) + EA(RO) \tag{3}$$

The ionization energy for hydrogen is 1312.05 kJ (13.58944 eV). Enthalpies of formation of alkoxide radicals and their anions can also be found via equations 4 and 5 below given $\Delta H^o_f(H)$ = 217.998 kJ/mol and using enthalpies of formation of the alcohols, $\Delta H^o_f(ROH)$, that are again readily available in the NIST database.

$$\Delta H^o_f(RO) = DH^o(RO - H) + \Delta H^o_f(ROH) - \Delta H^o_f(H) \tag{4}$$

$$\Delta H^o_f(RO^-) = \Delta H^o_f(RO) - EA(RO) \tag{5}$$

Table 3.3 presents four sets of acidities for these alcohols all of which can be found in the NIST database. We then use each of these four sets to calculate four sets of

BDE's presented in Table 3.4. Finally, Table 3.5 presents the sets of enthalpies of formation of the neutral radical, $\Delta H_f^o(RO)$ and the anion, $\Delta H_f^o(RO^-)$. The enthalpies of formation of the alcohols, $\Delta H_f^o(ROH)$, used to calculate the enthalpies in Table 3.5 are those found in the NIST database. The errors associated with the ionization energy and enthalpy of formation of hydrogen, are negligibly small relative to errors associated with the acidities and electron affinities of the alcohols and alkoxides respectively.

Some commentary on the values in Tables 3.3 and 3.4; errors in BDE's and the enthalpies of formation of the alkoxide radicals and anions arise primarily through the uncertainty in the gas phase acidities of their corresponding alcohols. Measurements by Ervin and coworkers[31] using threshold collision induced dissociation (TCID) of the acidities of methanol and ethanol have reduced the errors associated with these acidities. Other acidities are those of Haas and Harrison,[29] Boand and coworkers,[27] and Bartmess and coworkers[25,26,30] as designated in Table 3.3. Using the acidities from each of these

Table 3.3. ΔH^o_{acid}'s taken from the NIST Database. All values are in units of kJ/mol.

Species	ΔH^o_{acid} (ROH)[1]	ΔH^o_{acid} (ROH)[2,3]	ΔH^o_{acid} (ROH)[4]	ΔH^o_{acid} (ROH)[5]
CH_3OH	1599 ± 3	[2]1592 ± 9	1595 ± 8	
CH_3CH_2OH	1586 ± 0.4	[2]1579 ± 9	1582 ± 8	
$CH_3(CH_2)_2OH$		[2]1573 ± 9	1574 ± 8	
$CH_3(CH_2)_3OH$		[3]1571 ± 9	1570 ± 8	1569 ± 12
$CH_3(CH_2)_4OH$		[3]1565 ± 9	1568 ± 8	1564 ± 12
$CH_3(CH_2)_5OH$		[3]1565 ± 9	1565 ± 9	1561 ± 12
$CH_3(CH_2)_6OH$		[3]1567 ± 9	1564 ± 13	1559 ± 12
$CH_3(CH_2)_7OH$		[3]1566 ± 9	1563 ± 13	1556 ± 12
$CH_3(CH_2)_8OH$		[3]1567 ± 9	1561 ± 13	1553 ± 12

[1]DeTuri and Ervin, see reference 31.
[2,3] Bartmess, Scott, and McIver, reference 25 and Higgins and Bartmess, reference 30.
[4]Haas and Harrison, reference 29.
[5]Boand, Houriet, and Gaumann, reference 27.

Table 3.4. BDE's calculated using our EA's and the acidities presented in Table 3.3 via the themochemical cycle presented in the discussion. All values are in units of kJ/mol.

Species	$DH^o(RO\text{-}H)$[1]	$DH^o(RO\text{-}H)$[2,3]	$DH^o(RO\text{-}H)$[4]	$DH^o(RO\text{-}H)$[5]
CH_3OH	439 ± 4	432 ± 9	435 ± 8	
CH_3CH_2OH	439 ± 2	432 ± 9	435 ± 8	
$CH_3(CH_2)_2OH$		433 ± 9	434 ± 8	
$CH_3(CH_2)_3OH$		437 ± 9	436 ± 8	435 ± 12
$CH_3(CH_2)_4OH$		434 ± 10	437 ± 9	433 ± 13
$CH_3(CH_2)_5OH$		436 ± 10	436 ± 10	432 ± 13
$CH_3(CH_2)_6OH$		440 ± 10	437 ± 14	432 ± 13
$CH_3(CH_2)_7OH$		442 ± 10	439 ± 14	432 ± 13
$CH_3(CH_2)_8OH$		446 ± 10	440 ± 14	432 ± 13

[1] Acidities from DeTuri and Ervin.
[2,3] from Bartmess, Scott, and McIver, reference 25 and Higgins and Bartmess, reference 30.
[4]Haas and Harrison, reference 29.
[5]Boand, Houriet, and Gaumann, reference 27.

groups produces the BDE's presented in Table 3.4. The greatest disparity is found in the BDE of 1-nonanol using the acidity from Boand's work which produces a BDE of 432 kJ/mol, 12 kJ/mol smaller than that using Harrison's acidity value, yet still within experimental error. The BDE for 1-propanol, despite being somewhat smaller than the others in the series is in good agreement with the BDE from Zhang's photodissociation experiments of 433 ± 2 kJ/mol.[34]

Table 3.5. ΔH^{o}_{f} (RO)'s, and ΔH^{o}_{f} (RO^{-})'s are calculated as described in the text using BDE's from Table 3.4 and once again our EA's. All values are in units of kJ/mol.

Species	ΔH^{o}_{f} $(RO)^{1}$	2,3	4	5	ΔH^{o}_{f} $(RO^{-})^{1}$	2,3	4	5
CH_3OH	20 ± 4	13 ± 9	16 ± 8		-132 ± 2	-139 ± 9	-136 ± 8	
CH_3CH_2OH	-14 ± 2	-21 ± 9	-18 ± 8		-179 ± 5	-186 ± 9	-183 ± 8	
$CH_3(CH_2)_2OH$		-40 ± 9	-39 ± 8			-212 ± 9	-211 ± 8	
$CH_3(CH_2)_3OH$		-56 ± 9	-57 ± 8	-58 ± 12		-234 ± 9	-235 ± 8	-236 ± 12
$CH_3(CH_2)_4OH$		-79 ± 10	-76 ± 9	-80 ± 13		-260 ± 11	-257 ± 10	-261 ± 14
$CH_3(CH_2)_5OH$		-98 ± 10	-98 ± 10	-102 ± 13		-281 ± 11	-281 ± 11	-285 ± 14
$CH_3(CH_2)_6OH$		-115 ± 10	-118 ± 14	-123 ± 13		-300 ± 11	-303 ± 15	-308 ± 14
$CH_3(CH_2)_7OH$		-132 ± 10	-135 ± 14	-142 ± 13		-320 ± 11	-323 ± 15	-330 ± 14
$CH_3(CH_2)_8OH$		-149 ± 10	-154 ± 14	-163 ± 13		-340 ± 11	-345 ± 15	-354 ± 14

[1] Acidities from DeTuri and Ervin.
[2,3]Bartmess, Scott, and McIver, and Higgins and Bartmess.
[4]Haas and Harrison.
[5]Boand, Houriet, and Gaumann.

Nevertheless, it would be expected that the BDEs of the linear alcohols longer than C_3 or so should be relatively constant. There is no known effect that a distant alkyl group might exert to alter these. Thus the values based on acidities obtained from the kinetic method[27,29] would appear more likely, per Table 3.4. However, the kinetic method has been shown to yield acidities appreciably different than those obtained from the equilibrium method, when there are strong α,ω interactions between the ionic head of a chain and a distal group, such as in 1,n-diols.[44] The acidities measured via the equilibrium method[30] for the long chain alcohols show a distinct leveling off, and even slight reversal, of the acidity-strengthening effect. This is in contrast to the monotonic

trend of the detachment energies of the alkoxides reported here. The thermochemical result from this, via Eqn 3, is the apparent strengthening of the BDE with increasing alkyl size. There are several possible explanations for this apparent anomaly. The equilibrium method measures the free energy of acidity, and the conversion to enthalpies involves the assumption of a near-constant entropy of acidity for this series. It may be that restricted motion in the longer alkoxides, due to the polarizability interaction of the anionic head with the tail, reduces the entropy of acidity from the assumed small alcohol value of ca. 97 J/mol-K; a value of 77 J/mol-K for the C_8 alcohol would make the derived BDEs relatively constant. Alternately, it may be that the multiple conformations of the long chain alkoxides result in more complex photodetachment spectra than usual, from which the adiabatic EA values is not simply derived. The most stable coiled alkoxide on vertical detachment would give rise to a coiled alkoxy radical, which is higher in energy than the likely most stable all-anti conformation, resulting in a greater-than-thermochemical VDE. The all-anti alkoxide which would give the most stable alkoxy radical, is not the most stable anion. We are exploring these point computationally at present.

REFERENCES

1. Engelking, P.C.; Ellison, G. B.; Lineberger, W. C. *J. Chem. Phys*. **1978**, *69*, 1826.
2. Ellison, G. B.; Engelking, P. C.; Lineberger, W. C. *J. Phys. Chem*. **1982**, *86*, 4873.
3. Osborn, D. L.; Leahy, D. J.; Kim, E. H.; de Beer, E.; Neumark, D. M. *Chem. Phys. Lett*. **1998**, *292*, 651.
4. Raymond, T. M.; Davico, G. E.; Schwartz, R. L.; Lineberger, W. C. *J. Chem. Phys*. **2000**, *112*, 1158.
5. Nee, M. J.; Osterwalder, A.; Zhou, J.; Neumark, D. M. *J. Chem. Phys*. **2006**, *125*, 014306.
6. Neumark, D. M. *J. Phys. Chem*. **2008**, *112*, 13287.
7. Janousek, B. K.; Zimmerman, A. H.; Reed, K. J.; Brauman, J. I. *J. Am. Chem. Soc*. **1978**, *100*, 6142.
8. Alconcel, L. S.; Deyerl, H.-J.; Continetti, R. E. *J. Am. Chem. Soc*. **2001**, *123*, 12675.
9. Alconcel, L. S.; Continetti, R. E. *Chem. Phys. Lett*. **2002**, *366*, 642.
10. Geers, A.; Kappert, J.; Temps, F.; Wiebrecht, J. E. *J. Chem. Phys*. **1993**, *99*, 2271.
11. Liu, J.; Chen, M.-W.; Melnik, D.; Yi, J. T.; Miller, T. A. *J. Chem. Phys*. **2009**, *130*, 074302.
12. Inoue, G.; Okuda, M.; Akimoto, H. *J. Chem. Phys*. **1981**, *75*, 2060.

13. Tan, X. Q.; Williamson, J. M.; Foster, S. C.; Miller, T. A. *J. Phys. Chem*. **1993**, *97*, 9311.

14. Temps, F.; Dai, H. L.; Field, R. W. (Eds.), Molecular Spectroscopy and Dynamics by Stimulated Emission Pumping, World Scientific, Singapore, 1995, p. 375.

15. Zhu, X.; Kamal, M. M.; Misra, P. *Pure Appl. Opt*. **1996**, *5*, 1021.

16. Jin, J.; Sioutis, I.; Tarczay, G.; Gopalakrishnan, S.; Bezant, A.; Miller, T. A. *J. Chem. Phys*. **2004**, *121*, 11780.

17. Gopalakrishnan, S.; Zu, L.; Miller, T. A. *J. Phys. Chem. A* **2003**, *107*, 5189.

18. Zu, L.; Liu, J.; Gopalakrishnan, S.; Miller, T. A. *Can. J. Chem*. **2004**, *82*, 854.

19. Carter, C. C.; Gopalakrishnan, S.; Atwell, J. R.; Miller, T. A. *J. Phys. Chem. A* **2001**, *105*, 2925.

20. Young Jr., R. A.; Yarkony, D. R. *J. Chem. Phys.* ***2006****, 125,* 234301.

21. Dillon, J. J.; Yarkony, D. R. *J. Chem. Phys*. **2009**, *131*, 134303.

22. Dillon, J. J.; Yarkony, D. R. *J. Chem. Phys*. **2009**, *130*, 154312.

23. Gao, A.; Jiao, Z.; Li, A. *Theochem*. **2008**, *848*, 40.

24. Brauman, J. I.; Blair, L. K. *J. Am. Chem. Soc*. **1968**, *90*, 6561.

25. Bartmess, J. E.; Scott, J. A.; R.T. McIver, Jr., *J. Am. Chem. Soc*. **1979**, *101*, 6046.

26. Bartmess, J. E.; Scott, J. A.; McIver, Jr., R. T. *J. Am. Chem. Soc*. **1979**, *101*, 6056.

27. Boand, G.; Houriet, R.; Gaumann, T. *J. Am. Chem. Soc*. **1983**, *105*, 2203.

28. Majumdar, T. K.; Clairet, F.; Tabet, J.-C.; Cooks, R. G. *J. Am. Chem. Soc*. **1992**, *114*, 2897.

29. Haas, M. J.; Harrison, A. G. *Int. J. Mass Spec. Ion Proc*. **1993**, *124*, 115.

30. Higgins, P. R.; Bartmess, J. E. *Int. J. Mass Spec. Ion Proc*. **1998**, *175*, 71.

31. DeTuri, V. F.; Ervin, K. M. *J. Phys. Chem*. **1999**, *103*, 6911.

32. Bartmess, J. E.; Pittman, J. L.; Aeschleman, J. A.; Deakyne, C. A. *Int. J. Mass Spec*. **2000**, *195*, 215.

33. Ervin, K. M.; DeTuri, V. F. *J. Phys. Chem. A* **2002**, *106*, 9947.

34. Zhou, W.; Yuan, Y.; Zhang, J. *J. Chem. Phys*. **2003**, *119*, 7179.

35. Neumark, D. M.; Lykke, K. R.; Andersen, T.; Lineberger, W. C. *Physical Review A: Atomic, Molecular, and Optical Physics*. **1985**, *32*, 1890.

36. Coe, J. V.; Snodgrass, J. T.; Freidhoff, C. B.; McHugh, K. M.; Bowen, K. H. *J. Chem. Phys.* **1986**, *84*, 618.

37. Ervin, K. M.; Ho, J.; Lineberger, W. C. *J. Phys. Chem*. **1988**, *92*, 5405.

38. **Williams, J. M.; Hamill, W. H. *J. Chem. Phys*. 1968**, *49*, 4467.

39. Janousek, B. K.; Reed, K. J., Brauman, J. I. *J. Am. Chem. Soc*. **1980**, *102*, 1025.

40. Gao, A.; Liang, X.; Li, L.; Cui, J. *J. Mol. Model*. **2013**, *19*, 3225.

41. Afeefy, H. Y.; Liebman, J. F.; Stein, S. E. Neutral Thermochemical Data in ***NIST Chemistry WebBook, NIST Standard Reference Database Number 69***, Linstrom, P. J.; Mallard, W. G. Eds.; National Institute of Standards and Technology, Gaithersburg MD, 20899, http://webbook.nist.gov, (retrieved May 31, 2013).

42. Burgess, D. R. Thermochemical Data in ***NIST Chemistry WebBook, NIST Standard Reference Database Number 69***; Linstrom, P. J.; Mallard, W. G. Eds.; National Institute of Standards and Technology, Gaithersburg MD, 20899, http://webbook.nist.gov, (retrieved May 31, 2013).

43. Bartmess, J. E. Negative Ion Energetics Data in ***NIST Chemistry WebBook, NIST Standard Reference Database Number 69***; Linstrom, P. J.; Mallard, W. G., Eds.; National Institute of Standards and Technology, Gaithersburg MD, 20899, http://webbook.nist.gov, (retrieved May 31, 2013).

44. Crowder, C. A.; Bartmess, J. E. *J. Am. Soc. Mass Spectrom*. **1993**, *4*, 723.

CHAPTER 4

Section 4.1. Photoelectron Spectroscopy of the Molecular Anions, ZrO^-, HfO^-, $HfHO^-$, and HfO_2H^-

Section 4.2. The Reaction Rates of O_2 with Closed-Shell and Open-Shell Al_x^- and Ga_x^- Clusters Under Single Collision Conditions: Experimental and Theoretical Investigations Toward a Generally Valid Model for the Hindered Reactions of O_2 with Metal Atom Clusters

Our groups continued interest in metal clusters, metal oxide clusters, and their reactivity is presented in this chapter.

Transition metal oxides have gained technological importance over recent years due to applications in chemical catalytic processes, nanotechnology, materials science, and medicine. In fact, these clusters may be used as building blocks to bridge the gap between small molecules and the design of extended solids, offering a variety of tunable properties possibilities. Yet, to know how the bulk material reacts, it is of importance to better understand the structural and chemical properties of the transition metal oxides on the molecular scale. Section **4.1** presents such an example with zirconium and hafnium oxides. Zirconium and hafnium are in the same column of the periodic table and from appearance their oxides should also be expected to exhibit similar physiochemical properties. However, as focused on in this section, ZrO^- and HfO^- show dissimilarities in their chemical properties.

The study of metal clusters also provides motivation towards use in cluster assembled materials.[1-3] Specifically our group and our collaborator Hansgeorg

Schnöckel, have focused primarily on the Al_{13}^-cluster. From previous studies,[4] Al_{13}^- is one of a specific type electronic structure which exhibits unique stability and therefore termed as "magic." Magic clusters were first recognized for sodium clusters,[5-6] Na_n^- and arose from applying the jellium model to simple metals with electron numbers n= 2, 8, 20, 40, 70, etc.[7,8] The unusual properties of Al_{13}^- and its inertness to reactivity are contributed to its closed-shell structure with n=40 electrons. Thus in order to incorporate Al_{13}^- as a building block material, the reactivity and stability with respect to reactants of preference must be further studied.

Schnöckel and coworkers studied a series of Al_{13}^- reactivity which has included HCl,[9] Cl_2,[10,11] and O_2[12] as reactants. The reactivity trend of Al_n^- clusters has been known to have an odd/even effect where odd-numbered (closed-shell) clusters react significantly slower than even-numbered (open-shell) clusters.[13-15] For improved characterization of these reactions, section **4.2** continues with this collaborative work to better understand the inertness of metals toward oxygen, with applications towards characterization of bulk metallic surfaces. The surrounding clusters of Al_{13}^-, where Al_n^- n=9-14, are studied to quantify these odd/even properties. Gallium clusters of the same size Ga_n^- n=9-14 are also incorporated to compare metals of similar chemical properties would experience similar reactivity studies with O_2. These experimented were performed in the lab at Karlsruhe Institute of Technology (KIT), Germany under the advisement of Professor Hansgeorg Schnoeckel using their commercial FT-ICR mass spectrometer.

REFERENCES

1. Khanna, S. K.; Jena, P. *Phys. Rev. B* **1995**, *51*, 13705.
2. Hoshino, K.; Watanabe, K.; Konishi, Y.; Taguwa, T.; Nakajima, A.; Kaya, K. *Chem. Phys. Lett*. **1994**, *231*, 499.
3. Zheng, W.-J.; Thoms, O. C.; Lippa, T. P.; Xu, S.-J.; Bowen Jr., K. H. *Chem. Phys.* **2006**, *124* (14), 144304.
4. Bergeron, D. E.; Castleman, A. W. J.; Morisato, T.; Khanna, S. N. *Science* **2004**, *304*, 84.
5. Martin, T. P.; *Physics Reports* **1996**, *273*, 199.
6. Knight, W. D.; Clemenger, K.; de Heer, W. A.; Saunders, W. A.; Chou, M. Y.; Cohen, M. L. *Phys. Rev. Lett.* **1984**, *52*, 2141.
7. Brack, M. *Rev. Mod. Phys.* **1993**, *65*, 677.
8. de Heer, W. A.; *Rev. Mod. Phys.* **1993**, *65*, 611.
9. Burgert, R.; Stokes, S. T.; Bowen, K. H.; Schnöckel, H. *J. Am. Chem. Soc*. **2006**, *128*, 7904.
10. Burgert, R.; Schnöckel, H.; Olzmann, M.; Bowen, Jr., K. H. *Angew. Chem. Int. Edit*. **2006**, *45*, 1476.
11. Olzmann, M.; Burgert, R.; Schnöckel, H. *J. Chem. Phys*. **2009**, *131*, 174304.
12. Burgert, R.; Schnöckel, H.; Grubisic, A.; Li, X.; Stokes, S. T.; Bowen, K. H.; Ganteför, G.; Kiran, B.; Jena, P. *Science*, **2008**, *319*, 438.
13. Jarrold, M. F.; Bower, J. E. *Chem. Phys. Lett.* **1988**, *144*, 311.
14. Leuchtner, R. E.; Harms, A. C. Castleman, Jr., A. W. *J. Chem. Phys.* **1991**, *94*, 1093.
15. Hettich, R. L. *J. Am. Chem. Soc.* **1989**, *111*, 8582.

Section 4.1. Photoelectron Spectroscopy of the Molecular Anions, ZrO^-, HfO^-, $HfHO^-$, and HfO_2H^-

Xiang Li,[†] Weijun Zheng,[†] Angela Buonaugurio,[†] Allyson Buytendyk,[†] Kit Bowen[†]*

[†]*Departments of Chemistry and Materials Science, Johns Hopkins University, Baltimore, Maryland 21218, USA*

Krishnan Balasubramanian[§,‡,&]

[§]*College of Science, California State University, East Bay, Hayward, California 94542, USA*

[‡]*Chemistry and Material Science Directorate, Lawrence Livermore National Laboratory, Livermore, California 94550, USA*

[&]*Lawrence Berkeley National Laboratory, Berkeley, California 94720, USA*

ABSTRACT

Negative ion photoelectron spectra of ZrO^-, HfO^-, $HfHO^-$, and HfO_2H^- are reported. Even though zirconium and hafnium containing molecules typically exhibit similar chemistries, the negative ion photoelectron spectral profiles of ZrO^- and HfO^- are dramatically different from one another. By comparing these data with relevant theoretical and experimental studies, as well as by using insights drawn from atomic spectra, spin-orbit interactions, and relativistic effects, the photodetachment transitions in the spectra of ZrO^- and HfO^- were assigned. As a result, the electron affinities of ZrO and HfO were determined to be 1.26 ± 0.05 eV and 0.60 ± 0.05 eV, respectively. The anion photoelectron spectra of $HfHO^-$ and HfO_2H^- are similar to one another and their

structural connectivities are likely to be H–Hf–O^- and O–Hf–OH^-, respectively. The electron affinities of HfHO and HfO_2H are 1.70 ± 0.05 eV and 1.73 ± 0.05 eV, respectively.

*Corresponding author: email: kbowen@jhu.edu. Fax: +1 410 516 8420

INTRODUCTION

Transition metal oxides are technologically important be- cause of the roles they play in catalytic processes and in high temperature chemistry. While zirconium and hafnium are generally thought to have similar chemical properties, some of their oxides show dissimilarities. In particular, ZrO_2 and HfO_2 show significant differences,[1,2] which our previous work had attributed to subtle differences in their electronic structures.[3]

In the present work, we focus on the molecules, ZrO, HfO, HfHO, and HfO_2H and their anions. ZrO has been the subject of many spectroscopic investigations.[4-12] Based on both experiments and theoretical calculations,[13,14] the ground state of ZrO is generally thought to be $^1\Sigma^+$, although some calculations[15] found it to be $^3\Delta$. Kaledin et al.[5] have provided copious information on the electronic states of ZrO via wavelength-resolved fluorescence excitation studies. In addition, thermochemical and thermodynamic properties of ZrO have also been reported.[16,17] Furthermore, there have been two previous anion photoelectron studies of ZrO^-, with the more recent one suggesting that ZrO may mimic the chemistry of palladium.[18–20]

HfO has also been the subject of both spectroscopic and theoretical studies, these as in the case of ZrO also suggesting that its ground state is $^1\Sigma^+$.[6, 11, 21–23] Again, Kaledin et al.[21] measured the term energies of its electronic states. In addition, the thermodynamic properties of HfO,[16] as well as the lifetimes[24] and dipole moments[25] of some HfO excited states have also been studied.

Here, we report the anion photoelectron spectra of ZrO^-, HfO^-, $HfHO^-$, and HfO_2H^-. The photoelectron spectra of ZrO^- and HfO^- are quite different from each

other, suggesting significantly different electronic structures between these two, same-group transition metal monoxides. Information on the neutral electronic states of ZrO[5] and HfO[21] was used to make assignments of our anion photoelectron spectra, and the electron affinities (EA) of ZrO and HfO were extracted from their respective anion photoelectron spectra. The anion photoelectron spectra of $HfHO^-$ and HfO_2H^- show a strong similarity to one another. Electron affinity values for HfHO and HfO_2H, along with structural insights, are reported.

EXPERIMENTAL METHODS

Negative ion photoelectron spectroscopy is conducted by crossing a mass-selected beam of negative ions with a fixed-frequency laser beam and energy-analyzing the resultant photodetached electrons. This technique is governed by the energy-conserving relationship, $h\nu$ = EBE + EKE, where $h\nu$ is the photon energy, EKE is the measured electron kinetic energy, and EBE is the electron binding energy, i.e., the anion-to-neutral transition energy. These experiment were conducted on an apparatus consisting of a Nd:YAG laser vaporization source, a linear time-of-flight mass spectrometer, a mass gate, a momentum decelerator, a second Nd:YAG laser (for photodetachment), and a magnetic bottle electron energy analyzer. The resolution of our magnetic bottle electron energy analyzer was ~35 meV at an EKE of ~1 eV. The apparatus has been described in detail in Ref. 26.

The anions, ZrO^- and HfO^-, were generated in a laser vaporization source by focusing the pulsed (10 Hz), second harmonic (532 nm) beam of a Nd:YAG laser onto a continuously rotating, translating zirconium or hafnium rod. The carrier gas used in the

laser vaporization source was highly purified helium, which issued through a pulsed valve with a backing pressure of ~ 4 atm. The oxides on the surfaces of the zirconium and hafnium rods were found to be adequate for generating the metal oxide anions of interest without the addition of oxygen.

RESULTS

The anion photoelectron spectra of ZrO^- and HfO^- are shown in Figure 4.1.1, and those of $HfHO^-$ and HfO_2H^- are presented in Figure 4.1.2.

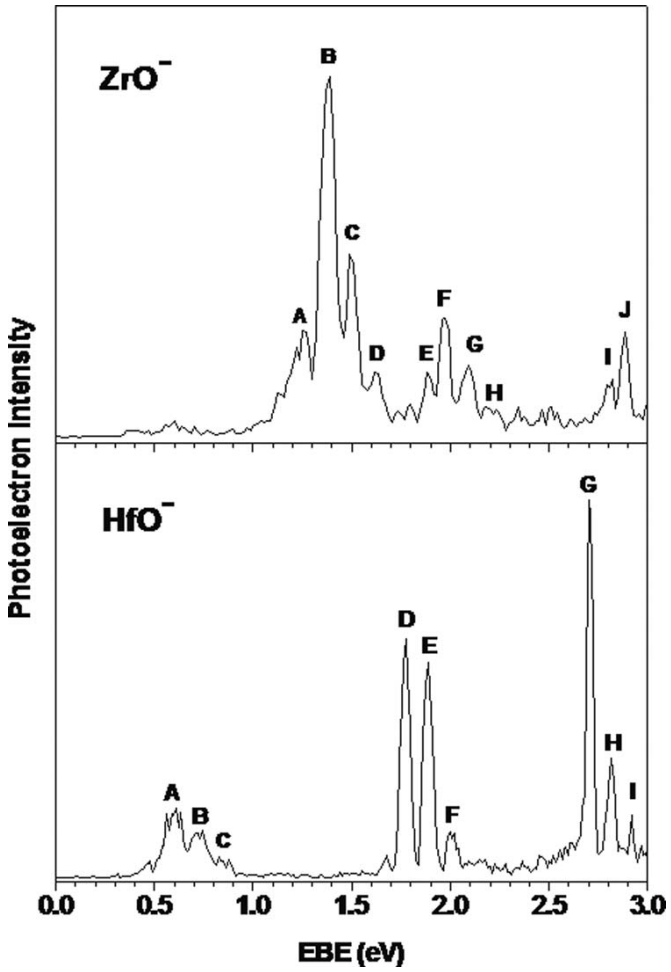

Figure 4.1.1. Anion photoelectron spectra of ZrO^- and HfO^- recorded with 3.493 eV (355nm) photons.

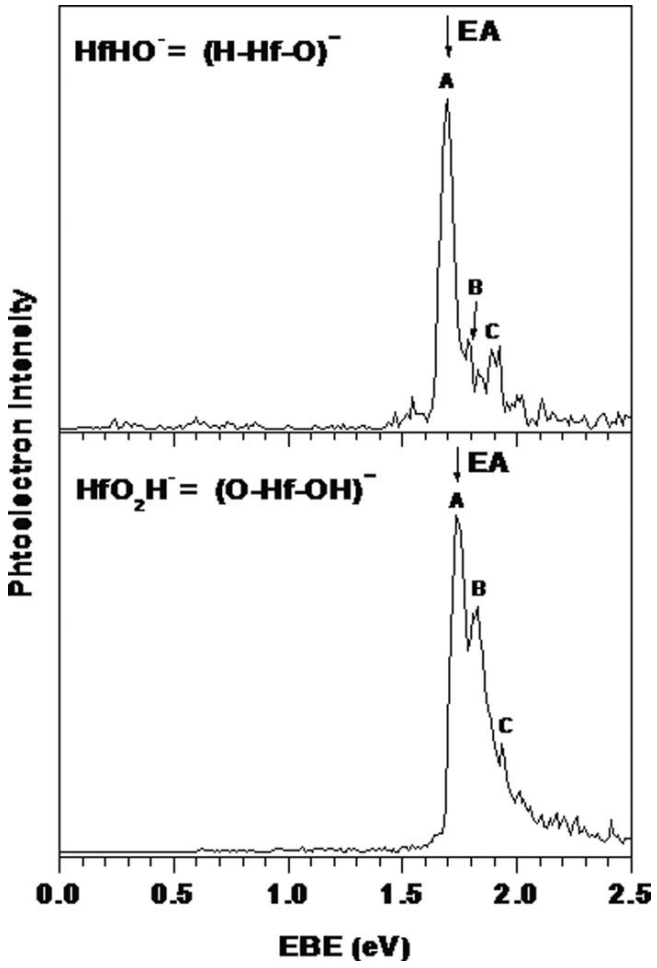

Figure 4.1.2. Anion photoelectron spectra of $HHfO^-$ and $OHfOH^-$ taken with 3.493 eV (355 nm) photons.

All of these spectra were recorded with 3.49 eV photons. In all cases, the principal peaks in these spectra are labeled with capital letters; the EBE values of their centers are tabulated in Tables 4.1.1–4.1.3 (with uncertainties of ±0.05 eV). The spectra of ZrO^- and HfO^- each exhibit three main groupings of peaks, with peak (**B**) at EBE = 1.39 eV dominating the spectrum of ZrO^-, and with peaks (**D**, **E**, **G**) at EBE = 1.78, 1.89, and 2.71 eV dominating the spectrum of HfO^-. The spectra of $HfHO^-$ and HfO_2H^- show

similar spectral profiles to one another, where in each case strong, relatively sharp peaks (labeled **A** in both cases) located at EBE = 1.70 and 1.73 eV, respectively, dominate their spectra.

DISCUSSION

ZrO$^-$

Our anion photoelectron spectrum of ZrO^- is consistent with the previously reported anion photoelectron spectra of ZrO^-,[19,20] although due to differences in resolution and photon energy windows, the present spectrum shows more spectral detail. We assign peak **A** at EBE = 1.26 eV as the origin transition in the photoelectron spectrum of ZrO^-, i.e., the transition from the ground vibrational ($v''= 0$) and electronic ($^2\Delta$) state of the ZrO^- anion to the ground vibrational ($v'= 0$) and electronic ($^1\Sigma^+$) state of neutral ZrO. The ground state of anion was determined based on the fact that the relativistic mass-velocity stabilization of the 6*s* orbital of Zr would favor the σ orbital over the δ orbital of ZrO^-. It means that the ground state of HfO^- should have been arisen from the $\sigma^2\delta$ configuration ($^2\Delta$) rather than $\sigma\delta^2$ ($^2\Sigma^-$). This assignment determines the adiabatic EA of ZrO to be 1.26 eV, in agreement with previous experiments and calculations.[14,15,18–20] Peak **A** is the lowest EBE peak which does not vary in intensity with source conditions relative to the other higher EBE peaks. The two slightly lower EBE, shoulder peaks at EBE ~1.1 and ~1.2 eV vary with source conditions and are likely to be due to the photodetachment of vibrationally excited ground state anions; they are vibrational hot bands. The low intensity signal in the EBE region between 0.3–0.7 eV was also seen in a

previous study and was assigned as an electronic hot band, i.e., as being due to photodetachment transitions from an electronically excited anion.

Table 4.1.1. Transition assignments for the photoelectron spectrum of ZrO^-. T_e is the term energy in eV. (Uncertainty of EBE is ±0.05 eV).

Peaks	EBE (eV)	Te (eV)	Peak assignment: $^2\Delta \rightarrow$	ωe (cm^{-1})
A	1.26	0	$X^1\Sigma^+$ ($v'=0, 5s^2, \sigma\delta^2$)	…
B	1.39	0.13	$A^3\Delta_1$($v'=0, 4d^15s^1, \sigma^2\delta$) and $X^1\Sigma^+$ ($v'=1$)	890
C	1.50	0.24	$A^3\Delta_1$ ($v'=1$) and $^3\Delta_2(4d^15s^1, \sigma^2\delta)$	
D	1.62	0.36	$A^3\Delta_1$ ($v'=2$) and $^3\Delta_3(4d^15s^1, \sigma^2\delta)$	
E	1.88	0.62	$(^2\Sigma^- \rightarrow {}^1\Delta_2)$[a] $(4d^15s^1, \sigma^2\delta)$	…
F	1.98	0.72	$A^1\Delta_2$ ($v'=, \sigma^2\delta$)	880
G	2.09	0.83	$A^1\Delta_2$ ($v'=1$) and $^3\Phi_2$ ($4d^2, \sigma^2\delta$)	
H	2.20	0.94	$A^1\Delta_2$ ($v'=2$) and $^3\Phi_3$ ($4d^2, \sigma^2\delta$)	
I	2.80	1.54	$b^3\prod_0(4d^2, \sigma^2\pi)$	…
J	2.88	1.62	$b^3\prod_1(4d^2, \sigma^2\pi)$	…

[a] Assigned to a transition from an excited state of the anion to the neutral.

With the EBE value of the origin transition established, the spectroscopic assignments of neutral ZrO by Kaledin et al.[5] were used to assign the other significant transitions in the anion photoelectron spectrum of ZrO^-. These assignments are presented in Table 4.1.1.[5,36] The most intense feature in the spectrum is peak **B**, located at EBE = 1.39 eV. It and its associated vibronic peaks, **C** and **D**, correspond to transitions from the ground state anion to the various components of the first excited $^3\Delta_1$ state of neutral ZrO. While the **B**-**C** and **C**-**D** spacings were measured to be 890 cm^{-1}, the vibrational

frequency of the $^3\Delta_1$ state cannot be unambiguously determined from this spectrum, since the $^3\Delta_2$ spin-orbit component lies in the same region as the vibrational transitions to the $^3\Delta_1$ state, causing the features associated with both to overlap. Nevertheless, we expect the vibrational frequency of the $^3\Delta_1$ state to be very close to the spin-orbit splitting between $^3\Delta_1$ and $^3\Delta_2$ components. (Peak **E** is discussed and assigned below.) Similarly, peak **F**, located at EBE = 1.98 eV and its associated vibronic peaks, **G** and **H**, correspond to transitions from the ground state anion to the second excited state of neutral ZrO, $^1\Delta_2$. The peaks, **G** and **H**, are probably comprised of both transitions to vibrational levels of the $^1\Delta_2$ state and $^3\Phi_2$ and $^3\Phi_3$ spin-orbit components, which arise from the Zr^{2+} ($4d^2$) configuration. Based on the measured **F-G** and **G-H** spacings, the vibrational frequency of the $^1\Delta_2$ state is determined to be 880 cm^{-1}. Furthermore, peak **I**, located at EBE = 2.80 eV and peak **J**, located at EBE = 2.88 eV are, respectively, assigned to the transitions from the anion ground state to the $^3\Pi_0$ and $^3\Pi_1$ excited states of neutral ZrO. All of these assignments are presented in Table 4.1.1.

In proposing these assignments, we have considered both prior assignments and an analysis of analogous electronic states for neutral ZrO. Due to the strong ionic nature of ZrO, we expect that the bonding can be described as being predominantly $Zr^{2+}O^{2-}$. Thus, the excited electronic states of ZrO can be analyzed and rationalized using the atomic energy levels of Zr^{2+}. Since the isoelectronic Y^+ atomic energy levels[27] are readily available, we have used the energy separations between Y^+ electronic states to provide additional guidance in the assignment of the observed photoelectron spectra of ZrO^- (see Figure 4.1.3). As seen from Moore's atomic spectra data,[27] the ground state of Y^+ is ^1S with $^3D_1$, $^3D_2$, and $^3D_3$ excited states located at 840, 1045, and 1450 cm^{-1}, respectively,

above the ground state. These states could correspond to the observed transitions **B**, **C**, and **D** in the anion photoelectron spectrum of ZrO^-. Moreover, the $^1D_2$ excited state of Y^+ at 3296 cm^{-1} corresponds to the $^1\Delta_2$ excited state of neutral ZrO, which correlates with the ($4d^15s^1$) configuration of Zr^{2+}. A transition from the $^2\Sigma^-$ electronically excited state of the ZrO^- anion to the $^1\Delta_2$ excited state of neutral ZrO can be assigned to peak **E**, which is an electronic hot band. In addition, the ^3F state of Y^+, arising from the $4d^2$ configuration,[33] has a T_e of 8003 cm^{-1}, thereby supporting our assignment of peaks, **G** and **H**, to the $^3\Phi_2$ and $^3\Phi_3$ spin orbit components. Finally, the $^3P_0$ state of Y+ is observed at 13883 cm^{-1}, which supports our assignment of peak **I** to a transition terminating on the $^3\Pi_0$ excited state of neutral ZrO and our assignment of peak **J** to a transition terminating on the $^3\Pi_1$ excited state of neutral ZrO.

HfO$^-$

We assign peak **A**, located at EBE = 0.60 eV as the origin transition in the anion photoelectron spectrum of HfO^-, i.e., the transition from the ground vibrational (v″=0) and electronic ($^2\Delta$) state of the HfO^- anion to the ground vibrational (v′=0) and electronic ($^1\Sigma^+$) state of neutral HfO. Similarly to ZrO^-, the ground state of HfO^- anion was determined to have arisen from the $\sigma^2\delta$ configuration. This assignment determines the adiabatic electron affinity (EA) of HfO to be 0.60 eV. Peak **A** is the lowest EBE peak which does not vary in intensity with source conditions relative to the other higher EBE peaks. The intensity of the shoulder peak at slightly lower EBE (at 0.48 eV) varies with source conditions and is assigned as being due to the photodetachment of a vibrationally excited, ground electronic state anion; it is a vibrational hot band. Peaks **B** and **C**

correspond respectively to transitions from the ground vibrational and electronic state of the HfO^- anion to the v′ = 1 and the v′ = 2 vibrational levels of the ground electronic state of neutral HfO. The **A**-**B** and **B**-**C** spacings were measured to be 1050 cm^{-1}, and this is a measure of the vibrational frequency of neutral HfO. This value is higher than the literature value,[21] which is 967 cm^{-1}. We attribute this slight discrepancy to the low signal-to-noise ratio observed for this particular band. A Franck-Condon analysis of the band containing peaks **A**, **B**, **C** (using a program developed by Ervin and Lineberger[28]) found the bond length of the HfO^- anion to be 1.759 Å. The literature value of the neutral HfO bond length (and thus the input value utilized in the program) is 1.723 Å. This difference is consistent with the expectation of a weaker bond and longer bond length for the HfO^- anion relative to its neutral HfO counterpart.

With the origin transition tentatively located, the spectroscopic assignments of neutral HfO by Kaledin et al.[21] (see Ref. 36) were used to assign the other significant transitions in the anion photoelectron spectrum of HfO^-. The most intense features in the spectrum are peaks **D**, located at EBE = 1.78 eV, peak **E**, located at EBE = 1.89 eV, and peak **G**, located at EBE = 2.71. Relative to the EBE of peak **A**, peak **D** lies at an EBE which corresponds to a photodetachment transition from the ground state of the HfO^- anion to the $a^3\Delta_1$ excited state of neutral HfO, as assigned by Kaledin.[21] Likewise, peak **E** lies at an EBE which corresponds to a transition to the similarly assigned $a^3\Delta_2$ excited state of neutral HfO. Peak **F** is a vibronic peak, corresponding to a transition from the ground state anion to v′ = 1 of the $a^3\Delta_2$ state of neutral HfO. The **E**-**F** spacing, measured to be 890 cm^{-1}, is a measure of the vibrational frequency of the $a^3\Delta_2$ excited state of HfO. In similar fashion, peak **G** lies at an EBE which corresponds to a transition to the $b^3\Pi_0$

excited state of neutral HfO. Peaks **H** and **I** correspond to transitions to higher components of $b^3\Pi$ excited states of neutral HfO. The close correspondence between the energy levels of neutral HfO measured by Kaledin and the peak locations in our observed spectrum confirms our assignment of the origin transition to peak **A**.

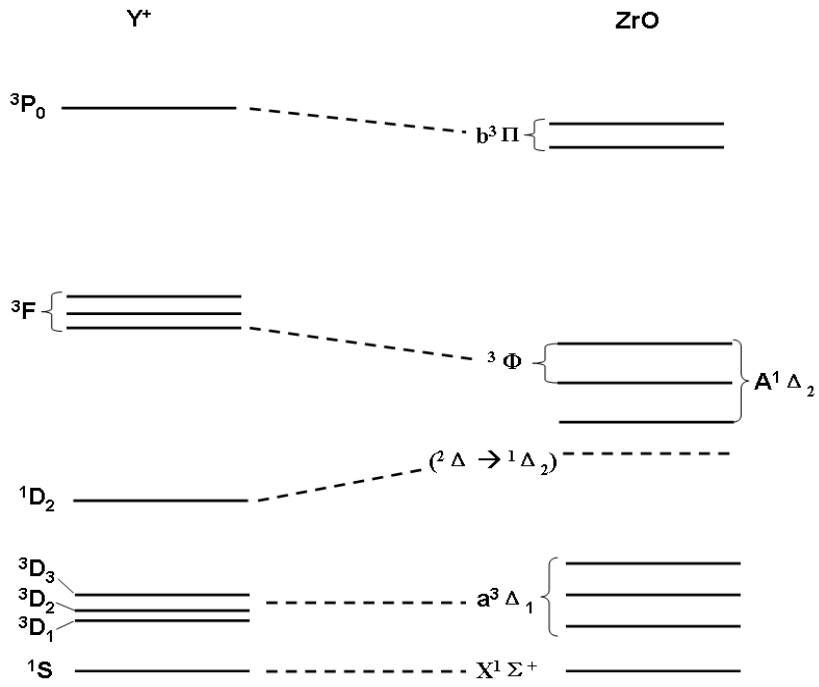

Figure 4.1.3. Comparison between the atomic energy levels of Y^+ and the assigned molecular energy levels of neutral ZrO as extracted from the anion photoelectron spectrum of the ZrO^- anion.

As was the case for ZrO above, we have also conducted an analysis of analogous electronic states for neutral HfO in order to further assist in making assignments. This approach involved utilizing the atomic energy levels[27] of La^+. However, because there are lanthanide atoms between lanthanum and hafnium in the periodic table, we scaled the

energies of the La^+ states by the atomic numbers of hafnium and lanthanum in order to make a meaningful comparison. The assignment of peak **A** as the origin transition remains unchanged. However, the assignments of peaks **D** and **E** differ slightly under this approach. Under the assignment based on Kaledin's work,[21] peak **D** is due to a transition from the ground state of the HfO^- anion to the $a^3\Delta_1$ excited state of neutral HfO. Alternatively, peak **D** could be assigned to the $^2\Delta \rightarrow \Omega = 2$ ($^3\Delta_2$+ $^1\Delta_2$) transition. Note that the mixing of $^3\Delta_2$ and $^1\Delta_2$ is expected to be substantial in hafnium due to its large spin-orbit interaction,[29,30] and thus this state could be lowered in energy relative to the $\Omega = 1$ ($^3\Delta_1$) state. This argues for peak **E** being assigned to the $^2\Delta \rightarrow \Omega = 1$ ($^3\Delta_1$) transition. In other words, the Kaledin- based assignments of peaks **D** and **E** should perhaps be switched. In support of this possibility, we note that the corresponding states of La^+ violate Hund's rule in that the $^1D_2$ state of La^+ is lower than the spin-orbit components of the ^3D state due to the mixing of the J=2 components of $^1D_2$ and $^3D_2$.[33] Thus, we tentatively assign peak **D** to a Ω =2 state, even though an assignment of peak **D** to $^3\Delta_1$ and of peak **E** to $\rightarrow \Omega = 2$ ($^3\Delta_2$+ $^1\Delta_2$) cannot be ruled out. Peak **G** remains assigned to the $^2\Delta \rightarrow {}^3\Pi_0$ transition. Peaks **H** and **I** may simply be transitions to vibrational levels of the $^3\Pi_0$ state. However, the other two spin-orbit components of the $^3\Pi$ state, namely Ω =1 and Ω = 2 states, can also be candidates for the assignments of peaks **H** and **I**. These assignments are presented in Table 4.1.2.

Upon comparing the anion photoelectron spectra of ZrO^- and HfO^-, it is clear that these two systems show dramatically different spectral profiles. Such differences suggest that a single oxygen atom binding to these transition metals can induce significant

changes in electronic properties, even though zirconium and hafnium are usually considered to be nearly chemically identical. More surprisingly, the difference between

Table 4.1.2. Transition assignments for the photoelectron spectrum of HfO^-. T_e is the term energy in eV, and ω_e is the measured vibrational frequency in cm^{-1}. (Uncertainty of EBE is ±0.05 eV).

Peaks	EBE (eV)	T_e(eV)	Peak assignment: $^2\Delta \rightarrow$	$\omega_e(cm^{-1})$
A	0.60	0	$X^1\Sigma^+$ ($v'=0, 6s^2, \sigma\delta^2$)	1050
B	0.73	0.13	$X^1\Sigma^+$ ($v'=1$)	
C	0.86	0.26	$X^1\Sigma^+$ ($v'=2$)	
D	1.78	1.18	$a(^3\Delta_1 + {}^1\Delta_2)$ $v'=0, 5d^16s^2, \sigma^2\delta$)	890
E	1.89	1.29	$a^3\Delta_1$ ($v'=0, 5d^16s^2, \sigma^2\delta$)	
F	2.00	1.40	$a^3\Delta_1$ ($v'=1, 5d^16s^2, \sigma^2\delta$)	
G	2.71	2.11	$b^3\prod_0(v'=0)$ ($5d^2, \sigma^2\pi$)	890
H	2.82	2.22	$b(^3\prod_0 + {}^1\prod_1(v'=0)$ ($5d^2, \sigma^2\pi$)	
I	2.92	2.32	$b^3\prod_2(v'= 0, 5d^2)$	

ZrO^- and HfO^- observed here is more substantial than that between ZrO_2^- and HfO_2^-.[3] We suggest that these spectral differences between HfO and ZrO are due to much larger relativistic effects in hafnium than in zirconium, and indeed, relativistic effects are most dramatically manifested in diatomic species.[31] The relativistic mass-velocity effect stabilizes the 5s orbital of Zr and 6s orbital of Hf. The same effect destabilizes the 4d

orbital of Zr and 5d orbital of Hf. Specifically, using HfO as an example, the σ orbital of HfO is expected to be relativistically stabilized by mass-velocity effect while the δ orbital of HfO is expected to be destabilized, due to the fact that its s orbital is composed of the $6s\text{-}5d^{z^{**}2}$ orbital of Hf, while the δ orbital is purely atomic Hf (5d). Indeed, the $^3\Delta$ state of HfO is placed 1.18 eV above the $^1\Sigma^+$ state, which evidently supports relativistic mass-velocity stabilization of the σ orbital of HfO and destabilization of the δ orbital of HfO. In addition, the relativistic mass-velocity stabilization of 6s and the destabilization of 5d is more pronounced for Hf, as it is heavier than Zr (the $^3\Delta$ state of ZrO is only 0.24 eV above the ground state of ZrO whereas the corresponding lowest $^3\Delta$ spin-orbit component is 1.18 eV above the $^1\Sigma^+$ state).

The dissociation energies of the ZrO^- anion into Zr and O^-, $D_0(Zr\text{--}O^-)$, and of the HfO^- anion into Hf and O^-, $D_0(Hf\text{--}O^-)$, can be extracted from our data by utilizing the identity,

$$D_0(X\text{--}O^-) = D_0(X\text{--}O) + EA(XO) - EA(O) \qquad (1)$$

where X is either Zr or Hf. Here, we determined that EA(ZrO) = 1.26 eV and that EA(HfO) = 0.60 eV, and EA(O) is known to be 1.461 eV.[32] Furthermore, the dissociation energies of neutral ZrO and HfO, i.e., $D_0(Zr\text{--}O)$ and $D_0(Hf\text{--}O)$, are 7.91 eV[30] and 8.19 eV,[12] respectively. Thus from these values, we can obtain the dissociation energy for their corresponding anions. The results are: $D_0(Zr\text{--}O^-)$ = 7.71 eV and $D_0(Hf\text{--}O^-)$ = 7.33 eV. Note that the value of $D_0(Zr\text{--}O^-)$ is very close to that of $D_0(Zr\text{--}O)$, i.e., only a difference of 0.20 eV. By comparison, the difference between $D_0(Hf\text{--}O^-)$ and $D_0(Hf\text{--}O)$ is much bigger, i.e., a difference of 0.86 eV.

$HfHO^-$ and HfO_2H^-

The anion photoelectron spectra of $HfHO^-$ and HfO_2H^- are presented in Figure 4.1.2. These two spectra have very similar profiles, in which each displays a strong peak (labeled peak **A**) and two higher EBE transitions (labeled peaks **B** and **C**). All of these transitions are listed in Table 4.1.3. In each case, we assign the peak **A** as the origin transition, this assignment determining the electron affinities of HfHO and HfO_2H to be 1.70 eV and 1.73 eV, respectively. We further assign peaks **B** and **C** in both cases as vibrational transitions

Table 4.1.3. Measured EA values of HHfO and OHfOH, and the measured vibrational frequency of $OHfOH^-$. (Uncertainty of EBE is ±0.05 eV).

Systems	Peaks	EBE (eV)	ωe (cm^{-1})
HHfO	A	1.70	730
	B	1.79	
	C	1.89	
OHfOH	A	1.73	810
	B	1.83	
	C	1.93	

associated with their corresponding peak **A**, i.e., transitions to v′ = 1 and v′ = 2, respectively. The **A**-**B** and **B**-**C** spacings in the spectrum of $HfOH^-$ are essentially the same, at 730 cm^{-1}, while the **A**-**B** and **B**-**C** spacings in the spectrum of HfO_2H^- are the same, at 810 cm^{-1}. In both spectra, their relatively narrow spectral profiles and the curtailed extent of their vibrational progressions suggest that their anionic and neutral

structures may be similar. Previous infrared and computational studies have shown that hafnium atoms can insert into O-H bonds to form HHfO.[34,35] Thus, we propose that HfHO and $HfHO^-$ exhibit the structural connectivity, H-Hf-O rather than Hf-O-H and that HfO_2H and HfO_2H^- have the connectivity, O-Hf-O-H.

ACKNOWLEDGEMENTS

This material is based upon work supported by the Division of Materials Science and Engineering, Basic Energy Sciences, U.S. Department of Energy, under KHB's Grant No. DE-FG02-09ER46558. We also thank Maciej Gutowski and Jun Li for helpful discussions.

REFERENCES

1. Gutowski, M.; Jaffe, J. E.; Liu, C.-L.; Stoker, M.; Hegde, R. I.; Rai, R. S.; Tobin T, P. *J. Appl. Phys. Lett.* **2002**, *80*, 1897.
2. Lowther, J. E. *Mater. Res. Bull*. **2003**, *28*, 189.
3. Zheng, W.; Bowen, K. H.; Li, J.; Dabkowska, I.; Gutowski, M. *J. Phys. Chem. A* **2005**, *109*, 11521.
4. Brewer, L.; Green, D. W. *High Temp. Sci*. **1969**, *1*, 26.
5. Kaledin, L. A.; McCord, J. E.; Heaven, M. C. *J. Mol. Spectro*. **1995**, *174*, 93.
6. Suenram, R. D.; Lovas, F. J.; Fraser, J. T.; Matsumura, K. *J. Chem. Phys*. **1990**, *92*, 4724.
7. Tatum, J. B.; Balfour, W. J. *J. Mol. Spectro*. **1973**, *48*, 292.
8. Jonsson, J. *J. Mol. Spectro*. **1994**, *167*, 42.
9. Littleton, J. E.; Davis, S. P.; Song, M. *Astrophys. J.* **1993**, *404*, 412.
10. Simard, B.; Mitchell, S. A.; Humphries, M. R.; Hackett, P. A. *J. Mol. Spectro*. **1988**, *129*, 186.
11. Weltner, W.; McLeod, D. J. Phys. Chem. **1965**, *69*, 3488.
12. Chertihin, G. V.; Andrews, L. *J. Phys. Chem*. **1995**, *99*, 6356.
13. Langhoff, S. R.; Bauschlicher, C. W. *Astrophys. J.* **1990**, *349*, 369.
14. Siegbahn, P. E. M. *Chem. Phys. Lett*. **1993**, *201*,15.
15. Song, P.; Guan, W.; Yao, C.; Su, Z.; Wu, Z.; Feng, J.; Yan, L. *Theoretica. Chimica. Acta*. **2007**, *117*, 407.
16. Ackermann, R. J.; Rauh, E. G. *J. Chem. Phys*. **1974**, *60*, 2266.
17. Murad, E.; Hildenbrand, D. L. *J. Chem. Phys*. **1975**, *63*, 1133.

18. Thomas, O. C.; Xu, S.; Lippa, T. P.; Bowen, K. H. *J. Cluster Sci*. **1999**, *10*, 525.

19. Peppernick, S.J.; Gunaratne, K. D. D.; Castleman, A. W. *Proc. Natl. Acad. Sci.* **2009**, *107*, 975.

20. Castleman, A. W. *J. Phys. Chem. Lett*. **2011**, *2*, 1062.

21. Kaledin, L. A.; McCord, J. E.; Heaven, M. C. *J. Mol. Spectro*. **1995**, *173*, 37.

22. Ram, R. S.; Bernath, P. F. *J. Mol. Spectro*. **1995**, *169*, 268.

23. Yao, C.; Guan, W.; Song, P.; Su, Z.; Feng, J.; Yan, L.; Wu, Z.; Theoretica. Chimica. Acta. **2007**, *117*, 115.

24. Aldener, M.; Hansson, A.; Pettersson, A.; Sassenberg, U. *J. Mol. Spectro*. **2002**, *216*, 131.

25. Hansson, A.; Pettersson, A.; Royen, P.; Sassenberg, U. *J. Mol. Spectro*. **2004**, *224*, 157.

26. Gerhards, M.; Thomas, O.C.; Nilles, J. M.; Zheng, W. J.; Bowen, K. H. *J. Chem. Phys*. **2002**, *116*, 10247.

27. Moore, C. E. Tables of Atomic Energy Levels, Vol II & III, NSRDS-NBS 35, National Institute of Standards & Technology, Washington DC 1971

28. PESCAL Fortran program, written by K. M. Ervin and W. C. Lineberger

29. Huber, G. H. *Molecular spectra and molecular structure, Vol IV. Constants of diatomic molecules*. Van Nostrand Reinhold Company, New York, 1979.

30. Andrae, D.; Häußermann, U.; Dolg, M.; Stoll, H.; Preuß, H. *Theoretica. Chimica. Acta*. **1990**, *77*, 123.

31. Balasubramanian, K. "Relativistic Effects in Chemistry", Vols I and II, Wiley Interscience 1997.

32. Neumark, D.M.; Lykke, K. R.; Andersen, T.; Lineberger, W. C. *Phys. Rev. A* **1985**, *32*, 1890.

33. Gibson, N. D.; Davies, B. J.; Larson, D. J. *J. Chem. Phys*. **1993**, *98*, 5104.

34. Wang, X.; Andrews, L. *Inorg. Chem*. **2005**, *44*, 7189.

35. Zhou, M.; Zhang, L.; Dong, J.; Qin, Q. *J. Amer. Chem. Soc*. **2000**, *122*, 10680.

36. See Supplementary Material at http://dx.doi.org/10.1063/1.4704127 for assignments of the electronic states of neutral ZrO and HfO.

SUPPLEMENTAL MATERIAL

Table 4.1.S1.Term energies and assignments of the electronic states of neutral ZrO and HfO.

ZrO[1]			HfO[2]		
State	T_e (eV)	ω_e (cm^{-1})	State	T_e (eV)	ω_e (cm^{-1})
$X^1\Sigma^+$	0	969.8	$X^1\Sigma^+$	0	967.655
$a^3\Delta_1$	0.13395	936.5	$a^3\Delta_1$	1.14447	917.899
$a^3\Delta_2$	0.16959	936.5	$a^3\Delta_2$	1.25873	918.794
$a^3\Delta_3$	0.21118	936.5	$b^3\Pi_{0-}$	2.01987	905.149
$A^1\Delta$	0.732	938.1	$b^3\Pi_{0+}$	2.05652	907.491
$b^3\Pi_{0d}$	1.45869	–	$b^3\Pi_1$	2.17323	900.246
$b^3\Pi_{0c}$	1.461	–			
$b^3\Pi_1$	1.49647	–			
$b^3\Pi_2$	1.54081	–			

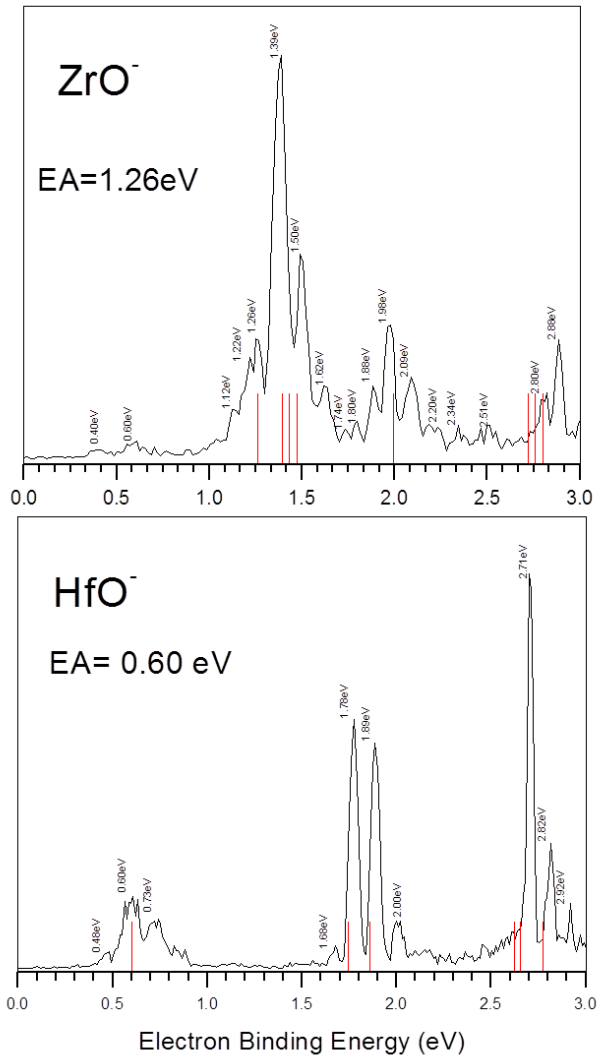

Figure 4.1.S1. Overlap of red stick spectra showing transitions based on data in the table 4.1.S1 with the photoelectron spectra.

SUPPLEMENTAL MATERIAL REFERENCES

1. (a) Kaledin, L. A.; McCord, J. E.; Heaven, M. C. *J. Mol. Spectro*. **1995**, *174*, 93.
   (b) Langhoff, S. R.; Bauschlicher, Jr., C. W. *Astrophys. J.* **1990**, *349*, 369.
2. Kaledin, L. A.; McCord, J. E.; Heaven, M. C. *J. Mol. Spectro*. **1995**, *173*, 23.

Section 4.2. The Reaction Rates of O_2 with Closed-Shell and Open-Shell Al_x^- and Ga_x^- Clusters Under Single Collision Conditions: Experimental and Theoretical Investigations Towards a Generally Valid Model for the Hindered Reactions of O_2 with Metal Atom Clusters

Marco Neumaier,[†] Matthias Olzmann,*[†] Kiran Boggavarapu,[§] Kit H. Bowen,[‡] Bryan Eichhorn,[&] Sarah T. Stokes,[‡] Angela Buonaugurio,[‡] Ralf Burgert,[†] Hansgeorg Schnöckel*[†]

[†]*Institut für Anorganische Chemie and Institut für Physikalische Chemie, Karlsruher Institut für Technologie (KIT) Campus Süd, Postfach 6980, D-76049 Karlsruhe, Germany*

[§]*Department of Chemistry, McNeese State University, 4205 Ryan Street, Lake Charles, LA 70609, USA*

[‡]*Department of Chemistry, John Hopkins University, 3400 North Charles Street, Baltimore, MD 21218, USA*

[&]*Department of Chemistry and Biochemistry, University of Maryland, College Park, MD 20742, USA*

ABSTRACT

In order to characterize the oxidation of metallic surfaces, the reactions of O_2 with a number of Al_x^- and, for the first time, Ga_x^- clusters, as molecular models, have been investigated and the results are presented here for x = 9–14. The rate coefficients were determined with FT-ICR mass spectrometry under single collision conditions at O_2 pressures of ~10^{-8} mbar. In this way, the qualitatively known differences in the reactivities of the even- and odd-numbered clusters towards O_2 could be quantified

experimentally. To obtain information about the primary steps, we additionally performed density functional theory calculations. The results show that for both even- and odd-numbered clusters the formation of the most stable dioxide species, $[M_xO_2]^-$ proceeds via the less stable peroxo species, $[M_x^+\cdots O_2^{2-}]^-$, which contains M–O–O–M moieties. We conclude that the formation of these peroxo intermediates may be a reason for the decreased reactivity of the metal clusters towards O_2. This could be one of the main reasons why O_2 reactions with metal surfaces proceed more slowly than Cl_2 reactions with such surfaces, even though O_2 reactions with both Al metal and Al clusters are more exothermic than are reactions of Cl_2 with them. Furthermore, our results indicate that the spin-forbidden reactions of $^3O_2$ with closed-shell clusters and the spin-allowed reactions with open-shell clusters to give singlet $[M_x^+\cdots O_2^{2-}]^-$ are the root cause for observed even/odd differences in reactivity.

*Corresponding authors: email: matthias.olzmann@kit.edu,
hansgeorg.schnoeckel@chemie.uni-karlsruhe.de

INTRODUCTION

The hindered reactivity of O_2 with metal surfaces, in contrast to their fast reactions with Cl_2, is well-known in classical inorganic chemistry[1] and is based on some important differences between these reactants.

In the case of a base metal such as Al, the O_2 reaction is strongly exothermic with respect to the formation of Al_2O_3 ($2Al + 3/2\ O_2 \rightarrow Al_2O_3$:$\Delta H_f° = -1676$ kJ mol^{-1}, that is, 838 kJ per 1 mol Al), while less energy is gained in the Cl_2 reaction, where $AlCl_3$ is formed ($Al + 3/2Cl_2 \rightarrow AlCl_3$: $\Delta H_f° = -705$ kJ mol^{-1}).[2] Because of the high stability of Al_2O_3, it remains steadfastly on the surface of the aluminum metal, protecting it and prohibiting further oxidation of the metal. Only at high temperatures >1200°C, where Al_2O_3 reacts with Al metal to form the low valent oxide molecule Al−O−Al, can alumina be vaporized and removed from the metal surface.[3] The formation of this linear molecule, Al−O−Al, is the essential step in the deterioration of the aluminum surface after reaction of O_2 with solid Al and, as we will see, with Al_x^- clusters:[4]

$$Al_x^- + O_2 \rightarrow Al_{x-4}^- + 2\ Al_2O_{(g)} \qquad (1a)$$

If an excess of O_2 is applied, the Al_2O molecules are easily oxidized to solid Al_2O_3, and simultaneously a large amount of energy is gained:

$$Al_2O_{(g)} + O_{2(g)} \rightarrow Al_2O_{3(s)} \qquad (1b)$$

with $\Delta_R H° = -1530.5$ kJ mol^{-1}.[2] In contrast, the chlorination of Al runs at even low temperatures (>200°C), and the reaction proceeds completely to $AlCl_3$ (or to Al_2Cl_6), which is a volatile solid compound even at these temperatures. Therefore, this reaction continues until the Al metal is consumed.[5,6]

Besides the thermodynamic data and experimental results, which favor a fast and complete reaction of Al metal with Cl_2 in comparison to O_2, there is a molecular-kinetic reason for the slower reaction of O_2, a stepwise transfer of four electrons from Al to O_2 via several intermediates containing AlO bonds:

$$O_2 \xrightarrow{e^{\ominus}} O_2^- \xrightarrow{e^{\ominus}} O_2^{2-} \xrightarrow{2e^{\ominus}} 2O^{2-}$$

(superoxo) (peroxo) (oxide)

In contrast, in the case of Cl_2 only one intermediate is possible, which contains two AlCl bonds, because every Cl_2 molecule takes two electrons to form two Cl^- anions.

The investigation of the complex reaction of O_2 molecules with metal atom surfaces was and still is a challenging problem for theory and experiment.[7] On the experimental side, it mainly had been dealt with by physicists using surface methods such as atomic force microscopy (AFM) and scanning tunneling microscopy (STM).[7] However, the investigation of surfaces of base metals bears a fundamental difficulty. This is because the 5 eV bond energy (BE) of an Al−O bond (in an Al−O−O−Al fragment) is equivalent to the energy necessary to cleave the O−O bond in the O_2 molecule, producing two O atoms (the O_2 BE is 5.16 eV).[2] A peroxo intermediate fragment Al−O−O−Al, containing two Al−O bonds, will therefore be highly excited (5 eV excess energy) and thus O atoms can also be ejected from the surface.[8] In order to avoid such difficulties, mainly O_2 reactions with surfaces of noble metals have been investigated. There, the M−O bond energy is much smaller (e.g., for Pd−O, 2.87 eV from PdO (g)[2] and for Pt−O, 3.28 eV[9a]), and therefore it is possible to detect intermediate fragments, for example, Pt−O−O−Pt, with microscopic methods.[9–11]

Besides the investigations of the hindered O_2 reactions with metal surfaces by using microscopic methods (AFM, STM), a further experimental approach, namely, mass spectrometric investigations of metal atom clusters and their O_2 reactions, promises to give a deeper insight into this complex reaction mechanism.

$Al_n^{\pm}$ clusters have been investigated in many experimental and theoretical papers during the last two decades.[6,13–16] However, only the Al_{13}^- cluster appears to be an ideal molecular model for studying reactions involving bulk metals. The surprising similarity for the chlorination of the Al_{13}^- cluster and Al metal illustrates the similar thermodynamic behavior.[12,13]

$$Al_{13}^- + 3Cl_2 \rightarrow Al_{11}^- + 2AlCl_{3(g)}$$

$$\Delta_R H = -1137 \text{ kJ mol}^{-1} \quad \text{(calcd)}$$

$$2\ Al(s) + 3Cl_2 \rightarrow 2AlCl_{3(g)}$$

$$\Delta_R H = -1166 \text{ kJ mol}^{-1} \quad \text{(expt)}$$

However, for the observed hindered reaction of the Al_{13}^- cluster with O_2, note that also the reaction of O_2 with bulk Al is unexpectedly slow,[7,15,18] there have been given several different explanations: (1) the outstanding electronic stability of Al_{13}^- with its 40 valence electron jellium core,[17] (2) the exceptional geometry in which a central Al atom is surrounded by 12 additional Al atoms, which form an icosahedron around it, that is, a magic geometry, (3) the outstanding electron affinity (3.6 eV) of Al_{13}, which is as large as that of the atomic chlorine atom, and finally (4) the spin-forbidden reaction of triplet O_2 with the singlet Al_{13}^- species to give singlet Al_9^- and $2Al_2O$.[18–21]

It was demonstrated that isolated Al_{13}^- ions in an O_2 atmosphere of about 10^{-8} mbar in an ion cyclotron resonance (ICR) trap do not form Al_9^- species even after about

600s.[18] In order to show that this hindered Al_{13}^- + O_2 reaction is not just a special case but is of general interest, we measured the rate coefficients of O_2 reactions with a number of Al_x^- clusters near the Al_{13}^- species with closed- and open-shell structure. We found slow reactions for Al_9^-, Al_{11}^-, and Al_{13}^- and comparatively fast reactions for Al_8^-, Al_{10}^-, Al_{12}^-, and Al_{14}^-. The doublet character of the last four species eliminates hindrances caused by the violation of the spin conservation rule and allows one to compare these rate coefficients with those of the spin-allowed Cl_2 reactions. In order to show the importance of this rule, O_2 reactions with $Al_{13}H^-$ (open shell) and $Al_{14}H^-$ (closed shell) are also investigated. In an ongoing investigation, we study the acceleration of the Al_{13}^- + O_2 reaction by increasing the collisional energy. The experimental findings and the analysis of these complex results are the subject of a further publication.[22]

To further study the general importance of the O_2 + metal reaction, we have extended our investigation to a number of Ga_x^- clusters. Though Ga is a homologue of Al, it exhibits many differences: Unexpectedly, the electronegativity (EN) of Ga, at 1.8, is higher than that of Al (1.5). Ga has seven crystalline modifications; these vary in their bond formation from covalent bonding as in the case of boron toward metallic bonding as in a real metal. The α-Ga modification, with one short Ga−Ga bond, often is called a molecular metal,[1,15] a property that is also reflected in its low melting point of 28°C. Also, true metal structures like Ga(IV) are observed under high pressure.[15,23,24] However, the electronic behavior of naked Ga_x^- should be similar to that of Al_x^- clusters since the same number of valence electrons are involved in bonding, for example 40 in the jellium-like Ga_{13}^- cluster. Therefore, while reactions of O_2 with Ga_x^- clusters should be electronically similar to reactions with Al_x^- clusters, they are different from a

thermodynamic point of view, because the Ga−O bond energy is considerably smaller than that of Al−O. The Al−O bond strength is much larger, however, than that of all noble metal−oxygen bonds, as the following comparison shows: Al−O = 5.35 eV (from Al_2O), Ga−O = 4.59 eV (from Ga_2O), and Pd−O = 2.87 eV (from Pd−O(g)).[2] Accordingly, the mass spectrometric results for the Ga_x^- clusters presented here can be expected to show whether the model for the Al_x^- + O_2 reactions is valid for other metals that exhibit different thermodynamic properties. The different thermodynamic properties of Ga compounds in comparison to Al compounds are also reflected in procedures for forming Ga_x^- and Al_x^- clusters. While Al_x^- clusters were formed by laser desorption of solid $LiAlH_4$, Ga_x^- species can be obtained after laser irradiation of solid GaN, which will be described here for the first time.[2,25,26]

The rate coefficients presented in this work were determined by bringing either single-sized clusters or a collection of clusters with different sizes into reaction with O_2 under (nearly) single collision conditions (10^{-8} mbar). This means that the reaction products are generally detected before a second collision with O_2 occurs. This approach is essential in order to study the single elementary steps of the reaction. In contrast, in recent flow tube experiments by other authors at about 0.5 mbar, up to 100 collisions between O_2 and a single cluster occur before the products are detected.[11] In these experiments, rate coefficients of O_2 with a large number (ca. 50) of Al_x^- clusters of different size were estimated via a data analysis based on a Monte Carlo model.[20,21]

A comparison of measured rate coefficients with predictions from kinetic theories would allow further conclusions regarding the underlying reaction mechanisms. However, the calculation of rate coefficients from first principles with molecular and

transition state data from quantum chemical methods requires a reliable knowledge of barrier heights. For the reactions of $^3O_2$ with closed- and open-shell Al_x^- and Ga_x^- clusters, these calculations are complicated not only by failure of single determinant methods but also by the existence of multiple isomeric intermediates.[27]

On the basis of our experimental results and supported by DFT calculations, we obtained evidence for a model in which the peroxo intermediate $[M_x \cdots O_2]^-$, as the earliest species along the reaction coordinate that exhibits a typical arrangement of valence electrons, plays an essential role. This peroxo intermediate is also the prominent species in a more general, hypothetical reaction scheme that is, a Gedanken experiment, which should allow predictions to be made for O_2 reaction rates of any metal atom clusters. Within this broader scheme, the oxidation of the M_x^- cluster to a M_x^+ species with simultaneous reduction of O_2 to the O_2^{2-} peroxo moiety plays the major role.[28,1]

RESULTS AND DISCUSSION

Mechanisms and Rate Coefficients. Prior to the determination of rate coefficients, we studied qualitatively the reaction pattern of all $M_{m/n}^-$ clusters (m = even-numbered; n = odd-numbered; M = Al, Ga) with O_2. The clusters were first isolated and brought to collision with oxygen at a pressure of about 4×10^{-8} mbar for several seconds. Let us consider Ga_m^- cluster anions first. For these even-numbered clusters (Ga_{10}^-–Ga_{28}^-), the following spontaneous reactions were observed.[29]

$$Ga_{10}^- + O_2 \rightarrow Ga_6^- + 2\ Ga_2O$$

$$Ga_{10}^- + O_2 \rightarrow Ga_5^- + Ga_2O + Ga_3O$$

$Ga_{12}^- + O_2 \rightarrow Ga_7^- + Ga_2O + Ga_3O$

$Ga_{14}^- + O_2 \rightarrow Ga_{10}^- + 2\ Ga_2O$

$Ga_{16}^- + O_2 \rightarrow Ga_{12}^- + 2\ Ga_2O$

$Ga_{16}^- + O_2 \rightarrow Ga_{11}^- + Ga_2O + Ga_3O$

$Ga_{18}^- + O_2 \rightarrow Ga_{13}^- + Ga_2O + Ga_3O$

$Ga_{20}^- + O_2 \rightarrow Ga_{16}^- + 2\ Ga_2O$

$Ga_{20}^- + O_2 \rightarrow Ga_{15}^- + Ga_2O + Ga_3O$

$Ga_{22}^- + O_2 \rightarrow Ga_{18}^- + 2\ Ga_2O$

$Ga_{24}^- + O_2 \rightarrow Ga_{20}^- + 2\ Ga_2O$

$Ga_{26}^- + O_2 \rightarrow Ga_{22}^- + 2\ Ga_2O$

$Ga_{28}^- + O_2 \rightarrow Ga_{24}^- + 2\ Ga_2O$

In contrast to all these spontaneous reactions, the odd-numbered, closed-shell Ga_n^- clusters react at least one order of magnitude more slowly with O_2, and only upper limits to the rate coefficients can be given.[30]

For the corresponding $Al_{m/n}^-$ clusters, qualitatively the analogous reactions were observed that is, spontaneous reactions for even-numbered Al_m^- clusters with formation of $Al_{(m-4)}^-$ or $Al_{(m-5)}^-$ fragments. Odd-numbered Al_n^- clusters were found to be much less reactive, Al_{13}^- and Al_9^- being nearly stable in agreement with our former observations[18] and those of Castleman et al.[21]

For the determination of rate coefficients, O_2 was admitted to the ICR cell by a manual leak valve (Varian) allowing us to maintain a constant partial pressure of 3×10^{-10} to 4×10^{-8} mbar in the cell. Note that with this method the maximum pressure was

limited to ~4 × 10^{-8} mbar, because ion detection took place while the reaction gas (O_2) was present in the ICR cell. Rate coefficients for all $Ga_{m/n}^-$ clusters are shown in Figure 4.2.1.

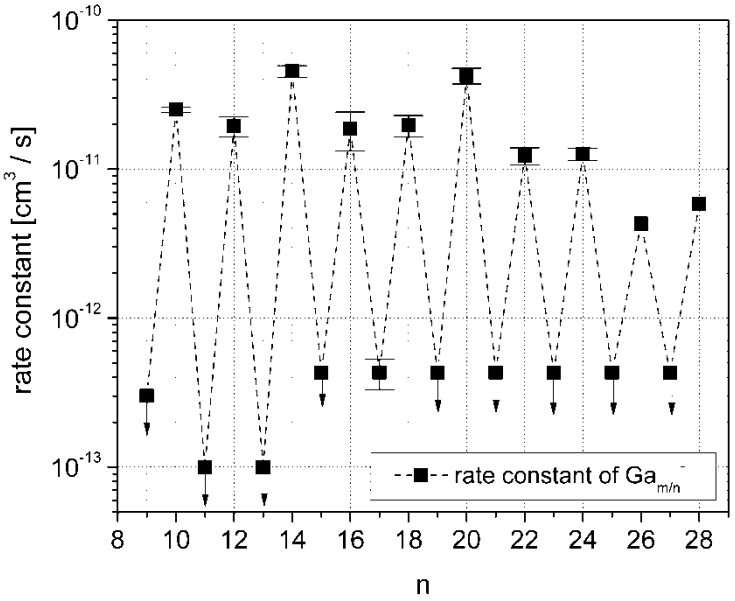

Figure 4.2.1. Measured rate coefficients of $Ga_{m/n}^-$ clusters with O_2. Error bars originate from at least two independent measurements carried out on different days. For numerical values of Ga_9^- see Table 4.2.2.

By knowing the reaction behavior of some single-sized clusters M_n^- (see above), we were also able to study and characterize the reactivity of a whole collection of differently sized clusters (e.g., Ga_{11}^- – Ga_{28}^-) at once and to numerically fit the integrated rate equations of the consecutive reaction steps to the experimental data to obtain pseudo-first-order rate coefficients, k_i (see Supporting Information). For these calculations, the software *DetMech*[31] was used.

Since for several cluster types the rate coefficient ki was determined by isolating the single clusters first (e.g., Ga_{10}^-, Ga_{13}^-, Ga_{22}^-, and Al_{13}^-), the reliability of the collective measurements has been confirmed because values from both measurements agree well.

In order to derive reliable reaction rates of the $M_{m/n}^-$ clusters, all ion intensities were normalized to the intensity of Ga_9^-. This is justified because (1) the rate coefficient of M_9^- with O_2 is much smaller (about a factor of 100) compared with the other (even-numbered) clusters and (2) there is no cluster that reacts to give M_9^- because for Al_{13}^- and Ga_{13}^-, even at prolonged reaction times of up to 600s, no reaction with O_2 was observed (cf. above).

In order to generate $Al_{m/n}H^-$ clusters, the $Al_{m/n}^-$ clusters were exposed to a hydrogen atmosphere at 10^{-6} mbar for 1−3 s.[18]

Model for the Primary, Rate-Determining Step. The overall reactions of Al_x^- and Ga_x^- clusters with O_2 are exemplarily summarized for Al_x^- clusters in the following equations, which are divided into spin-forbidden (2a) and spin-allowed reactions (2b):

$$\text{odd-numbered clusters } {}^1Al_n^- + {}^3O_2 \rightarrow {}^1Al_{n-4}^- + 2\ {}^1Al_2O \qquad (2a)$$

$$\text{even-numbered clusters } {}^2Al_m^- + {}^3O_2 \rightarrow {}^2Al_{m-4}^- + 2\ {}^1Al_2O \qquad (2b)$$

Note, however, that this four electron reaction[32] is only the simple summarization of a very complex reaction route in which many intermediates are involved. Since quantum chemical calculations of the complex potential energy surface (PES) for the

Al_x^- + O_2 reactions are not expected to give reliable results for transition states, we tried to develop a plausible model by correlating our measured rate coefficients with the potential energies of stable and metastable species. Additional information is gained from the different reaction rates of Al_x^- clusters with Cl_2 and with O_2 if no spin transition occurs. From our DFT calculations, it follows that the first well-defined intermediate in every $Al_{n/m}^-$ + O_2 reaction is a $[Al_{n/m}^+\cdots O_2^{2-}]^-$ species (in the following denoted by **X**) in which a peroxo (O_2^{2-}) group is polar bonded to the $Al_{n/m}^-$ cluster via two oxidized Al atoms (Al^+). In Figure 4.2.2, the situation is exemplified for Al_{13}^- + O_2, with $^1[Al_{13}^+\cdots O_2^{2-}]^-$ as the intermediate **X**. Note that in the following, the stabilization energy of **X** with respect to the reactants is denoted by ΔE^X. For all even-numbered Al_m^- clusters, this intermediate **X** is in a doublet state and formed without spin restrictions; for the odd-numbered clusters Al_n^-, however, X is in a singlet state, and a spin flip is necessary.

The peroxo moiety O_2^{2-} within these intermediates (also present in H_2O_2, for example),[1] bonded to two different metal atoms of the cluster, represents a chemically well-known situation with classical bonding,[28] which is isoelectronic to that of the $\mathbf{F}_2$ molecule. Therefore, an intermediate **X** of this type can be expected to have a pronounced local minimum on the PES in accordance with our DFT results.

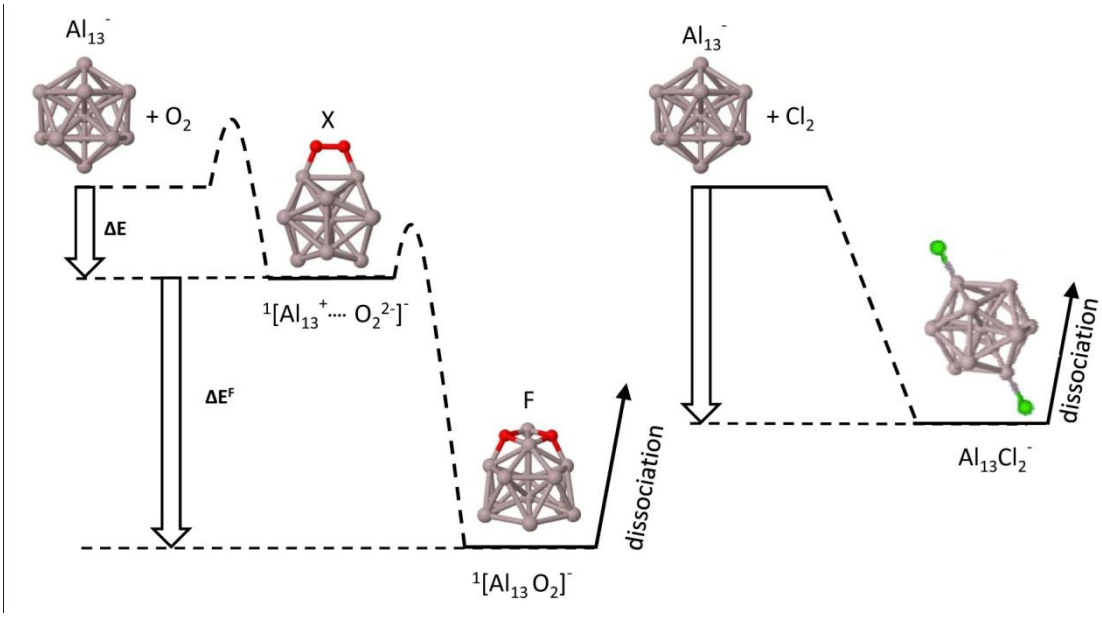

Figure 4.2.2. (left) Schematic presentation of the reaction path of an $Al_{n/m}^-$ cluster with $^3O_2$. As a spin-forbidden example, the hindered reaction of the Al_{13}^- cluster is shown: Al_{13}^- reacts via spin transition to the peroxo-bonded O_2^{2-} intermediate **X** ($^1Al_{13}^- + {}^3O_2 \rightarrow {}^1[Al_{13}^+\cdots O_2^{2-}]^-$) (energy gain ΔE^X) and finally to the more stable anion **F**, $^1[Al_{13}O_2]^-$ (ΔE^F) corresponding to complete oxidation of the Al_{13}^- cluster with a single O_2 molecule (cf. text). (right) Spontaneous reaction of Al_{13}^- cluster with Cl_2 to the completely oxidized $[Al_{13}Cl_2]^-$ intermediate, which rapidly decomposes to Al_{11}^- + 2AlCl.[33]

Thus, the $[Al_{n/m}^+\cdots O_2^{2-}]^-$ intermediate **X** with its local energy minimum ΔE^X (Table 4.2.1) corresponds to the first well defined step along the reaction route, where the O_2 molecule has obtained two electrons from the $Al_{n/m}^-$ cluster. The $[Al_{n/m}^+\cdots O_2^{2-}]^-$ intermediate has O_2 bonded side-on, bridging between two aluminum atoms. With the

Table 4.2.1. Calculated (DFT) values of ΔE^X and $\Delta E^X + \Delta E^F$ (unit: eV) for the energy gain from the reactants (e.g. $Ga_{13}^- + {}^3O_2$) to the side-on bonded intermediate **X** (e.g. $[Ga_{13}^+\cdots O_2^{2-}]^-$) and to the ground state **F** (e.g. $[Ga_{13}O_2]^-$).[a]

	Ga_9^-	Ga_{10}^-	Ga_{11}^-	Ga_{12}^-	Ga_{13}^-	Ga_{14}^-	Al_{13}^-	Al_{14}^-
$-\Delta E^X$	1.84	1.92	1.87	1.83	1.14	2.1	2.21	3.1
$-\Delta E^X + -\Delta E^F$	4.58	5.45	4.62	4.73	4.64	5.12	6.99	8.10

[a]For explanation, see Figure 4.2.2.

transfer of two electrons, the $Al_{n/m}^-$ cluster is oxidized to an $Al_{n/m}^+$ unit, and the O−O bond distance is elongated becoming an O−O single bond in the O_2^{2-} moieties, the normal octet of electrons is maintained on each oxygen atom. This $[Al_{n/m}^+\cdots O_2^{2-}]^-$ intermediate reflects just the first step of the complete reaction with a four-electron transfer to two bridging O^{2-} ions of the final $[Al_{n/m}O_2]^- = [Al_{n/m}^{3+}\cdots 2O^{2-}]^-$ dioxide cluster **F** (Figure 4.2.2), which represents the global minimum.

Under high-vacuum conditions, collisional stabilization of the vibrationally excited dioxide $[Al_{n/m}O_2]^-$ cluster **F** (see Table 4.2.1) can be neglected because a low-lying decomposition channel giving $Al_{n/m-4} + 2Al_2O$ exists (Figure 4.2.3).[34] As illustrated in Figure 4.2.2 and discussed in the following, it is probably not the formation of this final, highly vibrationally excited dioxide cluster **F**, ($\Delta E^X + \Delta E^F$), that determines the overall rate constant but instead, the formation of the above-mentioned peroxo-bonded $[Al_{m/n}^+\cdots O_2^{2-}]^-$ intermediate **X** (Figure 4.2.2) with a much lower energy gain ΔE^X in the range of 2−3 eV. The calculated energies of the ground state **F** and the intermediate **X** of all $Al_{n/m}^-$ and $Ga_{n/m}^-$ clusters under discussion are listed in Table 4.2.1, and the corresponding structures are presented in the Supporting Information.

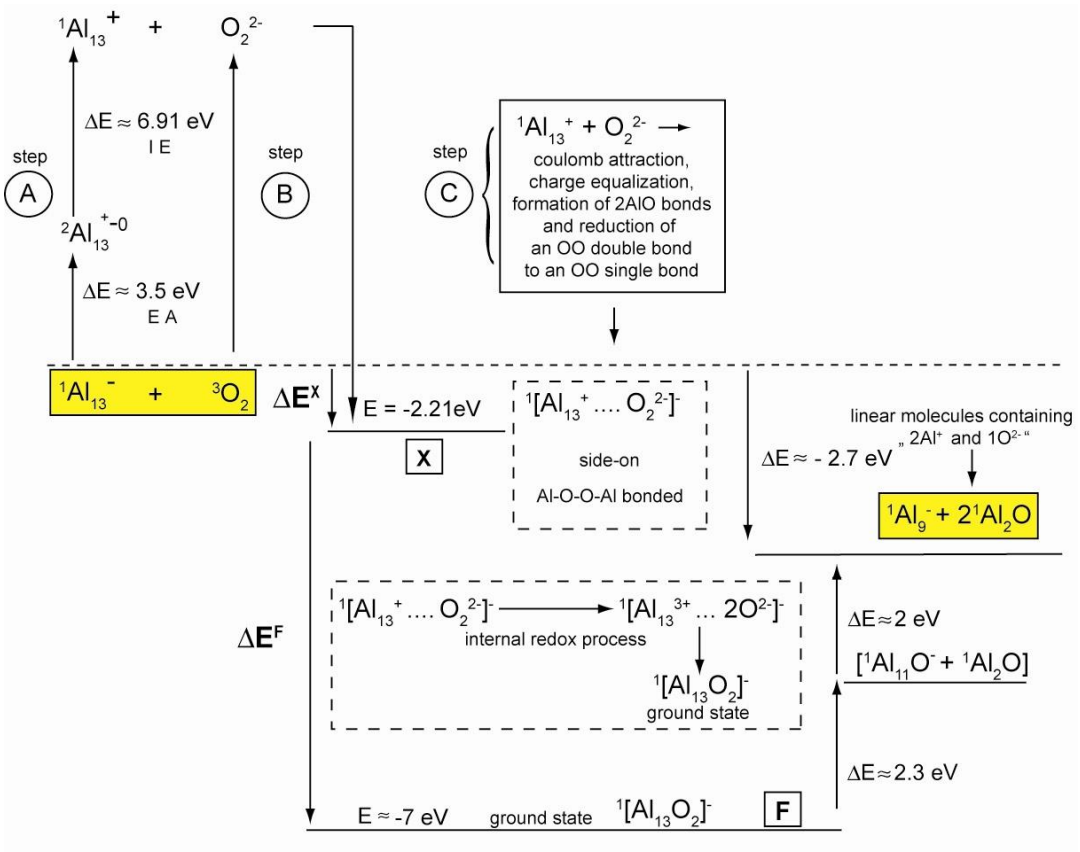

Figure 4.2.3. A schematic energy cycle of the $^1Al_{13}^- + {}^3O_2$ reaction (reactants and final products are yellow; see text). In order to understand the formation of the side-on bonded intermediate $[Al_{13}^+\cdots O_2^{2-}]^-$, **X**, (Figure 4.2.2) an alternative route via a hypothetical set of steps **A**, **B**, and **C** is constructed. The multistage process from the $^1[Al_{13}^+\cdots O_2^{2-}]^-$ intermediate to the ground state $^1[Al_{13}O_2]^-$, species **F**, (Figure 4.2.2) and its subsequent decomposition to the observed Al_9^- cluster is simplified. The primary reaction of the reactants proceeds via a weakly bonded charge/induced dipole complex (not shown) and a spin transition barrier (not shown) to the peroxo intermediate $[Al_{13}^+\cdots O_2^{2-}]^-$, **X**. Its energy corresponds to the value of $\Delta E^X = E(\mathbf{A}) + E(\mathbf{B}) + E(\mathbf{C})$.

This conclusion is supported by our previous investigations on (spin-allowed) reactions of Al_{13}^- with Cl_2, in which Al_{11}^- and 2AlCl molecules are formed spontaneously via decomposition of the excited $[Al_{13}Cl_2]^-$ cluster and which are faster (3−6 times)[6,33] than those of the even- numbered Al_m^-/Ga_m^- clusters with O_2, which are also spin-allowed.

Despite the smaller energy gain in forming the most stable oxidized cluster (4.5 eV for $Al_{13}^- + Cl_2 \rightarrow [Al_{13}Cl_2]^-$ compared with 7 eV for $Al_{13}^- + O_2 \rightarrow [Al_{13}O_2]^-$), the overall reaction $Al_{13}^- + Cl_2$ is faster than the overall reaction $Al_{13}^- + O_2$. From this observation, we conclude that for the $Al_{m/n}^- + O_2$ reactions, a less excited intermediate is likely to exist that determines the rate of the overall reaction. From our quantum chemical calculations, it follows that this intermediate is the peroxo species, **X**, $[Al_{m/n}^+...O_2^{2-}]^-$.

On the basis of these arguments, we propose the following general model for the $Al_{m/n}^- + O_2$ reaction: The energy gain ΔE^X for the formation of the peroxo intermediate determines the overall rate of reaction. The larger the energy gain, the larger the rate coefficient. This could be a manifestation of the Evans−Polanyi principle (see e.g., ref 35). If the reaction is spin-forbidden, the rate is slowed down.

Table 4.2.2. Experimentally determined rate coefficients [10^{-11} cm^3 s^{-1}].[a]

	Ga_9^-	Ga_{10}^-	Ga_{11}^-	Ga_{12}^-	Ga_{13}^-	Ga_{14}^-	Ga_{15}^-	Ga_{16}^-
	0.03[b]	2.5 +/- 0.1	0.01[b]	2.0 +/- 0.3	0.01[b]	4.5 +/- 0.4	0.04[b]	1.9 +/- 0.5
Al_8^-		Al_{10}^-		Al_{12}^-		Al_{14}^-		Al_{16}^-
8.8 +/- 3.9		6.0 +/- 0.6		3.0 +/- 0.3		4.5 +/- 0.6		4.2 +/- 0.9

[a]The given error is derived from at least two independent measurements. Note that the absolute error is estimated to be on the order of ±50% and is mainly due to uncertainties of the pressure measurement. [b]Only the upper limit could be determined.

The High Reactivity of the Even-Numbered Al_m^- and Ga_m^- Clusters. In order to verify the above-mentioned model, we examined first the open-shell gallium clusters Ga_{10}^-, Ga_{12}^-, and Ga_{14}^-, for which the rate coefficients can be determined more accurately than for the similar Al_{10}^-, Al_{12}^-, and Al_{14}^- clusters. This is because the intensities and particle densities of the $Ga_{n/m}^-$ clusters are higher than those for the $Al_{n/m}^-$ clusters due to their different formation process. In any case, the reactions of even-numbered Al_m^- and Ga_m^- clusters with $^3O_2$ are spin-allowed (cf. eq 2b) and therefore can proceed spontaneously, which is confirmed by our experiments. The experimentally determined rate coefficients are displayed in Figure 4.2.1 and collected in Table 4.2.2.

Clearly, the rate coefficients increase in the sequence, $Ga_{12}^- \approx Ga_{16}^- < Ga_{10}^- < Ga_{14}^-$. Even accounting for absolute errors, the measured rate coefficients are below the Langevin limit by a factor of 20, this limit being on the order of 5×10^{-10} cm^3 $s^{-1}$for the $Ga_{m/n}^- + O_2$ reactions (polarizability of O_2 = 1.58 $\times 10^{-30}$ cm^3).[36] Obviously, the capture of O_2 by the cluster ion (ion/induced dipole interactions) is not the rate-determining step, and an energy barrier or an entropic bottleneck, in the case of the even-numbered

clusters, between a weakly bound charge/induced dipole complex and the more stable $[Ga_m^+\cdots O_2^{2-}]^-$ intermediate is likely to exist. This conclusion is supported by the approximately two times faster, more exoergic O_2 reaction of Al_m^- clusters versus the analogous Ga_m^- clusters (see Table 4.2.2).[37] This is strong evidence for explaining the origin of the different rate coefficients of Al_m^- and Ga_m^- clusters. The rate-determining formation of the peroxo intermediate $^2[M_m^+\cdots O_2^{2-}]^-$ is more exoergic (ΔE^X) for the Al_m^- clusters; that is, more energy (about 1 eV) is gained for Al_{14}^- than for Ga_{14}^-. Obviously, a correlation exists between the measured rate coefficient and the calculated ΔE^X values.

Assuming a similar reaction mechanism for the different Ga_m^- clusters, the Ga_{10}^- cluster should react somewhat faster than Ga_{12}^-, and Ga_{14}^- should react significantly faster than Ga_{10}^- and Ga_{12}^-, which is in line with the experimental observation of the reaction rates (see preceding); that is, the Ga_{14}^- cluster exhibits the highest reactivity of all even-numbered Ga_m^- clusters because of its high exoergicity for the formation of the rate-determining peroxo intermediate, **X**, for example, 2.1 eV for $[Ga_{14}^+\cdots O_2^{2-}]^-$. This interpretation is surprisingly supported by kinetic investigations of the O_2 reactions with alkyl radicals,[38] a completely different reaction system. As can be seen from Table 4.2.3, for both reactions (with open-shell Ga_m^- clusters and alkyl radicals), not only are the absolute rate coefficients very similar, but also a correlation is seen between the rate coefficients and the exoergicity of the association step.

Table 4.2.3. Experimental rate coefficients and calculated exoergicity for selected $^2Ga_m^-$ + O_2 and alkyl radical + O_2 reactions.[a]

Cluster	k / 10^{-11} (cm^3 s^{-1})	ΔE^X (eV)	radical[38]	k / 10^{-11} (cm^3 s^{-1})	–BDE (eV)
Ga_{10}^-	2.5	–1.92	primary alkyl	0.8	–1.54
Ga_{12}^-	2.0	–1.83	secondary alkyl	1.2	–1.62
Ga_{14}^-	4.5	–2.10	tertiary alkyl	2.0	–1.68

[a]BDE, bond dissociation energy of the R–O_2 bond.[38]

The Low Reactivity of Odd-Numbered Al_n^- and Ga_n^- Clusters. The fast O_2 reactions of all even-numbered Ga_m^- clusters are in contrast to the hindered reactions of the odd-numbered Ga_n^- clusters with rate coefficients below the Langevin limit by a factor of >1000 (cf. Figure 4.2.1 and Table 4.2.2). Like in the case of the Al_{13}^- and Ga_{13}^- clusters, an energy barrier has to be overcome during which the spin transition proceeds. This barrier, as with the even-numbered Ga_m^- clusters, should depend also on the stability of the peroxo intermediate **X**, for example, $[M_{13}^+\cdots O_2^{2-}]^-$. For the Ga_{13}^- cluster, the energy gain for this side-on intermediate is −1.14 eV. Furthermore, also for adjacent odd-numbered Ga_n^- clusters, the relationship between ΔE^X and the rate coefficient can be expected to apply. For Ga_9^- and Ga_{11}^-, the following ΔE^X values are calculated: −1.84 and −1.87 eV (Table 4.2.2). From these more exoergic reactions, in comparison to Ga_{13}^- (−1.14 eV), a faster reaction than for Ga_{13}^- should be expected. But unfortunately, for each of these three clusters, the rate coefficient is too small to be measured exactly under our experimental conditions; that is, only an upper limit can be given. Moreover, since the situation for the O_2 reaction with Ga_{11}^- is unexpectedly complex (see Supporting Information),one should only compare Ga_9^- and Ga_{13}^-. Specifically, Ga_{13}^- exhibits the

smallest and Ga_9^- the largest upper limit, which is at least in line with our proposed correlation.

Comparison of Even- and Odd-Numbered Clusters. So far it seems as if a consistent picture can be drawn within the series of odd- and even-numbered $Al_{n/m}^-$ and $Ga_{n/m}^-$ clusters in the limited size windows, Ga_9^- to Ga_{14}^- and Al_{13}^- to Al_{14}^-. Furthermore, this picture is also valid, if one compares the slowest and the fastest reaction of an even/odd cluster pair. The ΔE^X values for the formation of the peroxo intermediates **X** of Al_{13}^- and Al_{14}^- are −2.2 and −3.1 eV, respectively. For the analogous Ga_{13}^-/Ga_{14}^- pair, the following ΔE^X values are calculated: −1.14 and −2.1 eV, respectively. In the case of the Ga clusters, an increase of a factor of ~ 400 is observed for the rate coefficients (Table 4.2.2).[39]

The moderate correlation between the ΔE^X values and the rate coefficients for the M_{13}^-/M_{14}^- pair gives a first indication that there must be an additional influence, besides energy, on the reaction rate. This assumption is confirmed by the following example, for which drastically different reaction rates are observed even though the ΔE^X values are similar. As shown above, there are fast spontaneous reactions for Ga_{10}^- and Ga_{12}^- with ΔE^X values of −1.92 and −1.83 eV, respectively. Though the ΔE^X values for Ga_9^- and Ga_{11}^- (−1.84 and −1.87 eV, respectively) are in the same range, the rate coefficients for the latter ones are about 100 times slower (see Table 4.2.2).

Obviously, there is a rate-decreasing process for the odd-numbered Ga_n^- clusters, because an accelerating process for the even-numbered Ga_m^- clusters can be ruled out.[40]

The spin-forbidden transition during the slow reaction of the odd-numbered clusters (e.g., singlet Al_{13}^- with $^3O_2$ toward the singlet $^1[Al_{13}^+\cdots O_2^{2-}]^-$ intermediate)

should cause an additional increase of the barrier, which in a first approximation was discussed above, as being based only on the relatively low exoergicity ΔE^X of the reaction.

Therefore, the striking difference between the rate coefficients for the even- and odd-numbered clusters gives a strong indication that the hindered $^3O_2$ reaction with closed-shell clusters is based on an additional barrier caused by the spin transition.

Can Reactivities for Size-Similar Open- And Closed-Shell Clusters Be Estimated? Besides the special effect of the spin transition, which causes a dramatic decrease of the reaction rate, there is clearly a significant correlation between the $Al_{n/m}^-/Ga_{n/m}^-$ + O_2 reaction rates of different clusters and the energy gain ΔE^X from the educts to the peroxo intermediates, which have been calculated with DFT methods. Now the question arises whether it is possible to make a simpler prediction about the reactivity of such clusters based on the ΔE^X correlation.

In order to illustrate this approach, we have developed a thermodynamic cycle leading to the peroxo intermediate **X**, which is shown in Figure 4.2.3. Using the Al_{13}^- cluster as a prominent example, the cycle involves the reactants $^1Al_{13}^-$ and $^3O_2$, which react with a ΔE^X value of −2.21 eV (Table 4.2.2) to form **X**, $^1[Al_{13}^+\cdots O^{2-}]^-$.

This model process begins with the two-step oxidation (EA + IE) of Al_{13}^- to Al_{13}^+ (**A**) and the two-step reduction of $^3O_2$ to the singlet dianion O_2^{2-} (**B**) (isoelectronic to the F_2 molecule). Subsequently, the Coulomb attraction between Al_{13}^+ and O_2^{2-} and the formation of two Al−O bonds via charge neutralization proceed, releasing energy, and finally the $^1[Al_{13}^+\cdots O_2^{2-}]^-$ intermediate, **X**, is formed (**C**). Since during this whole process[41] step **C** is nearly the same for $Al_{m/n}^-$ and $Ga_{m/n}^-$ clusters, provided they are of

similar size as those discussed in this paper (e.g., Ga_9^-, Ga_{11}^-, and Ga_{13}^- or Ga_{10}^-, Ga_{12}^-, and Ga_{14}^-), the energy gain ΔE^X calculated with DFT methods should be mainly reflected by the differences in step **A**. The energy values of step **A** for some $Al_{n/m}^-$ and $Ga_{n/m}^-$ clusters have been calculated and are collected in Table 4.2.4. These values mainly determine the ΔE^X values and therefore the rate coefficients (Figure 4.2.3): The smaller the value of E(**A**) = EA + IE, the more negative the value of ΔE^X, as the exoergic formation of Ga−O/Al−O bonds, step **C**, will further exceed **A**.

In the following, we will concentrate on the Ga_m^- cluster reactions. First we look at the spontaneous reactions of Ga_{10}^-, Ga_{12}^-, and Ga_{14}^-. The reaction with Ga_{14}^- exhibits the largest rate coefficient. This property of Ga_{14}^- is in line with its smallest value of E(**A**) (8.57 eV), while for the slower reaction of Ga_{12}^-, the largest value of E(**A**) (8.87 eV) has been obtained. Therefore, as mentioned above, the values of E(**A**) for the clusters Ga_{10}^-, Ga_{12}^-, and Ga_{14}^- are in line with the observed increasing reactivity toward O_2 of these Ga_n^- clusters: $Ga_{12}^- < Ga_{10}^- < Ga_{14}^-$.

This simple ionic model is also in line with the reactivity of the closed-shell clusters Ga_9^-, Ga_{11}^-, and Ga_{13}^-. The largest value of E(**A**) is obtained as expected for Ga_{13}^-, which is in line with the lowest reactivity. The Ga_{11}^- cluster should exhibit a higher reactivity than the Ga_{13}^- cluster, and the Ga_9^- cluster should show the highest reactivity of these three species. Though the experiments result in a similar reactivity of Ga_{13}^- and Ga_{11}^- with respect to the upper limits, this rough prediction without the consideration of the spin transition for the three clusters at least seems to reflect the principal trend. Thus, within the series of even-numbered and odd-numbered clusters, the

simple ionic model is in line with experiments as well as with the results of DFT calculations.

Table 4.2.4. Electron affinities (EA, eV) and ionization energies (IE, eV) of neutral $Al_{m/n}$ and $Ga_{m/n}$ clusters (n/m = 9−14) obtained from our DFT calculations.

	$Al_{m/n}$			$Ga_{m/n}$		
m/n	EA	IE	[EA + IE] [a]	EA	IE	[EA + IE] [a]
9	2.76	6.37	9.13	2.87	5.94	8.81
10	2.67	6.42	9.09	2.47	6.24	8.71
11	2.84	6.24	9.08	2.79	6.37	9.17
12	2.78	6.39	9.17	2.58	6.29	8.87
13	3.50	6.91	10.41	3.29	6.10	9.39
14	2.61	5.95	8.56	2.42	6.15	8.57

[a]This value corresponds to **A** in Figure 4.2.3.

Consequences from the Predicted Reactivity Based on the Ionic Model: Spin Transition Causes an Additional Hindrance. What about the validity of this simple model if one compares even- and odd-numbered Al_x^-/Ga_x^- clusters?[42] The difference, ΔE(**A**), of the E(**A**) values (Figure 4.2.3, Table 4.2.4) for Ga_{13}^- and Ga_{14}^- (ΔE(**A**) = 9.39 − 8.57 eV = 0.82 eV) corresponds to a strong increase in the O_2 reactivity from Ga_{13}^- to Ga_{14}^- by over three orders of magnitude. The acceleration of the reaction is less prominent from Ga_{11}^- to Ga_{12}^- (ΔE(**A**) = 0.3 eV) and the smallest difference is to be expected for the pair Ga_9^- to Ga_{10}^- (ΔE(**A**) = 0.1 eV). However, since even the low value of ΔE(**A**) = 0.1 eV is contrasted by an observed increase in the O_2 reactivity from Ga_9^- to Ga_{10}^- of about two orders of magnitude, there must be an additional factor that will be responsible for this large difference in the reaction rates. Furthermore, even the large

$\Delta E(\mathbf{A})$ value between Ga_{13}^- and Ga_{14}^- may be not sufficient to explain the strongly different reaction rates between the slowest (Ga_{13}^-) and the fastest (Ga_{14}^-) reacting cluster alone. Consequently, there has to be a further factor that decreases the reaction rate of the odd clusters (Ga_9^-, Ga_{11}^-, Ga_{13}^-) so drastically. This contribution, as discussed above, can only be the hindered spin transition, which, for example, makes the $Ga_{13}^- + O_2$, as well as the $Al_{13} + O_2$, reaction extremely slow.

The Reactivity of $Al_{13}H^-$ and $Al_{14}H^-$ Clusters. All in all, our proposed model seems to be on solid ground. Nevertheless, we expand our discussion to two hydrogen-containing Al clusters, which already had given strong experimental indications of the essential influence of the spin conservation rule.[18,20] If one H atom is added, then also one electron is added to the cluster, and consequently, the O_2 reactivity changes dramatically. The $Al_{13}H^-$ species as an open-shell cluster is highly reactive in contrast to the inert Al_{13}^- cluster, and the $Al_{14}H^-$ closed-shell cluster is strongly unreactive in contrast to the fast reaction of Al_{14}^-. We have roughly verified this change, which has been shown experimentally for $Al_{13}H^-$ and $Al_{14}H^-$,[18] by DFT calculations. A detailed discussion would require a separate paper, since many isomers have to be included for these Al_nH^- clusters in which the H atom can easily migrate on the cluster surface.[43] Therefore, only a small number of isomers ($Al_{13}H^-/[Al_{13}H\cdots O_2]^-/Al_{13}HO_2^-$ and $Al_{14}H^-/[Al_{14}H\cdots O_2]^-/Al_{14}HO_2^-$) were considered in our calculations. As was the case in the hydrogen-free clusters, energy gains were seen when going from reactants to the intermediate **X** and again going from **X** to the final product **F**. Some results are listed in the Supporting Information, from which the following conclusion can be drawn: The ΔE^X and the ΔE^F values are similar to those of the H-free clusters Al_{13}^- and Al_{14}^-. Therefore,

these results once more confirm that it is not the formation of the highly excited species **F** but instead the formation of the intermediate **X** that determines the O_2 reaction rate. Furthermore, these results are in line with the conclusion that the spin conservation rule is responsible for the different reactivity of the open-shell and the closed-shell $Al_{n/m}^-$ and $Al_{n/m}H^-$ clusters with $^3O_2$.

CONCLUSION AND OUTLOOK

In order to understand the slower reactions of Al_x^- clusters with O_2 compared with their fast reactions with Cl_2, we have investigated a number of spin-allowed and spin-forbidden O_2 reactions with Al_x^- clusters in the size neighborhood of the Al_{13}^- cluster. Furthermore, we have extended our investigations to similar Ga_x^- clusters to examine whether our results are restricted to Al or are also valid for other metal atom clusters, as well as for the oxidation of metal surfaces in general. Accordingly, rate coefficients of the reactions of O_2 with Al_x^- and Ga_x^- (x = 9−14) near the size of the exceptional M_{13}^- have been measured by FT-ICR mass spectrometry under single collision conditions, that is, subsequent fast unimolecular reactions proceed before the next collision occurs. These measurements, which quantify the even/odd properties of these clusters, in particular, the fast reaction of the even-numbered, open-shell clusters and the slow, spin-forbidden reactions of the odd-numbered, closed-shell clusters, have been complemented by DFT calculations in which we have computed the ground state energies of the reactants, the intermediates, and the products. These results provide guidelines for the discussion of the experimentally determined rate coefficients. The critical intermediate that determines the reaction rate has a normal valence bonding

character, because it contains the well-known peroxo unit $(O{-}O)^{2-}$, which is bonded to two neighboring metal atoms on the surface of the M_x^- cluster, after it is partially oxidized to a M^+ cluster. Simultaneously, the O_2 molecule is reduced to the O_2^{2-} moiety. The energy gain, ΔE^X, during formation of this $[M_x^+\cdots O_2^{2-}]^-$ intermediate is correlated to the rate coefficient of the M_x^- + O_2 reaction. The larger ΔE^X, the larger is the rate coefficient observed (for the spin-allowed reactions). This fundamental conclusion is furthermore supported by (a) the faster O_2 reactions of the Al_x^- clusters in comparison to the Ga_x^- clusters, because the formation of Al−O bonds is more exothermic than the formation of Ga−O bonds, and (b) the spin-allowed reaction of Al_x^- clusters with Cl_2 being faster than the spin-allowed reactions with O_2. This result is in line with our model if in reactions with chlorine, the formation of the highly excited dichloride cluster $Al_xCl_2^-$ is the rate-determining step (e.g., $Al_{13}Cl_2^-$ is excited with 4.5 eV and reacts to give Al_{11}^- + 2 AlCl) and if in reactions with oxygen the intermediate **X** (e.g., $[Al_{14}^+\cdots O_2^{2-}]^-$ with 3.1 eV) represents the critical, rate-determining species.

However, the energy of this intermediate $[M_x^+\cdots O_2^{2-}]^-$ cannot, by itself, completely account for the experimental findings regarding the reactivity of similar even- and odd-numbered clusters (e.g., Ga_{13}^- and Ga_{14}^-). The spin transition during the reaction of the odd-numbered cluster causes an additional hindrance for the $^3O_2$ reaction. This conclusion has been convincingly confirmed in calculations related to the recent experimental results for the H-containing clusters $Al_{13}H^-$ and $Al_{14}H^-$. Though the ΔE^X values of the O_2 reactions with $Al_{13}H^-$ and Al_{13}^- as well as with $Al_{14}H^-$ and Al_{14}^- are very similar, the reactivity changes radically. The addition of one H atom turns spin-forbidden reactions into spin-allowed reactions and vice versa; thus rates of reactions

with an even number of aluminum atoms are strongly increased, and rates of reactions with odd numbers of aluminum atoms are conversely strongly decreased.

Furthermore, we developed a model that allows us to make predictions on the trends in O_2 reactivity within a small number of similar metal atom clusters. In this simple model, the formal oxidation of the metal cluster anion, M_x^-, to the cluster cation (e.g., $Al_x^- \rightarrow Al_x^+$) determines the ΔE^X value and therefore is responsible for the differing reactivity of the clusters.

To summarize, the quantification of the rate coefficients for a small number of Al_x^- and Ga_x^- clusters in the size vicinity of the exceptional Al_{13}^-/Ga_{13}^- species in principle seems to allow a deeper insight into all reactions of O_2 with metal atom clusters and possibly also with surfaces of bulk metals;[7] that is, also small changes within the geometric structure of surfaces will change the reactivity. Therefore, our results may also be of fundamental interest for many catalytic processes on metal surfaces where the addition or substitution of a single atom can change the reactivity dramatically.

In our ongoing experiments, we plan to quantify the spin-forbidden reactions of O_2 with Al_{13}^- and Ga_{13}^- clusters via well defined excitation of the clusters to overcome the reaction barrier during the spin transitions. These results will be published in a separate paper.[22]

EXPERIMENTAL SECTION

All experiments were carried out in a commercial FT-ICR mass spectrometer (Ion Spec, Ultima) equipped with a 7T actively shielded magnet (Cryomagnetics, Oak Ridge,

TN, USA). Since the experimental setup and methodology was described elsewhere in detail,[6,18,44–46] only the essentials are given here.

Negatively charged aluminum and gallium clusters ($Al_{m/n}^-$, $Ga_{m/n}^-$) were generated by laser desorption from $LiAlH_4$[6,44] and GaN, respectively,[25] where the commercial MALDI (matrix-assisted laser desorption/ionization) source of the FTICR-MS was used (nitrogen laser, λ = 337.1 nm, pulse energy = 300 μJ, pulse width ≈ 4 ns (FWHM)).

After cluster formation, the ions were transferred into a cylindrical ICR cell via a quadrupole ion guide. To ensure efficient ion trapping (gas assisted dynamic trapping) and translational cooling of the cluster ions, argon (Argon 6.0, basi Sch berl GmbH & Co. KG) was admitted into the cell with a pulsed valve (General Valve) at a pressure of around 1×10^{-5} mbar for ~1 s.

For the study of ions with one particular mass-to-charge ratio (e.g., m/z = 351.77 for Al_{13}^-), the species were isolated by the SWIFT (stored waveform inverse Fourier transform) excitation technique.[47] A second thermalization step was carried out in some cases to prevent possible (re)excitation of the ions due to the isolation process and to ensure thermal conditions. Because the second thermalization step did not change the measured rate coefficient within the experimental error, we conclude that ion (re)excitation by the SWIFT method can be neglected.

QUANTUM CHEMICAL CALCULATIONS

The theoretical studies concerning the kinetics are analogous to those presented recently.[33] It should be noted that interpretation of experimentally observed rate

coefficients by computations demand clear knowledge of the potential energy surface with accurate estimation of threshold energies of the various intermediates, which in turn depend on the computational method; therefore we use reaction energies as a guide to understand the reactivity of the various clusters presented here. All the calculations were performed using the generalized gradient approximation (GGA) within the framework of the DFT. The gradient corrected exchange and correlation functionals due to Becke−Perdew were employed here.[48] Split valence basis set supplemented with polarization functions was used for all the atoms.[49] The computations were carried out using the Turbomole software.[49] In the self-consistent field (SCF) calculations, the density and energy tolerances were set to 10^{-6} *e*/bohr^3 and 10^{-6} hartree, respectively. In the geometry optimization, all the structural parameters were fully optimized without any symmetry constraints, with an energy convergence of 10^{-5} hartree and a maximum gradient of 10^{-4} hartree/bohr. The lowest and other higher energy isomers of all oxide clusters were obtained using an unbiased systematic structure search based on genetic algorithm method.[50,51] In this procedure, all the structures generated either through initial population or cross breeding were fully optimized without any constraints using the same methods mentioned above.

ACKNOWLEDGEMENTS

This work was supported by the Karlsruhe Institute of Technology (KIT), Deutsche Forschungsgemeinschaft (DFG), and Fonds der Chemischen Industrie. This material is based in part on work supported by the Air Force Office of Scientific Research (AFOSR) under Grant Numbers, FA9550-11-1-0068 (K.H.B.) and FA9550-11-1-0171 (B.E.). K.H.B. and B.E. also thank the Defense Threat Reduction Agency (DTRA) for partial support under Grant Number HDTRA-1-12-1-007. B.K. acknowledges financial support from the BoR-RCS grant. This manuscript is dedicated to Peter Jutzi on the occasion of his 75th birthday and his outstanding contributions in main group organometallic chemistry.

REFERENCES

1. (a) *Holleman-Wiberg, Inorganic Chemistry*; Academic Press: San Diego, London, 2001. (b) *Holleman-Wiberg, Lehrbuch der Anorganischen Chemie*, 102. erweiterte Auflage; Wiberg, N., Wiberg, E., Holleman, A., Eds; Walter de Gruyter: Berlin, New York, 2007.
2. Binnewies, M.; Milke, E. *Thermodynamical Data of Elements and Compounds*; Wiley-VCH: Weinheim, Germany, 1999.
3. Chase, M. W., Jr. *J. Phys. Chem. Ref. Data* **1998**, No. Monograph 9, 1−1951.
4. Al_2O is also the essential gaseous molecule after the O_2 oxidation of Mg-doped $Al_xM_g^-$ cluster anions. Luo, Z.; Grover, C. J.; Reber, A. C.; Khanna, S. N.; Castleman, A. W., Jr. *J. Am. Chem. Soc*. **2013**, *135*, 4307−4313.
5. If the Cl_2 partial pressure is low and the temperature of the Al metal is about 700 °C, AlCl molecules are formed first, which are afterwards oxidized to $AlCl_3$: $Al + ½Cl_2 \rightarrow AlCl_{(g)}$; $AlCl_{(g)} + Cl_2 \rightarrow AlCl_{3(g)}$ (see ref 6).
6. Burgert, R.; Schn ckel, H.; Olzmann, M.; Bowen, K. H., Jr. *Angew. Chem*. **2006**, *118*, 1505−1508; *Angew. Chem., Int. Ed*. **2006**, *45*, 1476− 1479.
7. (a) Ertl, G. *Reactions at Solid Surfaces*; John Wiley & Sons Inc.: Hoboken, NJ, 2009. (b) Carbogno, C.; Groß, A.; Meyer, J.; Reuter, K. O_2 Adsorption Dynamics at Metal Surfaces: Non-Adiabatic Effects, Dissociation and Dissipation. In *Dynamics of Gas-Surface Interactions: Atomic-level description of Elementary Processes*; Mui o, R. D., Busnengo, H. F., Eds.; Springer Series in Surface Sciences; Springer: Berlin, 2013; Vol. 50, pp 389−419.

8. (a) Brune, H.; Wintterlin, J.; Behm, R. J.; Ertl, G. *Phys. Rev. Lett*. **1992**, *68*, 624. (b) sterlund, L.; Zoric, I.; Kasemo, B. *Phys. Rev. B* **1997**, 15452. (c) Sasaki, T.; Ohno, T. *Surf. Sci.* **2000**, *454−456*, 337−340. (d) Carbogno, C.; Behler, J.; Groß, A.; Reuter, K. *Phys. Rev. Lett*. **2008**, *101*, No. 096104.
9. (a) Norman, J. H.; Staley, G.; Bell, W. E. *J. Phys. Chem*. **1967**, *71*, 3686. (b) Paglia, C.; Nilsson, A.; Hernass, B.; Karris, O.; Bennik, P.; Martensson, N. *Surf. Sci*. **1995**, *342*, 119.
10. Based on the same arguments $Ag_nO_2^-$ species were detected in the gas phase during detailed mass spectrometric and theoretical investigations recently.[11]
11. Luo, Z.; Gamboa, G. U.; Smith, J. C.; Reber, A. C.; Reveles, J. U.; Khanna, S. N.; Castleman, A. W., Jr. *J. Am. Chem. Soc*. **2012**, *134*, 18973.
12. The similarity of the Al_{13}^- cluster to the bulk metal regarding thermodynamics is based on the very special electronic structure of this cluster (spherical jellium model with 40 valence electrons) as well as on its topological similarity concerning the coordination number. In both cases, a central Al atom is surrounded by 12 other Al atoms icosahedrally arranged in Al_{13}^- and cuboctahedrally arranged in the metal. Therefore, reactions of the Al_{13}^- are model reactions for those of the bulk metal, if the amount of energy necessary to remove two Al atoms from an Al_{13}^- cluster is compared with the energy change in the case of the bulk metal:[13] $Al_{13}^- \rightarrow Al_{11}^- + 2Al(g)$, $\Delta_R H = +698$ kJ mol^{-1} (calcd); $2Al(s) \rightarrow 2Al(g)$, $\Delta_R H = + 654 \pm 8$ kJ mol^{-1} (expt). Taking into account the usual error margin of DFT calculations, the energy needed for the removal of two Al atoms either from an Al_{13}^- cluster or from the bulk Al metal is almost identical.

Here Al atoms form the energetically equivalent reference system, and therefore all reactions of Al_{13}^- clusters and Al metal should be very similar with respect to their energy balance.

13. Burgert, R.; Schn ckel, H. *Chem. Commun*. **2008**, *18*, 2075−2089.

14. Schn ckel, H. *Dalton Trans*. **2008**, *33*, 4344−4362.

15. Schn ckel, H. *Chem. Rev*. **2010**, *110*, 4125−4163.

16. (a) Jarrold, M. F.; Bower, J. E.; Kraus, J. S. *J. Chem. Phys*. **1987**, *86*, 3876−3885. (b) Jarrold, M. F.; Bower, J. E. *J. Am. Chem. Soc*. **1988**, *110*, 6706−6716. (c) Leuchtner, R. E.; Harms, A. C.; Castleman, A. W., Jr. *J. Chem. Phys*. **1989**, *91*, 2753−2754. (d) Leuchtner, R. E.; Harms, A. C.; Castleman, A. W., Jr. *J. Chem. Phys*. **1991**, *94*, 1093−1101. (e) Bach, S. B. H.; McElvany, S. W.; Wong, N. M.; Parent, D. C. *Chem. Phys. Lett*. **1993**, *209*, 57−62. (f) Hettich, R. L. *J. Am. Chem. Soc*. **1989**, *111*, 8582−8588.

17. (a) de Heer, W. A. *Rev. Mod. Phys*. **1993**, *65*, 611. (b) Knight, W. D.; Clemenger, K.; de Heer, W. A.; Saunders, W. A.; Chou, M. Y.; Cohen, M. L. *Phys. Rev. Lett*. **1984**, *52*, 2141. (c) Cheng, H. P.; Berry, R. S.; Whetten, R. L. *Phys. Rev. B: Condens. Matter Mater. Phys*. **1991**, *43*, 10647−10653. (d) Ahlrichs, R.; Elliott, S. D. *Phys. Chem. Chem. Phys.***1999**, *1*, 13−21.

18. Burgert, R.; Schn ckel, H.; Grubisic, A.; Li, X.; Stokes, S. T.; Gantef r, G. F.; Kiran, B.; Jena, P.; Bowen, K. H. *Science* **2008**, *319*, 438−442.

19. The hindered reactivity of O_2 with Al_{13}^- in a mixture of other Al_x^- clusters has been studied in recent papers, where also the unexpected stability has been discussed.[20,21]

20. Reber, A. C.; Khanna, S. N.; Roach, P. J.; Woodward, W. H.; Castleman, A. W. *J. Am. Chem. Soc*. **2007**, *129*, 16098−16101.

21. Woodward, W. H.; Eyet, N.; Shuman, N. S.; Smith, J. C.; Viggiano, A. A.; Castleman, A. W. J. *Phys. Chem. C* **2011**, *115* (20), 9903.

22. Neumaier, M.; Olzmann, M.; Kiran, B., Bowen, K. H.; Burgert, R.; Schn ckel, H. manuscript in preparation.

23. Schnepf, A.; Schn ckel, H. *Angew. Chem*. **2002**, *114*, 3683−3704; *Angew. Chem., Int. Ed.* **2002**, *41*, 3532−3554.

24. Schn ckel, H.; Schnepf, A. *The Group 13 Metals Aluminum, Gallium, Indium and Thallium*; Aldridge, S., Downs, A. J., Eds.; Wiley: Chichester, U.K., 2011.

25. The generation of Ga_x^- clusters via laser desorption of solid GaN has successfully been applied in our laboratory for many years. Koch, K. Metalloide Cluster in der Gasphase − FT/ICR-massenspektrometrische Untersuchungen, Dissertation, Universit t Karlsruhe, 2005. However, this method has not been published before.

26. The formation of Al_x^- clusters by irradiation of AlN was not successful, which seems plausible due to its higher thermodynamic stability; enthalpies of formation, $\Delta H°_{f,298K}$(AlN) = −318 kJ mol^{-1}, $\Delta H°_{f,298K}$ (GaN) = −109 kJ mol^{-1}.[2]

27. Obviously, because of these difficulties, controversial theoretical results have already been published: (a) Lu, Q. L.; Chen, L. L.; Wan, J. G.; Wang, G. H. *J. Comput. Chem.* **2010**, *31* (15), 2804−9. (b) Cooper, B. T.; Parent, D.; Buckner, S. W. *Chem. Phys. Lett*. **1998**, *284*, 401−406. (c) Hoshino, T.; Sekino, A.; Hata, M.; Tsuda, M. *Appl. Surf. Sci*. **2001**, 62−163, 435−439. (d) Yuan, Q. H.; Li, J. B.; Fan, X. L.; Lau, W. M.; Liu, Z.-F. *Chem. Phys. Lett*. **2010**, *489*, 16−19.

28. Though also superoxo-bonded (end-on) intermediates like that recently discussed for $Ag_{13}O_2$[11] are possible on the $Al_{13}^- + O_2$ PES, these species should be located in flat minima and exhibit a correspondingly short lifetime on their way to the peroxo species discussed here. This conclusion is plausible, since, as far as we know, in synthetic chemistry no molecules with an A-O-O constitution are known, where A represents a main group element. However, there are well-known examples for the normal valence A-O-O-A peroxo arrangement (e.g., peroxosulfates and peroxophosphates).[1]
29. The exoergic reactions of Ga_{10}^-, Ga_{12}^-, and Ga_{14}^- will be discussed in the text in more detail.
30. Of all larger odd-numbered Ga_n^- clusters (with $Ga_n^- > Ga_7^-$), only Ga_{17}^- was found to react spontaneously with oxygen presumably because of the high stability of the Ga_{13}^- product: $Ga_{17}^- + O_2 \rightarrow Ga_{13}^- + 2Ga_2O$.
31. Schumacher, E. *DETMECH − Chemical Reaction Kinetics Software*, University of Bern, 2003.
32. Four Al atoms are oxidized to four Al^+ ions in the two Al_2O molecules. This picture of the oxidation of the outer ligand-bearing Al atom to monovalent Al^+ entities has been discussed on the basis of experiments with metalloid Al_nR_m (n > m) clusters,[1,14,15] and two O atoms of the O_2 molecules are reduced to two O^{2-} in the Al_2O species.
33. Olzmann, M.; Burgert, R.; Schn ckel, H. *J. Chem. Phys*. **2009**, *131*, No. 174304.

34. In contrast, if the pressure in the reaction cell is high, collisional stabilization of the cluster oxides $Al1_4O^-$ and $Al_{15}O_2^-$ has been observed. Watanabe, T.; Tsukuda, T. *J. Phys. Chem. C* **2013**, *117*, 6664−6668.

35. Levine, R. D. *Molecular Reaction Dynamics*; Cambridge University Press: Cambridge, U.K., 2005.

36. *Handbook of Chemistry and Physics*, 75th ed.; Lide, D. R., Ed.; CRC Press: Boca Raton, FL, 1994.

37. The rate coefficients of Al_8^-, Al_{10}^-, Al_{12}^-, and Al_{14}^- are about 20−50% smaller than those discussed by other authors from flow tube experiments and from a sophisticated estimation of rate coefficients;[21] however, their error margins are about 10 times larger than those presented here. Furthermore, the variation of the even−odd reaction rates presented here shows a 100−200 faster reaction for the even-numbered clusters and not only a factor of 2−3 as mentioned earlier.[21]

38. Villano, S. M.; Huynh, L. K.; Carstensen, H.-H.; Dean, A. M. *J. Phys. Chem. A* **2011**, *115*, 13425.

39. For the Al_{13}^- cluster, a ΔE^X value of −2.21 eV results, and therefore a smaller hindrance and a higher rate coefficient can be expected than for the Ga_{13}^- + O_2 reaction.

40. This accelerating process between the $^3O_2$ molecule and the doublet $Ga_{10}^-/Ga_{12}^-/Ga_{14}^-$ clusters might be initiated by a preorientation of the magnetic species ($^3O_2/Ga_n^-$) with a short stabilization period of the loosely bonded magnetic contact pair, which is immediately followed by a strongly exoergic step; that is, these reactions proceed spontaneously. However, this hypothesis has to be

ruled out, because the energy of a hypothetic magnetic interaction is far below the thermal energy of the interacting species.

41. In step C, only Al−O/Ga−O single bonds are formed like those in the gaseous reaction products Al−O−Al and Ga−O−Ga, respectively. For these linear molecules, bond energies of 5.35 eV (Al_2O) and 4.59 eV (Ga_2O) are known from experimental data.[2,3]
42. Our simple model is also in line with the hindered $^3O_2$ reaction of Ag_{13}^- described recently:[11] The formation of neutral Ag_{13} (EA) (see Figure 4.2.3) requires the largest energy of all Ag_n^- clusters, that is, the lowest energy ($\Delta E^X = -0.5$ eV) is gained by the formation of the end-on $[O_2Ag_{13}]^-$ cluster, and consequently the electron transfer to an O_2^- species must overcome a high barrier, which is in line with an extremely slow reaction.
43. (a) Yuan, Q. H.; Li, J.; Liu, Z.-F *Phys. Chem. Chem. Phys*. **2011**, *13*, 9871. (b) Han, Y.-K. *Phys. Chem. Chem. Phys*. **2012**, *14*, 6639. (c) Yuan, Q.; Liu, Z.-F. *Phys. Chem. Chem. Phys*. **2012**, *14*, 6641.
44. Burgert, R.; Stokes, S. T.; Bowen, K. H.; Schn ckel, H. *J. Am. Chem. Soc*. **2006**, *128*, 7904.
45. Wei , K.; Schn ckel, H. *Int. J. Mass Spectrom*. **2002**, *214*, 383−395.
46. Koch, K.; Schn ckel, H. Z. *Anorg. Allg. Chem*. **2007**, *633*, 873−878.
47. Bach, S. B. H.; McElvany, S. W.; Wong, N. M.; Parent, D. C. *Chem. Phys. Lett*. **1993**, *209*, 57.
48. (a) Becke, A. D. *Phys. Rev. A* **1999**, *38*, 3098. (b) Perdew, J. P. *Phys. Rev. B* **1986**, *33*, 8822.

49. (a) Weigend, F.; H ser, M.; Patzelt, H.; Ahlrichs, R. *Chem. Phys. Lett*. **1998**, *294*, 143. (b) TURBOMOLE, V6.0, 2009, a development of University of Karlsruhe and Forschungszentrum Karlsruhe GmbH, 1989−2007, TURBOMOLE GmbH, since 2007; available from http:// www.turbomole.com.

50. Sierka, M. *Prog. Surf. Sci*. **2010**, 85, 398.

51. Kiran, B.; Kandalam, A. K.; Xu, J.; Ding, . H.; Sierka, M.; Bowen, K. H.; Schn ckel, H. *J. Chem. Phys*. **2012**, *137*, No. 134303.

SUPPORTING INFORMATION

Quantum chemical calculations, structures and energies (eV)

S1.1 Global minimum structures **(F)**

Figure 4.2.S1. Global minimum structures (**F**) of $Al_xO_2^-$ clusters

S1.2

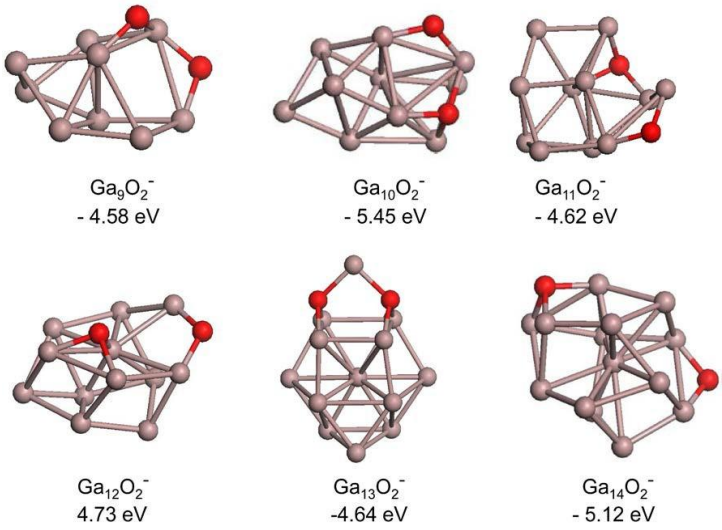

Figure 4.2.S2. Global minimum structures (**F**) of $Ga_xO_2^-$ clusters

S1.3

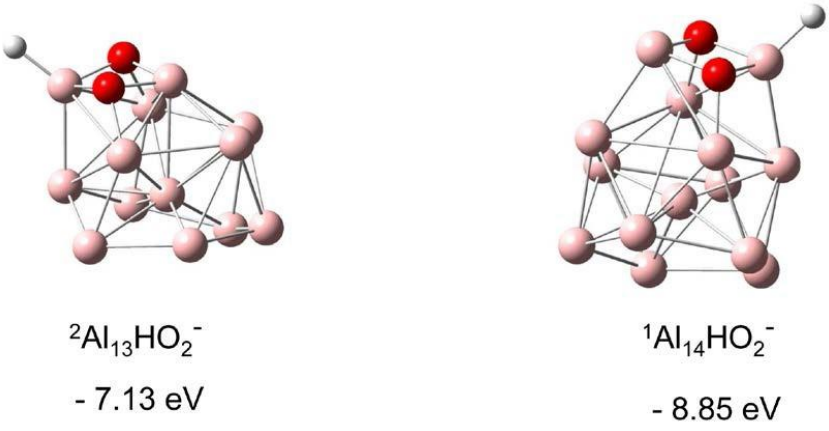

Figure 4.2.S3. Global minimum structures (**F**) of $^{2/1}Al_xHO_2^-$ clusters

S1.4 Structures of the peroxo-intermediates **X.**

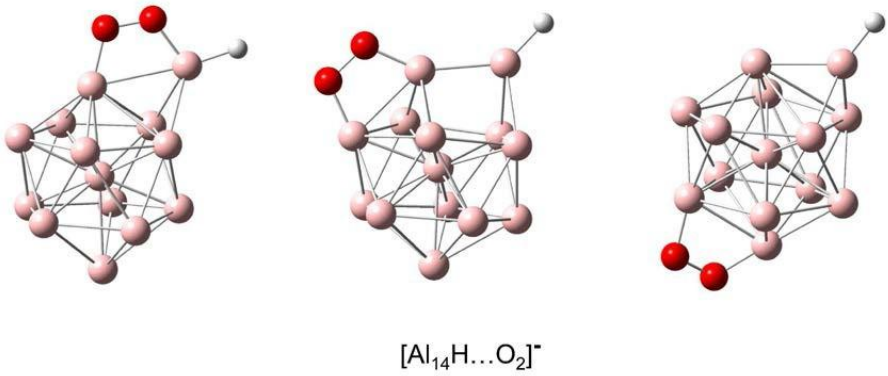

Figure 4.2.S4. Structures of the peroxo-intermediates (**X**) of $[Al_{14}H…O_2]^-$

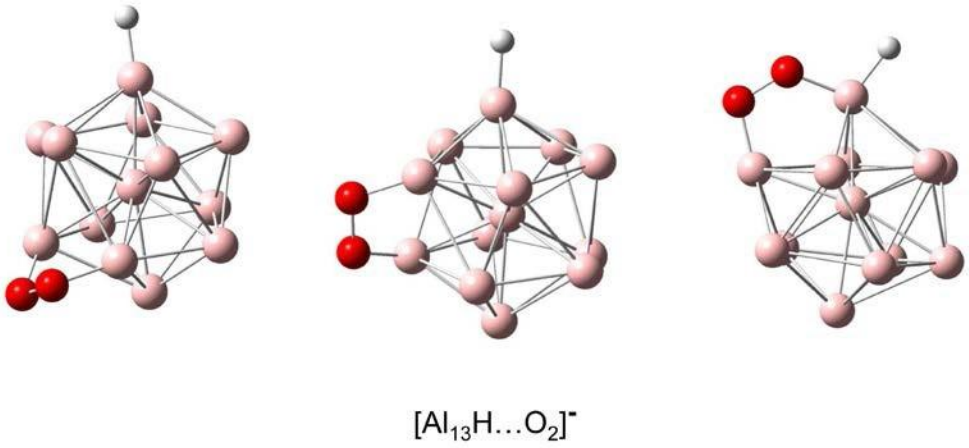

Figure 4.2.S5. Structures of the peroxo-intermediates (**X**) of $[Al_{13}H\ldots O_2]^-$

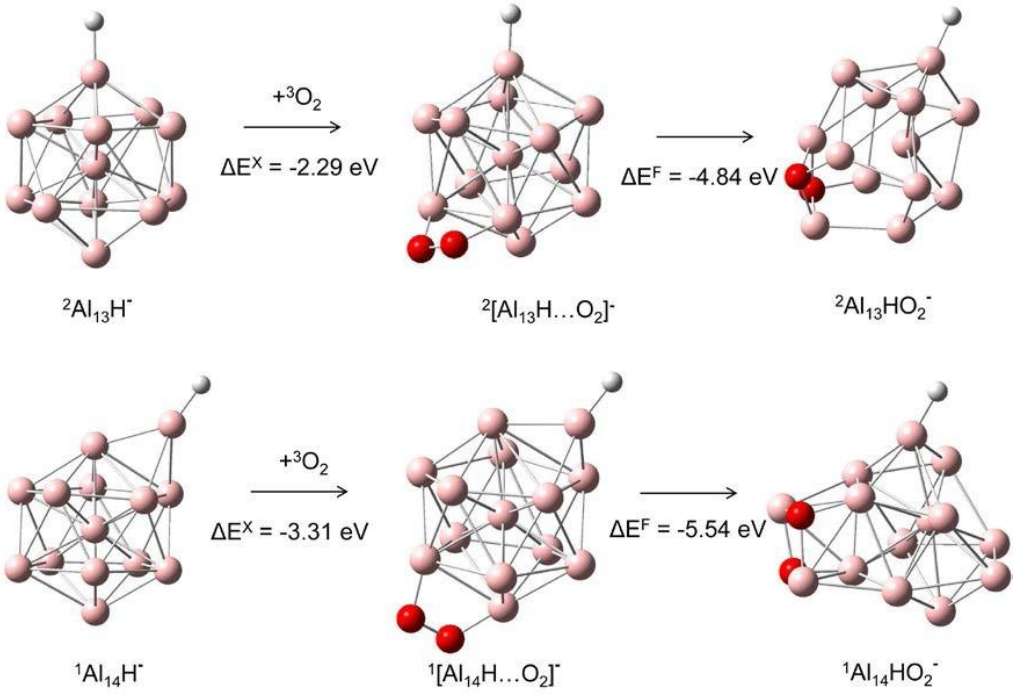

Figure 4.2.S6. Structures of peroxo-intermediates (**X**) of the schematic energy cycle of the $^2Al_{13}H^- + {}^3O_2$ reaction and $^1Al_{14}H^- + {}^3O_2$.

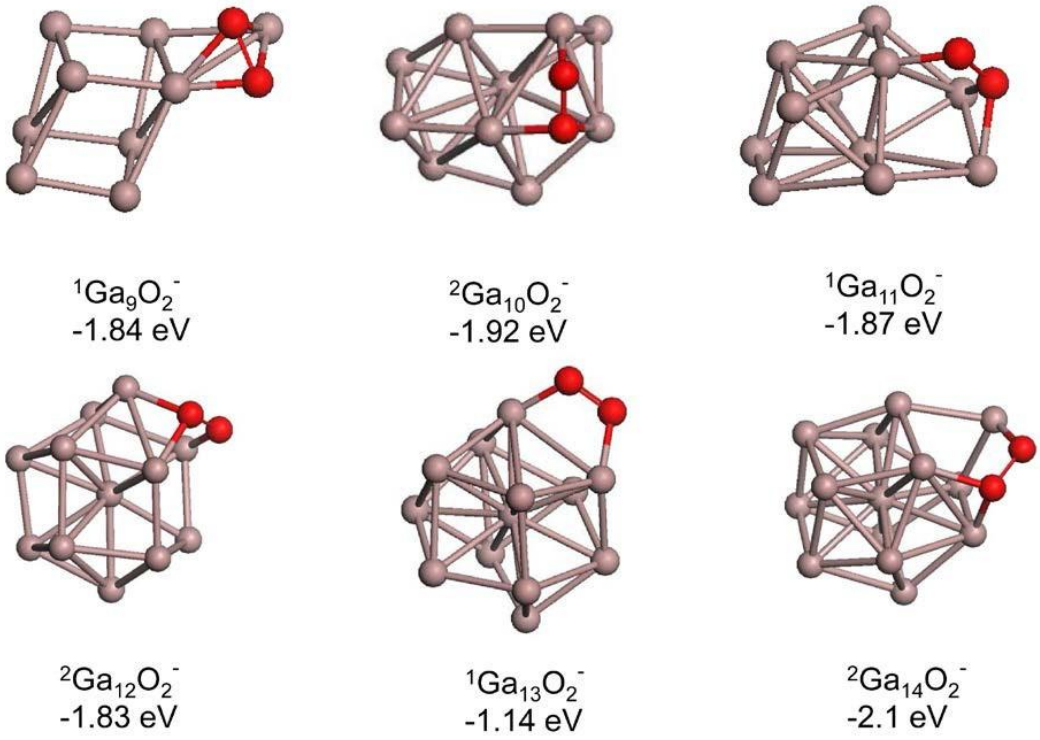

Figure 4.2.S7. Structures of the peroxo-intermediates (**X**) of $^1Ga_{9,11,13}O_2^-$ and $^2Ga_{10,12,14}O_2^-$.

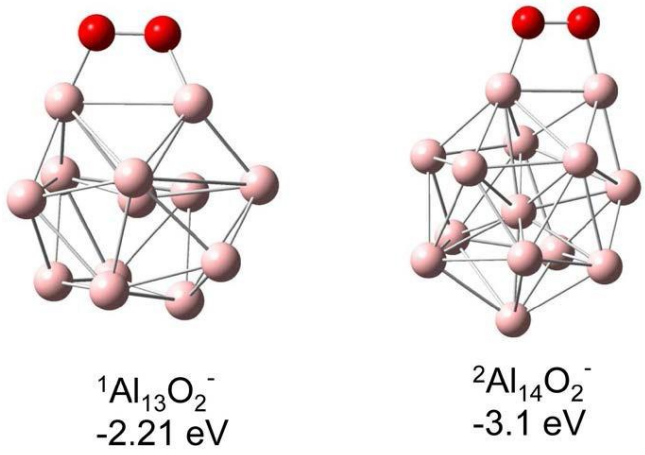

Figure 4.2.S8. Structures of the peroxo-intermediates (**X**) of $^1Al_{13}O_2^-$ and $^2Al_{14}O_2^-$.

S2. Further experimental details

S2.1. Unexpected reactions

S2.1.1 Ga_8^-

The spontaneous reaction of Ga_8^- with oxygen leads via Ga_4^- to the formation of GaO^-. $Ga_4^- + O_2 \rightarrow GaO^- + Ga_2O + Ga$ (Though GaO^- is an isolelectronic species to the high-temperature molecule GaF it has never been observed during the $Ga_x^- + O_2$ reactions before.)

S2.1.2

Ga_{11}^- was found to react with O_2 only after ion activation at a threshold energy (in the centre of mass frame) of $E_{cm} \sim 1.8$ eV. Surprisingly, the main reaction product was found to be the Ga_6^- species ($Ga_{11}^- + O_2 \rightarrow Ga_6^- + Ga_2O + Ga_3O$). The expected species Ga_7^- that should be formed via $Ga_{11}^- + O_2 \rightarrow Ga_7^- + 2Ga_2O$ is observed only in very small yields. We assume that formed Ga_7^- quickly loses an electron due to its rather small electron affinity of 2.55 eV (see [1a, b]). Via DFT calculations the overall reaction $Ga_{11}^- + O_2 \rightarrow Ga_7 + 2Ga_2O + e^-$ is exothermic by 0.45 eV.

S2.2. Reaction of the cluster ensemble $Ga_{11}^- - Ga_{28}^-$

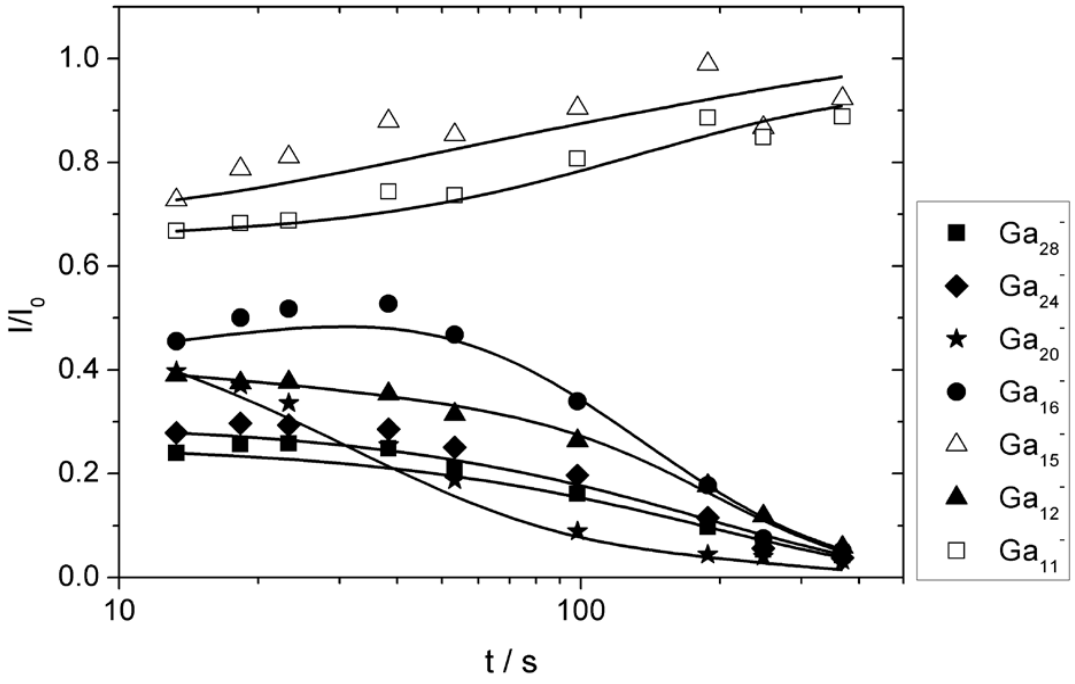

Figure 4.2.S9. Time evolution of the cluster ensemble Ga_{11}^-- Ga_{28}^- during the reaction with O_2. All ion signals *I* were normalized to the signal of Ga_9^- (= I_0). The solid lines represent fits to the experimental data points carried out with the software *DetMech* (DetMech; E. Schumacher; Universität Bern, 2003). For further details see text.

S3. Some considerations to the calculations of $Al_{13}H^-$ and $Al_{14}H^-$, their O_2 reactions and the comparison with the hydrogen-free cluster

Furthermore, the simple ionic model (Figure 4.2.5 text) convincingly confirms that the spin conservation rule accounts for the spontaneous spin allowed reactions of Al_{14}^- and $Al_{13}H^-$ and for the slow, spin forbidden reaction of Al_{13}^- and $Al_{14}H^-$: The calculated values of **A** (Figure 4.2.3 text) for the oxidation of $Al_{13}H^- \rightarrow Al_{13}H \rightarrow Al_{13}H^+$ are 9.56 eV, and for the oxidation of $Al_{14}H^- \rightarrow Al_{14}H \rightarrow Al_{14}H^+$ are 7.74 eV. The difference of

1.82 (9.56 – 7.74) eV corresponds well with a similar difference calculated between the pure clusters Al13$^-$ (10.41 eV) and Al_{14}^- (8.56 eV) of 1.85 eV (Table 4.2.4 text). Therefore, if a single H-atom is added to the pure Al_{13}^- and Al_{14}^- cluster, there is a parallel shift to smaller values of **A** ($Al_{13}^- \rightarrow Al_{13}H^-$: 10.41 eV → 9.56 eV; $Al_{14}^- \rightarrow Al_{14}H^-$: (8.56 eV → 7.74 eV), i.e. to larger ΔE^X values and consequently to faster reactions. This conclusion is in line for Al_{13}^- and $Al_{13}H^-$ because the inertness of Al_{13}^- to O_2 changes to a spontaneous reaction with $Al_{13}H^-$ [2,3]. However, the change from the spontaneous reaction of Al_{14}^- to the hindered one of $Al_{14}H^-$ contradicts the above mentioned conclusion of a faster reaction for $Al_{14}H^-$. Therefore, the inverted observed O_2 reactivity of O_2 with the pairs Al_{13}^- (very slow)/$Al_{13}H^-$ (spontaneous) and of Al_{14} (spontaneous)/$Al_{14}H^-$ (slow) is only in line with the prediction made above for each pair if the difference concerning the hindered spin transition for Al_{13}^- and $Al_{14}H^-$ is taken into account.

SUPPORTING INFORMATION REFERENCES

1. (a) Cha, C.-Y.; Ganteför, G.; Eberhardt, W.; J. *Chem. Phys*., **1994**, *100,* 995. (b) Cooper, B. T., Parent, D., Buckner, S. W.; *Chem. Phys. Lett.* **1998**, *284*, 401-406.
2. Burgert, R.; H. Schnöckel, H. Grubisic, Li, A. X.; Stokes, S. T.; Ganteför, G. F.; Kiran, B.; Jena, P.; Bowen, K. H.; *Science* **2008,** *319*, 438 – 442.
3. Reber, A.C.; Khanna, S.N.; Roach, P. J.;Woodward, W.H.; Castleman, A.W.; *J. Am. Chem. Soc.* **2007**, *129*, 16098-16101.

CHAPTER 5

This chapter presents experimental results on the parent anion of several novel aromatic molecules. Aromatic molecules display an enhanced chemical stability compared to their aliphatic counterparts due to the delocalization of electrons in their π molecular orbital. The first examined aromatic is the parent anion of benzaldehyde in Section **5.1**. Benzaldehyde is the simplest example of the aromatic aldehydes (R-CHO) and unarguably the most useful in organic synthesis reactions. Probing of this parent anion, also described as a ketyl radical anion, may provide better insight into anion intermediates formed in condensed phase reactions.

The remainder of this chapter focuses on experiments performed in collaboration with Professor R. N. Compton at the University of Tennessee. Our group contributed the photoelectron spectroscopic data on the molecules of interest Compton and coworkers performed collision-induced dissociation (CID) experiments and provided ab initio calculations. Benzene derivatives with polar substituents such as, p-nitroaniline discussed in Section **5.2**, have potential towards photonic applications. p-Nitroaniline is considered a "push-pull" system in which opposing electron accepting and electron donating groups

are connected by a π–conjugated linkage. In p-nitroaniline, opposing $–NO_2$ and $–NH_2$ groups are para to each other on a benzene molecule, and various experimental methods were employed to better characterize this anion.

The parent anions of the chiral molecules N-paranitrophenylsulfonylalanine (NPNPSA) and N-paranitrophenylalanine (NPNPA) are examined in Section **5.3**. These molecules were synthesized in both *(S)*- and *(R)*- enantiomers, and experiments were employed to see how small moieties may be used to better characterize the newly synthesized large molecules of NPNPSA and NPNPA.

Section 5.1. The Photoelectron Spectrum Of the Benzaldehyde Anion

Angela Buonaugurio,[†] Xinxing Zhang,[†] Sarah T. Stokes,[§] Yi Wang,[†] G. Barney Ellison,[‡] and Kit H. Bowen[†*]

[†]*Department of Chemistry, Johns Hopkins University, Baltimore, Maryland 21218, USA*

[§]*Department of Chemistry, Towson University, Baltimore, MD, 21204, USA*

[‡]*Department of Chemistry and Biochemistry, University of Colorado, Boulder, Colorado 80309-0215, USA*

ABSTRACT

The benzaldehyde radical anion was produced in the gas phase and studied using negative ion photoelectron spectroscopy. Analysis of the photoelectron spectrum found the adiabatic electron affinity, $EA_a(C_6H_5CHO)$, to be 0.35 ± 0.05 eV. Two active modes of benzaldehyde are observed in the photodetachment of the $C_6H_5CHO^-$ anion: ν_7, the C=O stretch (1728 cm^{-1}) and ν_6, the non-phenyl C–H stretch (2806 cm^{-1}). DFT electronic structure calculations have been carried out and are in agreement with the experimental spectrum. The optimized geometries of both C_6H_5CHO $\tilde{X}\ ^1A'$ and $C_6H_5CHO^-$ $\tilde{X}\ ^2A''$ are planar. The excess electron in the benzaldehyde anion is found to be delocalized in its π^* (a") anti-bonding orbital.

* Corresponding author: email: kbowen@jhu.edu (K.H. Bowen); Fax: +1 410 516 8420

INTRODUCTION

Mass spectrometry has made possible the development of many experimental techniques in physical chemistry. Among them is anion photoelectron spectroscopy, carried out with mass-selected negative ions. A variety of types of mass spectrometers have been utilized in identifying and mass-selecting atomic, molecular, and cluster anions studied by photoelectron spectroscopy, these including magnetic sector, quadrupole, Wien Filter, and time-of-flight instruments. Here, we present a study of the benzaldehyde anion, facilitated by a magnetic sector mass analyzer and selector.

Radical anions of aldehydes and ketones are thought to be intermediates and reactants within many important condensed phase reactions of organic chemistry. Alkali metals are used to reduce aldehydes and ketones to produce ketyls, i.e., carbonyl radical anions.[1,2] For example, pinacols[3] are the result of dimerization reactions involving acetone ketyls. Direct studies of the intermediate radical anions produced in the condensed phase are hampered due to solvent interferences. Thus, gas-phase studies provide insight by isolating the radical anion of interest from such interactions.

Benzaldehyde is the simplest aromatic aldehyde (see Figure 5.1.1), and as such it is an important precursor for synthesis of many organic compounds. Gas-phase infrared and Raman spectroscopic studies supported by calculations[4,5] have provided vibrational assignments of the benzaldehyde molecule. Additional studies have queried its excitation and relaxation dynamics,[6-8] photochemical pathways,[9-12] and surface chemistry.[13] Nevertheless, even though the neutral benzaldehyde molecule has been well characterized, there are fewer studies dealing with its negative ion, i.e. its radical anion.

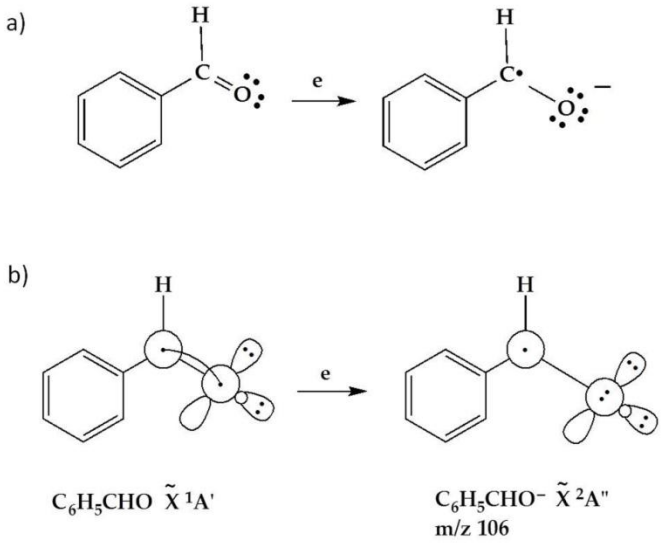

Figure 5.1.1. (a) Pictorial representation of the formation of the benzaldehyde radical anion and uncoupling of the carbonyl group upon attachment of an excess electron. (b) GVB diagram to model the symmetry of the benzaldehyde neutral and corresponding radical anion formed.

The electron affinity (EA) of benzaldehyde has been estimated through both experimental[14-16] and theoretical[17] approaches to be ~0.4 eV. Furthermore, threshold excitation using the SF_6 scavenger technique[18] and electron transmission spectroscopy (ETS)[19,20] concluded that benzaldehyde must have a small positive electron affinity, and thus should be capable of forming a stable anion. More importantly, there are few negative ion photoelectron studies of intact ketone radical anions,[21,22] and those who have attempted to see the radical anions of aldehydes have observed only their deprotonated forms,[23] i.e. not the intact aldehyde radical anion.

Here, we present the negative ion photoelectron spectrum of the intact (parent) benzaldehyde radical anion. From its photoelectron spectrum, the adiabatic electron affinity (EA_a) was determined to be 0.35 ± 0.05 eV. This assignment was supported by a

Franck-Condon (FC) fit. Our density functional theory (DFT) calculations show that the excess electron occupies the π* anti-bonding orbital, and that both the anion and its corresponding neutral geometries are planar. The active vibrational frequencies observed in our spectrum compare favorably with the experimentally known vibrational modes of benzaldehyde.

METHODS

Experimental

Negative ion photoelectron spectroscopy is conducted by crossing a mass-selected beam of anions with a fixed-frequency photon beam and energy-analyzing the resultant photodetached electrons. The photodetachment process is governed by the relationship hν = EBE + EKE, where hν is the photon energy, EBE is the electron binding energy, and EKE is the electron kinetic energy.

The anion photoelectron spectrometer used to measure the photoelectron spectrum of the benzaldehyde parent anion has been described previously.[24] Briefly, the apparatus utilized a supersonic expansion nozzle-ion source (biased at -500 V). Benzaldehyde liquid was placed in the stagnation chamber of this source, heated up to 100 °C, and co-expanded with 1-2 atm of argon gas through a 25 μm orifice into a high vacuum region. Negative ions were formed by injecting low energy electrons from a hot and negatively biased, thoriated tungsten filament into the expanding jet, where a microplasma was formed in the presence of a weak external magnetic field. The anions were extracted and transported via a series of ion optics through the flight tube of a 90° magnetic sector mass spectrometer (mass resolution, ~400). Mass-selected anions were then crossed with an intracavity argon ion laser beam, where photodetachment occurred. The resultant

photodetached electrons were then energy-analyzed by a hemispherical electron energy analyzer with a resolution of 30 meV. The photoelectron spectrum reported here was recorded with 488 nm (2.540 eV) photons and calibrated against the well known photoelectron spectrum of the O^- anion.[25]

Computational

DFT calculations were conducted by applying Becke's three-parameter hybrid functional (B3LYP)[26-28] and using the GAMESS[29] software package to determine the electron affinity of benzaldehyde. Geometries of the anion and its corresponding neutral were fully optimized without geometrical constraints with the aug-cc-pVDZ basis set.[30,31] The electronic energies were improved by single-point calculations with a larger basis set, i.e., aug-cc-pVTZ, at the optimized geometries.[30,31] With the aug-cc-pVDZ basis set, Hessian calculations were also performed to calculate the vibrational frequencies of the neutral and its anion. Franck-Condon factors for fitting the photoelectron spectrum of the benzaldehyde anion were calculated with the Hutchisson Method (independent harmonic oscillators) using the PESCAL program.[32]

RESULTS AND DISCUSSION

The photoelectron spectrum of the benzaldehyde parent anion is shown in Figure 5.1.2; it exhibits a vibrationally-resolved profile. Its peaks are centered at electron binding energies (EBE) of 0.35 eV (peak **A**), 0.56 eV (peak **B**), 0.69 eV (peak **C**) and ~0.76 eV (peak **D**). There is also a shoulder on the low EBE side of peak **B**, i.e., at 0.48 eV (peak $\mathbf{B_{sh}}$). (See Table 5.1.1) We assign peak **A** as the $\upsilon'' = 0 \rightarrow \upsilon' = 0$ transition, i.e.,

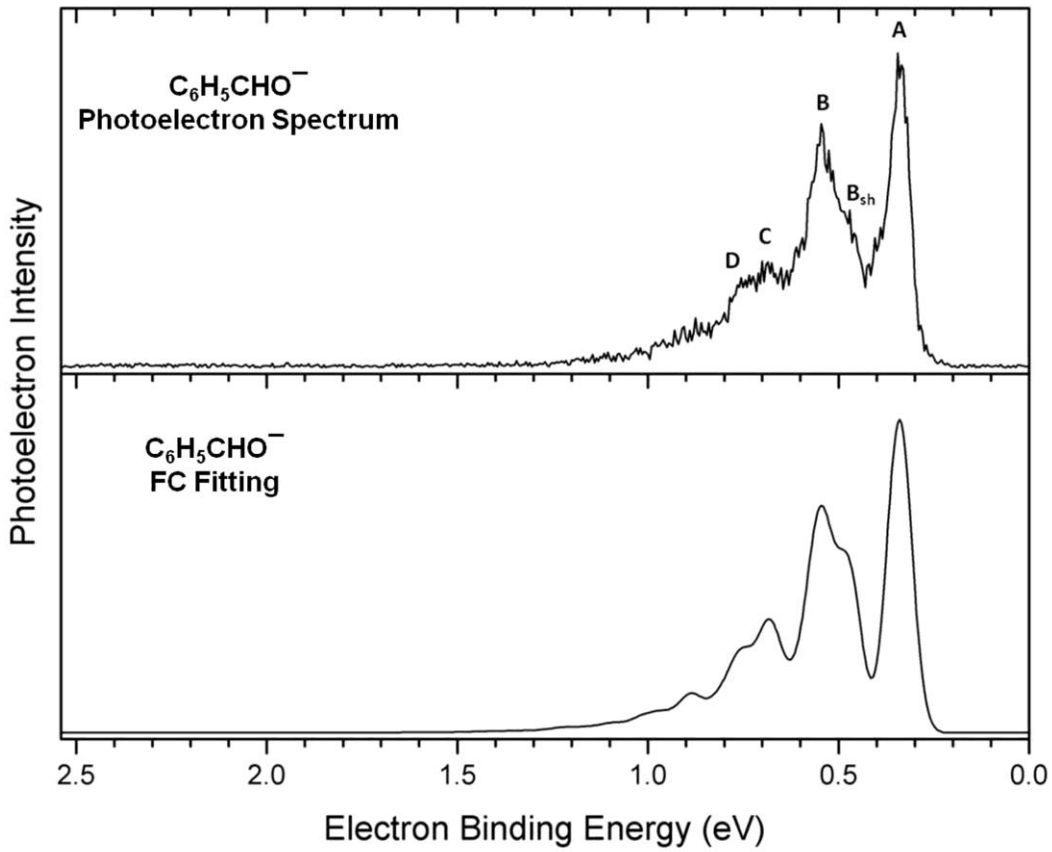

Figure 5.1.2. (Upper trace) The measured photoelectron spectrum of the benzaldehyde anion recorded using 2.540 eV photons and (lower trace) its corresponding Franck-Condon profile fitting.

the origin transition, and thus the adiabatic electron affinity value, is determined to be $EA_a(C_6H_5CHO) = 0.35 \pm 0.05$ eV. This EA_a value is in good agreement with our DFT calculation of 0.37 eV and with previous literature estimates.[14-17] If we include the zero-point energy correction calculated with the vibrational frequency analysis, this increases the EA_a value by approximately ~0.1 eV. We see no significant indication of vibrational hot bands in the spectrum. This may be better explained using a generalize valence bond (GVB) diagram,[33] showing electron attachment to the C_6H_5CHO $\tilde{X}$ $^1A'$ to produce the

radical anion, $\tilde{X}\ ^2A''$ (see Figure 5.1.1b). Since the electron is added to a closed shell molecule, the electron affinity is expected to be small, i.e. less than 0.5 eV. This implies that hot bands may not be visible, since most electrons in the anion can autodetach.

The optimized geometries of both the benzaldehyde anion and its neutral counterpart were calculated and found to be planar, although there are differences in their bond lengths. The highest occupied molecular orbital (HOMO) structure for the benzaldehyde anion is shown in Figure 5.1.3. The excess electron is delocalized in the π^* anti-bonding orbital. The calculated Mulliken charge distribution shows the C=O bond of the aldehyde chromophore to be strongly polarized, i.e. negatively charged, where the carbon atom is -0.46 and oxygen atom is -0.90.

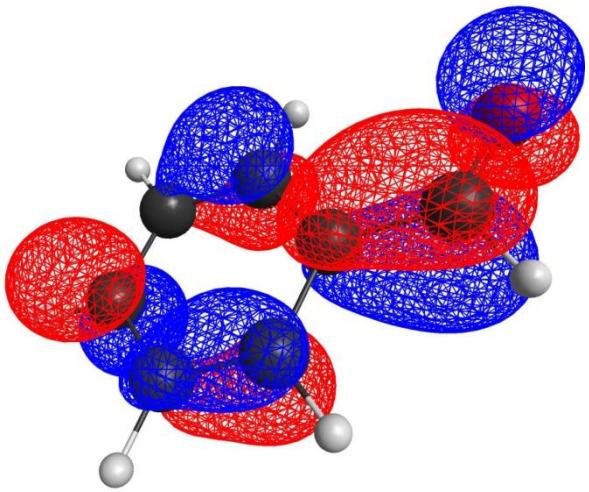

Figure 5.1.3. The highest occupied molecular orbital (HOMO) of the ground state of the benzaldehyde anion, as determined at the B3LYP/aug-cc-pVDZ level of theory.

The photoelectron spectrum in Figure 5.1.2 demonstrates that there is a significant geometry change between the anion and the neutral: $C_6H_5CHO^-\ \tilde{X}\ ^2A'' + h\upsilon_{488nm} \rightarrow e^- +$

C_6H_5CHO $\tilde{X}$ $^1A'$. The structures in Figure 5.1.1 predict that the $C_6H_5C(H)=O$ and C_6H_5CO-H stretches will be the active modes upon photodetachment. Benzaldehyde is a planar molecule[34] as is that of the $C_6H_5CHO^-$ anion. The infrared spectrum of C_6H_5CHO has been measured and assigned in the gas phase[4] and in CCl_4 solution.[5] Since they are planar species, the 36 vibrational modes of both benzaldehyde and its radical anion can be classified as even or odd: 36 fundamentals = 25 a' ⊕ 11a". Only the a' modes will be active in a photoelectron experiment. The vibrational frequencies from Figure 5.1.2 were measured as the energy spacings between peak centers in the spectrum and are presented in Table 5.1.1. Features B and C in the spectrum are easily assigned to ν_7, the carbonyl

Table 5.1.1. Vibrational frequencies extracted from the experimental photoelectron spectrum and compared with calculations from this study and those report in the literature.

Peak Location (eV)		**Expt.[a] Vibrational Spacing**			**B3LYP/ aug-cc-pVTZ[b]**	**Expt. IR Spectra[c]**	**Assignment**	
		Δ	**(eV)**	**(cm^{-1})**	**(cm^{-1})**	**(cm^{-1})**		
A	0.35				0.37		Electron Affinity	(0,0)
B_{sh}	0.48	B_{sh}-A	0.13	1049	1212	ν_{18} = 1074		18_0^1
B	0.56	B-A	0.21	1694	1725	ν_7 = 1728		7_0^1
C	0.69	C-A	0.34	2742	2816	ν_6 = 2806		6_0^1
D	0.76	D-B	0.20	1613	1725			7_0^2

a) Deduced from the vibrational spacing between peaks within the recorded photoelectron spectrum.
b) Calculations from present work using GAMESS software package.
c) Reference 4.

stretch, and ν_6, the non-phenyl C–H stretch. The small peak at D is likely the overtone of ν_7 while the soft shoulder, $B_{sh,}$ is more difficult to assign.

We also conducted a Franck-Condon analysis and fit. For comparison, the resulting simulated photoelectron spectrum is shown directly below the experimental spectrum in Figure 5.1.2. The calculated spectral profile matches reasonably well with the measured photoelectron spectrum and is consistent with the origin transition, $\upsilon(0,0)$, being at 0.35 ± 0.05 eV. As compared to neutral benzaldehyde, the benzaldehyde anion showed significant lengthening of the C=O bond (by approximately 0.065 Å), of the C-C bonds of the benzene ring (by about 0.076 Å), and to a lesser effect the C-H bond of the aldehyde chromophore (by roughly 0.002 Å). These are the dominant vibrational frequencies observed in the photoelectron spectrum; the remaining vibrational modes had a negligible effect. This conclusion was reached by ranging both the displacement and frequency parameters for each vibrational mode, while monitoring the resultant Franck-Condon spectral fit to the experimental spectrum. Thus, the fit was obtained by using a select number of modes for simulation, i.e. the three active stretching modes. All input parameters, related to $\upsilon(0,0)$ position, resolution, displacement, and frequency, were treated as live variables and optimized to obtain the best fit. The temperature parameter did not affect the Franck-Condon fitting in assigning the EA_a value, consistent with a dearth of hot band activity in the spectrum.

ACKNOWLEDGEMENTS

This material is based upon work supported by the National Science Foundation under Grant Number, CHE-1360692 (KHB). GBE acknowledges support from the National Science Foundation under Grant No. CHE-1112466.

REFERENCES

1. March, J. (1985). *Advanced Organic Chemistry: Reactions, Mechanisms, and Structure* (3rd ed). New York City, NY: John Wiley & Sons.
2. Fox, M. A. & Whitesell, J. K. (2004). *Organic Chemistry*. Boston,MA.: Jones and Bartlett.
3. Streitwieser, A., Heathcock, C. H., & Kosower, E. M. (1977). *Introduction to Organic Chemistry (4th ed.)*. Upper Saddle River, NJ: Prentice Hall.
4. Green, J. H. S.; Harrison, D. J. *Spectrochimica Acta*, **1976**, *32A*, 1265.
5. Lampert, H.; Mikenda, W.; Karpfen, A. *J. Phys. Chem. A* **1997**, *101*, 2254.
6. Leopold, D. G.; Hemley, R. J.; Vaida, V.; Roebber, J. L. *J. Chem. Phys*. **1981**, *75*, 4758.
7. Biron, M.; Longin, P. *Chem. Phys. Lett*. **1985**, *116*, 250.
8. Silva, C. R.; Reilly, J. P. *J. Phys. Chem. A* **1997**, *101*, 7934.
9. Berger, M.; Goldblatt, I. L.; Steel, C. *J. Am. Chem. Soc*. **1973**, *95*, 1717.
10. Hirata, Y.; Lim, E. C. *J. Chem. Phys*. **1980**, *72*, 5505.
11. Brühlmann, U.; Nonella, M.; Russegger, P.; Huber, J. R. *Chem. Phys*. **1983**, *81*, 439.
12. Itoh, T. *Chem. Phys. Lett*. **1988**, *151*, 166.
13. Huang, H. G.; Zhang, Y. P.; Cai, Y. H.; Huang, J. Y.; Yong, K. S.; Xu, G. Q. *J. Chem. Phys*. **2005**, *123*, 104702.
14. Wentworth, W. E.; Chen, E. *J. Phys. Chem*. **1967**, *71*, 1929.
15. Wentworth, W. E.; Kao, L. W.; Becker, R. S. *J. Phys. Chem*. **1975**, *79*, 1161.

16. Zlatkis, A.; Lee, C. K.; Wentworth, W. E.; Chen, E. C. M. *Anal. Chem*. **1983**, *55*, 1596.

17. Chuchev, K.; Tadjer, A.; Nikolova, N.; Nenov, V. *Oxidation Communications* **2005**, *28*, 837.

18. Naff, W. T.; Compton, R. N.; Cooper, C. D. *J. Chem. Phys*. **1972**, *57*, 1303.

19. Modelli, A.; Burrow, P. D. *J. Phys. Chem*. **1984**, *88*, 3550.

20. Modelli, A.; Scagnolari, F.; Distefano, G. *Chem. Phys*. **1999**, *250*, 311.

21. Yagi, I.; Maeyama, T.; Fujii, A.; Mikami, N. *J. Phys. Chem. A* **2007**, *111*, 7646.

22. Guo, J.-C.; Hou, G.-L.; Li, S.-D.; Wang, X.-B. *J. Phys. Chem. Lett*. **2012**, *3*, 304.

23. Nimlos, M. R.; Soderquist, J.A.; Ellison, G. B. *J. Am. Chem. Soc*. **1989**, *111*, 7675.

24. Coe, J. V.; Snodgrass, J. T.; Freidhoff, C. B.; McHugh, K. M.; Bowen, K. H. *J. Chem. Phys.* **1986**, *84*, 618.

25. Neumark, D. M.; Lykke, K. R.; Anderson, T.; Lineberger, W. C. *Phys. Rev. A: Gen. Phys.* **1985**, *32*, 1890.

26. Becke, A. D. *Phys. Rev. A* **1988**, *38*, 3098.

27. Becke, A. D. *J. Chem. Phys*. **1993**, *98*, 5648.

28. Lee, C.; Yang, W.; Parr, R. G. *Phys. Rev. B* **1988**, *37*, 785.

29. Schmidt, M. W.; Baldridge, K. K.; Boatz, J. A.; Elbert, S. T.; Gordon, M. S.; Jensen, J. H.; Koseki, S.; Matsunaga, N.; Nguyen, K. A.; Su, S. J.; Windus, T. L.; Dupuis, M.; Montgomery, J. A. *J. Comput. Chem*. **1993**, *14*, 1347.

30. Woon, D. E.; Dunning, Jr., T. H. *J. Chem. Phys*. **1989**, *90*, 1007.

31. Woon, D. E.; Dunning, Jr., T. H. *J. Chem. Phys*. **1993**, *98*, 1358.

32. Ervin, K. M.; Ho, J.; Lineberger, W. C. *J. Phys. Chem*. **1988**, *92*, 5405.

33. Goddard III, W. A.; Harding, L. B. *Annu. Rev. Phys. Chem*. **1978**, *29*, 363.

34. Kakar, R. K.; Rinehart, E. A.; Quade, C. R.; Kojima, T. *J. Chem. Phys*. **1970**, *52*, 3803.

Section 5.2. Negative Ions of p-Nitroaniline: Photodetachment, Collisions, and Ab Initio Calculations

Byron H. Smith,[†] Angela Buonaugurio,[§] Jing Chen,[§] Evan Collins,[§] Kit H. Bowen,[‡,*] Robert N. Compton,[†,‡,*] and Thomas Sommerfeld[&]

[†] *Department of Physics, University of Tennessee, Knoxville, Tennessee 37996, USA*

[§]*Department of Chemistry, Johns Hopkins University, Baltimore, Maryland 21218, USA*

[‡]*Department of Chemistry, University of Tennessee, Knoxville, Tennessee 37996, USA*

[&]*Department of Chemistry and Physics, Southeastern Louisiana University, Hammond, Louisiana 70402, USA*

ABSTRACT

The structures of parent anion, M^-, and deprotonated molecule, $[M-H]^-$, anions of the highly polar p-nitroaniline (*p*NA) molecule are studied experimentally and theoretically. Photoelectron spectroscopy (PES) of the parent anion is employed to estimate the adiabatic electron affinity (EA_a = 0.75 ± 0.1 eV) and vertical detachment energy (VDE = 1.1 eV). These measured energies are in good agreement with computed values of 0.73 eV for the EA_a and the range of 0.85 to 1.0 eV for the VDE at the EOM-CCSD/aug-cc-pVTZ level. Collision induced dissociation (CID) of deprotonated *p*NA, $[pNA - H]^-$, with argon yielded $[pNA - H - NO]^-$ (i.e., rearrangement to give loss of NO) with a threshold energy of 2.36 eV. Calculations of the energy difference between $[pNA - H]^-$ and $[pNA - H - NO]^-$ give 1.64 eV, allowing an estimate of a 0.72 eV

activation barrier for the rearrangement reaction. Direct dissociation of [*p*NA − H]$^-$ yielding NO_2^- occurs at a threshold energy of 3.80 eV, in good agreement with theory (between 3.39 eV and 4.30 eV). As a result of the exceedingly large dipole moment for *p*NA (6.2 Debye measured in acetone), we predict two dipole-bound states, one at ~110 meV and an excited state at 2 meV. No dipole-bound states are observed in the photodetachment experiments due the pronounced mixing between states with dipole-bound and valence character similar to what has been observed in other nitro systems. For the same reason, dipole-bound states are expected to provide highly efficient "doorway states" for the formation of the *p*NA$^-$ valence anion, and these states should be observable as resonances in the reverse process, that is, in the photodetachment spectrum of *p*NA$^-$ near the photodetachment threshold.

*Corresponding authors: email: rcompton@utk.edu, kbowen@jhu.edu

INTRODUCTION

The highly polar p-nitroaniline (*p*NA) molecule captures free electrons to form the pNA^- anion while deprotonation of *p*NA occurs in solution to form the $[pNA - H]^-$ anion. This research represents a combined experimental and computational investigation of the valence (parent and deprotonated) as well as dipole-bound anions of *p*NA. p-Nitroaniline represents a classic "push-pull" aromatic molecule as a result of the electron donating NH_2 and electron accepting NO_2 moieties at the para postions on the π-conjugated benzene ring (Figure 5.2.1).[1]

Such donor-acceptor molecules show great promise as nonlinear optical crystals for a host of applications.[2] The dipole moment of p-nitroaniline has been measured in acetone to be 6.2 Debye[3] while calculations of isolated *p*NA give values between 7.0 and 8.1 Debye.[4] The dipole moment of the excited singlet state of *p*NA has been determined to be 13.35 D.[5] Such large dipole moments assure strong binding of an electron to the ground and excited states to form dipole-bound anions and electronically excited Feshbach resonances, respectively.

A number of studies have considered the negative ion properties of *p*NA. In one study, thermal electrons were found to attach to *p*NA to form a long-lived, so-called nuclear-excited or vibrationally excited Feshbach resonance with an auto-detachment lifetime of ~15 μs.[6] Dissociative electron attachment processes at higher electron energies were not reported. Huh et al.[7] obtained electron affinities (EA_as) for a series of substituted benzenes by determining the electron transfer equilibria in the gas phase using an EA_a scale established with nitrobenzene (EAa = 0.99 eV)[8] to provide an absolute calibration. This method resulted in an EA_a of *p*NA to be 0.91 eV. One photoionization

study of *p*NA has given an ionization potential of 8.34 ± 0.01 eV[9] while another electron impact ionization study gave an ionization potential of 8.6 eV[10] as well as reporting appearance energies for $C_6H_6N^+$ and $C_6H_6NO^+$. The former ion results from NO_2 loss and the occurrence of the latter product implies considerable rearrangement in the loss of NO. Many studies have also reported NO loss from molecules similar to *p*NA and discuss the possible rearrangement pathways.[11,12]

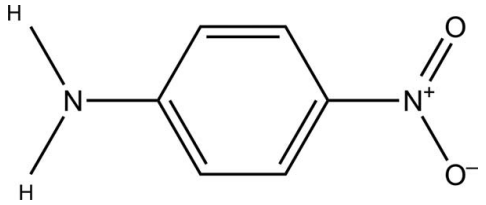

Figure 5.2.1. Stick diagram of the p-nitroaniline molecule showing the donor (NH_2) and acceptor (NO_2) moieties responsible for the large dipole moment of this molecule.

In this study, we present the experimental valence adiabatic electron affinity (EA_a) and vertical detachment energy (VDE) for the *p*NA parent anion by means of photoelectron spectroscopy (PES). In addition, the deprotonated *p*NA anion was produced by electrospray ionization followed by collision-induced dissociation (CID). Experimental measurements of these photodetachment and dissociation energy thresholds are compared to computed values. We also present ab initio calculations of dipole-bound vertical electron affinities for *p*NA as well as a comparison of experimental and calculated binding energies for all dipole-bound affinities reported, thus far, in the

literature for polar molecules having moments from ~ 2.4 to 7 Debye. The experiments to be reported in this work are not designed to detect dipole-bound anions; however, we conjecture on the possible transport of electrons through polar molecules in the gaseous and liquid state which might be facilitated by dipole-bound or quadrupole-bound anions.

COMPUTATIONAL AND EXPERIMENTAL METHODS

Photoelectron Spectroscopy

PES was conducted by crossing a mass-selected negative ion beam with a fixed-frequency photon beam and energy analyzing the resultant photodetached electrons. This technique is governed by the energy conserving relationship hν = EKE + EBE, where hν is the photon energy, EKE is the photodetached electron kinetic energy, and EBE is the electron binding energy or the transition energy needed to take the anion to a particular vibrational state of its neutral counterpart.

Negative ions were formed by slow-electron attachment to *p*NA. The ion source was a biased (−500 V), supersonic expansion nozzle-ion source, where the *p*NA sample was placed inside its stagnation chamber and heated between 30 and 60°C. The vapor was then co-expanded with approximately 1–2 atm of argon gas through a 25 μm nozzle into ~10^{-4} torr vacuum. Electron attachment occurs by injecting low energy electrons from a hot and even more negatively biased thoriated iridium filament into the expanding jet, where a weak external magnetic field helps to form a microplasma. The newly formed anions were then extracted, collimated, and transported via ion optics through the flight tube of a 90° magnetic sector mass spectrometer with a typical mass resolution of ~400. The mass-selected beam of *p*NA parent anions of interest was then crossed with an

intracavity operated argon ion laser beam, and the photodetached electrons were energy-analyzed by a hemispherical electron energy analyzer with a resolution of ~ 30 meV. The photoelectron spectrum was recorded with 2.540 eV photons and calibrated against the well-known photoelectron spectrum of the O^- anion.[13] A detailed description of this apparatus has been described previously.[14]

Collision Induced Dissociation

All CID studies were performed with a QStar Elite triple-quadrupole mass spectrometer (ABSciex) using argon as the collision target (Figure 5.2.2). Ions were created via electrospray ionization (TurboIonSpray®) by passing a dilute solution containing the analyte through a 0.005 in. inlet syringe tip with a bias voltage of −4.2 kV and a flow rate of 20 μL/min. The resultant charged vapor was carried into the instrument by a nitrogen "curtain" gas. The ions then passed through a declustering region and focusing potential before being spatially separated in the first of three quadrupoles (Q0), mass selected in the second quadrupole (Q1), followed by collision in the final quadrupole (Q2). The collision energy (CE) is set by the difference in potential of the first quadrupole and the offset voltage (RO2) on the sheath of the final quadrupole (CE= Q0–RO2). Final mass analysis of the collision products was performed using a reflectron time-of-flight (TOF) mass spectrometer.

The CAD pressure was held at approximately 3.5×10^{-5} torr throughout the collision process. This is consistent with previous threshold CID experiments.[15–23] The collision cell in the QStar Elite system is 21.2 cm long which is shorter than the expected mean free path of collisions at this pressure.

Calibration of the laboratory energy for the CID studies was carried out using two procedures. First, a retardation analysis was carried out resulting in a vanishing ion signal at 0 ± 0.5 eV. In the QStar Elite system, the presence of the collision gas could not be eliminated because it is used in many of the other instrument processes such as ion cooling. In a second procedure, the energy scale was calibrated using previous studies of the tri-iodide anion, I_3^-.[15–17] Thresholds from these two methods agreed within error bars; however, the I_3^- calibration method is believed to be more precise and accurate.

Following calibration with I_3^-, a concentrated stock solution of *p*NA in methanol was prepared and further diluted (~2.5 μg/mL) for use in the electrospray ionization source. The CE was varied from 8 to 27.5 eV in steps of 0.5 eV in the lab frame.

All ion peak magnitudes were calculated by integrating the mass peak using the Analyst® software package. The cross-section was calculated as the ratio of the target's fragment peak to the sum of the parent ion's peak and the rest of the fragments' peaks. Modeling of the data was carried out using the empirical line of centers model of Armentrout et al.[18–23]

$$\sigma(E) = \sigma_0 \sum_i g_i \frac{(E + E_i - E_0)^n}{E}, \quad (1)$$

where E refers to the CE in the center of mass, while each E_i is an internal energy with respective Boltzmann populations, g_i. Multiplicities and corresponding Boltzmann populations were directly computed using the Beyer-Swinehart algorithm using an effective temperature of 300 K.[24] Constants σ_0, E_0, and n are fit parameters physically interpreted as a scaling factor, the threshold energy, and a factor to account for discrepancies between CID and hard-sphere collisions, respectively. To account for the

thermal distribution of the collision target and the deficiency of energy transfer to the reaction coordinate from uncentered collisions, we used the method of Nalley et al.[25] to develop a distribution of relative velocities.

The transition state utilized in the loss of NO is characterized by the rearrangement of the nitro group to form an ONO chain prior to dissociation. After this rearrangement, the dissociation process is expected to follow a monotonically uphill fragmentation. The transition state used in the modeling of the loss of NO_2^- is a tight transition state with vibrational modes corresponding to the vibrational modes of the deprotonated molecule minus that which corresponds to the reaction coordinate. In this case, the vibrational mode corresponding to the C–N stretch of the nitro group at 1339.03 cm^{-1}. This choice was motivated by the direct cleavage process resulting in NO_2^- anions which is a purely uphill process.

Nonlinear regressions were carried out using a Bayesian Markov Chain Monte Carlo simulation with normal prior probability distributions. The mean of the priors were established by performing a coarse maximum likelihood grid search over the parameter space. In addition to parameter estimates, this fitting method allows for the calculation of model parameters without using numerical approximations to the derivatives which has been shown to be unstable in some cases of energy resolved dissociation modeling.[26] Following this procedure, the CID results in a center-of-mass threshold energy of 1.34 eV, within experimental error of the previously reported value of 1.31 ± 0.06 eV.[15–17] This means that the correction to the ion energy obtained by using the voltage difference between the ion source and target is 0.4 eV in the lab frame.

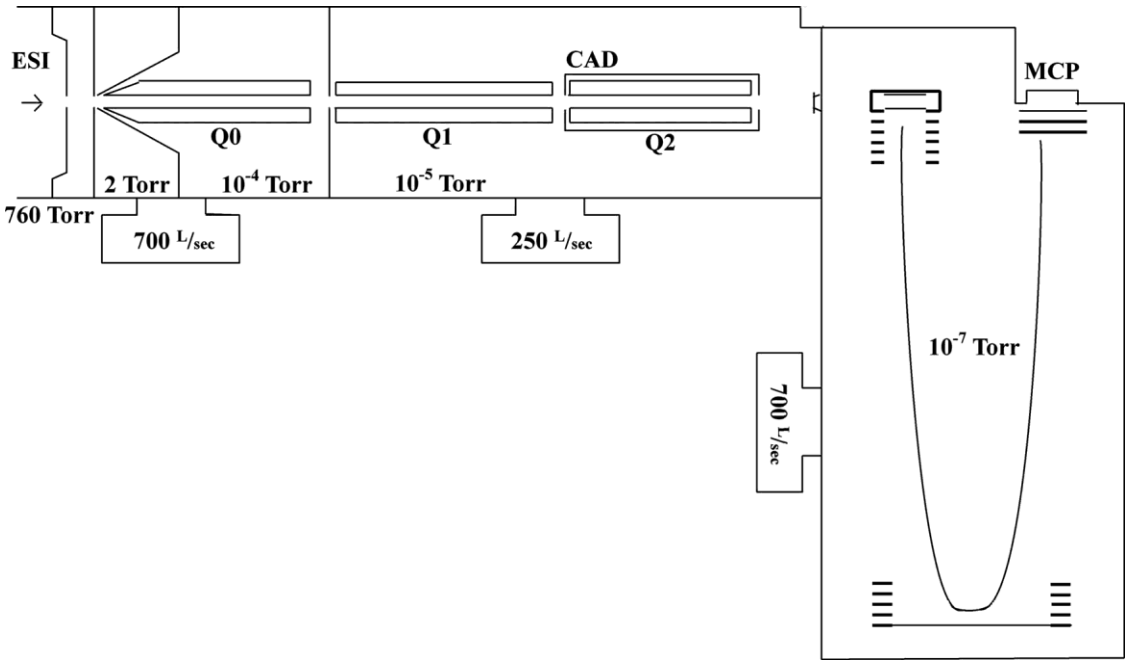

Figure 5.2.2. Schematic of the CID apparatus (QStar Elite TOFMS) showing the quadrupole Q1 for isolation of the electrospray ions and the collision region containing argon gas (CAD) followed by product ion identification by the TOF Mass Spectrometer. Differential pumping occurs at each chamber as shown along with approximate operating pressures in each region.

Ab Initio Methods

Computational investigations focused on characterizing valence and dipole-bound states of the anions of *p*NA. p-Nitroaniline is too large to use highly reliable ab initio methods typically required for predicting electron affinities accurately, and therefore more approximate methods must be used. An additional challenge is that self-consistent-field (SCF) calculations of the valence anion show very large spin contamination rendering second-order Møller–Plesset perturbation theory (MP2) for the valence anion calculations unreliable. Consequently, minimum energy structures and vibrational

frequencies of the neutral were computed using both MP2 and the TPSS density functional,[27] while only the TPSS functional was used for the valence anion. The basis set used in these calculations is Ahlrichs's redefined triple-ζ set augmented with a minimal set of diffuse functions (ma-Def2-TZVP).[28,29]

Vertical electron affinities and vertical electron detachment energies were computed directly with the equation of- motion coupled-cluster with single and double excitations method for electron affinities (EA-EOM-CCSD). The VDE was also computed indirectly as the difference between coupled-cluster with single, double, and perturbative triple excitations energies of the neutral and the anion (ΔCCSD(T)). Owing to the spin contamination problem in Hartree-Fock calculations for the anion, coupled-cluster calculations for the anion were performed using the orbitals of the neutral (so called QRHF coupled-cluster calculations). Two basis sets were used in the coupled-cluster calculations, Dunning's correlation consistent double-ζ (aug-cc-pVDZ) and triple-ζ (aug-cc-pVTZ) sets,[30,31] which were further augmented with a 6*s*6*p*6*d* set (even-tempered exponents between 0.01 and 3.16×10^{-5}) of extra diffuse functions centered at the center of mass of the molecule to characterize dipole-bound states (aug-cc-pVDZ+ and aug-cc-pVTZ+). In the MP2 and in al coupled-cluster calculations, the core electrons were frozen in their SCF orbitals. Three program packages were employed, GAUSSIAN09,[32] Orca,[33] and CFOUR.[34]

The adiabatic electron affinity was computed initially using the B3LYP/6-311++G* level of theory to compute both geometries and single-point energies of the neutral and the valence anion. A more robust value was obtained by combining our best estimates of the following three properties: The VDE (EOM-CCSD/aug-cc-pVTZ), the

deformation energy of the closed-shell neutral, and the zero-point correction (TPSS-DFT frequencies). GAUSSIAN09[32] was used to computationally investigate the dissociations required for the loss of NO and NO_2^-. Calculations of the dissociation energy were performed at the B3LYP/6-311++G* and MP2/aug-ccpVDZ levels of theory.

RESULTS AND DISCUSSION

Photoelectron Spectrum

Attempts were first directed to produce the dipole-bound anion of p-nitroaniline, since its dipole moment is above both the theoretical critical value for a point dipole of 1.625 D and the empirical minimum value of 2.5 D necessary to support a stable dipole-bound state (see Ref. 35 and others cited therein). However, the dipole-bound anion of *p*NA was not evident in the photodetachment data, characterized in a photoelectron spectrum as a single, narrow peak close to zero electron binding energy (EBE) which reflects the nearly identical geometries between the anion and neutral. This dipole-bound feature was not observed due to the nozzle-ion source's tendency to produce only the most stable anionic state of a molecule, which in this case was the valence anion state of p-nitroaniline.

In our experiment, we observed the photoelectron spectrum signature of a typical valence anion and this is shown in Figure 5.2.3. This spectrum consists of a broad, unresolved band with an onset at 0.75 ± 0.10 eV and a maximum intensity at EBE 1.1 eV. The latter value corresponds to the best estimate of the VDE of the parent anion.

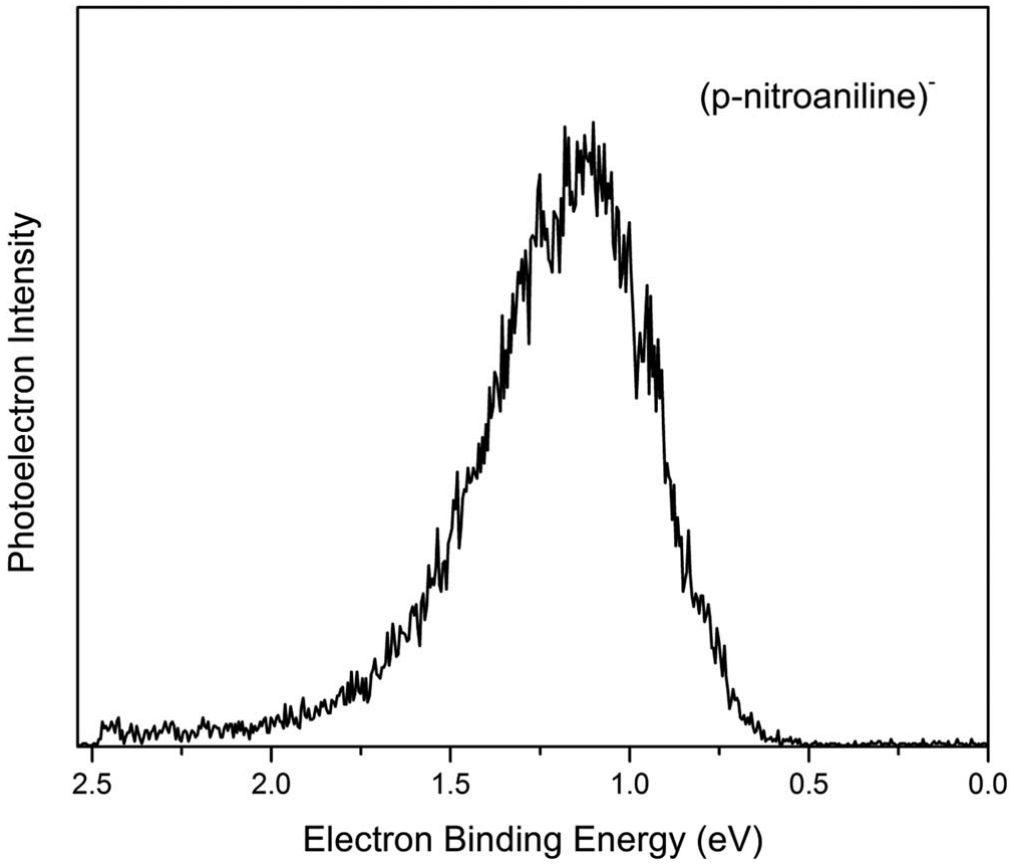

Figure 5.2.3. The photoelectron spectrum of the valence p-nitroaniline anion recorded at 2.540 eV photons. The EA_a is estimated as the signal onset at 0.75 ± 0.1 eV and a VDE of 1.1 eV.

Photodetachment is essentially an instantaneous process; therefore the resultant photoelectron spectral profile is governed by Franck-Condon overlap between the vibrational levels of the ground electronic state of the anion (v″) and those of the ground electronic state of the neutral (v′). In the case of the *p*NA molecule, the structures of the anion and its neutral are not thought to differ greatly, suggesting that there is good overlap between the v″ = 0 and v′ = 0 levels. Nevertheless, its photoelectron spectrum exhibits little vibrational structure, making the precise assignment of the origin transition

difficult. Furthermore, as evidenced by its low EBE spectral tail and the source conditions utilized, vibrational hot bands are probably present. Since vibrational hot bands often account for the first 0.1 to 0.2 eV of the low EBE tail and since there is a discernible steep rise in signal at EBE = 0.75 eV, we estimate the value of EA_a to be 0.75 ± 0.10 eV. This value is in good agreement with theoretical calculations estimate of 0.73 eV.

Collision Induced Dissociation

Figure 5.2.4 shows the deprotonated pNA molecule $[pNA\text{-}H]^-$, and the appearance of ions corresponding to the loss of NO and NO_2^- from $[pNA\text{-}H]^-$. The CID pathways of the $[pNA\text{-}H]^-$ anion is given below:

$$p\text{NA-H}^- \rightarrow [p\text{NA} - \text{H} - \text{NO}]^- + \text{NO}$$

and

$$p\text{NA-H}^- \rightarrow [p\text{NA} - \text{H} - \text{NO}_2] + \text{NO}_2^-$$

are listed in order of increasing energy required to induce dissociation (see Figure 5.2.5). The two fragmentation pathways observed here are commonly seen in many similar molecules.[11,12]

Calculations of the threshold for both reaction pathways were carried out with the results shown in Table 5.2.1. The CRUNCH package has been used to show similar results (see the supplementary materials).[22,23,36–48] There are considerable differences in the ab initio thresholds depending upon the method employed. Despite these differences some conclusions can be drawn concerning the dissociation mechanisms.

Table 5.2.1. Dissociation barrier energies of [*p*NA-H]$^-$. Calculated energies are the difference between deprotonated *p*NA and the transition state.

Method	Loss of NO	Loss of NO_2^-
B3LYP/6-311++G*	0.99	4.30
MP2/aug-cc-pVDZ	. . .	3.39
Experiment	2.36	3.80

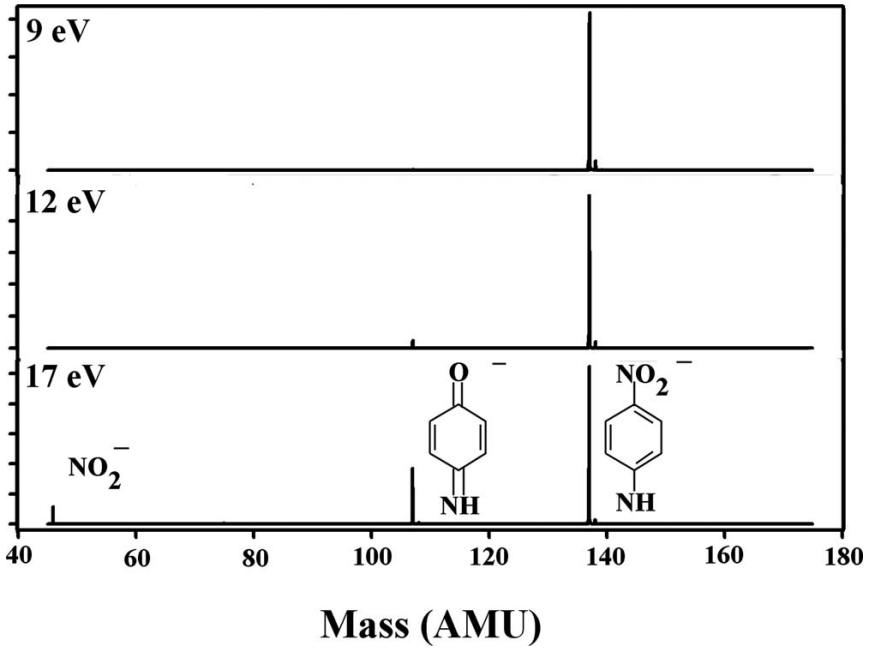

Figure 5.2.4. Appearance of fragments caused by collision of [*p*NA-H]$^-$ with argon at lab frame energies of 9 eV, 12 eV, and 17 eV. Relative abundances are normalized to the parent anion peak.

In comparing experiment with calculations, one can see that there is good agreement between the values for the dissociation pathway leading to NO_2^- loss (pathway 2), while a significant barrier prevents the loss of NO from deprotonated *p*NA. This is attributed to the rearrangement of the molecule in order to foster the loss of nitric oxide (see the supplementary material).[48] The rearrangement requires the rotation of the nitro group to form a CNO ring which is finally cleaved from the rest of the molecule.[11] A minimal energy geometry for this transition state was computed using the B3LYP/6-311++G* level of theory while calculations at the MP2 level failed to converge.

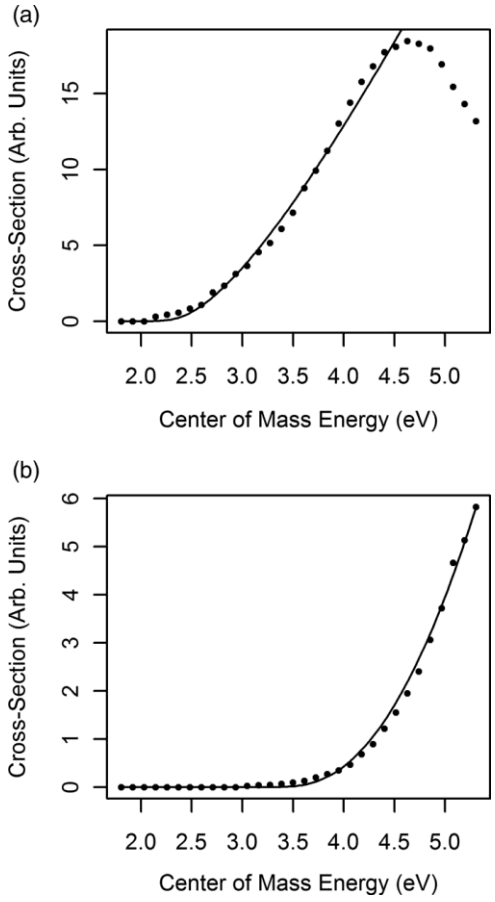

Figure 5.2.5. Nonlinear fits of the CID cross-section of $[pNA\text{-}H]^-$ into (a) $[pNAH\text{-}NO]^-$ and (b) NO_2^-.

Ab Initio Calculations

Calculations at both the MP2 and TPSS-DFT level of theory suggest that the minimal energy geometry of neutral *p*NA has Cs symmetry where the benzene ring and the nitro group are essentially planar, but the amino group is pyramidal. However, the completely planar C_{2v} symmetrical conformation, which is a transition state with respect to the NH_2 wagging motion, is very close in energy (about 3 kJ/mol using TPSS and 1 kJ/mol using MP2). Comparing this to the frequency of the wagging motion, 540 cm^{-1} or 3.2 kJ/mol, it is apparent that this vibrational mode will be highly anharmonic, showing a large amplitude motion. Computing properties of the neutral accurately is thus challenging because it involves a weighted average over a large Franck-Condon zone and here we limit ourselves to reporting properties computed at the C_s and C_{2v} stationary points. It should be noted that these values will contribute strongly to the vibrationally averaged results. For the valence anion of *p*NA the situation is more straightforward: The electron occupies the lowest π^*-like orbital which increases the barrier associated with the amino wagging motion to 13.5 kJ/mol and while the valence anion may invert, it can clearly be thought of as having C_s symmetry. Note that due to the large spin contamination at the SCF level, MP2 calculations for the valence anion are expected to be unreliable, similar to what has been found for nitrobenzene.[49]

First, vertical electron attachment to *p*NA was studied with the EA-EOM-CCSD method using aug-cc-pVDZ+ and aug-cc-pVTZ+ basis sets. At both geometries the anion is predicted to have three bound states, two with EBE on the order of 100 meV, and one very weakly bound state with a binding energy of about 2 meV (Table 5.2.2). The two

states with approximately 100 meV binding energy represent a pair of strongly coupled diabatic states, one with dipole-bound and one with valence bound character; the third

Table 5.2.2. Vertical electron affinities, in meV, computed with the EAEOM-CCSD method. The standard augmented double-ζ and triple-ζ basis set were further augmented with a 6*s*6*p*6*d* set of extra diffuse functions at the center of mass of the molecule. At the C_{2v} symmetric transition state dipole-bound states have A′ symmetry while the valence state has B_1 symmetry. In C_s symmetry all bound states have A′ symmetry, and only the third state can be characterized as dipole-bound, whereas the lower two states show a mixed character.

	C_{2v} symmetry		
	1st $^2A_1$	2nd $^2A_1$	1st $^2B_1$
aug-cc-pVDZ+	104	2.0	47
aug-cc-pVDZ+	107	2.0	208
	C_s symmetry		
	1st $^2A'$	2nd $^2A'$	3rd $^2A'$
aug-cc-pVDZ+	110	80	1.5
aug-cc-pVDZ+	261	96	1.5

state is very diffuse and does not mix appreciably with the lower two states. The lower two states can be untangled at the planar geometry, because in C_{2v} symmetry the two states are decoupled with the dipole-bound state showing $^2A_1$ symmetry while the valence state has $^2B_1$ symmetry (Figure 5.2.6). The valence state is compact with an <|r|> value of

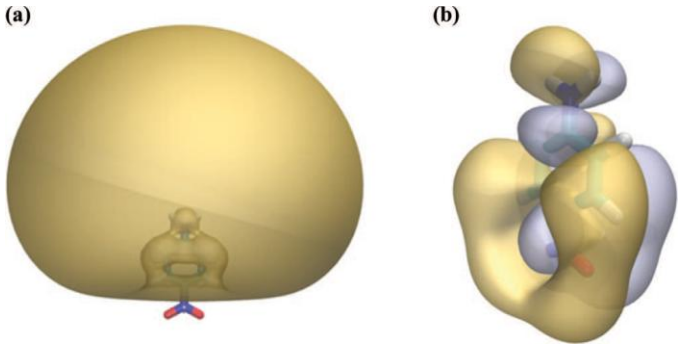

Figure 5.2.6. Natural orbitals from EA-EOM-CCSD/aug-cc-pVDZ+ calculations for the two lowest states of the *p*NA$^-$ anion. At the C_{2v} symmetrical transition state the two lower states of the anion have different symmetries, $^2A_1$ and $^2B_1$. Therefore, they are completely decoupled, and can be characterized as dipole-bound and valence. (a) shows the 80% enclosing iso-surface of the dipole-bound state and (b) shows the 90% enclosing iso-surface of the valence state. Note the different length scale of the two figures; <|r|> is 8.5 Å for the natural orbital of the dipole-bound state and just 2.6 Å for that of the valence state.

2.6 Å in contrast to the diffuse dipole bound state which has an <|r|> of 8.5 Å. As expected for a valence state, the EBE increases substantially in going from a double-zeta to a triple-zeta basis set (Table 5.2.2). At non-planar geometries, the valence and dipole states mix (both have $^2A'$ symmetry) with the state lower in energy being somewhat more compact and therefore having somewhat more valence character (Figure 5.2.7).

Second, the VDE of the *p*NA anion has been computed at its C_s symmetrical minimal energy structure and at the planar C_{2v} symmetrical transition state (Table 5.2.3). The EA-EOM-CCSD/aug-cc-pVTZ results suggest that the VDE depends strongly on the

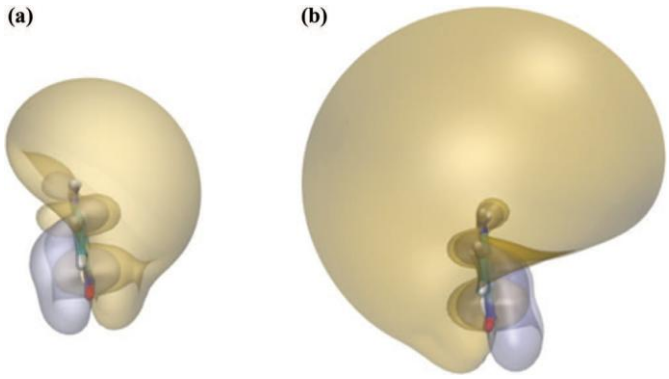

Figure 5.2.7. Natural orbitals from EA-EOM-CCSD/aug-cc-pVDZ+ calculations for the two lowest states of the *p*NA$^-$ anion. At the Cs symmetrical minimal energy geometry, the two lower states of the anion both have $^2A'$ symmetry are strongly coupled, and cannot consequently be characterized as either dipole-bound or valence. Eighty-percent enclosing iso-surfaces of the first and second states are shown in (a) and (b), respectively. Note the comparable length scale of the two figures; <|r|> of the respective natural orbital is 4.3 Å for the lower and 6.8 Å for the higher state.

Table 5.2.3. Vertical detachment energy, in eV, computed with different methods and basis sets. Two geometries are considered, the C_s symmetrical minimal energy structure of the *p*NA anion, and the associated C_{2v} symmetrical transition state of the NH_2 inversion.

		C_s minimum energy structure	C_{2v} transition state
aug-cc-pVDZ	ΔCCSD(T)	0.83	0.69
	EA-EOM-CCSD	0.76	0.62
aug-cc-pVTZ	ΔCCSD(T)	. . .	0.84
	EA-EOM-CCSD	0.94	0.80

precise geometry of the NH_2 group, which in turn suggests that the VDE at the minimal energy structure may not be a reliable measure for the vibrationally averaged VDE (cf. discussion above). For a reliable prediction of the photoelectron spectrum, one would need to map out the VDE in the Franck-Condon zone and perform a Franck-Condon analysis for the anion to neutral transition. Moreover, finite temperature effects may be expected to shift the maximum of the photoelectron signal to lower energies because higher temperature should be associated with effectively planar NH_2 groups. Mapping and properly averaging the VDE are well beyond the scope of this paper, and again we have to limit ourselves to properties evaluated at stationary points, which suggest a VDE in the 0.85 to 1.0 eV range. This range is based on the ΔCCSD(T)/aug-cc-pVTZ VDE of the C_{2v} symmetrical conformation, the energy difference between the C_{2v} and C_s symmetrical structure computed at the EOM-CCSD level, and the expectation that the aug-cc-pVTZ basis set is reasonably well converged.

Finally, the adiabatic electron affinity (EA_a) for the valence *p*NA anion was calculated at the B3LYP/6-311++G* level using C_s geometry for the anion and C_{2v} for the neutral and the result is 0.88 eV. A presumably more reliable value for the EA_a of the valence state can be derived from (1) our best VDE (EOM-CCSD), (2) the CCSD(T) deformation energy of the neutral (that is, the energy difference of the neutral at its own equilibrium geometry and the neutral at the equilibrium geometry of the valence anion), and (3) the zero-point correction from the TPSS-DFT frequencies. Again, there are caveats regarding the floppy nature of the neutral, but for the EA_a these effects should be small. The EA_a obtained from the EOM-CCSD/aug-cc-pVTZ VDE of 0.94 eV, the deformation energy of 0.32 eV (CCSD(T)/aug-cc-pVTZ), and the zero-point correction

of 0.11 eV (TPSS/maDef2-TVZP) is 0.73 eV. The biggest error likely arises from the VDE, which is, as discussed above, expected to be an underestimate. In any event, the value compares favorably with the experimental findings.

CONCLUDING REMARKS

Properties of the parent ion and the ion resulting from deprotonation of the highly polar p-nitroaniline molecule have been studied both experimentally and theoretically. The theoretical adiabatic electron affinity of *p*NA (0.73 eV) is in excellent agreement with the measured value of 0.75 ± 0.1 eV. Also, there is good agreement between theory and experiment for the dissociation energy leading to NO_2^- loss from $[pNA - H]^-$; however, combined theory and experiment predicts a significant barrier to the loss of NO from the dehydrogenated *p*NA anion.

In addition to the valence anions, we predicted two dipole-bound anion states, one at 100 meV and an excited state bound by about 2 meV. While there cannot be any doubt that *p*NA supports dipole-bound states, these states were not directly observed in this experiment. There are several reasons for this behavior: first, dipole-bound states are difficult to observe directly in such "doorway" cases as explained in our earlier studies of nitroethane,[50] nitromethane,[51] and nitrobenzene.[52] Second, we did not attempt to observe the dipole-bound anion of *p*NA with a predicted binding energy of 100 meV using Rydberg electron transfer (RET). Any formation of this dipole-bound anion using RET would occur at such low principle quantum numbers that signal would be too low to detect due to the inability of the ion-pair to separate as reported in earlier experiments with highly polar (~ 5.5 D) molecules.[53] Also the dipole-bound state with an energy of 3

meV would be masked by the RET to the valence state much like that seen in our earlier studies.[50–52] Rotational resonances have been well studied previously for dipole-bound *radical anions*.[58,59] *p*NA$^-$ represents an excellent candidate to search for threshold rotational resonances at both of the valence to dipole-bound excitation energies (i.e., EA_a = 0.75 eV or 1653 nm). The presence of two dipole bound states should make for interesting spectroscopy.

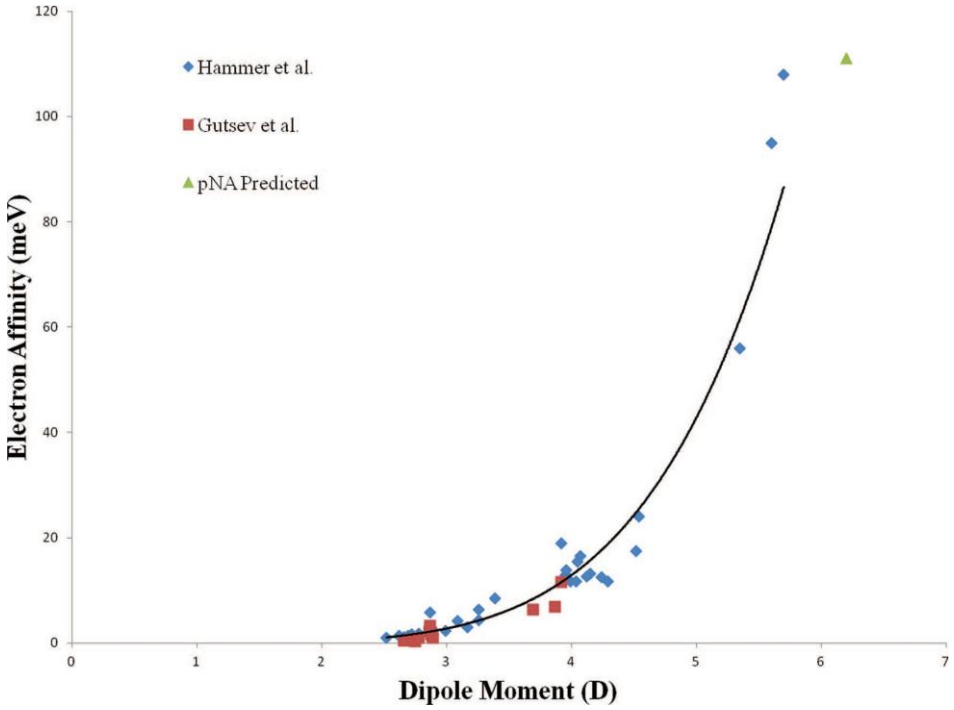

Figure 5.2.8. A compilation of experimental electron binding energies versus molecular dipole moment.[52–57] There is some uncertainty as to the dipole moment of the isolated *p*NA molecule; however, it has been measured in acetone to be 6.2 D.[3]

It is instructive to place the highly polar *p*NA molecule in reference to other dipole-bound anions. Figure 5.2.8 presents a comparison of all dipole-bound electron affinities reported from both experiment and theory versus dipole moment including our calculated value for *p*NA at 6.2 D. More experiments and theories are needed for polar molecules above 5 D in order to evaluate the molecular properties other than dipole moment which contribute to electron binding. For large dipole moment molecules, the electron is much "closer" to the molecular framework and at some point the electron can be bound into a valence type state. A solution to this problem for a high dipole moment molecule would be a better method used in the production of the dipole-bound anion. It is known that if the dipole moment is too high the detection of the anion is extremely difficult for Rydberg electron transfer processes due to the inability of the ion-pair to separate at such small internuclear separations.[51] To this end we are currently working on a method to accommodate fast Rydberg atoms in RET reactions to allow better separation of dipole-bound anion and alkali cation pairs to prepare dipole-bound anion signals intense enough for further studies.

Finally, we have previously pointed out that dipole-bound anions can act as "doorway states" to the formation of valence bound anions in nitroethane,[50] nitromethane,[51] and nitrobenzene.[52] One might call this intramolecular charge transfer within the molecule. This may be particularly important in large biomolecules (i.e., those involving amino acid moieties). In an extended system of such polar (or quadrupolar) molecules, electrons may flow from the dipole-bound state through the molecular framework to be stabilized on the electronegative end. Electrons might also be envisioned to pass through an extended chain of amino acids in a particular direction determined by

the energy level of the dipole-bound anion (i.e. magnitude of the dipole moment). The works of Simons[60–62] and colleagues are beginning to address this important problem.

ACKNOWLEDGEMENTS

Parts of this research are based on work supported by the National Science Foundation under Grant Nos. CHE-1111693 (K.H.B.) and CHE-0848487 (R.N.C.). We would also like to acknowledge the donors of The American Chemical Society Petroleum Research Fund for support of this research through Grant No. PRF 52486-UR6. We are indebted to Dr. Peter Armentrout for providing us with the CRUNCH program used in the supplementary materials.

REFERENCES

1. Moran, A.M.; Kelly, A. M.; Tretiak S. *Chem. Phys. Lett*. **2003**, *367*, 293.
2. Nalwa, H. S.; Hanack, M.; Pawlowski, G.; Engel M. K. *Chem. Phys*. **1999**, *245*, 17.
3. Cheng, L-T.; Tam, W.; Stevenson, S. H.; Meredith, G. R.; Rikken, G.; Marder, S. R. M. *J. Phys. Chem*. **1991**, *95*, 10631.
4. Soscún, H.; Castellano, O.; Bermúdez, Y.; Toro, C.; Cubillán, N.; Hinchliffe, A.; Phu, X. N. *Int. J. Quantum Chem*. **2006**, *106*, 1130.
5. Kawski, A.; Kukli´nski, B.; Bojarski, P. *Chem. Phys*. **2006**, *330*, 307.
6. Hadjiantoniou, A.; Christophorou, L. G.; Carter, J. G. *J. Chem. Soc., Faraday Trans. 2* **1973**, *69*, 1691.
7. Huh, C.; Kang, C. H.; Lee, H. W.; Nakamura, H.; Mishima, M.; Tsuno, Y.; Yamataka, H. *Bull. Chem. Soc. Jpn*. **1999**, *72*, 1083.
8. Chowdhury, S.; Kishi, H.; Dillow, G. W.; Kebarle, P. *Can. J. Chem*. **1989**, *67*, 603.
9. Potapov, V. K.; Kardash, I. E.; Sorokin, V. V.; Sokolov, S. A.; Evlasheva, T. I. *Khim. Vys. Energ.* **1972**, *6*, 392.
10. Brown, P.; *Org. Mass Spectrom.* **1970**, *4(suppl.),* 533.
11. Bowie, J. H.; Blumenthal, T.; Walsh, I. *Org. Mass Spectrom*. **1971**, *5*, 777.
12. Gierczyk, B.; Grajewski, J.; Zalas, M. *Rapid Commun. Mass Spectrom*. **2006**, *20*, 361.
13. Neumark, D. M.; Lykke, K. R.; Andersen, T.; Lineberger, W. C. *Phys. Rev. A* **1985**, *32*, 1890.

14. Coe, J. V.; Snodgrass, J. T.; Freidhoff, C. B.; McHugh, K. M.; Bowen, K. H. *J. Chem. Phys*. **1986**, *84*, 618.

15. Do, K.; Klein, T. P.; Pommerening, C. A.; Sunderlin, L. S. *J. Am. Soc. Mass Spectrom*. **1997**, *8*, 688.

16. Hoops, A. A.; Gascooke, J. R.; Faulhaber, A. E.; Kautzman, K. E.; Neumark, D. M. *J. Chem. Phys.* **2004**, *120*, 7901.

17. Lynden-Bell, R. M.; Kosloff, R.; Ruhman, S.; Danovich, D.; Vala, J. *J. Chem. Phys*. **1998**, *109*, 9928.

18. Khan, F. A.; Clemmer, D. E.; Schultz, R. H.; Armentrout, P. B. *J. Phys. Chem*. **1993**, *97*, 7978.

19. Muntean, F.; Armentrout, P. B. *J. Chem. Phys*. **2001**, *115*, 1213.

20. Amicangelo, J. C.; Armentrout, P. B. *Int. J. Mass Spectrom*. **2001**, *212*, 301.

21. Armentrout, P. B.; Ervin, K. M.; Rodgers, M. T. *J. Phys. Chem. A* **2008**, *112*, 10071.

22. Dalleska, N. F.; Honma, K.; Sunderlin, L. S.; Armentrout, P. B. *J. Am. Chem. Soc*. **1994**, *116*, 3519.

23. Rodgers, M. T.; Ervin, K. M.; Armentrout, P. B. *J. Chem. Phys*. **1997**, *106*, 4499.

24. Beyer, T.; Swinehart, D. F. *Commun. ACM* **1973**, *16*, 379.

25. Nalley, S. J.; Compton, R. N.; Schweinler, H. C.; Anderson, V. E. *J. Chem. Phys*. **1973**, *59*, 4125.

26. Narancic, S.; Bach, A.; Chen, P. *J. Phys. Chem. A* **2007**, *111*, 7006.

27. Tao, J.; Perdew, J. P.; Staroverov, V. N.; Scuseria, G. E. *Phys. Rev. Lett*. **2003**, *91*, 146401.

28. Weigend, F.; Ahlrichs, R. *Phys. Chem. Chem. Phys*. **2005**, *7*, 3297.

29. Papajak, E.; Truhlar, D. J. *J. Chem. Theory. Comput*. **2010**, *6*, 597.

30. Dunning, Jr., T. H. *J. Chem. Phys*. **1989**, *90*, 1007.

31. Kendall, R. A.; Dunning, Jr., T. H.; Harrison, R. J. *J. Chem. Phys*. **1992**, *96*, 6796.

32. Frisch, M. J.; Trucks, G. W.; Schlegel, H. B. *et al.*, GAUSSIAN 09, Revision B.01, Guassian, Inc., Wallingford, CT, 2009; GAUSSIAN 03, Revision 6.0, Gaussian, Inc., Wallingford, CT, 2003.

33. ORCA, version 2.8.0, Neese, F., with contributions from Becker, U.; Ganiouchine, D.; Koßmann, S.; Petrenko, T.; Riplinger, C.; Wennmohs, F. see http://www.thch.uni-bonn.de/tc/orca/.

34. CFOUR, version 1, Stanton, J. F.; Gauss, J.; Harding, M. E.; Szalay, P. G. with contributions from Auer, A. A.; Bartlett, R. G.; Benedikt, U.; Berger, C.; Bernholdt, D. E.; Bomble, Y. J.; Cheng, L.; Christiansen, O.; Heckert, M.; Heun, O.; Huber, C.; Jagau, T.-C.; Jonsson, D.; Jusélius, J.; Klein, K.; Lauderdale, W. J.; Matthews, D. A.; Metzroth, T.; Mück, L .A.; O'Neill, D. P.; Price, D. R.; Prochnow, E.; Puzzarini, C.; Ruud, K.; Schiffmann, F.; Schwalbach, W.; Stopkowicz, S.; Tajti, A.; Vázquez, J.; Wang, F.; Watts, J. D. and the integral packages MOLECULE (J. Almlöf and P. R. Taylor), PROPS (P. R. Taylor), ABACUS (T. Helgaker, H. J. Aa. Jensen, P. Jørgensen, and J. Olsen), and ECP routines by A. V. Mitin and C. van Wüllen. For the current version, see http://www.cfour.de.

35. Hammer, N. I.; Diri, K.; Jordan, K. D.; Defrançois, C.; Compton, R. N. *J. Chem. Phys.* **2003**, *119*, 3650.

36. Ervin, K. M.; Armentrout, P. B. *J. Chem. Phys*. **1985**, *83*, 166.

37. Weber, M. E.; Elkind, J. L.; Armentrout, P. B. *J. Chem. Phys*. **1986**, *84*, 1521.

38. Schultz, R. H.; Crellin, K. C.; Armentrout, P. B. *J. Am. Chem. Soc*. **1991**, *113*, 8590.

39. Shvartsburg, A. A.; Ervin, K. M.; Frederick, J.H. *J. Chem. Phys*. **1996**, *104*, 8458.

40. DeTuri, V. F.; Ervin, K.M. *J. Phys. Chem. A* **1999**, *103*, 6911.

41. Iceman, C.; Armentrout, P. B. *Int. J. Mass Spectrom*. **2003**, *222*, 329.

42. Su, T. *J. Chem. Phys.* **1994**, *100*, 4703.

43. Ervin, K. M. *Int. J. Mass Spectrom*. **1999**, *185*, 343.

44. Koizumi, H.; Armentrout, P. B. *J. Chem. Phys.* **2003**, *119*, 12819.

45. Koizumi, H.; Muntean, F.; Armentrout, P.B. *J. Chem. Phys*. **2004**, *120*, 756.

46. Amicangelo, J. C.; Armentrout, P. B. *J. Phys. Chem. A* **2004**, *108*, 10698.

47. Armentrout, P. B. *J. Chem. Phys*. **2007**, *126*, 234302.

48. See supplementary materials at http://dx.doi.org/10.1063/1.4810869 for detailed information about the CID modeling.

49. Lambert, J.; Chen, J.; Buonaugurio, A.; Bowen, K. H.; Do-Thanh, C.-L.; Wang, Y.; Best, M. D.; Compton, R. N.; Sommerfeld, T. "Combined photoelectron, collision-induced dissociation, and computational studies of parent and fragment anions of N-paranitrosulfophenylsufonyalanine and Nparanitrophenylalanine," *J. Chem. Phys*. (unpublished).

50. Stokes, S. T.; Bowen, K. H.; Sommerfeld, T.; Ard, S.; Mirsaleh-Kohan, N.; Steill, J. D.; Compton, R. N. *J. Chem. Phys*. **2008**, *129*, 064308.

51. Compton, R. N.; Carman, Jr., H. S.; Defrancois, C.; Hendricks, J. H.; Lyapustina, S. A.; Bowen, K. H. *J. Chem. Phys*. **1996**, *105*, 3472.

52. Desfrancois, C.; Périquet, V.; Lyapustina, S. A.; Lippa, T. P.; Robinson, D. W.; Bowen, K. H.; Nonaka, H.; Compton, R. N. *J. Chem. Phys*. **1999**, *111*, 4569.

53. Hammer, N. I.; Hinde, R. J.; Compton, R. N.; Diri, K.; Jordan, K. D.; Radisic, D.; Stokes, S. T.; Bowen, K. H. *J. Chem. Phys*, **2004**, *120*, 685.

54. Gutsev, G. L.; Adamowicz, L. *Chem. Phys. Lett*. **1995**, *235*, 377.

55. Nelson, Jr., R. D.; Lide, Jr., D. R.; Maryott, A. A. *Selected Values of Electric Dipole Moments for Molecules in the Gas Phase*, NSRDS-NBS, Vol. 10 (US GPO, Washington, 1967).

56. Lide, D. R. ed., *CRC Handbook of Chemistry and Physics* (CRC Press, Boca Raton, 1994).

57. Desfrançois, C.; Abdoul-Carime, H.; Khelifa, N.; Schermann, J. P. *Phys. Rev. Lett*. **1994**, *73*, 2436.

58. Mullins, A. S.; Murray, K. K.; Schultz, C. P.; Lineberger, W. C. *J. Phys. Chem*. **1995**, *97*, 10281.

59. Brinkman, E. A.; Berger, S.; Marks, J.; Brauman, J. I. *J. Chem. Phys*. **1993**, *99*, 7586.

60. Gutowski, M.; Skurski, P.; Simons, J. *Int. J. Mass Spectrom*. **2000**, *201*, 245.

61. Simons, J. *J. Am. Chem. Soc*. **2010**, *132*, 7074.

62. Neff, D.; Simons, J. *J. Phys. Chem. A* **2010**, *114*, 1309.

SUPPLEMENTAL MATERIAL

Modeling

The raw data is output from the Analyst software as a peak amplitude ascertained through the integration of a time-averaged mass peak paired with the corresponding collision energy. Because the target gas in the collision process is not stationary, the collision energy associated with a peak must be corrected. This energy can done by following Nalley et al.[1]

$$v \rightarrow v = \int_0^\infty v_R F_R(v_R) dv_R.$$

for

$$F_R(v_R) = \int_{-\infty}^{\infty} \frac{v_R}{v} \frac{1}{\sqrt{\pi} v_0} \left\{ \exp\left[-\frac{(v_R - v_0)^2}{v_0^2} \right] - \exp\left[-\frac{(v_R + v_0)^2}{v_0^2} \right] \right\} F(v) dv$$

where v_0 is the mean of the projectile velocity distribution, $F(v)$. The velocities of each projectile are assumed to be normally distributed about the collision energy with a standard deviation consistent with the uncertainty in the collision energy. The initial distribution of projectile velocities has been taken to be a Normal distribution with a mean equal to the collision energy. The variance of this distribution is chosen arbitrarily; because the Normal distribution is symmetric about the mean, the resultant transformed x-axis is independent of the variance. Similar results have been proven with alternative methods[2] and have been used thoroughly in collisional charge transfer experiments.[3]

The non-linear modeling of energy resolved CID data has been contentious.[4] Although several traditional methods exist to calculate the model parameters, a recent analysis by Narancic et al.[5] has shown that non-linear regression using the Marquardt-

Levenburg optimization may be insufficient. The authors cite the numerical estimation of derivatives used in the optimization procedure.

As an alternative to Marquardt-Levenburg optimization, a non-parametric optimization algorithm such as the Genetic Algorithm may be implemented. We instead use the Metropolis Algorithm to create a Bayesian posterior distribution of the model parameters. In this way we not only obtain information regarding the parameter estimates, but the full variance structure of each parameter and the correlation as well. To

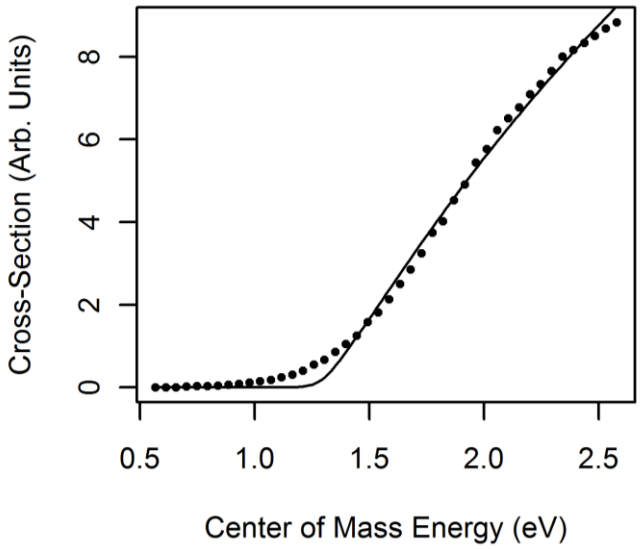

Figure 5.2.S1. Non-linear modeling of the cross-section of I^- dissociation from I_3^- colliding with argon.

use this algorithm we first use a coarse grid search over the parameter space for a minimum error solution. These initial values were then used as the mean of a Normal prior probability distribution for each parameter. A comparison of our results is performed with CRUNCH produced by the Armentrout et al. group (Figures 5.2.S1 and 5.3.S2).[4,6-19]

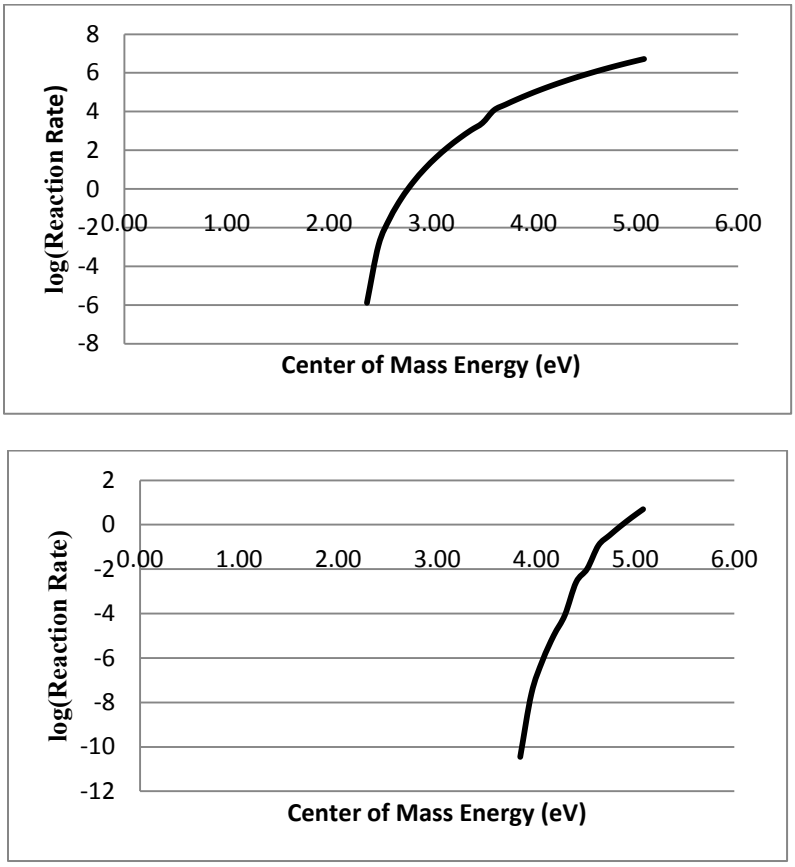

Figure 5.2.S2. RRKM reaction rates versus the center of mass collision energy for a) loss of NO and b) loss of NO_2^-.

Parameter error estimates in regression can be analytically derived in the case of linear regression. For non-linear regression parameter error estimates again arise from the numerical estimates of the derivatives. In contrast, the Bayesian paradigm allows for a direct estimate of the parameter error through the posterior probability distribution of the parameter estimates. Furthermore, the energy offset of the dependent variable observed in the fitting of I_3^- dissociation can be incorporated in the parameter error through repeated

fitting of the data after the introduction of random noise on the order of the offset or as a hyperparameter associated with the independent variable.

It is important to note that this empirical model shows a high level of inter-parameter correlation. This is not uncommon to non-linear models, but may play a role in the optimization procedure. In particular the parameters σ_0 and E_0 have a correlation around 0.9. In order to work around this correlation, the variance of each prior probability distribution was modified until the correlation was minimized. This correlation will affect the modeling procedure due to multiple solutions (and thus a wide spread of threshold energies) giving equivalent curves with respect to error.

Due to the existence of contact and surface potentials, specified voltages cannot be assumed to solely characterize the ion laboratory energy. Calibration of the ion energy as well as the energy spread was thus performed using the CID of I_3^-, i.e.

$$I_3^- \rightarrow I^- + I_2 \qquad (1)$$

Previous studies of this reaction place the threshold in the center of mass collision energy at 1.31 ± 0.06 eV using photodissociation as well as collision induced dissociation.[20-22] The observed and uncalibrated threshold for reaction (1) above is shown in Figure 5.2.S3. The tri-iodide anion vibrational frequencies were estimated from a combination of calculation and experiment.[21,23] A dilute solution of iodine in acetonitrile was tested repeatedly for the presence of I_3^- by iteratively increasing the concentration until enough ion signal was present to carry out a thorough analysis of the dissociation threshold. The collision energy was varied in the lab frame from 4 to 27 eV in steps of 0.5 eV.

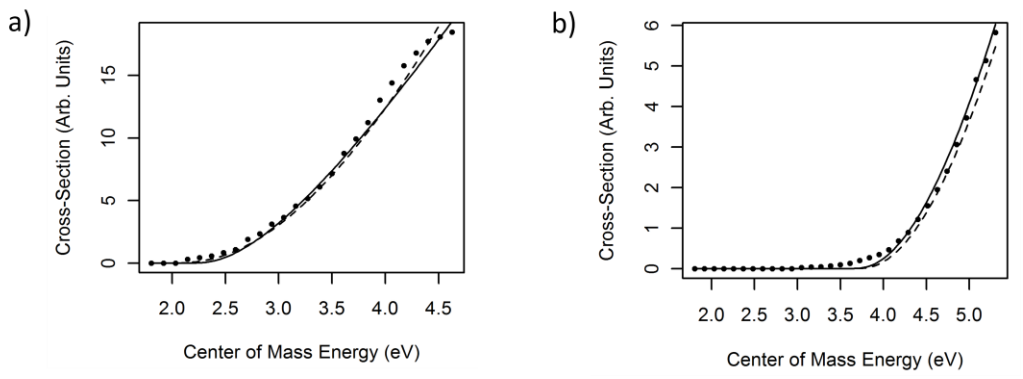

Figure 5.2.S3. A comparison of the Bayesian MCMC fit (solid line) to CRUNCH's Marquardt-Levenburg non-linear regression (dashed line) for loss of a) NO and b) NO_2^-.

Analysis of Error in CID

An assessment of the error in the modeling of CID data may be broken into two bases: Error endemic to the modeling and that which results from experimental error. The former of these may be addressed directly through the Bayesian MCMC by considering the 95% credible intervals generated through the simulation. In this respect there is no inherent distribution dependence (such as a Normal dependence in most parameter error estimates) because the posterior distribution is generated numerically. For I_3^- this modeling error is 0.03 eV while it is 0.07 eV for each of the p-nitroaniline fragments. This estimate may be further corroborated through repeated applications of the algorithm and analysis of the resultant fit parameters.

Furthermore, inclusion of a kinetic shift through the use of an RRKM reaction rate would result in a decrease in the modeled threshold typically on the order of 0.2 to 0.3 eV.[4-19] Absolute values are not included here due to instability in the model resulting in unreasonable values for the fit parameters. Nevertheless, we include a plot of the calculated reaction rates in CRUNCH (Figure 5.2.S2). Note that the RRKM reaction rates

corresponding to the loss of NO_2^- are relatively small indicating a more dramatic change in the expected CID threshold.

A comprehensive analysis of experimental errors would require careful measurements of the kinetic energy distribution of the projectile ions, the collision cell pressure, collision cell effective length (the length over which collision occur), and the time of flight of fragment anions. Each of these in turn may add to the error of the dissociation threshold. The zero of the distribution can be assessed through a retardation analysis. Under the assumption of linearity in the scale (dictated through uniform potential differences in the instrument), the mean of the distribution may then be ascertained. A stronger analysis is to use a calibrating sample (in this case I_3^-) in order to identify the scale.

By utilizing the independent axis transformation described above, the effect of the FWHM of the projectile distribution is minimized because it is integrated over. Therefore, the convolution process is closer to Chantry's single integral than to Tiernan's method.[2,3]

Table 5.2.S1. A comparison of the fit parameters resulting from the Bayesian MCMC used here and CRUNCH's fit.

Channel	Fit Method	σ_0	E_0	n
NO Loss	Bayesian MCMC	17.30	2.36	1.91
	CRUNCH	9.711	2.16	2.40
NO_2^- Loss	Bayesian MCMC	11.43	3.82	2.14
	CRUNCH	10.99	3.87	2.15

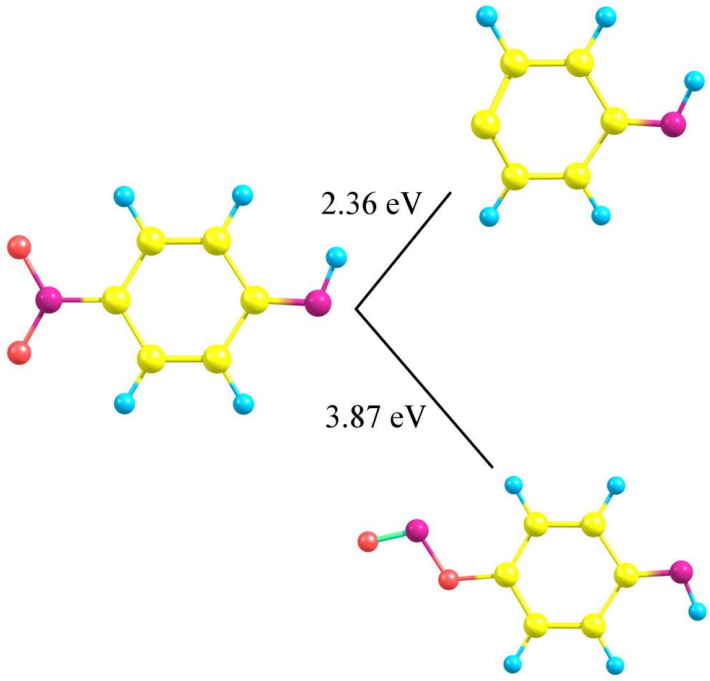

Figure 5.2.S4. Transition state structures used in the CRUNCH calculations.

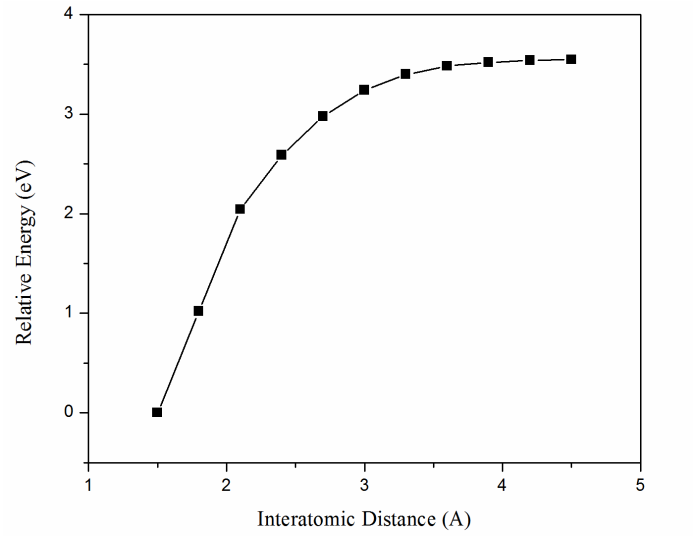

Figure 5.2.S5. Potential energy curve resulting in the loss of NO_2^- calculated using a mod-redundant algorithm at the B3LYP/6-31+G* level of theory. Note that the potential energy curve is strictly uphill as expected.

SUPPLEMENTAL MATERIAL REFERENCES

1. Nalley, S. J.; Compton, R. N.; Schweinler, H. C.; Anderson, V. E. *J. Chem. Phys.* **1973***, 59*, 4125.
2. Chantry, P. J. *J. Chem. Phys.* **1971**, *55*, 2746.
3. Lifshitz, C.; Wu, R. L. C.; Tiernan, T. O.; Terwilliger, D. T. *J. Chem. Phys.* **1978***, 68*, 247.
4. Armentrout, P. B.; Ervin, K. M.; Rodgers, M. T. *J. Phys. Chem. A* **2008,** *112*, 10071.
5. Narancic, S.; Bach, A.; Chen, P. *J. Phys. Chem. A* **2007**, *111*, 7006.
6. Ervin, K. M.; Armentrout, P. B. *J. Chem. Phys.* **1985***, 83*, 166.
7. Weber, M. E.; Elkind, J. L.; Armentrout, P. B. *J. Chem. Phys.* **1986**, *84*, 1521.
8. Schultz, R. H.; Crellin, K. C.; Armentrout, P. B. *J. Am. Chem. Soc.* **1991**, *113*, 8590.
9. Dalleska, N. F.; Honma, K.; Sunderlin, L. S.; Armentrout, *J. Am. Chem. Soc.* **1994**, *116* 3519.
10. Shvartsburg, A. A.; Ervin, K. M.; Frederick, J. M. *J. Chem. Phys.* **1996,** *104*, 8458.
11. Rodgers, M. T.; Ervin, K. M.; Armentrout, P. B. *J. Chem. Phys.* **1997***, 106*, 4499.
12. DeTuri, V. F.; Ervin, K. M.; *J. Phys. Chem. A* **1998**, *103*, 6911.
13. Iceman, C.; Armentrout, P. B. *Int. J. Mass Spectrom.* **2003**, *222*, 329.
14. Su, T. *Chem. Phys.* **1994**, *90*, 4703.
15. Ervin, K. M. *Int. J. Mass. Spectrom.* **1999**, *85*, 343.
16. Koizumi, H.; Armentrout, P. B. *J. Chem. Phys.* **2003**, *119*, 12819.

17. Koizumi, H.; Muntean, F.; Armentrout, P. B. *J. Chem. Phys.* **2004**, *120*, 756.

18. Amicangelo, J. C.; Armentrout, P. B. *J. Phys. Chem. A* **2004**, *108*, 10698.

19. Armentrout, P. B. *J. Chem. Phys.* **2007***, 126*, 234302.

20. Do, K.; Klein, T. P.; Pommerening, C. A.; Sunderlin, L. S. *J. Am. Soc. Mass Spectrom.* **1997***, 8*, 688.

21. Hoops, A. A.; Gascooke, J. R.; Faulhaber, A. E.; Kautzman, K. E.; Neumark, D. M. *J. Chem. Phys.* **2004**, *120*, 7901.

22. Lynden-Bell, R. M.; Kosloff, R.; Ruhman, S.; Danovich, D.; Vala, J. *J. Chem. Phys.* **1998**, *109*, 9928.

Section 5.3. Combined Photoelectron, Collision-Induce Dissociation, and Computational Studies of Parent and Fragment Anions of N-paranitrophenylsulfonylalanine and N-paranitrophenylalanine

Jason Lambert,[†] Jing Chen,[§] Angela Buonaugurio,[§] Kit H. Bowen,[§,*] Chi-Linh Do-Thanh,[‡] Yilin Wang,[‡] Michael D. Best,[‡] R. N. Compton,[†,‡,*] and Thomas Sommerfeld[&]

[†]*Department of Physics and Astronomy, University of Tennessee, Knoxville, Tennessee 37996, USA*

[§]*Department of Chemistry, Johns Hopkins University, Baltimore, Maryland 21218, USA*

[‡]*Department of Chemistry, University of Tennessee, Knoxville, Tennessee 37996, USA*

[&]*Department of Chemistry and Physics, Southeastern Louisiana University, Hammond, Louisiana 70402, USA*

ABSTRACT

After synthesizing the compounds *N*-paranitrophenylsulfonylalanine (NPNPSA) and *N*-paranitrophenylalanine (NPNPA), the photoelectron spectrum of the valence anion of *N*-paranitrophenylsulfonylalanine $(NPNPSA)^-$, was measured and the collision-induced dissociation (CID) pathways of deprotonated *N*-paranitrophenylsulfonylalanine $(NPNPSA\text{-}H)^-$ and deprotonated *N*-paranitrophenylalanine $(NPNPA\text{-}H)^-$ were determined. Pertinent calculations were conducted to analyze both sets of experimental data. From the valence anion photoelectron spectrum of $(NPNPSA)^-$, the adiabatic electron affinity (AEA) of NPNPSA was determined to be 1.7 ± 0.1 eV, while the vertical

detachment energy (VDE) of $(NPNPSA)^-$ was found to be 2.3 ± 0.1 eV. Calculations for four low lying conformers of $(NPNPSA)^-$ gave AEA values in the range of 1.6–2.1 eV and VDE values in the range of 2.0–2.4 eV. These calculations are in very good agreement with the experimental values. While the NPNPA anion $(NPNPSA)^-$ was not observed experimentally it was studied computationally. The six low lying $(NPNPSA)^-$ conformers were identified and calculated to have AEA values in the range of 0.7–1.2 eV and VDE values in the range of 0.9–1.6 eV. CID was used to study the fragmentation patterns of deprotonated NPNPA and deprotonated NPNPSA. Based on the CID data and calculations, the excess charge was located on the delocalized π-orbitals of the nitrobenzene moiety. This is made evident by the fact that the dominant fragments all contained the nitrobenzene moiety even though the parent anions used for the CID study were formed via deprotonation of the carboxylic acid. The dipole-bound anions of both molecules are studied theoretically using the results of previous studies on nitrobenzene as a reference.[1]

*Corresponding authors: email: rcompton@utk.edu, kbowen@jhu.edu

INTRODUCTION

Synthesized amino acid derivatives have become especially important in many areas of molecular biology where they often act as protein markers.[2] While addition of these unnatural amino acids to proteins has become routine procedure in site-specific functionality,[3–5] the properties of such complex systems need to be characterized for them to be useful. One method is to examine the influence of well-characterized properties of the smaller moieties on the extended molecular complex. A recent theoretical study has explored this concept of a "molecule-in-molecule (MIM) approach.[6]"

Within the past two decades, new experimental and theoretical methods have been developed to examine the properties of complex molecules and their ions in the gas phase. The conformational flexibility and fragility of these extended molecules require gentle heating into the gas phase for meaningful studies of photoelectron spectroscopy (PES) of their intact parent anions and the determination of electron affinities. Likewise, electrospray ionization also allows the preparation of molecular anions, albeit the ions are often formed via deprotonation, for study by collision induced dissociation (CID). Under well-controlled conditions, this method can provide direct information on the fragmentation pathways and, under proper conditions, can provide estimates of the energy required to break molecular bonds of interest.

Herein, we employ both PES and CID techniques to study the negative ion properties of two newly synthesized amino acid derivatives. *N*-paranitrophenylsulfonylalanine (NPNPSA) and *N*-paranitrophenylalanine (NPNPA) were synthesized and both (*S*)- and (*R*)-enantiomers studied as a check of experimental reproducibility. These complex molecules contain nitrobenzene, sulfur dioxide, and

alanine, all of which have had their negative ion properties well characterized. We present a combination of experiment and theory to examine how the negative ion properties of the individual components can be correlated to better characterize the negative ion properties of these newly synthesized amino acids.

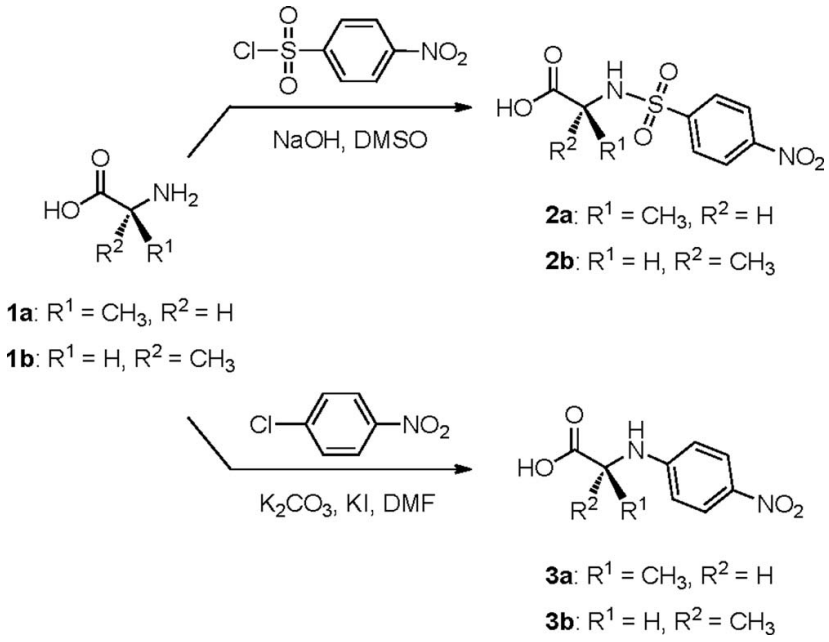

Figure 5.3.1. Preparation scheme of (*S*)-NPNPSA (**2a**), (*R*)-NPNPSA (**2b**), (*S*)-NPNPA (**3a**), and (*R*)-NPNPA (**3b**).

SAMPLE PREPARATION

Preparation of *(S-)*-NPNPSA (2a) and *(R)*-NPNPSA (2b)

The synthesis of *(S)*-NPNPSA (**2a**, see Figure 5.3.1) was performed by adding 1 M of sodium hydroxide solution (5 ml) to *(S)*-alanine (**1a**, 0.21 g, 2.40 mmol) and cooled to 0°C. Then 4-nitrobenzenesulfonyl chloride (0.82 g, 3.61 mmol) was added in small

portions to the reaction mixture and was stirred at room temperature overnight, followed by rinsing with ethyl acetate (20 ml). The aqueous layer was then acidified with 1M hydrochloric acid (10 ml) and extracted with ethyl acetate (15 ml). The resultant organic layer was dried with magnesium sulfate, filtered, and concentrated. Column chromatography over silica gel with gradient elution from 5%–20% methanol/dichloromethane gave the product **2a** as a yellow solid (0.29 g, 44%). Its enantiomer *(R)*-NPNPSA (**2b**) was similarly prepared using *(R)*-alanine (**1b**, 0.23 g, 2.58 mmol), 1 M sodium hydroxide (7 ml) and 4-nitrobenzenesulfonyl chloride (0.87 g, 3.86 mmol), which yielded **2b** as a white solid (0.24 g, 35%). The characterization using Nuclear Magnetic Resonance (NMR) [^{1}H NMR (300 MHz, DMSO (dimethyl sulfoxide)-d6) δ 8.37 (d, J = 7.1 Hz, 2H), 8.04 (d, J= 7.1 Hz, 2H), 3.68 (q, J = 7.1 Hz, 1H), 1.19 (d, J = 7.1 Hz, 3H)] match those reported in the literature.[7, 8]

Preparation of *(S)*-NPNPA (3a) and *(R)*-NPNPA (3b)

(S)-NPNPA (**3a**, see Figure 5.3.1) was synthesized by first adding 20 ml of *N,N*-dimethylformamide (DMF) to *(S)*-alanine (**1a**, 0.95 g, 10.7 mmol). Potassium carbonate (2.95 g, 21.3 mmol) and potassium iodide (1.77 g, 10.7 mmol) were then added to the stirring solution. 4-Chloronitrobenzene (3.36 g, 21.3 mmol) was added in small portions, and the reaction mixture was stirred and refluxed at 120°C overnight. The solvent was removed via rotary evaporation. The crude product was then dissolved in 50 ml of water, acidified with 1M hydrochloric acid (20 ml), and extracted with ethyl acetate (50 ml). The resultant organic layer was dried with magnesium sulfate, filtered, and concentrated. Column chromatography over silica gel with gradient elution from 1%–25%

methanol/dichloromethane gave the product as a yellow solid (1.21 g, 54%). Enantiomer **3b** was similarly prepared using *(R)*-alanine (**1b,** 0.88 g, 9.90 mmol), 20 ml of DMF, potassium carbonate (2.74 g, 19.8 mmol), tetrabutylammonium iodide (3.66 g, 9.90 mmol), and 4-chloronitrobenzene (3.12 g, 19.8 mmol), which yielded **3b** as a yellow solid (0.67 g, 32%). The characterization using NMR [^{1}H NMR (300 MHz, CD3OD) δ 8.02 (d, 2H, J =9Hz), 6.60 (d, 2H, J = 9 Hz), 3.96 (q, 1H, J = 9 Hz), 1.48 (d, 3H, J = 9 Hz)] match those reported in the literature.[9]

EXPERIMENTAL AND COMPUTATIONAL METHODS

Photoelectron Spectroscopy

Negative ion photoelectron spectroscopy (PES) was conducted by crossing a mass-selected beam of parent negative ions with a fixed-frequency photon beam and energy-analyzing the resultant photodetached electrons. The photodetachment process is governed by the relationship hν = EBE + EKE, where hν is the photon energy, electron binding energy (EBE) is the electron binding energy, i.e., the transition energy between the anion and a particular vibrational state of its neutral counterpart, and EKE is the electron kinetic energy.

The parent negative ions were formed in a supersonic expansion nozzle-ion source. Each synthesized enantiomer sample was placed in the stagnation chamber of the source, heated up to 100°C–130°C, and co-expanded with ~3–4 atm of argon gas through a 15 μm orifice into ~10^{-4} torr vacuum. Negative ions were then formed by injecting low energy electrons from a hot and even more negatively biased, thoriated iridium filament into the expanding jet where the microplasma was formed in the presence of a weak

external magnetic field. The anions were extracted and transported via a series of ion optics through the flight tube of a 90° magnetic sector mass spectrometer with a typical mass resolution (m/Δm) of ~400. The mass-selected anions of interest were then crossed with an intracavity operated argon ion laser beam, and the resultant photodetached electrons were energy-analyzed in a hemispherical electron energy analyzer with a resolution of ~30 meV. The photoelectron spectra reported herein were recorded with 2.540 eV photons and calibrated against the well-known photoelectron spectrum of the O^- anion.[10]

Collision Induced Dissociation

Because *(R)*- and *(S)*- are chiral designations and our experiment does not distinguish between enantiomers, the results of both enantiomers are expected be identical, therefore only CID of the *(S)*- enantiomer is presented. Deprotonated NPNPA and NPNPSA were produced using an electrospray ionization (TurboIonSpray ®) source. Solutions of *(S)*-NPNPSA and *(S)*-NPNPA were prepared at a concentration of 200 μg/ml in a 1:1 HPLC grade water and methanol mixture and then passed through a 0.005 in. inlet syringe tip with a flow rate of 5 to 20 μl/min. The temperature of the source was set to 100°C, and the ion spray bias voltage was optimized empirically for each CID spectrum to give the highest deprotonated parent signal intensity.

Collision induced dissociation was performed using an Applied Biosystems Q-Star Elite triple quadrupole mass spectrometer (MS) and is outlined in the paper by Smith et al.[11] Ions were formed by electrospray ionization and the mass selection and CID were performed in an initial quadrupole MS followed by introduction into the collision region.

The ions resulting from the collision region were then analyzed by a reflectron time-of-flight MS. The signals of all ions at each energy reported in the CID spectra were averaged for 30 sec. Argon was used as the collision gas for all reported experiments. The energy scale was determined using the collision induced dissociation process $I_3^- \rightarrow I_2 + I^-$ (see Ref. 11 for details). The lab frame energy step-size for deprotonated *(S)*-NPNPSA was 0.25 eV and 0.5 eV for deprotonated *(S)*-NPNPA. The energy calibration was further estimated by using a retardation analysis, which was in agreement with the $I_3^- \rightarrow I_2 + I^-$ analysis.[11]

It was found that the observed thresholds for the CID secondary ions shifted slightly to lower energy as the argon collision gas pressure increased. Although the energy shifts with pressure are small (~0.2 eV in the center of mass), we conclude that multiple ions collisions with the argon gas were adding internal energy into the large and flexible anions, which shows up as internal vibrational heating of the anion leading to a lower threshold. As a result we only present approximate ion dissociation energies. The dissociation energy was estimated by extrapolating the linear portion of the CID spectrum for each channel to zero intensity. Because the linear extrapolation will overestimate the dissociation energy and multiple collisions lower the estimated dissociation energy there is some cancellation of error but the extent of this cancellation is unknown.

Computational Methods

Computational investigations focused on characterizing both valence and dipole-bound states of the NPNPSA and NPNPA anions. These molecules are too large to use reliable ab initio methods typically required for accurately predicting electron affinities

so more approximate methods must be employed. This section reports all computational methods employed in detail, however, the full justification for selecting these methods is provided in the supplementary material.[33]

Three basis sets were employed, Dunning's correlation consistent double-ζ (aug-cc-pVDZ) and triple-ζ (aug-cc-pVTZ) sets,[12,13] and Ahlrichs's redefined triple-ζ set augmented with a minimal set of diffuse functions (ma-Def2-TZVP).[14, 15] For computing dipole-bound states an additional 6*s*6*p*5*d* set of diffuse functions was centered at the center-of-mass of the molecule (even-tempered exponents, smallest exponent 0.02 for all angular momenta, even-scaling factor $\sqrt{10}$). For consistency, all geometry optimizations of neutral and negatively charged conformers of nitrobenzene, NPNPSA, and NPNPA were carried out using the same method, the M06-2X hybrid functional[16] and the aug-cc-pVDZ basis set. The progression of ab initio methods, self-consistent field (SCF) calculations, second-order Moeller-Plesset perturbation theory (MP2), coupled-cluster calculations with single and double substitutions (CCSD), CCSD with a perturbative estimate of triple substitutions (CCSD(T)) was used for the nitrobenzene reference system, and its electron binding energies were also computed directly with the equation-of-motion couple-cluster method for electron affinities (EOM-CCSD) and the equation-of-motion MP2 method (EOM-MP2).[17,18] In the MP2 and the coupled-cluster calculations, all core electrons were frozen in their SCF orbitals. Moreover, for the open-shell valence state of the nitrobenzene anion, CCSD calculations were started from three sets of orbitals, unrestricted (UHF) and restricted (ROHF) SCF orbitals of the anion as well as from an anion like occupation of the SCF orbitals of the respective neutral (QRHF). Electron binding energies were also computed using the following density

functionals, the generalized-gradient approximation (GGA) functionals BLYP, BP86, PBE, and OLYP, the meta-GGA functional TPSS, and the hybrid functionals M06-2X, B3LYP, and O3LYP.[16, 19–24] Three program packages were employed: Gaussian09[25] for M06-2X calculations, Orca[26] for all other density functional and some of the MP2 calculations, and CFOUR[27] for MP2 and all coupled-cluster calculations.

Computing reliable electron affinities is in general a challenging task, and the present case is particularly difficult, because spin-contamination in the UHF wavefunction of the valence anion makes MP2 for these states effectively useless. Therefore, the only reasonable choice for predicting adiabatic attachment and vertical detachment energies in this context is to calibrate a density functional method with a reference system. Since the valence states of the NPNPSA and NPNPA anions are both well described by an excess electron occupying the nitrobenzene moiety of these larger species, a number of density functionals were tested using the well-characterized $^2B_1$ valence state of nitrobenzene as a basis of comparison. The details of these calculations are described in the supplementary material (see in particular Table 5.3.S1).[33] The main conclusion regarding electron binding energies of nitrobenzene-like anions is that the best option out of the eight functional tested is the GGA OLYP or the meta GGA TPSS with a triple-ζ basis sets such as the ma-Def2-TZVP set. We expect that with this type of approach the AEA of any NPNPSA or NPNPA conformer should be well reproduced within one or two tenths of an eV, while vertical detachment energy (VDEs) and Vertical Electron Affinities (VEA) are somewhat more sensitive and are expected to be overestimated by a few tenths of an eV.

Computing dipole-bound states is even more challenging because standard density functional methods at the present time cannot be used.[33] For the NPNPA conformers the usual sequence of Koopmans's Theorem (KT), ΔSCF, and ΔMP2 can be used, because for the dipole-bound states spin-contamination is negligible. Estimation of higher order correlation effects is based on comparison with the nitrobenzene reference system (see Table 5.3.S2 of the supplementary material).[33] For most conformers of NPNPSA, on the other hand, the valence states of the anion are already very low in energy, mix with the dipole-bound states, and none of the states resulting from vertical attachment can be characterized as purely dipole-bound or purely valence. Thus, for NPNPSA only a single conformer is discussed below.

RESULTS AND DISCUSSION

Photoelectron Spectra

Attempts were first directed to produce the dipole-bound anions of these systems. The dipole moments of NPNPSA and NPNPA were calculated to be 4.5 D and 7.6 D, respectively.[33] These values are well above both the theoretical critical value for a point dipole of 1.625 D and the empirical minimum value of 2.5 D necessary to support a stable dipole-bound state. Thus, it is believed that dipole-bound anions might be produced, however, slow free electron attachment to a polar molecule to form dipole-bound anions is unlikely. There is no mechanism for stabilization without a third body. Evidence of a dipole-bound anion is characterized in the photoelectron spectrum as a single, narrow peak close to zero EBE. The near zero EBE is indicative of the nearly identical geometries between the anion and neutral. However, as was also the case in the

photoelectron spectrum of nitrobenzene,[1] only the valence anions were observed. We postulate that, as in the case of nitrobenzene, the dipole-bound anions will act as a "doorway state" to the more stable valence anions.

The photoelectron spectra of the valence *(S)*- and *(R)*-NPNPSA anions are shown in Figure 5.3.2. As expected, both enantiomer anions exhibit very similar photoelectron spectral profiles. Each photoelectron spectrum has a maximum EBE value at 2.3 eV and a threshold EBE value at ~1.7 eV. Thus, the VDEs of both *(S)*- and *(R)*-NPNPSA anions are assigned at 2.3 ± 0.1 eV. Based on the location of the threshold and typical patterns of anion photoelectron spectral profiles, the AEA values are assigned as lying in the vicinity of 1.7 ± 0.1 eV, with vibrational hot bands accounting for the first 0.1–0.2 eV of the low EBE tail. Due to the Franck-Condon factors and large degrees of freedom for these anions, any vibrational structures in both spectra remain unresolved.

Surprisingly, after much searching, we were unable to produce parent anions of *(S)*- and *(R)*-NPNPA in the gas phase. A possible explanation is that the cross section for electron attachment to NPNPA is too small to be produced by slow electron attachment or that dissociation or autodetachment occurs more readily before our detection time scale (~10 μs). Gas phase electron attachment studies of this molecule using well-controlled electron beams could prove interesting.

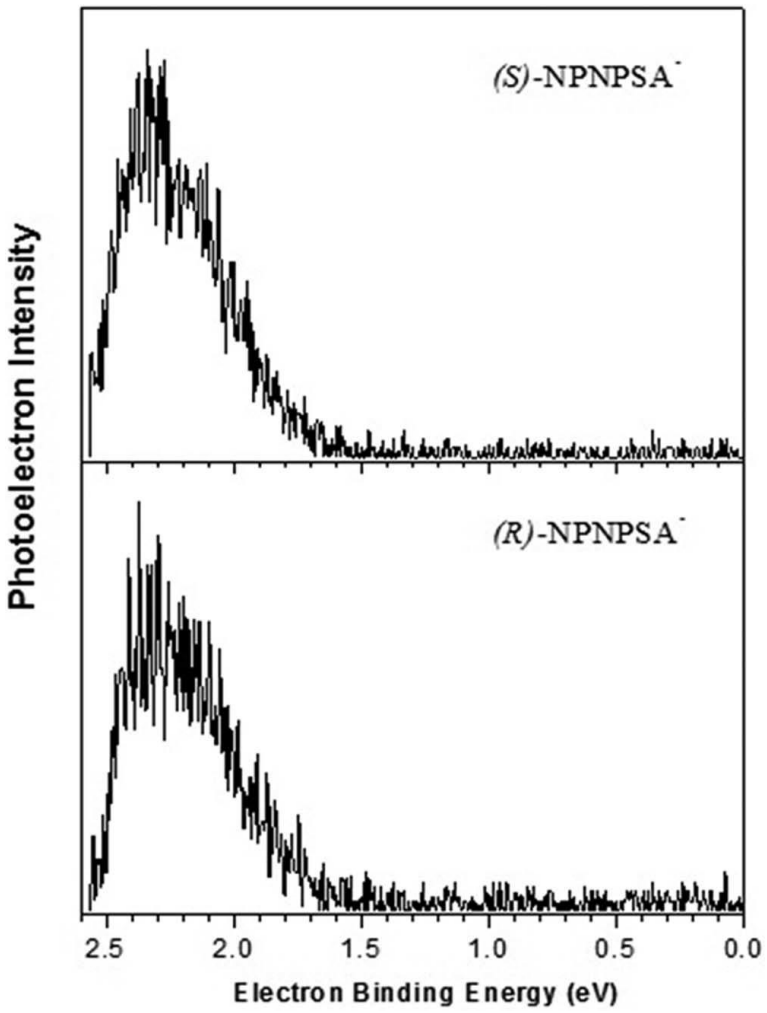

Figure 5.3.2. Photoelectron spectra of *(S)*- and *(R)*- NPNPSA valence anions recorded with 2.540 eV photons.

Collision Induced Dissociation

The secondary ion mass spectra of deprotonated *(S)*- NPNPSA [$(NPNPSA\text{-}H)^-$] and deprotonated *(S)*-NPNPA [$(NPNPA\text{-}H)^-$] following collision induced dissociation are shown in Figure 5.3.3. The measured CID spectra using argon as the collision gas as function of the center-of-mass collision energy are shown in the supplementary

material.[33] Figures 5.3.4 and 5.3.5 give the estimated cross-section for each channel of $(NPNPSA\text{-}H)^-$ and $(NPNPA\text{-}H)^-$. Extrapolations of the linear region of the cross-section to zero intensity provide the estimate of the dissociation energy.

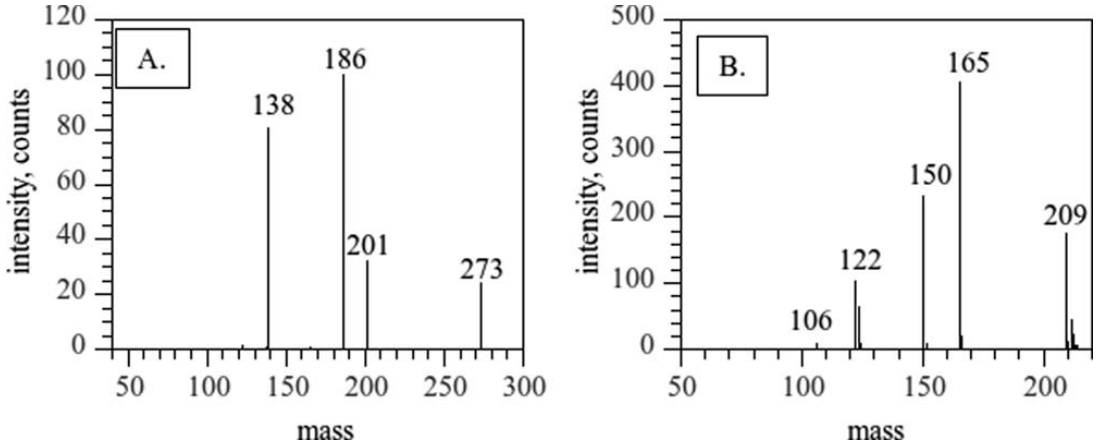

Figure 5.3.3. (a) The mass spectrum of *(S)*-$(NPNPSA–H)^-$ after CID and (b) the mass spectrum of *(S)*-$(NPNPA–H)^-$ after CID. The pathways corresponding to (a) and (b) are illustrated in Figures 5.3.4 and 5.3.5, respectively.

The primary fragments of $(NPNPSA\text{-}H)^-$ (273 amu) upon collisions with argon and the major pathways yielding these fragments are illustrated in Figure 5.3.6, and the predicted changes of the Gibbs free energy and the enthalpy are given in Table 5.3.S8 of the supplementary material.[33] The fragment *m*/*z* 201 anion is formed when the bond between the stereocenter of alanine and the amino nitrogen break. The *m*/*z* 186 anion is formed when the bond between the nitrogen and the sulfur breaks. We predict that the neutral 87 amu counterpart of the *m*/*z* 186 anion autodissociates into acetaldimine[28] and

CO_2 by breaking the bond between the alanine stereocenter and CO_2. This is supported by geometry optimization calculations using B3LYP/aug-cc-pVDZ of the 87 amu fragment. Figure 5.3.S3 of the supplementary material shows the final structure reached by optimization of this fragment, which is relevant to both deprotonated NPNPSA and deprotonated NPNPA.[33] The estimated dissociation energy for each channel of deprotonated NPNPSA is given in Table 5.3.1.

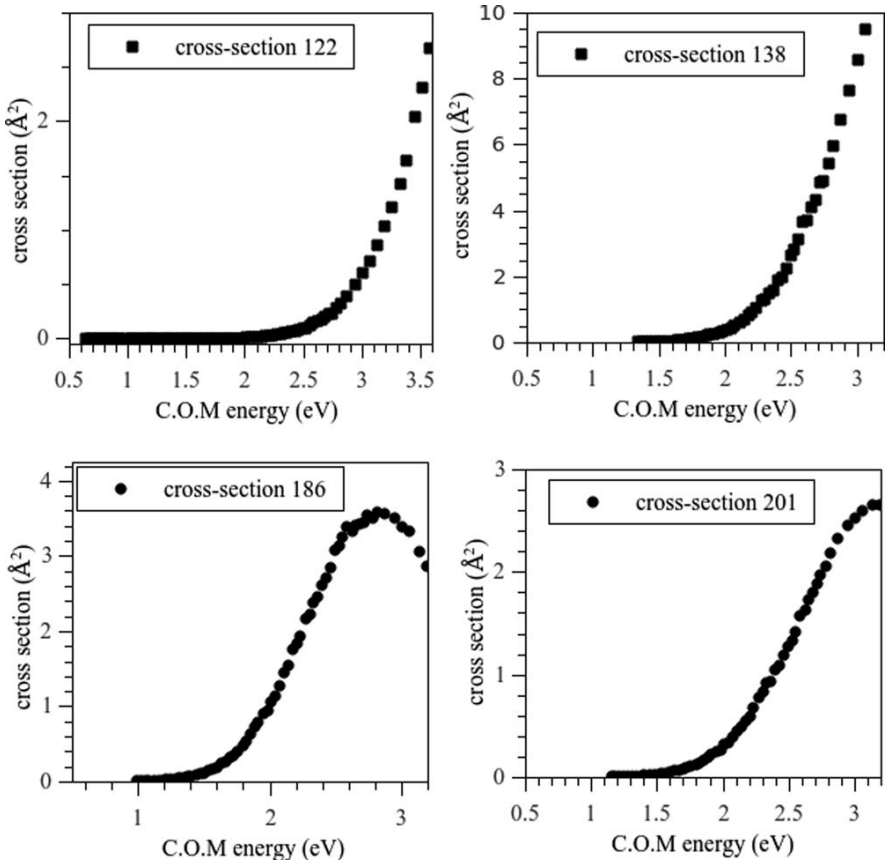

Figure 5.3.4. The estimated cross-section for each dissociation path of $(NPNPSA–H)^-$.

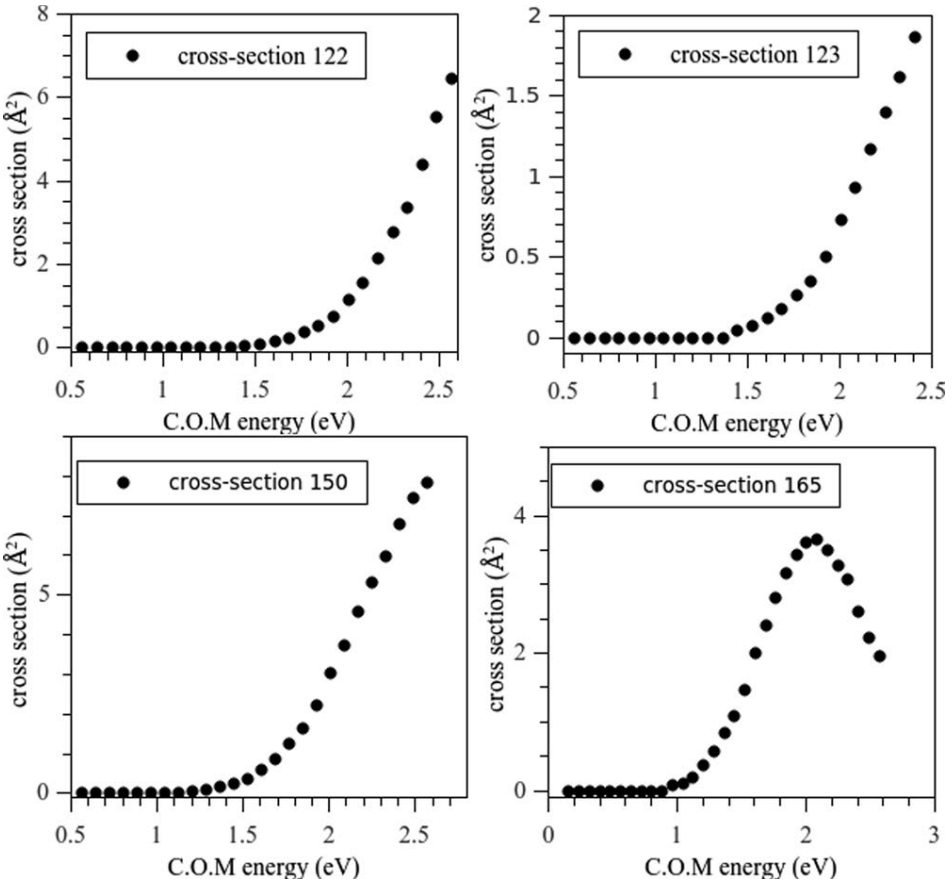

Figure 5.3.5. The estimated cross-section for each dissociation pathway $(NPNPA–H)^-$.

The pathway leading to the *m*/*z* 138 anion is attributed to the bonding of an oxygen atom to nitrobenzene in place of the sulfur at the para-position, forming a deprotonated nitrophenol. This requires a rearrangement reaction and is supported from geometry optimizations using B3LYP/aug-cc-pVDZ of the assumed *m*/*z* 138 anion and the neutral 135 amu counterpart of this dissociation pathway.[33] This rearrangement reaction involving the loss of SO_2 is not unprecedented. Wang et al.[29] observed a similar rearrangement reaction for a biologically derived sulfonamide β3 agonist, although they reported only the loss of SO_2. This differs in the experiments reported here because the oxygen atom is proposed to be scavenged from SO_2. Finally, the final pathway resulting

in the *m*/*z* 122 anion observed corresponds to the nitrobenzene anion minus a hydrogen atom.

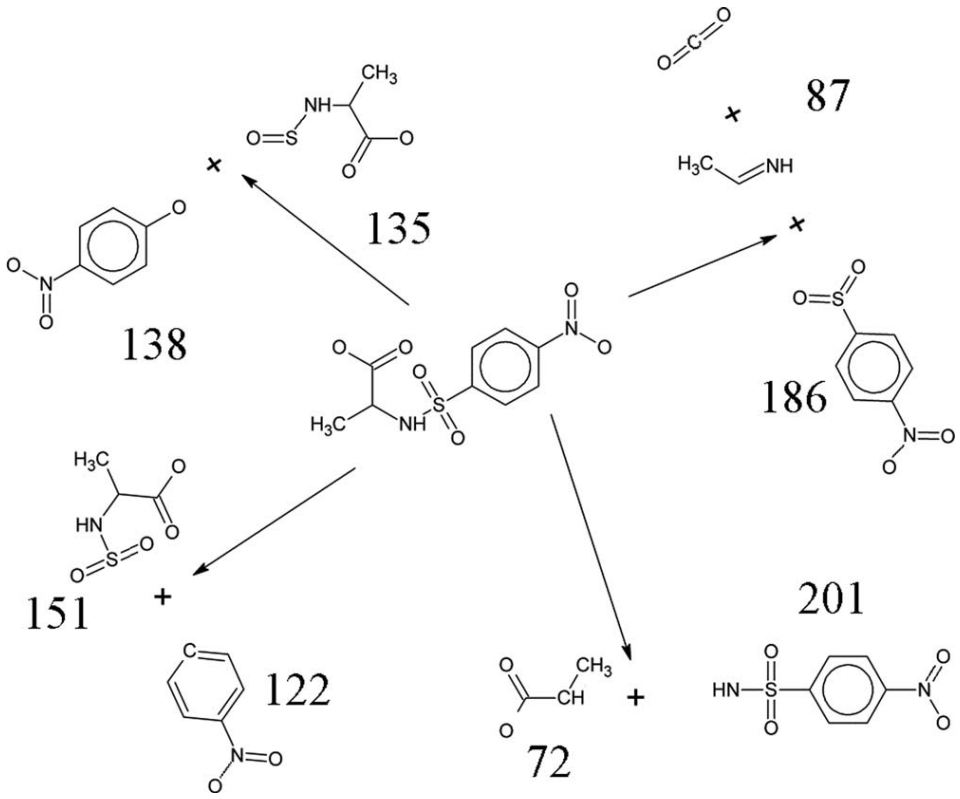

Figure 5.3.6. Collision induced dissociation pathways for $(NPNPSA–H)^-$.

Table 5.3.1. The estimated dissociation energies (DE) of deprotonated NPNPSA.

m/z	DE (eV)
201	2.01 ± 0.3
186	1.68 ± 0.3
138	2.42 ± 0.3
122	3.08 ± 0.3

The primary fragments of $(NPNPA\text{-}H)^-$ (209 amu) upon collisions with argon along with the major pathways yielding these fragments are illustrated in Figure 5.3.7. The predicted changes of the Gibbs free energy and the enthalpy are given in Table 5.3.S9 of the supplementary material.[33] The pathway producing the *m*/*z* 165 anion results from the loss of CO_2. We believe the *m*/*z* 150 anion results from the loss of both CO_2 and NH, then couple forming the neutral fragment counterpart. This requires a rearrangement reaction where the alanine stereocenter attaches to the para-position of the nitrobenzene, and produces an anion that satisfies the "even electron rule.[30,31]" The pathway producing the *m*/*z* 123 anion (nitrobenzene) and the last pathway producing the *m*/*z* 122 anion (deprotonated nitrobenzene) have similar thresholds, however the deprotonated nitrobenzene anion dominates. The remaining smaller fragments at 106 amu are attributed to the loss of oxygen from the deprotonated nitrobenzene. Likewise, the 92 amu anion is attributed to deprotonated phenol and the 46 amu anion is attributed to NO_2^-. Unfortunately, these mass fragments had extremely low abundance in the CID spectrum preventing an estimation of these dissociation energies. The estimated dissociation energy for each channel of deprotonated NPNPA is given in Table 5.3.S2.

The fragmentation pathways of $(NPNPSA\text{-}H)^-$ and $(NPNPA\text{-}H)^-$ revealed that all the anions were formed through deprotonation of the carboxylic acid, yet the charge was always found on the delocalized π orbitals of the nitrobenzene. An exception applies to the very weak case of the NO_2^- anion. The delocalized orbitals stabilized the negative ion by reducing the repulsive columbic interactions. This was evident from the observation that the nitrobenzene unit appeared in all the fragment anions produced in these experiments, along with the fact that the NO_2^- anion was only observed at very low

intensities in the NPNPA spectrum. Finally, because the lifetime of CO_2^- is 22–60 μs depending on its internal energy,[32] we cannot rule out the possibility that the metastable CO_2^- (*m*/*z* 44) is formed and then decays before the ion can be detected.

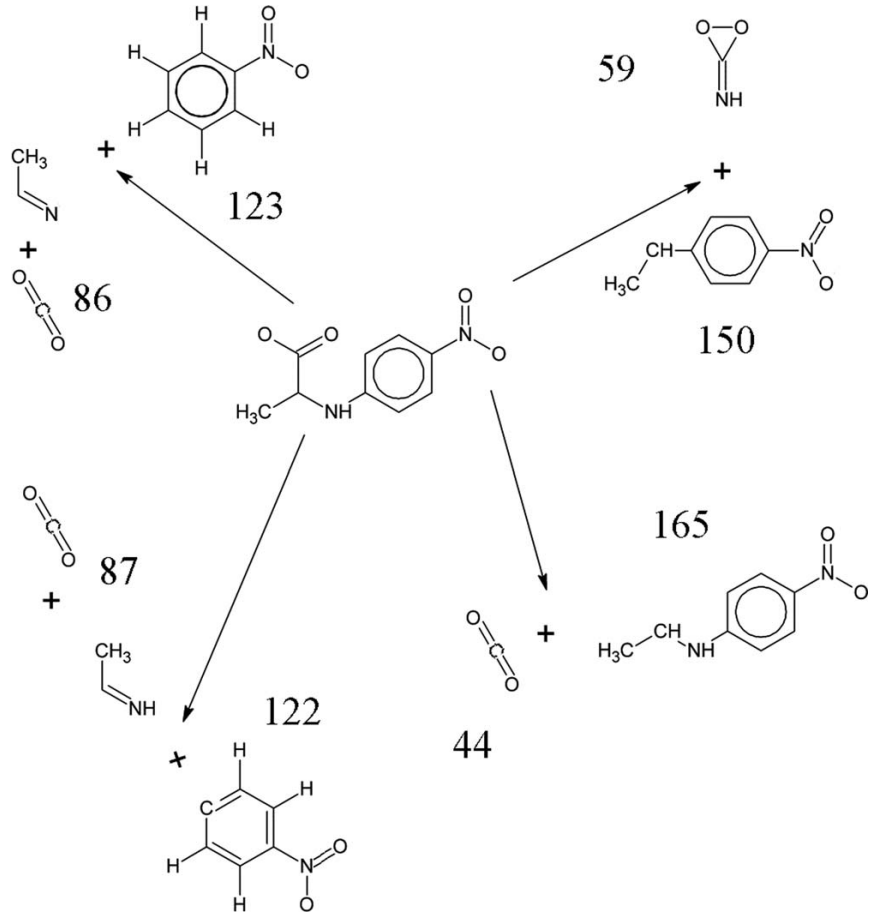

Figure 5.3.7.Collision induced dissociation pathways of $(NPNPA\text{-}H)^-$.

Table 5.3.2. The estimated dissociation energies (DE) of deprotonated NPNPA.

m/z	DE (eV)
165	1.2 ± 0.3
150	1.6 ± 0.3
123	1.7 ± 0.3
122	1.9 ± 0.3

Theoretical Calculations

This section investigates the negative ion properties of individual NPNPSA and NPNPA conformers. Both molecules have conformational flexibility regarding the single bonds of the alanine side-chain, and NPNPSA has additional flexibility regarding the N-S and the C-S bonds. Consequently, one may expect several conformers to be thermally accessible at room temperature, and many experimental observations will be averages of conformer populations. A manual conformer search for NPNPA yielded six distinct minimal energy structures shown in Figure 5.3.8 and four distinct minimal energy structures for NPNPSA shown in Figure 5.3.9. The relative energies computed for these conformers using the M06-2X density functional and the MP2 method with the aug-cc-pVDZ basis set are listed in Tables 5.3.S3 and 5.3.S4 of the supplementary material.[33] The MP2 method predicts somewhat smaller energy gaps between the conformers and since the relevant differences between the conformers are mostly intermolecular-like contacts, such as hydrogen bonds and hydrogen-π interactions, the MP2 results are probably more reliable. Nonetheless, the predicted energetic order is identical, and the same is true for the overall qualitative picture.

Both methods predict that for both neutral molecules the "stretched-out" conformers without any intermolecular-like contacts are most stable; however, there are two or three other conformers within about 20 kJ/mol. All of these conformers can attach electrons into dipole-bound or in valence states. However, in contrast to nitrobenzene, where these two types of states are cleanly separated by symmetry, the negative ion states for NPNPA and especially for NPNPSA are often of mixed character, similar to that found for para-nitroaniline.[11]

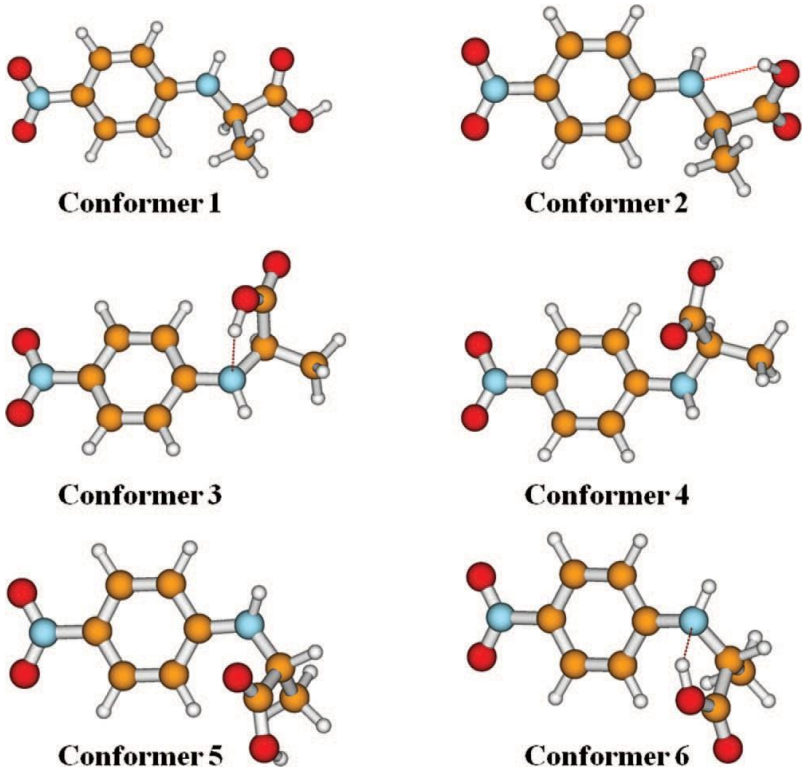

Figure 5.3.8. The six low energy conformers of neutral NPNPA.

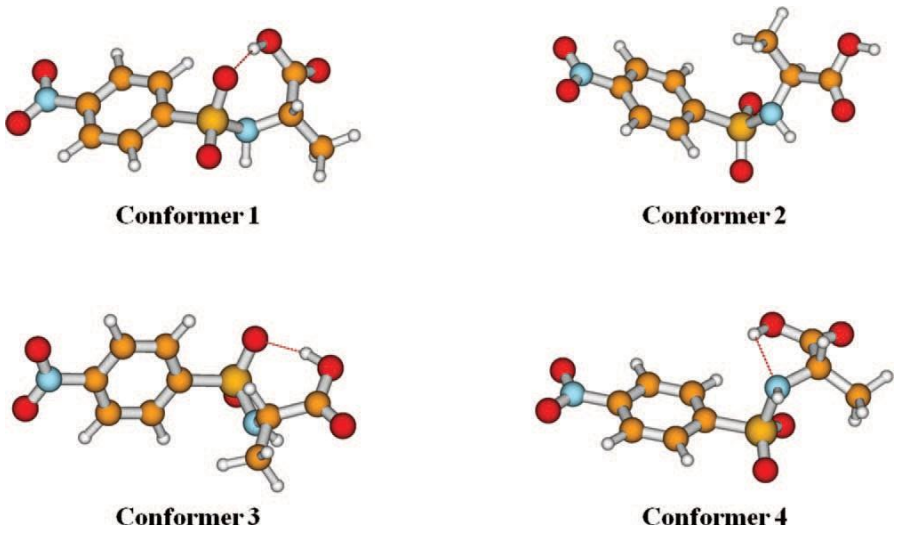

Figure 5.3.9. The four low energy conformers of neutral NPNPSA.

Dipole-bound states of NPNPSA and NPNPA are intrinsically fascinating, because of the interplay between the part of the molecule acting as a local dipole and other parts acting essentially as an excluded volume, which puts the MIM hypothesis to a test. Moreover, dipole-bound states have been shown to provide efficient "doorways" for attachment of low-energy (thermal) electrons into the valence orbitals, and represent therefore in many contexts an early intermediate in electron-induced reactions. Similar to other short-lived intermediates direct experimental observation can be challenging, and at least for the time being we can only report a theoretical characterization.

Regarding accurate characterization of dipole-bound states, most conformers of both the NPNPSA and NPNPA anions unfortunately require methods that we cannot apply due to the size of these molecules. Two major obstacles exist; first, the standard density functional methods cannot yet be applied to electronic states with diffuse densities and second for most NPNPSA conformers the dipole-bound state is very close in energy to the valence state. This not only makes unraveling these two states a formidable challenge but also adds the practical problem of achieving SCF convergence on the "right" state. Nevertheless, the relevant trends can be identified by making careful comparison to the reference system, nitrobenzene, as outlined in the supplementary material.[33]

All low-energy conformers of NPNPA show substantial dipole moments in excess of 6 D (conformer 2, which has an energy of 30 kJ/mol above the most stable neutral conformer, has a somewhat smaller dipole moment; see Table 5.3.S7 of the supplementary material).[33] Because the NPNPA conformers are far more polar than nitrobenzene and their VEAs are accordingly larger, higher order electron-correlation

corrections may be expected to be less important than for nitrobenzene. Therefore, the ΔMP2 values listed in the supplementary material[33] (40–140 meV; Table 5.3.S7) are probably reasonable predictions by themselves. Further corrections for both more complete basis sets and higher order correlation effects are expected to yield larger VEAs. Finally, nitrobenzene and other organic molecules can serve as guiding examples and these corrections may be expected to be somewhere in the 10%–20% range.

There are some interesting differences between the conformers in the sense that despite similar, fairly large dipole moments, the predicted VEAs of different conformers differ by as much as a factor of three. These differences can be explained by different interactions between local bond moments and excluded volume effects. The essential local dipole-moments stem from the NO_2 group and from the carbonyl group, whereas the phenyl ring acts as an excluded volume, that is, a region where the attractive potential due to the NO_2 group may be strong, but the repulsive potential due to Pauli repulsion with the valence electrons of the phenyl ring is even stronger. The relative orientation of these three groups is such that the excess electron can be closer to both local dipoles, which have the large electron binding energies and consequently a more compact distribution of the excess electron, in those conformers.

For NPNPSA it was only possible to identify the dipole-bound state of conformer 2.[33] At the equilibrium structures of all other conformers the mixing between valence and dipole-bound states is too strong, and a VEA associated with a "pure" dipole-bound state cannot be assigned. Conformer 2 of NPNPSA is predicted to have a dipole moment of 4.5 D, and its VEA is predicted to be 20 meV using the MP2 method, which is roughly twice the VEA predicted for nitrobenzene with the same method. Again, using nitrobenzene as

a guide, one may expect this conformer to have a dipole-bound state with a VEA of about 30 meV. Moreover, owing to the strong mixing of dipole-bound and valence states for most NPNPSA conformers, one may expect the doorway mechanism for this species to be efficient.

In addition to the dipole-bound states, all NPNPSA and NPNPA conformers are found to support bound valence states. Similar to the $^2B_1$ valence state of nitrobenzene the attached electron occupies a π^*-like orbital of the nitrobenzene moiety, and there is only a modest change in the bond lengths and bond angles of the nitrobenzene unit. What changes more dramatically are the torsion angles, in particular for those conformers with hydrogen bonds pointing in the direction of the phenyl ring and closely related with these structural changes there is a change in the energetic order upon electron attachment.

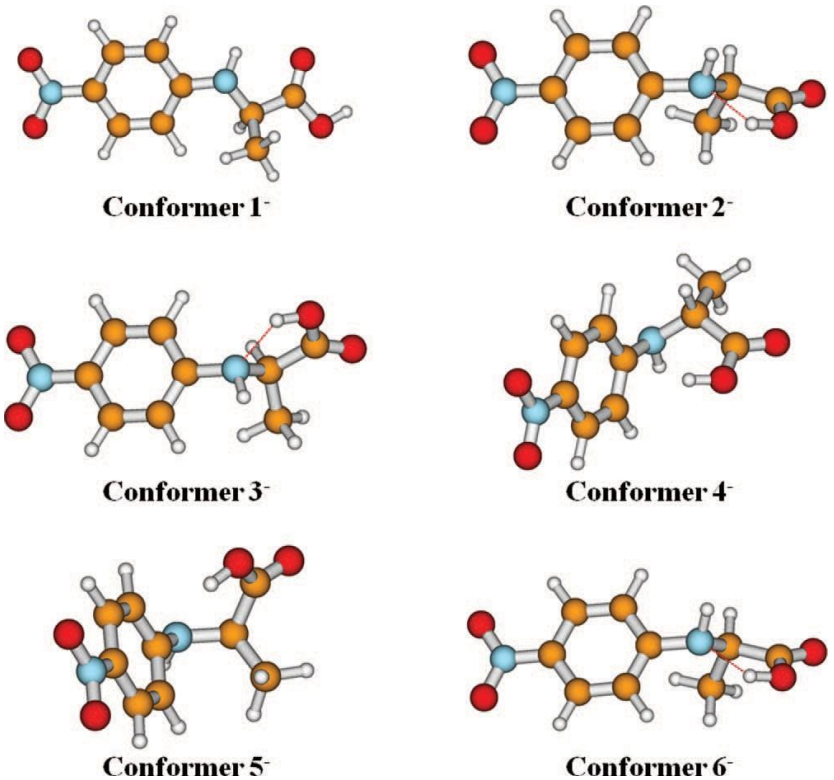

Figure 5.3.10. The six low energy conformers of the NPNPA valence anion.

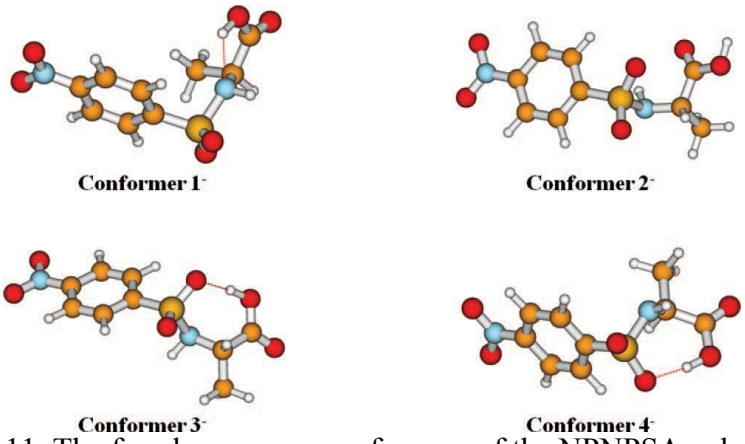

Figure 5.3.11. The four low energy conformers of the NPNPSA valence anion.

For the NPNPA anion the three conformers, shown in Figure 5.3.10, that have a the OH group of their alanine carboxyl group pointing towards the π-system of the phenyl ring are significantly more stable than all other conformers, showing that the excess negative charge localized on the ring is stabilized by the hydrogen bond. However, for the NPNPSA anion shown in Figure 5.3.11 we were unable to find this type of conformer, instead the most stable valence anion conformer type has a hydrogen bond to one of the sulfonyl oxygen atoms. Clearly the attached electron has a strong influence not only on the local bonding of the group that it is attached to but also on the more delicate intermolecular-like contacts and the preferred conformation of the larger molecule as a whole.

The computed VDEs and AEAs for the low-energy conformers of NPNPSA and NPNPA are collected in Tables 5.3.3 and 5.3.4. The reported AEAs are "local" in the sense that the energy difference listed is the one between *corresponding* conformers of

Table 5.3.3. The calculated adiabatic electron affinities (AEA) and vertical detachment energies (VDE) of the low-lying energy NPNPSA valence anion conformers, using OLYP/ma-Def2-TZVP energy differences at the M06- 2X/aug-cc-pVDZ minimal-energy geometries

Conformer (Anion)	AEA (eV)	VDE (eV)
1^-	2.02	2.32
2^-	1.66	2.06
3^-	2.06	2.42
4^-	2.01	2.40

Table 5.3.4. The calculated local adiabatic electron affinities (AEA) and vertical detachment energies (VDE) of the low-lying energy NPNPA anion conformers, using OLYP/ma-Def2-TZVP energy differences at theM06-2X/aug-cc- pVDZ minimal-energy geometries.

Conformer (Anion)	AEA (eV)	VDE (eV)
1^-	0.69	0.97
2^-	1.24	1.52
3^-	1.06	1.41
4^-	1.06	1.40
5^-	1.07	1.64
6^-	1.12	1.52

neutral and anion. It is termed “local,” because it can occur with small adjustments of geometry. The local AEA is expected to be relevant for interpreting the photoelectron spectra, because only detachment resulting in small changes of geometry can have favorable Franck-Condon factors. The true AEA is of course the energy difference between the most stable conformer of the neutral and the most stable conformer of the

respective anion, but for both NPNPSA and NPNPA the true AEA is expected to have virtually zero intensity in a PES. For NPNPSA the true AEA is predicted to be 1.87 eV, yet under the assumption that the experimental anion population consists essentially of the two most stable conformers (conformers 3^- and 4^-), and taking into account a zero-point correction on the order of 0.1 eV, the calculations predict a local AEA on the order of 1.9 eV and a VDE of 2.3 eV.

For NPNPA the situation is less clear cut. The local AEAs of the anion conformers are listed in Table 5.3.4. Three or four conformers (conformers 2^-, 3^-, 4^-, and 6^-,) could have significant abundance in an experimental anion population. These four conformers have significantly different AEAs and VDEs; therefore, substantial inhomogeneous broadening may be expected for the photoelectron spectrum of NPNPA, if one were obtained. The predicted range for the local AEA is 0.9–1.1 eV and for the VDE is 1.3–1.4 eV with the true AEA calculated to be 1.08 eV (energy difference between neutral conformer 1 and anion conformer 3^-).

CONCLUSION

The gas phase negative ion properties of two extended molecular structures-NPNPSA and NPNPA were examined both experimentally and theoretically. Conformers 1 and 3 of NPNPA and conformer 2 of NPNPSA are predicted to support a dipole bound state (see Figure 5.3.12). These were not observed experimentally because the ion source was not appropriate for creating dipole bound anions.[33] The calculated adiabatic electron

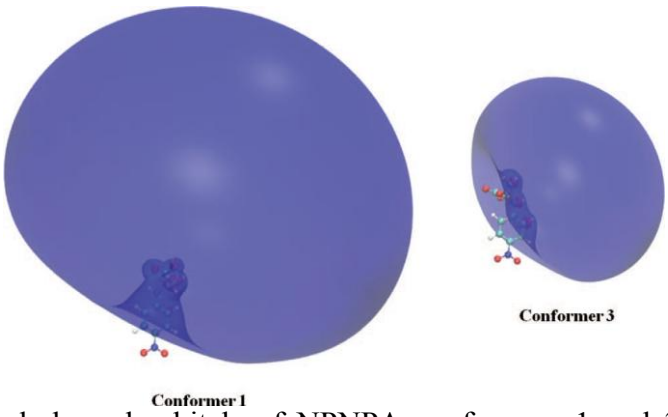

Figure 5.3.12. Dipole-bound orbitals of NPNPA conformers 1 and 3. The isosurfaces shown enclose 75% of the electron density that corresponds to isocontour values of 0.0010 and 0.0022, respectively. The associated electron binding energies are listed in Table 5.3.S7 of the supplementary material.[33]

affinity was in good agreement with the experimentally measured AEA of 1.7 ± 0.1 eV for NPNPSA. This value is almost twice that for nitrobenzene (1.00 eV[1]) showing the effect of the extended system. Also, the vertical detachment energy of the NPNPSA negative ion was measured to be approximately 2.3 ± 0.1 eV, which compares quite well with the calculated VDE of 2.3 eV. The experimental and theoretical agreement for *(S)*- and *(R)*-NPNPSA as well as that of nitrobenzene provide confidence for at least the predicted AEA and VDE of the NPNPA conformers.

Every observed fragmentation pathway of $(NPNSA\text{-}H)^-$ and $(NPNPA\text{-}H)^-$ anions, excluding the very weak channels of the NO_2 anion and a deprotonated nitrosobenzene at the para-position, contained the nitrobenzene moiety even though the anions were created via a deprotonation of a carboxylic acid. This was due to the stabilizing effect due to delocalization of the excess electron on the π orbitals of the nitrobenzene molecule. Estimates of the energy thresholds for dissociation into the

various ion channels are presented but multiple collisions are present and that limits the accuracy of the estimations. The thresholds are lowered by collision induced vibrational excitation (heating) of the $(NPNPSA\text{-}H)^-$ and $(NPNPA\text{-}H)^-$ anions.

ACKNOWLEDGEMENTS

Parts of this research are based on work supported by the National Science Foundation under Grant Nos. CHE-1111693 (K.H.B.), CHE-0848487 (R.N.C.), and CHE-0954297 (M.D.B.). Acknowledgment is made to the Donors of the American Chemical Society Petroleum Research Fund for partial support of this research.

REFERENCES

1. Desfrancois, C.; Periquet, V.; Lyapustina, S. V.; Lippa, T. P.; Robinson, D. W.; Bowen, K. H.; Nonaka, H.; Compton, R. N. *J. Chem. Phys*. **1999**, *111*, 4569.
2. Noren, C. J.; Anthony-Cahill, S. J.; Griffith, M. C.; Schultz, P. G. *Science* **1989**, *244*, 182.
3. Johnson, D. B. F.; Xu, J.; Shen, Z.; Takimoto, J. K.; Schultz, M. D.; Schmitz, R. J.; Xiang, Z.; Ecker, J. R.; Briggs, S. P.; Wang, L. *Nat. Chem. Biol*. **2011**, *7*, 779.
4. Xie, J.; Schultz, P. G. *Nat. Rev. Mol. Cell Biol*. **2006**, *7*, 775.
5. Dougherty, D. A. *Curr. Opin. Chem. Biol*. **2000**, *4*, 645.
6. Wen, S.; Nanda, K.; Huang, Y.; Beran, G. J. O. *Phys. Chem. Chem. Phys*. **2012**, *14*, 7578.
7. Di Gioia, M. L.; Leggio, A.; Le Pera, A.; Liguori, A.; Siciliano, C. *J. Org. Chem*. **2005**, *70*, 10494.
8. Kowalik-Jankowska, T.; Kozlowski, H.; Pawelczak, K.; Makowski, M. *J. Chem. Soc. Dalton Trans.* **1995**, *17*, 2729.
9. Meo, P. L.; D'Anna, F.; Gruttadauria, M.; Riela, S.; Noto, R. *Tetrahedron* **2004**, *60*, 9099.
10. Neumark, D. M.; Lykke, K. R.; Andersen, T.; Lineberger, W. C. *Phys. Rev. A* **1985**, *32*, 1890.
11. Smith, B. H.; Buonaugurio, A.; Chen, J.; Collins, E.; Bowen, K. H.; Compton, R. N.; Sommerfield, T. *J. Chem. Phys*. **2013**, *138*, 234304.
12. Dunning, T. H. *J. Chem. Phys*. **1989**, *90*, 1007.
13. Kendall, R. A.; Dunning, T. H.; Harrison, R. J. *J. Chem. Phys*. **1992**, *96*, 6796.

14. Weigend, F.; Ahlrichs, R. *Phys. Chem. Chem. Phys*. **2005**, *7*, 3297.

15. Papajak, E.; Truhlar, D. G. *J. Chem. Theory Comput*. **2010**, *6*, 597.

16. Zhao, Y.; Truhlar, D. G. *J. Phys. Chem. A* **2006**, *110*, 5121.

17. Nooijen, M.; Bartlett, R. J. *J. Chem. Phys*. **1995**, *102*, 3629.

18. Stanton, J. F.; Gauss, J. *J. Chem. Phys*. **1995**, *103*, 1064.

19. Perdew, J. P.; Burke, K.; Ernzerhof, M. *Phys. Rev. Lett*. **1996**, *77*, 3865.

20. Becke, A. D. *Phys. Rev. A* **1988**, *38*, 3098.

21. Lee, C.; Yang, W.; Parr, R. G. *Phys. Rev. B* **1988**, *37*, 785.

22. Becke, A. D. *J. Chem. Phys*. **1993**, *98*, 5648.

23. Cohen, A. J.; Handy, N. C. *Mol. Phys.* **2001**, *99*, 607.

24. Tao, J.; Perdew, J. P.; Staroverov, V. N.; Scuseria, G. E. *Phys. Rev. Lett*. **2003**, *91*, 146401.

25. Gaussian 09, Revision D.01, Frisch, M. J.; Trucks, G. W.; Schlegel, H. B.; Scuseria, G. E.; Robb, M. A.; Cheeseman, J. R.; Scalmani, G.; Barone, V.; Mennucci, B.; Petersson, G. A.; Nakatsuji, H.; Caricato, M.; Li, X.; Hratchian, H. P.; Izmaylov, A. F.; Bloino, J.; Zheng, G.; Sonnenberg, J. L.; Hada, M.; Ehara, M.; Toyota, K.; Fukuda, R.; Hasegawa, J.; Ishida, M.; Nakajima, T.; Honda, Y.; Kitao, O.; Nakai, H.; Vreven, T.; Montgomery, J. A., Jr.; Peralta, J. E.; Ogliaro, F.; Bearpark, M.; Heyd, J. J.; Brothers, E.; Kudin, K. N.; Staroverov, V. N.; Kobayashi, R.; Normand, J.; Raghavachari, K.; Rendell, A.; Burant, J. C.; Iyengar, S. S.; Tomasi, J.; Cossi, M.; Rega, N.; Millam, N. J.; Klene, M.; Knox, J. E.; Cross, J. B.; Bakken, V.; Adamo, C.; Jaramillo, J.; Gomperts, R.; Stratmann, R. E.; Yazyev, O.; Austin, A. J.; Cammi, R.; Pomelli, C.; Ochterski, J. W.;

Martin, R. L.; Morokuma, K.; Zakrzewski, V. G.; Voth, G. A.; Salvador, P.; Dannenberg, J. J.; Dapprich, S.; Daniels, A. D.; Farkas, Ö.; Foresman, J. B.; Ortiz, J. V.; Cioslowski, J.; Fox, D. J. Gaussian, Inc., Wallingford CT, 2009.

26. ORCA, version 2.8.0, Neese, F.; with contributions from Becker, U.; Ganiouchine, D.; Koßmann, S.; Petrenko, T.; Riplinger, C.; Wennmohs, F. see http://www.thch.uni-bonn.de/tc/orca/.
27. CFOUR, version 1, Stanton, J. F.; Gauss, J.; Harding, M. E.; Szalay, P. G. with contributions from Auer, A. A.; Bartlett, R. G.; Benedikt, U.; Berger, C.; Bernholdt, D. E.; Bomble, Y. J.; Cheng, L.; Christiansen, O.; Heckert, M.; Heun, O.; Huber, C.; Jagau, T.-C.; Jonsson, D.; Jusélius, J.; Klein, K.; Lauderdale, W. J.; Matthews, D. A.; Metzroth, T.; Mück, L .A.; O'Neill, D. P.; Price, D. R.; Prochnow, E.; Puzzarini, C.; Ruud, K.; Schiffmann, F.; Schwalbach, W.; Stopkowicz, S.; Tajti, A.; Vázquez, J.; Wang, F.; Watts, J. D. and the integral packages MOLECULE (J. Almlöf and P. R. Taylor), PROPS (P. R. Taylor), ABACUS (T. Helgaker, H. J. Aa. Jensen, P. Jørgensen, and J. Olsen), and ECP routines by A. V. Mitin and C. van Wüllen. For the current version, see http://www.cfour.de.
28. Afeefy, H. Y.; Liebman, J. F.; Stein, S. E. IR and Mass Spectra. In *NIST Chemistry WebBook*; Mallard, W.G.; Linstrom, P.J., Eds. NIST Standard Reference Database Number 69; National Institute of Standards and Technology: Gaithersburg, MD, 2000, Acetaldimine (http://webbook.nist.gov).
29. Wang, Z.; Hop, C. E. C. A.; Kim, M.-S.; Huskey, S.-E. W.; Baillie, T. A.; Guan, Z. *Rapid Commun. Mass Spectrom*. **2003**, *17*, 81.

30. Karni, M.; Mandelbaum, A. *Org. Mass Spectrom*. **1980**, *15*, 53.

31. Levsen, K.; Schiebel, H.-M.; Terlouw, J. K.; Jobst, K. J.; Elend, M.; Preiss, A.; Thiele, H.; Ingendoh, A. *J. Mass Spectrom*. **2007**, *42*, 1024.

32. Cooper, C. D.; Compton, R. N. *Chem. Phys. Lett*. **1972**, *14*, 29.

33. See supplementary material at http://dx.doi.org/10.1063/1.4834675 for additional CID results, additional calculations, and discussion on the dipole-bound anions of nitrobenzene, NPNPSA, and NPNPA.

SUPPLEMENTAL MATERIAL

Methods for computing the AEA, VDE, and VEA associated with the $^2B_1$ valence state of the nitrobenzene anion

Nitrobenzene is a useful reference system for NPNPSA and NPNPA, because both of the larger molecules form analogous valence anion states where the excess electron is essentially localized on the nitrobenzene moiety. Moreover, the experimental AEA of nitrobenzene of 1.00 eV,[1] is well known. However, the experimental result includes zero-point effects and for validation purposes, the AEA value without corrections is more useful. To obtain a zero-point-effect-free "experimental" value, the zero-point correction of the AEA of nitrobenzene was computed using three density functionals, M06-2X, B3LYP, and TPSS, with the aug-cc-pVDZ basis set. The three functionals agreed with each other reasonably well and yielded corrections of 84, 71, and 73 meV, respectively. Therefore, the experimental value for the purely electronic AEA of nitrobenzene should be close to 0.92 eV, and this is the value we will subsequently compare with.

The first set of methods considered is the usual sequence of ab initio methods, SCF, MP2 and coupled-cluster based methods. Unfortunately, the UHF wavefunction for the anion shows a large spin-contamination, so that neither ΔSCF nor ΔMP2 are expected to yield useful results, which is indeed the case (see Table 5.3.S1). Coupled cluster calculations are known to be able to recover from spin contamination in the reference wavefunction, and UHF-based CCSD(T) calculations do yield results much more reasonable than UHF or UHF-based MP2. Yet, CCSD(T) calculations started from a ROHF reference, or from a reference constructed using the orbitals of the neutral (QRHF)

yield virtually identical results, which are quite a bit higher than the UHF based coupled-cluster results (~70 meV) suggesting that in this case recovery from spin-contamination is not complete. Another test is *direct* computation of the electron affinity with the EOM-CCSD method, which gives results in close agreement with ROHF-based ΔCCSD(T). Regarding basis sets effects, the coupled cluster values follow the usual trend that the experimental value is approached from below reflecting that there is more electron correlation in the anion than there is in the neutral. With the aug-cc-pVDZ basis set the result is about 0.1 eV too low, with the aug-cc-pVTZ set this difference is down to less than 50 meV, and thus the CCSD(T) calculations clearly approach the "experimental" value of 0.92 eV is a systematic manner. Based on this finding, the ROHF-based CCSD(T) and EOM-CCSD values for the VDE and VEA are also expected to represent good guidelines for the validation of density functional methods.

Eight different density functionals were used to compute the VEA, VDE, and AEA of nitrobenzene, the M06-2X, B3LYP, and O3LYP hybrid functionals, the less expensive meta-GGA functional TPSS, and the GGA functionals BLYP, BP86, PBE, and OLYP. All functionals systematically over-bind the electron with the most recently developed functional used, M06-2X, doing in fact the worst job at predicting the respective detachment and attachment energies. All density functional methods show the trend that the experimental value is approached from above as the basis set is expanded, and even with the aug-cc-pVTZ set, most functionals over-bind by more than 0.1 eV. The exception is the OLYP GGA, which yields AEAs in perfect agreement with the experimental AEA if the aug-cc-pVTZ basis set is used. The situation is worse for the VDE and even more so for the VAE. The formerly more reliable hybrid functionals tend

to over-bind by 0.3 eV or more, while the GGAs do not show a clear trend. In particular OLYP, and to some extend the BLYP and TPSS functionals, perform significantly better than the hybrid functionals, a trend that has been noticed before but even those two functionals significantly overestimate the VAE of the $^2B_1$ state.

Since density functional results tend to be less dependent on diffuse functions than ab initio methods and this is in particular true for GGAs, a triple-z set augmented with a diffuse sp-set on the heavy atoms and a single diffuse s function on H was considered.[44] Indeed using Ahlrich's Def2-TZVP (ma-Def2-TZVP) set with this minimal augmentation yields results in very close agreement with the aug-cc-pVTZ results for both the OLYP and TPSS functionals.

In conclusion, CCSD(T) or EOM-CCSD are as expected needed to compute reliable electron binding energies, yet, for systems larger than nitrobenzene these methods are not practicable even with the "minimal" aug-cc-pVDZ set. In the nitrobenzene case ΔMP2 is not an alternative, because of the large spin-contamination in the unrestricted SCF calculation for the anion, and the only alternative are density functional based methods. Regarding the geometry optimizations, hybrid functionals such as B3LYP, or better M06-2X, are anyway expected to be the best tradeoff between reliability and computational cost. However, our results show that these functionals are not the best choice for computing electron attachment energies, but that the OLYP GGA functional, and to some extend the TPSS and BLYP functional yields results in better agreement with CCSD(T) and experiment. Based on our results one may expect that for systems similar to nitrobenzene AEAs of will be well reproduced if triple-ζ basis sets are

employed, while VDEs and VEAs are expected to be overestimated by a few tenth on an eV.

Table 5.3.S1. Ab initio and DFT calculations for the EBEs (in eV) of the $^2B_1$ valence state of nitrobenzene.

	aug-pVDZ	aug-pVTZ				
	VAE	**VDE**	**AEA**	**VAE**	**VDE**	**AEA**
SCF	0.31	1.33				
MP2	-0.81	-0.25				
UHF-CCSD	0.33	1.08			1.21	
UHF-CCSD(T)	0.26	0.92	0.77		1.05	0.81
ROHF-CCSD(T)	0.31	0.98	0.83	0.45	1.12	0.88
ORHF-CCSD(T)	0.31	0.98	0.83			
EOM-CCSD	0.25	0.95	0.79	0.42	1.12	0.88
M06-2x	0.70	1.44	1.08	0.78	1.53	1.12
B3LYP	0.69	1.33	1.12	0.71	1.35	1.08
O3LYP	0.73	1.34	1.05	0.75	1.36	1.03
BLYP	0.65	1.20	1.15	0.63	1.19	1.08
BP86	0.84	1.40	1.30	0.83	1.39	1.23
PBE	0.76	1.31	1.19	0.75	1.30	1.13
OLYP	0.57	1.13	0.97	0.57	1.12	0.92
TPSS	0.66	1.23	1.12	0.65	1.23	1.06

Methods for computing the VEA associated with the Dipole Bound state of the nitrobenzene anion

Computing attachment energies associated with dipole-bound states is far more challenging than those with valence states. First, large sets of additional diffuse functions are needed, and saturating the basis set in this respect is critically important. Second,

DFT methods cannot be used in the same straightforward way as for valence bound states. On the one hand, dipole-bound states are very diffuse, and therefore the long-range part of the functional must be free of electron self-interaction, so that the asymptotic electron-molecule interaction is correct. This is a principle problem, and uncorrected functionals such as B3LYP will give infinite binding energies in the complete basis set limit. On the other hand, there is the practical problem of choosing a suitable integration grid for Gaussian functions with very small exponents. In fact, in many programs it becomes practically impossible to reach convergence for the Kohn-Sham iterations, if three or four sets of progressively more diffuse functions are added to the basis set. Last, the attachment energies of dipole-bound states are very sensitive to long-range electron correlations effects, and reliable results often require CCSD(T) calculations with large valence basis sets. Nitrobenzene is to some extent a typical case. On an absolute scale the VEA of the dipole-bound state nitrobenzene is small, in the order of 15 meV, and Koopmans's Theorem as well as ΔSCF and ΔMP2 seem to be fairly close, but in relative terms the deviations are of cause significant. The often reliable, and more importantly robust direct methods EOM-MP2 and EOM-CCSD, overestimate the VEA making nitrobenzene a particular challenging case. For larger systems, such as NPNPSA or NPNPA, computing VEAs with CCSD(T) and triple-ζ quality basis sets is clearly out of question, and ΔMP2 seems to be the most promising tradeoff for larger system. Unfortunately, this tradeoff is partly spoiled by the presence of nearby valence states, which are easily separated by symmetry for nitrobenzene, but which cannot be separated for most conformers of NPNPSA or NPNPA.

Table 5.3.S2. Calculations for the VEAs (in meV) of the dipole-bound state of nitrobenzene.

	aug-cc-pVDZ+6s6p5d	aug-cc-pVTZ+6s6p5d
KT	6.4	6.3
DSCF	7.1	
DMP2	8.9	
DCCSD	16.6	
DCCSD(T)	15.6	
EOM-MP2	29.9	
EOM-CCSD	23.5	24.6

Table 5.3.S3. Relative energies of conformers of neutral NPNPA. Minimal energy structures have been computed using M06-2X/aug-cc-pVDZ; the MP2/aug-cc-pVDZ energies have been evaluated at these geometries. All Cartesian coordinates are found in the supplementary data.

Conformer (Neutral)	M06-2X Energy (kJ/mol)	MP2 Energy (kJ/mol)
1	0	0
2	36.9	30.6
3	10.9	2.7
4	28.5	22
5	41.3	36.6
6	16.8	9

Table 5.3.S4. Relative energies of conformers of neutral NPNPSA. Minimal energy structures have been computed using M06-2X/aug-cc-pVDZ; the MP2/aug-cc-pVDZ energies have been evaluated at these geometries. All Cartesian coordinates are found in the supplementary data.

Conformer (Neutral)	M06-2X Energy (kJ/mol)	MP2 Energy (kJ/mol)
1	21.6	19.8
2	0.0	0.0
3	13.1	13.2
4	9.3	9.1

Table 5.3.S5. Relative energies of conformers of the NPNPA valence anion. The aug-cc-pVDZ basis set has been used. All Cartesian coordinates are found in the supplementary data.

Conformer (Anion)	M06-2X Energy (kJ/mol)
$\mathbf{1}^-$	28.1
$\mathbf{2}^-$	6.3
$\mathbf{3}^-$	0
$\mathbf{4}^-$	13.3
$\mathbf{5}^-$	32.7
$\mathbf{6}^-$	6.6

Table 5.3.S6. Relative energies of conformers of the NPNPSA valence anion. The aug-cc-pVDZ basis set has been used. All Cartesian coordinates are found in the supplementary data.

Conformer (Anion)	M06-2X Energy (kJ/mol)
$\mathbf{1}^-$	21.6
$\mathbf{2}^-$	29.5
$\mathbf{3}^-$	4.5
$\mathbf{4}^-$	0.0

Table 5.3.S7. Dipole moment of NPNPA conformers and VEA associated with NPNPA dipole-bound states. The dipole moments have been computed using the M06-2X functional, and the VEA of the dipole-bound states has been computed at the M06-2X geometries, using KT, ΔSCF, and ΔMP2 with the aug-cc-pVDZ set further augmented with a 6s6p5s set centered at the center of mass of the molecule.

Conformer	dipole moment (Debye)	VEA KT (meV)	VEA ΔSCF (meV)	VEA ΔMP2 (meV)
1	7.6	20	22.6	36.5
2	2.9	2	2.4	11.2
3	7	54.2	67.3	106.6
4	8.5	58.6	70.4	111.5
5	8.5	58.7	68.6	103.1
6	6.9	65	84.4	141.3

Table 5.3.S8. Calculated changes in Gibbs Free Energy (ΔG**)** and Enthalpy (ΔH**)** of NPNPSA-H with B3LYP/aug-cc-pVDZ, including vibrational corrections.

Products	**ΔG (eV)**	**ΔH (eV)**
273→201+72	1.52	2.05
273→186+44+43	-0.53	-1.57
273→138+135	-1.06	-0.54
273→122+151	3.20	3.73

Table 5.3.S9. Calculated changes in Gibbs Free Energy (ΔG) and Enthalpy (ΔH) of NPNPA-H with B3LYP/aug-cc-pVDZ, including vibrational corrections.

Products	ΔG (eV)	ΔH (eV)
209 →165+44	1.43	1.92
209 →150+59	4.21	4.92
209 →123+42+44	1.53	2.58
209 →122+43+44	1.95	2.97

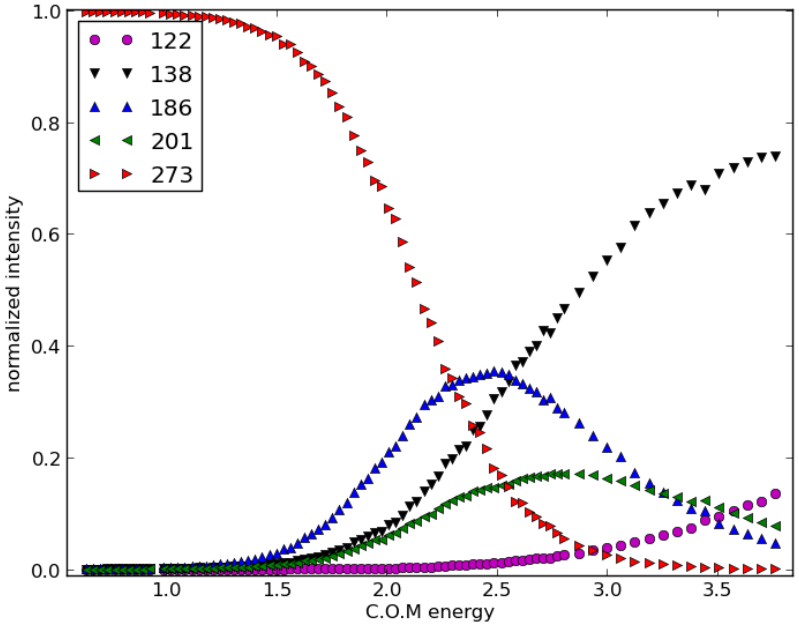

Figure 5.3.S4. The CID spectrum of deprotonated NPNPSA.

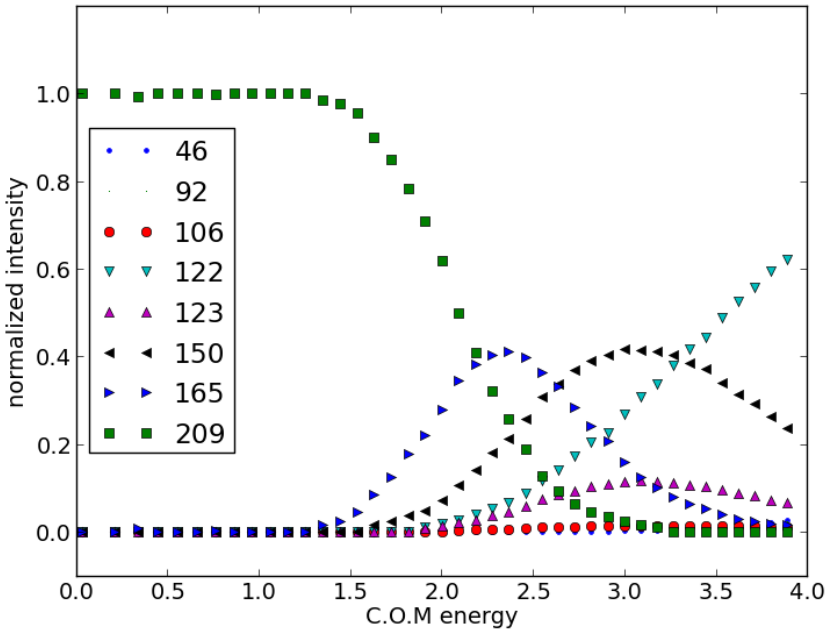

Figure 5.3.S5. The CID spectrum of deprotonated NPNPA.

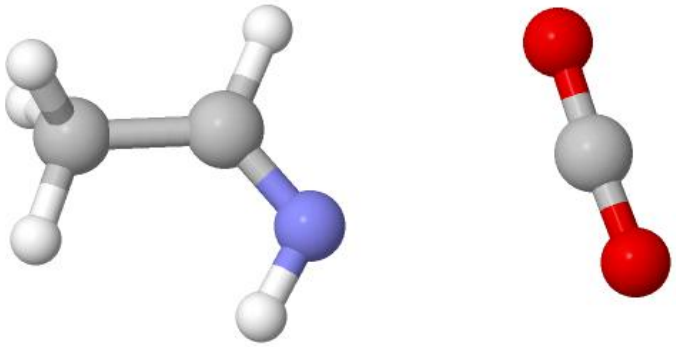

Figure 5.3.S6. Optimized structure of neutral 87 amu fragment for both NPNPA and NPNPSA. The CO_2 was originally bound to the carbon bound to the nitrogen.

APPENDIX A: Laser Maintenance

Continuous Argon Ion Laser Maintenance

1) Spectra-Physics; Model 265 Power Supply; Model 164 Plasma Tube; Single Wavelength 488 nm (optics may be purchased for additional wavelengths- see manual)

The spectra-physics laser is currently located behind SNIPES. The power supply was recently rebuilt by Dr. Chuck Long (in 2010). This laser should be turned on and let run for a full day every 6-8 weeks to burn off and relieve gas build-up within the laser tube.

Start- up Procedure:

- Turn on the main power breaker for the laser: PBW6-25,27,29
- Turn on Water Lines, there are 3: 1 for incoming water and 2 for outgoing; one of these outgoing lines flows directly into a small sink due to the building's low water flow compared to what is needed for the laser system to function properly.
- Check to make sure water lines are not visibly leaking; then check to make sure water LED "on" lights up. (if water LED "hot" lights, do not turn on the laser. This means the building water is too warm for the laser and the power supply to be cooled properly)
- Make sure the laser output is covered for any passersby.
- Check to make sure the set of LEDs labeled "line" are lit. If so, then the power switch may be flipped on (up position).
- The system may need a few seconds before the LED for the "ready" lights up. Once this LED lights, then the "start" button may be pressed.

- The laser being on and lasing is indicated by the meter on the power supply and by the visible lasing at the output of the tube of the 488nm blue line. (If the meter on the power supply indicates the laser is on and running but a low intensity of blue light or no light is visible at all, it may be the laser is out of alignment which can be of course corrected- see manual)
- Run laser for at least 6-8 hours with regular monitoring.

Shut-down Procedure:

- When the laser is being turned off, flip the main bar switch off (down position).
- Leave the water running for at least 10-20 minutes to cool down the system as you would the Coherent Laser. (Unlike the Coherent laser, this laser does not have an automatic digital system, so making sure the water is running for an ample amount of time to cool down the laser tube and power supply is extremely important!)
- Once the system is cooled down, the main power breaker may be switched off and the water lines turned off.

2) SNIPES main laser currently in use: Coherent INNOVA Argon Sabre R Series Ion Laser; INNOVA Heat Exchanger and Power Supply; Sabre DBW 25 Laser Tube (this tube does not have UV capability)

Start- up and Shut-down Procedures:

- Refer to J. M. Nilles Thesis. (A copy of protocol is also located next to the laser).

Laser Tube History:

As previously detailed in J. Chen's thesis, the argon ion laser tube was replaced in June 2011. Since installation of the new laser tube, a laser tube log has been kept and all parameter values are recorded every time the laser is turned on. This laser tube log is located on the desktop of the SNIPES computer. Again, when this laser is not in regular use, particularly over holiday breaks, the laser must be run for a full day at least once a month to keep gas from building up within the laser tube.

***Heat Exchanger Water Filter*:**

The water filter, also known as the de-ionizing/de-oxygenating (DI/DO) filter cartridge is located in the heat exchanger. While the laser manual says this should be replaced every year, it can last for several years as long as the water resistivity remains >100 kΩ–cm. If the water resistivity is below this value, the laser will automatically stop the laser initiation sequence; the user will not be able to use the laser until the problem is resolved. The water resistivity may be managed by changing the distilled water in the reservoir of the heat exchanger every few months. See manual for distilled water specifications. The latest DI/DO cartridge was replaced in November 2013, and will most likely not need a replacement for 2-3 years. There is not a current back-up cartridge ordered because it should only be shelf-stored for up to 3 months maximum before installation, as emphasized by the heat exchanger manual. The last cartridge purchased from Coherent cost approximately $600. Instructions on how to replace this filter may be

found in the heat exchanger manual print out kept near SNIPES (Section Five: Maintenance and Troubleshooting).

Pure Nitrogen Purge:

The pure nitrogen purge line must be used with every run (read as ~ 1cu. Ft./min on in line flow meter). Only pure nitrogen 5.0 ultra high purity (CGA 580 connection) should be purchased. The use of pure nitrogen is to ensure This is typically bought from Airgas, cost ~$100.

Other Notes:

- Regularly check the alignment of the laser beam by changing the aperture setting on the back of the laser from "18" to "OA". The laser aperture is always kept at the smallest open parameter, i.e. "18", while "OA" changes the aperture to the largest open parameter. The laser output power should not decrease by more than 4% when changed between these two values; otherwise the laser beam is not well aligned.
- The building water pressure and temperature will fluctuate on occasion. To better keep track of the temperature of the inlet water of the laser, always keep the display panel on the water temperature/pressure readings. That way if the inlet temperature increases above 35°C the user will know to either turn down the current (A) to the minimum of 40 A or to turn the laser completely off (if the inlet temperature of the water does not return below 35°C after a few minutes).

APPENDIX B: Cr^- Photoelectron Spectrum

This section describes the generation of the chromium anion, Cr^-, for calibration by using chromium hexacarbonyl, $Cr(CO)_6$, in the supersonic expansion nozzle ion source.

Calibrant anions used for experiments on our continuous ion photoelectron spectrometer include O^-, NO^-, and Cr^-. In general, the photoelectron spectrum of O^- is used, which consists of six closely spaced transitions (EA_a = 1.46 eV[1]). However it is useful to check the well-being of the instrument using the calibrant Cr^- because the atomic transitions are separated, narrow and precisely located peaks. The use of Cr^- allows for certain instrumental parameters to be checked, and tuned up if necessary, such as the energy scale compression factor, γ.[2]

The $Cr(CO)_6$ sample is placed in the stagnation chamber, heated, and co-expanded with argon gas. $Cr(CO)_6$ is used in place of pure chromium metal to obtain Cr^- because of the temperature limit of the source (~215°C due to the o-ring seals) is not high enough to generate vapors from a pure metal sample. When analyzing the mass spectrum produced from running $Cr(CO)_6$ in the system, signal ion intensity is made up mostly $Cr(CO)_n^-$ anions while Cr^- itself is barely detectable. The Cr^- signal intensity may be visible only up to 0.2-0.4 pA on the faraday cup located at the end of the beamline. However, during the photodetachment process, and setting the mass/charge ratio equal to Cr^- anions to pass through the mass selector, the large cross-section allows for a strong photoelectron signal intensity (see Figure B.1). Therefore, if the signal is not visible in the mass spectrum, that does not mean the anion is not being made in the source;

determination if Cr^- anions are being produced must always be checked via photodetachment.

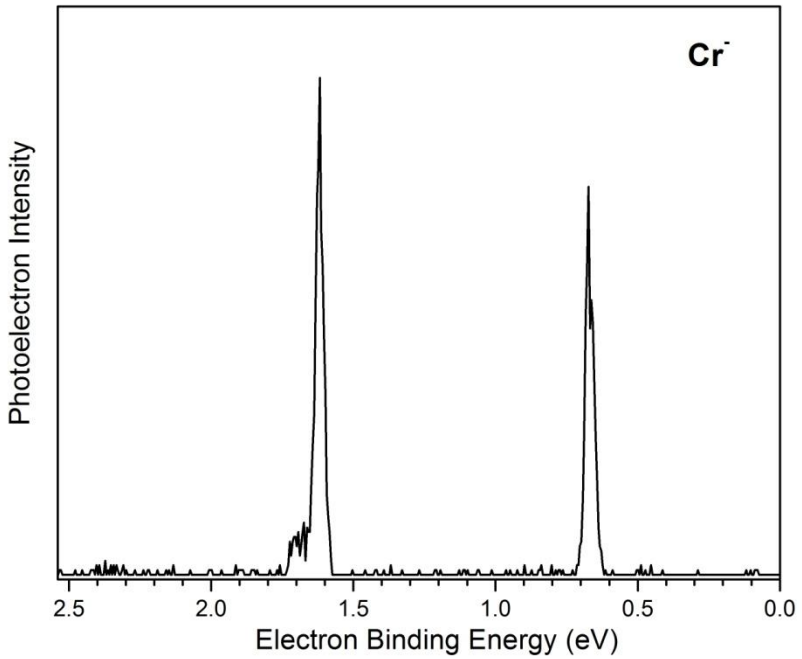

Figure B.1. Photoelectron Spectrum of the Cr^- anion recorded with 2.540 eV photons.

REFERENCES

1. Neumark, D. M.; Lykke, K. R.; Andersen, T.; Lineberger, W. C. *Phys. Rev. A* **1985**, *32*, 1890-1892.
2. Feigerle, C. S.; Corderman, R. R.; Bobashev, S. V.; Lineberger, W. C. *J. Chem. Phys*. **1981**, *74*, 1580-1598.

APPENDIX C: Pyridine$(CO_2)^-$ Photoelectron Spectrum

The mixed dimer anion of Pyridine$(CO_2)^-$ was originally recorded and published by S. K. Kim et al.[1] The original project idea on SNIPES was to look at what molecules would activate CO_2, i.e. form a chemical bond. A combination of experimental and calculations by Kim et al. suggested that a chemical bond, or at least chemisorption, occurs between the O_2C-N bond, forming the 1:1 anion complex.

This experiment using pyridine and CO_2 was repeated on SNIPES to see if it was possible to first form the same mixed dimer anion on our continuous apparatus. Indeed, this experiment is possible on our apparatus (see Figure C.1). The VDE is 1.46 eV which is in excellent agreement to our own DFT calculations within the group as well as with Kim et al.[1]

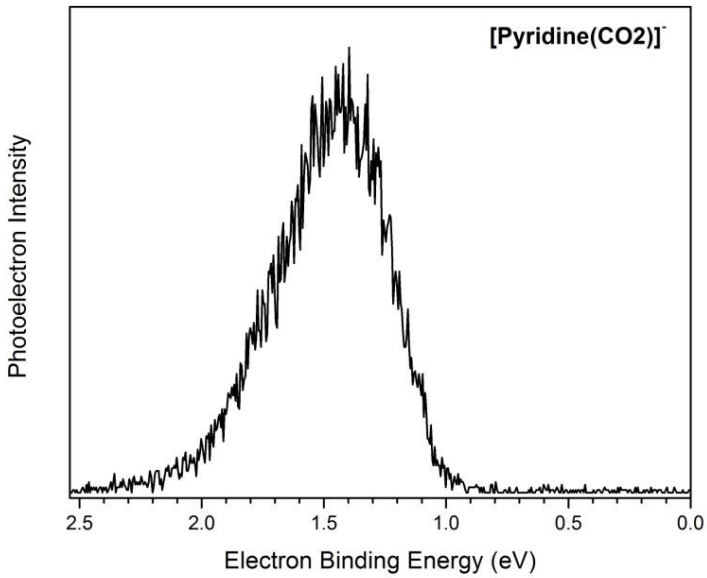

Figure C.1. Photoelectron Spectrum of the Pyridine(CO_2) anion recorded with 2.540 eV photons.

Kim et al. expanded their experiments with other azabenzene complexes with CO_2, including pyrazine, pyridazine, and triazine.[2] With the knowledge that these systems are able to generate the parent anion, there could implications for future projects in this area. Table C.1 lists the start of preliminary ab initio calculations on several molecules with similar characteristics to pyridine. This list may be useful in finding systems that may be interesting with furthers calculations and study.

Table C.1. List of molecules similar to pyridine (consisting of benzene rings, excess electron stabilization via π conjugation, etc.) that may be useful for future projects.

Molecule (+ CO_2)	EA_a	VDE	CO_2 Angle from Neutral → Anion	Shows O_2C-N Bond/ Notes
DFT B3LYP/6-311++G(d,p)				
Adenine	0.284	1.339	176.64 → 132.58	Yes
Melamine	1.3556	0.991	172.44 →129.96	Yes
Purine	0.772	1.907	177.32 → 133.01	Yes
Thiazole	0.1125	1.769	177.15 → 134.00	Yes
UHF/6-311G++(d,p)				
Acetaldehyde	0.8413	2.663	174.20 →135.72	Yes/ C Bonds to O
Acridine	2.299	2.697	175.06 → 134.95	Yes
Allopurinal	1.550	2.6345	125.84 → 133.43	Yes/ Seen in Neutral
Amitrol	0.9536	1.802	171.15 → 131.89	Yes
Cytosine	1.368	--	173.13 → 131.79	Yes/ H detaches in A
Imidazole	0.5658	0.8353	170.39 → 137.33	Yes
Imidazoline	0.813	1.145	142.98 → 133.77	Yes
Succinonitrile	1.278	3.585	177.26 → 133.86	Yes
Quinoline	1.910	2.386	168.03 → 132.41	Yes
Did not show C-N bonding but CO_2 still bent/activated				
Anthracene	1.576	--	178.12 → 135.45	No
Azobenzene	--	--	175.15 → 136.22	No
Benzonitrile	--	--	--	No
Monoethanolamine	0.4282	--	165.44 → 141.57	No
Pyrrole	--	--	177.46 →135.85	No
Tetrafluorobenzene	--	--	176.81 → 145.55	No

REFERENCES

1. Han, S. Y.; Chu, I.; Kim, J. H.; Song, J. K.; Kim, S. K. *J. Chem. Phys*. **2000**, *113*, 596.
2. Lee, S. H.; Kim, N.; Ha, D. G.; Kim, S. K. *J. Am. Chem. Soc*. **2008**, *130*, 16241.

APPENDIX D: Ethylene Carbonate Containing Cluster Anions

Experimental studies on ethylene carbonate (EC) began in our group with the photoelectron spectrum of the EC^- monomer anion.[1] Research of this molecule is now extending towards generating cluster anions of EC, which for example may model the solvent of EC in lithium batteries. Thus, to analyze the solvated electron with multiple EC molecules has various applications in better understanding EC as a bulk solvent.

Attempts to form clusters anions of EC were attempted on both continuous and pulsed instruments. The most success so far has come from the new pulsed apparatus, even though the EC monomer anion was originally observed on SNIPES. However, there are some species that were observed and photoelectron spectra collected, which may be of interest. While masses have yet to be confirmed (i.e. checking for any possible mass coincidences), the following estimates and spectra were collected for EC_2^-, $[EC(H_2O)]^-$, and $[EC(Ar)(H_2O)]^-$ (see Figures D.1-D.3). This data may be interesting for other potential studies on dipole-bound or weakly bound states.

Experimental Conditions

- Chamber 0 pressure: ~ 1 x 10^{-4} Torr
- Stagnation Chamber pressure: ~ 40 psig Argon (15 μm nozzle)
- Filament Bias: -55 to -65 V
- ECR: 0.02 mA/1.5 V (using Th/Ir filament)
- Filament Heater: N/A V/ 6 A
- Skimmer: < 1 V
- Extractor: + 700 V
- Beam : -500 V

The solid EC sample was placed in body of the stagnation chamber and heated between 50-100°C; depending on the nozzle size being used. Heat given off by the close

proximity of the filament also helped with heating the sample. Water was not added to the sample; since EC is hygroscopic, the water in the spectra is from what EC had absorbed from moisture in the air prior to being pumped under vacuum. Once temperature reached about 100°C, all signal related to EC would disappear. (More details recorded in laboratory notebook). Water clusters may also be observed at lower temperature depending on source conditions.

REFERENCE

1. Hammer N. I.; Hinde, R. J.; Compton, R. N.; Diri, K.; Jordan, K. D.; Radisic, D.; Stokes, S. T.; Bowen, K. H. *J. Chem. Phys.* ***2004, 120***, 685.

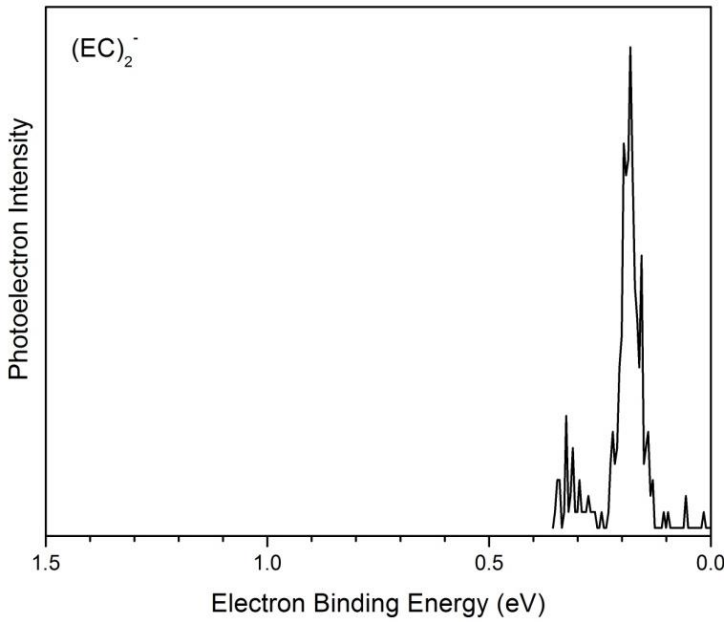

Figure D.1. Photoelectron Spectrum of possible EC_2^- anion at 2.540 eV photons (showing PES from 0-1.5 eV).

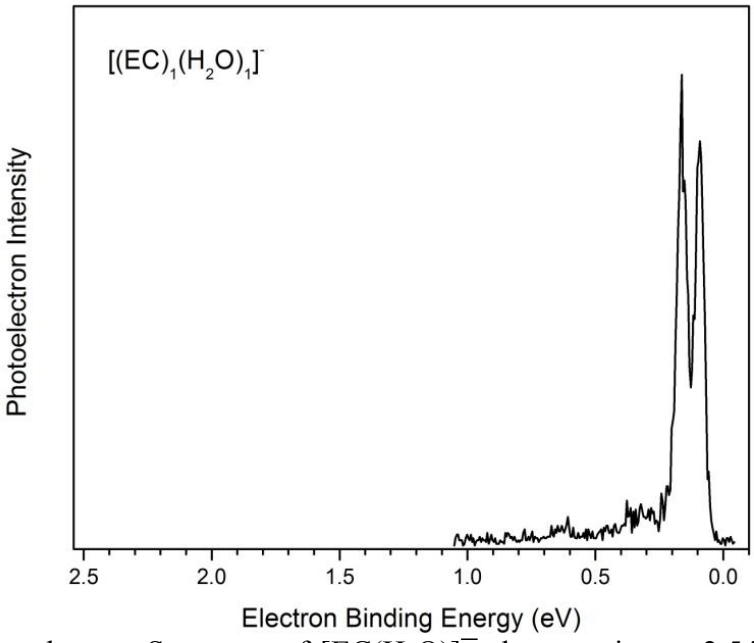

Figure D.2. Photoelectron Spectrum of $[EC(H_2O)]^-$ cluster anion at 2.540 eV photons. Note the appeance of two resolved peaks of near equal intensity at very low EBE.

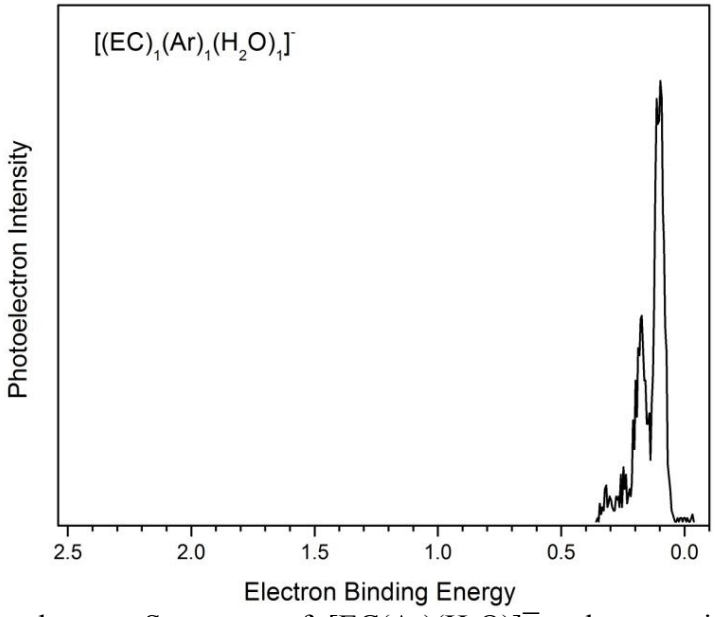

Figure D.3. Photoelectron Spectrum of $[EC(Ar)(H_2O)]^-$ cluster anion at 2.540 eV photons. Note the appearance of the same two resolved peaks at very low EBE but now significantly differ in intensity.

APPENDIX E: Photoelectron Spectra of Azobenzene

Azobenzene is the simplest representative of the azo compounds (R-N=N-R). The emphasis on its chemically stability and robustness allows for this molecule to be at the structural core for derivatives synthesized for photocontrolled applications.[1-3] Its ability to strongly absorb light, and thus has a rich optical absorption spectrum,[4] makes it an interesting case observing a cis-trans photoisomerization. Trans-azobenzene undergoes isomerization to its cis form, which sits ~0.5 eV higher in energy, through a ~2 eV barrier.

From this information, we collected a set of unique photoelectron spectra analyzed at several different photons energies. Figure E.1 shows the photoelectron spectrum taken of azobenzene on the continuous source apparatus (SNIPES) with the CW Argon ion laser operating at 488nm (2.540 eV photons). This spectrum features two broad bands. The higher electron binding energy (EBE) band is due to access to the cis isomer from an excited anion resonant state, while the lower EBE band is due mostly to access to the trans isomer from the same resonant state.

Figure E.2 shows the photoelectron spectra of azobenzene taken on the pulsed source apparatus (PIPES) using a Nd:YAG laser operating at second (532nm, 2.33 eV/photon, third (355 nm, 3.49 eV/photon), and fourth (266nm, 4.66 eV/photon) harmonic wavelengths. The peaks observed in these three spectra are labeled as follows: peaks labeled A refer to access to the (0,0) transition, peaks labeled R refer to access due to the anion's absorption resonance, peaks B refer to access to the triplet state[5] of the neutral, and peaks C refer to access to the electronically-excited state of the neutral. In

conclusion, the three processes in our spectra include; direct photodetachment to the ground and known excited states of neutral azobenzene, several resonant transitions to electronically-excited azobenzene anion states, and decay from one of those excited anion states to not only the trans- but also the cis- isomers of neutral azobenzene.

REFERENCES

1. Merino, E.; Ribagorda, M. *J. Org. Chem*. **2012**, *8*, 1071.
2. Liu, Z. F.; Hashimoto, K..; Fujishima, A. *Nature* **1990**, *347*, 658.
3. Ikeda, T.; Tsutsumi, O. *Science* **1995**, *268*, 1873.
4. Neta, P; Levanon, H. *J. Phys. Chem*. **1977**, *81*, 2288
5. Dubecký, M.; Derian, R.; Horv thov , L.; Allan, M.; Štich, I. *Phys. Chem. Chem. Phys*. **2011**, *13*, 20939.

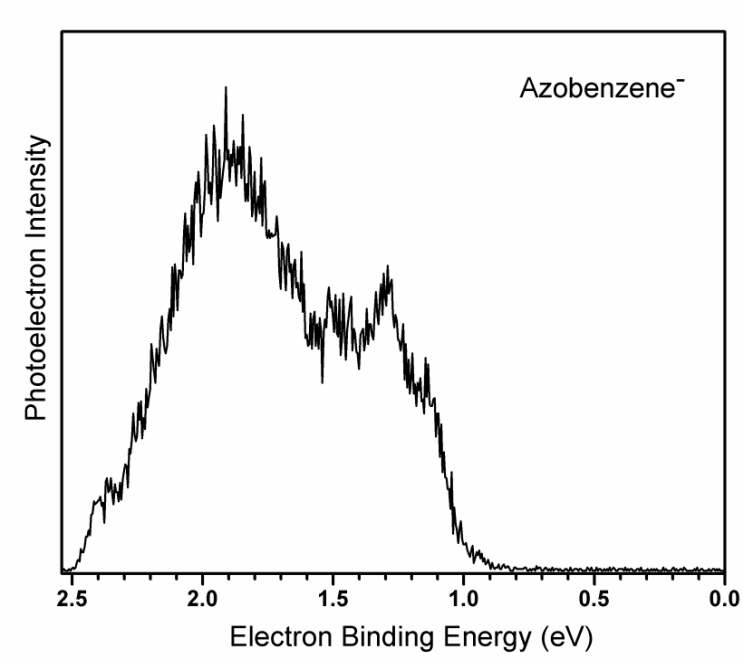

Figure E.1. Photoelectron spectrum of azobenzene recorded using 2.540 eV photons.

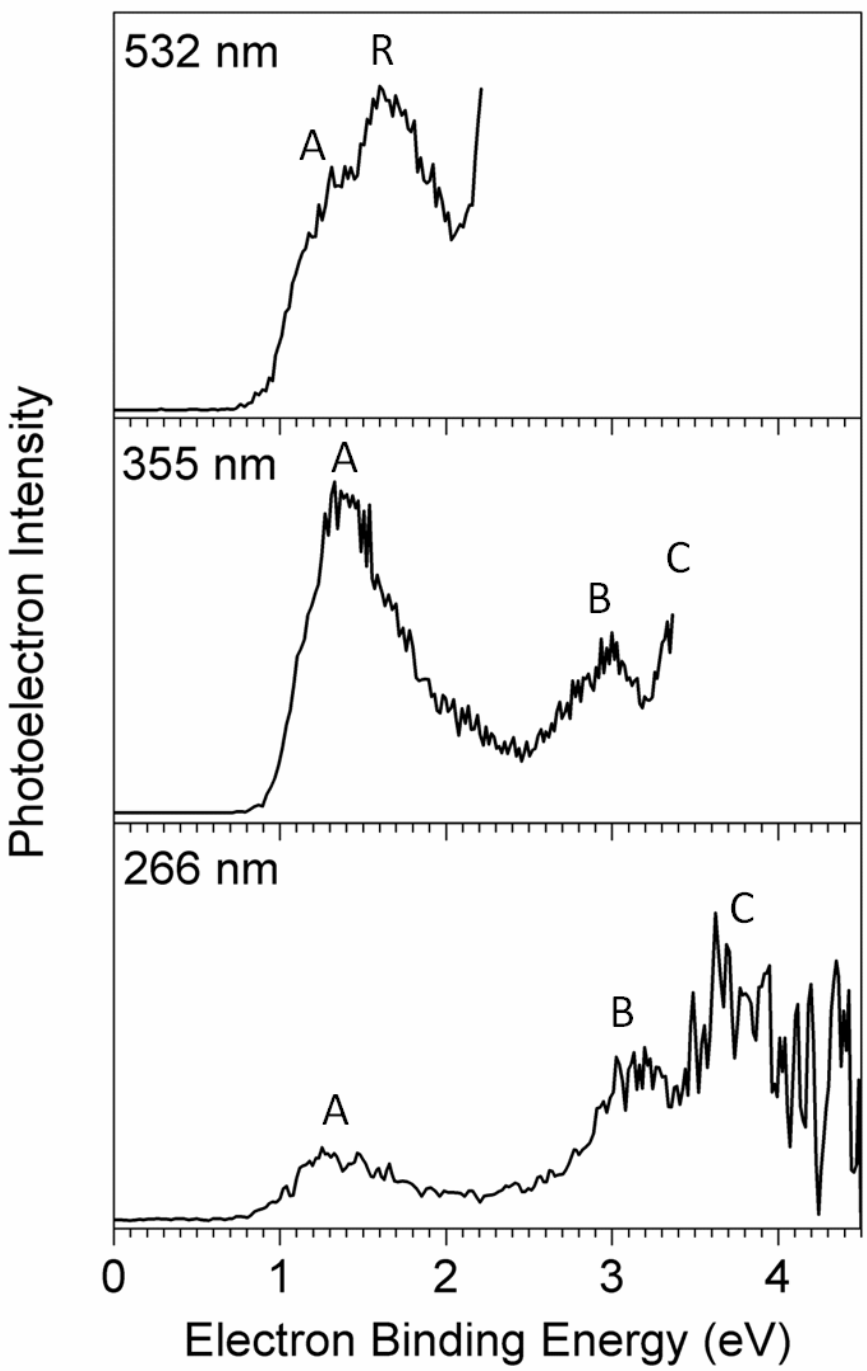

Figure E.2. Photoelectron spectra of azobenzene recorded using 2.33 (532 nm), 3.49 (355 nm), and 4.66 (266 nm) eV photons.

CURRICULUM VITA

Angela Marie Buonaugurio
Department of Chemistry • Johns Hopkins University
3400 North Charles Street • Baltimore, MD 21218
(410) 516-4675 • angelab@jhu.edu

EDUCATION

Ph.D. Physical Chemistry, Johns Hopkins University
May 2014 Advisor: Dr. Kit H. Bowen, Jr.

M.A. Physical Chemistry, Johns Hopkins University May 2011

B.A. Chemistry/Minors in Mathematics & Physics May 2008
summa cum laude, Notre Dame of Maryland University

RESEARCH EXPERIENCE

Graduate Student Research

Johns Hopkins University, Department of Chemistry, Baltimore, MD 2008 –*present*
(Dr. Kit H. Bowen, Jr.)

- Conducted investigations on size-selected gas phase clusters using the technique of negative ion photoelectron spectroscopy. Such studies bridge the conceptual gap between the individual molecule and the bulk, exploring energetic properties such as electron affinities and step-wise solvation energies. Cluster systems studied include nucleobases, modified nucleobases, metal oxides, organic compounds, and acid-base pairs.
- *Developed Chemical/Analytical Skills:* Mass spectrometry (magnetic sector, quadrupole, Wien velocity filter, TOF), hemispherical analyzers, photoelectron spectroscopy, UV-VIS spectroscopy, ICR, NMR
- *Developed Theoretical/Software Skills:* OriginPro, Gaussian 03W, GAMESS, SIMION, Chem3D Pro 13.0, LabVIEW, Mathematica, Microsoft Office
- *Other Specialized Skills*: Vacuum equipment, ion sources, use of ion optics, oscilloscopes, lasers, design and development of instrumentation and electronic circuits, training of new graduate and undergraduate students

Lab Support Technician- Science & Technology Corporation (STC) 2007-2009
Edgewood Chemical Biological Center (ECBC) Research and Technology Directorate, BioDefense Team, Aberdeen Proving Ground, MD

- Analyzed UV-based biological collection and detection to determine instrumentation performance; when exposed to inactivated agents, simulants, and interferrent materials.
- *Developed Chemical/Analytical Skills:* Fourier-Transform Infrared (FTIR) spectroscopy, Raman spectroscopy, preparing of biological samples, temperature monitoring, processing spectra results

- *Other Specialized Skills:* Provided general microbiology lab technical support and laboratory maintenance, medical and hazardous waste disposal; regulatory compliance, versed in Good Laboratory Practices (GLP) for biosafety Levels 1 and 2 microbiology labs

Undergraduate Student Research 2007-2008
Notre Dame of Maryland University, Department of Chemistry, Baltimore, MD
(Dr. Jocelyn McKeon).

- Analyzed solute-micelle binding constants with various dilute sulfa-compounds solutions using HPLC methods.

Summer Intern, Science & Engineering Apprenticeship Program (SEAP)
2003-2006
Edgewood Chemical Biological Center (ECBC) Research and Technology Directorate, BioDefense Team, Aberdeen Proving Ground, MD

- Conducted analysis of bacillus spores over cell lifecycle under differing growth conditions (temperature, medium) using infrared spectroscopy to distinguish genera, species, and/or strains of bacterial spores from one another.
- *Chemical/Analytical Skills:* FTIR, Raman, sample processing, processing of FTIR and Raman Spectra results

TEACHING EXPERIENCE

Teaching/Research Assistant, Johns Hopkins University 2008-2011

- Physical Chemistry III Laboratory
- General Chemistry II Lecture
- Experimental Methods in Physical Chemistry Lecture

Chemistry Tutor, Notre Dame of Maryland University 2005-2008

- General Chemistry I and II for Department

AWARDS AND HONORS

- Eugene W. and Susan C. Zeltmann Fellowship, Johns Hopkins University (May 2012)
- Chemistry Department Award, Notre Dame of Maryland University (May 2008, February 2006)
- American Chemical Society Award, Maryland Chapter, Notre Dame of Maryland University (December 2007)
- Academic Honors every semester, Notre Dame of Maryland University (2004-2008)

MEMBERSHIPS

- American Chemical Society
- Kappa Mu Epsilon Mathematic Honor Society
- Delta Epsilon Sigma National Scholastic Honor Society, Alpha Delta Chapter

CONFERENCE POSTERS/PRESENTATIONS

- 67th International Symposium on Molecular Spectroscopy, Ohio State University, Ohio, 6/18 -6/22, 2012 *Presentation*: *"**Photoelectron Spectroscopy of Rare-Gas Solvated Nucleobase Anions**."*
- XVIIth Symposium on Atomic, Cluster and Surface Physics (SASP) 2010, University of Obergurgl, Austria, 1/24-1/29, 2010 *Poster: "**Electron-Induced Proton Transfer in Acid-Base Reactions: Anion Photoelectron Spectroscopic Studies**."*

- S^3C: Symposium on Size Selected Clusters 2009, Brand, Austria, 3/8-3/13, 2009 *Poster: "**Electron-Induced Proton Transfer in Acid-Base Reactions: Anion Photoelectron Spectroscopic Studies**."*

PUBLICATIONS

- **A. Buonaugurio**, X. Zhang, S. T. Stokes, Y. Wang, G. B. Ellison, and K. H. Bowen, *accepted* ***"The Photoelectron Spectrum of the Benzaldehyde Anion".***

- **A. Buonaugurio**, J. Graham, A. Buytendyk, K. H. Bowen, M. R. Ryder, Z. G. Keolopile, M. Haranczyk, and M. Gutowski, *submitted* ***"Remarkable Electrophilicity of the Oxalic Acid Monomer Anion: A Photoelectron Spectroscopy and Theoretical Study".***

- J. T. Kelly, S. Xu, J. D. Graham, J. M. Nilles, D. Radisic, **A. M. Buonaugurio**, K. H. Bowen Jr., N. I. Hammer, and G. S. Tschumper, *submitted* ***"Photoelectron Spectroscopic and Computational Study of Hydrated Pyrimidine Anions.".***

- M. Neumaier, M. Olzmann, K. Boggavarapu, K. H. Bowen, B. Eichhorn, S. Stokes, **A. Buonaugurio**, R. Burgert, H. Schnoeckel, *J. Am. Chem. Soc*., **136**, 3607 (2014) ***"The Reaction Rates of O_2 with closed-shell and Open-Shell Al_x^- and Ga_x^- Clusters Under Single Collision Conditions: Experimental and theoretical Investigations Towards a Generally Valid Model for the Hindered Reactions of O_2 with Metal Atom Clusters".***

- L. Chomicz, M. Zdrowowicz, F. Kasprzykowski, J. Rak, **A. Buonaugurio**, Y. Wang, and K. H. Bowen, *J. Phys. Chem. Lett*., **4**, 2853 (2013) ***"How to Find Out Whether a 5-Substituted Uracil Could Be a Potential DNA Radiosensitizer".***

- J. Lambert, J. Chen, **A. Buonaugurio**, K. H. Bowen, C.-L. Do-Thanh, Y. Wang, M. D. Best, R. N. Compton, and T. Sommerfeld, *J. Chem. Phys.* **139,** 224308 (2013) ***"Combined Photoelectron, Collision-Induced Dissociation, and Computational Studies of Parent and Fragment Anions of N-paranitrophenylsulfonylalanine and N-paranitrophenylalanine".***

- B. H. Smith, **A. Buonaugurio**, J. Chen, E. Collins, K. H. Bowen, R. N. Compton and T. Sommerfeld, *J. Chem. Phys.* **138**, 234304 (2013) ***"Negative ions of p-nitroaniline: Photodetachment, collisions, and ab initio calculations".***

- J. Chen, **A. Buonaugurio**, O. Dolgounitcheva, V. G. Zakrzewski, K. H. Bowen and J. V. Ortiz, *J. Phys. Chem. A*, **117**, 1079 (2013) ***"Photoelectron Spectroscopy of the 6-Azauracil Anion".***

- X. Li, W. Zheng**, A. Buonaugurio**, A. Buytendyk, K.H. Bowen, and K. Balasubramanian, *J. Chem. Phys.*, **136**, 154306 (2012) ***"Photoelectron spectroscopy of the molecular anions, ZrO^-, HfO^-, $HfHO^-$, and HfO_2H^-".***

- **A. Buonaugurio**, J. D. Graham, A. M. Buytendyk, and K. H. Bowen, *to be submitted* ***"Electron Induced Proton Transfer from HCl to the Superbase 1,8-Bis(dimethylamino)naphthalene".***

- Z. G. Keolopile, M. Gutowski, **A. Buonaugurio**, E. Collins, X. Zhang, J. Erb, T. Lectka, K. Bowen, and M. Allan, *to be submitted* ***"Intramolecular Proton Transfer in Acetoacetic Acid Induced by a π* Excess Electron".***

- S. T. Stokes**, A. Buonaugurio**, Y. Wang, S. N. Eustis, and K. H. Bowen, *to be submitted* ***"Anion Photoelectron Spectroscopy of the Linear $C_nH_{2n+1}O^-$ (n=1-9) Alkoxides".***

- J. Chen, **A. Buonaugurio**, and K. H. Bowen, *manuscript in preparation* ***"Photoelectron Spectroscopy of Rare Gas-Solvated Nucleobase Anions".***

- A. Whiteside, M. Haranczyk, M. Gutowski, J. Chen, S. N. Eustis, J. H. Hendricks**, A. Buonaugurio**, K. H. Bowen, *manuscript in preparation* ***"Electron-Driven Proton Transfer in Hydrogen Bonded Dimers".***

- **A. Buonaugurio**, X. Zhang, K. H. Bowen, and R. N. Compton, *manuscript in preparation* ***"Photoelectron Spectroscopy of the Azobenzene Anion".***